The Processing and Characterisation of Recycled NdFeB-type Sintered Magnets

By

Malik John Jamaji Degri

A thesis submitted to the University of Birmingham
for the degree of DOCTOR OF PHILOSOPHY

School of Metallurgy and Materials
College of Engineering and Physical Sciences
University of Birmingham

August 2014

Synopsis

A study of the processing and characterisation of sintered NdFeB magnets made from recycled feed stock was undertaken. Initially the hydrogen decrepitated (HD) powder was investigated using two different milling techniques ball milling and burr milling. The powders were analysed with optical microscopy, with the aid of a magnetic field. It was found that with light milling (burr milling) the HD powder breaks up to a similar particle size to that of the grain size of the starting material, with the fracture mechanism mainly intergranular in nature. A data logging system was built to investigate the desorption behaviour of green compacts during sintering. Desorption traces showed desorption from the matrix phase and the intergranular Nd-rich phase. The start of desorption was seen to shift to lower temperatures as the mean particle size of the green compact was reduced. For the processing route used in this work intergranular additions of neodymium hydride were required to increase the density and magnetic properties.

To investigate the oxidation behaviour of lightly milled HD powder, powder was exposed to air for varying times. The exposed powder was aligned pressed and sintered. The Nd-rich desorption peak reduced with exposure time, the density and magnetic properties also reduced. Post exposure additions of Intergranular neodymium hydride to the powder recovered density and magnetic properties. The exposure of the rare earth lean milled HD powder was compared with milled HD powder with a higher dysprosium and cobalt content. A difference in the behaviour of the Nd-rich peak reduction with time was observed. Using a Pirani gauge based logging system the information on the desorption behaviour of bulk samples of hydrogenated material up to 15g has been observed. The addition of intergranular neodymium hydride to heavily oxidised powder displayed a recovery in the density and magnetic properties.

This thesis is dedicated the memory of

Dr. Andrew John Williams

to whom I will be eternally grateful for inspiring me to continue studying the field of magnetic materials.

Acknowledgement

I would like to thank Dr Allan Walton and professor Rex Harris for their supervision since the untimely passing of Dr Andy Williams. I would like to thank them for their encouragement and advice throughout the project especially towards the latter stages. Thanks to Dr Alex Bevan and Andy Bradshaw for technical assistance and advice and the odd beer at Staff House, it has been greatly appreciated. I would like to thank all the members of the magnetic materials group, it has been a pleasure working with you all. I would like to thank everyone in the Metallurgy and Materials department it has been an enjoyable experience. I am grateful for the support of the EPSRC.

A special thanks to my family who have supported me throughout.

Contents

List of Abbreviations

ADC	– Analog-to-digital conversion
at%	– Atomic Percent
$(BH)_{max}$	– Maximum Energy Product
Br	– Remanence
BSE	– Back Scattered Electron
CSV	– Comma Separated Values
DSC	– Differential Scanning Calorimetry
DTA	– Differential Thermal Analysis
dhcp	- double hexagonal close packed
Fe2B	– Ferro-boron
f.c.c	– face centred cubic (crystal structure)
G	– Gauss
HAST	– Highly Accelerated Stress Test
H	– Applied Field
H2	– Hydrogen
Hc	– Coercivity
h.c.p	– hexagonal close packed
HD	– Hydrogen Decrepitation

HDDR	– Hydrogenation, Disproportionation, Desorption and Recombination
HDTA	– Hydrogen Differential Thermal Analysis
ICP	– Inductively Coupled Plasma
J	– Polarisation
jHc	- coercivity
kA m-1	– kilo Amps per metre
kJ m-3	– kilo Joules per metre cubed
KOe	– Kilo-oersted, unit of magnetic field strength
M	– Magnetisation
MGOe	– Mega Gauss Oersted
Ms	– Saturation Magnetisation
Nd2O3	– Neodymium Oxide
NdFeB	– Neodymium Iron Boron
NdH	– Neodymium Hydride
NdH_2	– Neodymium Dihydride
nm	– nanometres
ppm	– parts per million
RE	– Rare Earth
REE	– Rare Earth Element
RIP	– Rubber Isostatic Pressing

SD	– Secure Digital (card)
SEI	– Secondary Electron Imaging
SEM	– Scanning Electron Microscope
SmCo	– Samarium Cobalt
T	– Tesla
Tc	– Curie Temperature
TPD	– Temperature Programmed Desorption
TM	– Transition Metal
TMA	– Thermomanometric analysis
TEM	– Transmission Electron Microscopy
USB	– Universal Serial Bus
χ	– Magnetic Susceptibility
VCM	– Voice Coil Motor
WEEE	– Waste Electronics and Electrical Equipment
wt%	– Weight Percent
XRD	– X-Ray Diffraction

Chapter 1. Introduction

Products containing NdFeB-type magnets are already ubiquitous and demand is set to increase due to the shift towards more energy efficient and renewable technologies, such as hybrid and electric vehicles and wind turbines.

The increasing demand is causing pressure on the production of the rare earths required to make the magnets, thus causing price fluctuations. The production of the rare earths is also energy intensive and is associated with potentially harmful waste material such as thorium and uranium.

“The demand for rare earths is increasing as we transition towards a green, low-carbon economy. This is putting strain on supply.” (Binnemans et al, 2013).

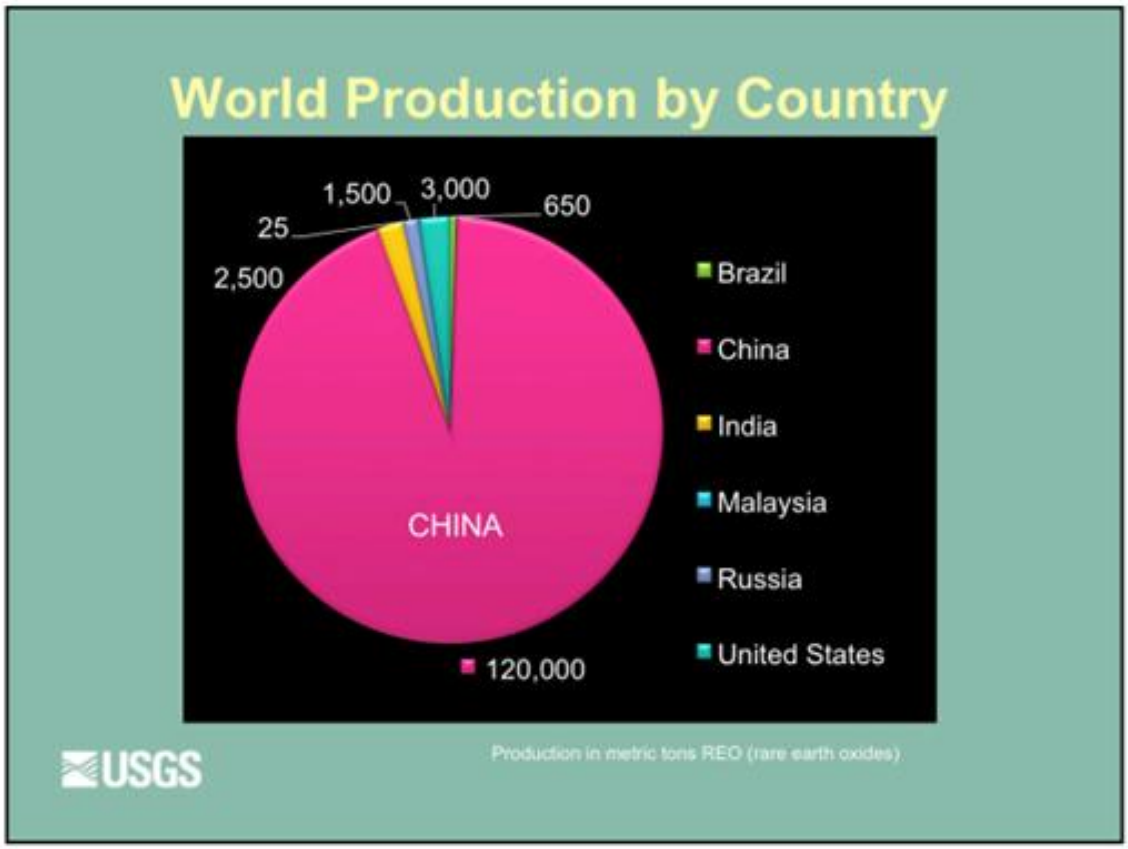

Fig.1. Global production of rare earth elements (expressed as total rare earth oxides in metric tons for 2009).

Source of data: US Geological Survey Mineral Commodity Summaries, 2010.

As of 2013, China produced approximately 87% of the worlds light rare earth elements (U.S Geological Survey, 2013) whilst possessing less than 40% of proven reserves, (fig.1). (Binnemans et al, 2013). China also specialises in the processing and production of higher value end products such as rare earth permanent magnets and phosphors. Due to the rising global demand for Rare Earth Elements (REEs) for current and future use, China is using quotas to limit exports and satisfy their increasing domestic demand.

In 2010 the European Commission produced the Critical Raw Materials for the European Union Report. The report highlighted the REEs as the most critical raw materials group, with the highest supply risk, (European commission 2010). Similar views were expressed by the

U.S. Department of Energy. Fig.2. shows the U.S. Department of Energy Medium Term (2015 - 2025) Criticality Matrix, showing the five rare-earth elements they perceive as being most critical in terms of risk to supply.

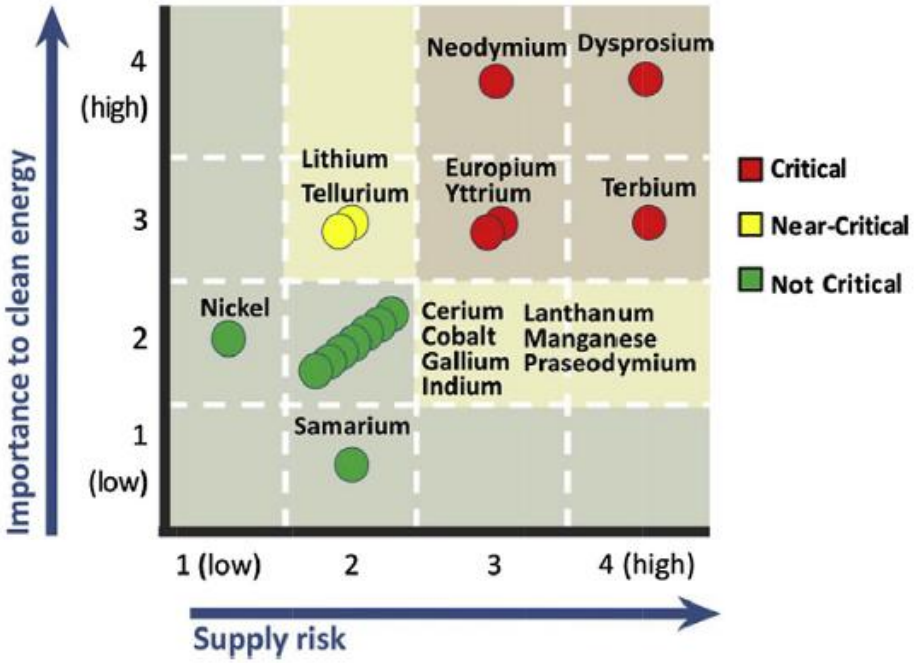

Fig.2. Medium term (2015 - 2025), criticality matrix, (showing the five most critical rare-earth elements: Y, Nd, Eu, Tb and Dy.) U.S. Department of Energy, 2011.

The five most critical REEs are said to be neodymium (Nd), europium (Eu), terbium (Tb), dysprosium (Dy) and yttrium (Y). The cost of production in China is likely to increase due to environmental and social costs and there is also the potential for labour costs in China to rise. This is likely to have an impact on China's potential to increase production significantly in order to drive prices down, (Humphries, 2013).

The current risk to supply can be mitigated by investing in sustainable primary mining either from old deposits or new REE deposits to diversify supply. The time frame for mines to come

on stream can be significant and investment in the processing and refining stages will also be required, (Humphries, 2012). One other possible solution would be to recycle the existing stock of rare earth materials contained in spent electrical equipment.

Recycling would improve the security of supply, be more environmentally friendly and could potentially be more cost effective. The processing of rare earths to form NdFeB-type magnets usually employs the HD (hydrogen decrepitation) process. The cast material reacts with hydrogen, forming a hydride and a hydrogenated solution. During this process, the material breaks up (decrepitates). The process reduces the amount of mechanical milling required to achieve a suitable particle size distribution for sintering.

This project is focused on the recycling of rare earth lean sintered magnets using the HD process. Investigating various aspects of the processing including desorption, milling and addition of intergranular additions.

1.1. Introduction to Magnetism

A magnetic field exists whenever a charge is in motion. Fig.3. shows the magnetic field generated by the flow of electrons in a wire.

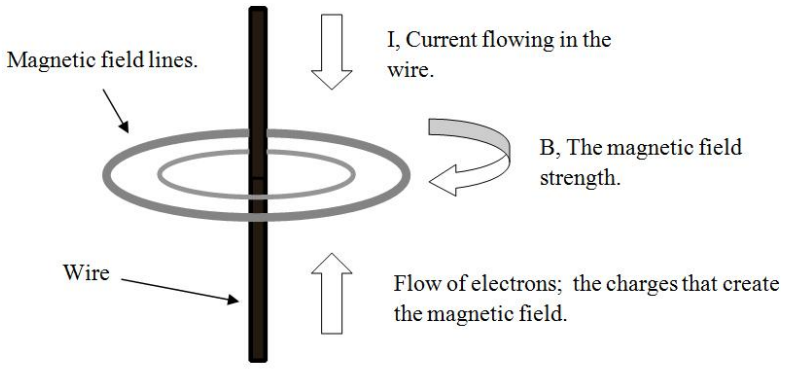

Fig.3. Magnetic field generated by current in a straight wire.

In an atom, the spin and orbital motion of the electrons both have a magnetic moment associated with them. The total magnetic moment is a combination of the spin, orbital moments and precession of the electron about the nucleus in an applied field. A magnetic dipole can be described as a tiny magnet equivalent to a flow of charge around a loop.

In the case of a magnetic material the magnetic moment is dominated by the electron spin. An atom will possess an overall magnetic moment when there are unpaired electrons and the spin moments are not cancelled. The magnetic moment is at a maximum when the outer shell is half full. Magnetisation is a vector field that expresses the density of these magnetic dipole moments in a material.

$$M = \frac{N}{V} m$$

M = magnetisation N = number of magnetic moments in the sample

V = volume m = vector that describes the magnetic dipole

Equation 1. Magnetisation.

1.2. Magnetic Behaviour of Solids

The behaviour of materials when under the influence of a magnetic field may be different and can be categorised into five types, ferromagnetism, paramagnetism, diamagnetism, antiferromagnetism and ferrimagnetism. Fig.4. shows the periodic table and the types of magnetism associated with each element. The types of magnetism can be expressed by the magnetic susceptibility of the materials. The magnetic susceptibility is a constant that indicates the degree of magnetisation of a material in response to an applied magnetic field.

$$\chi = \frac{M}{H}$$

χ = magnetic susceptibility (dimensionless) H = the applied field (Am^{-1})

M = magnetisation of the material ($JT^{-1}m^{-3}$)

Equation 2. Magnetic susceptibility.

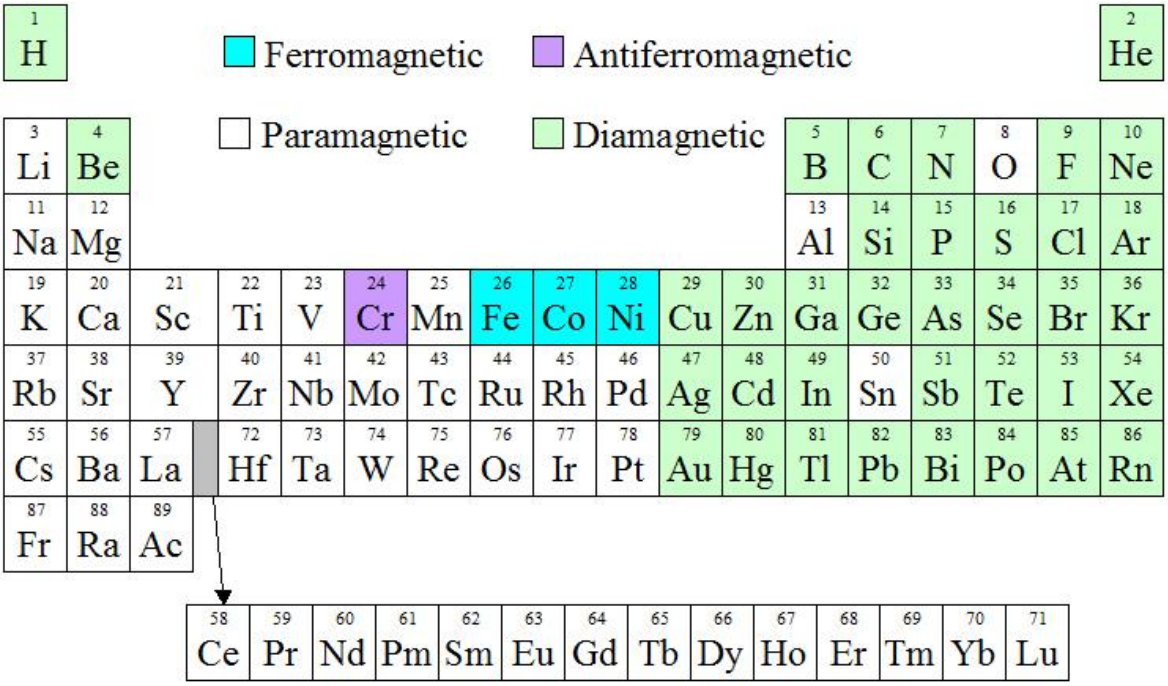

Fig.4. The ferromagnetic, antiferromagnetic, paramagnetic and diamagnetic (elements)

1.2.1. Diamagnetism

All materials exhibit diamagnetic behaviour, which weakly repels an applied field. However, due to the weakness of the diamagnetic effect, the results are often overshadowed by other magnetic behaviours such as paramagnetism. The origin of diamagnetism is due to precession of the orbital motion of electrons around the nucleus in response to an applied field. The change opposes the applied field giving a small negative value for the susceptibility. Fig.5. shows that the atoms have no magnetic moment, but they have a small negative response to an applied field. Examples are Cu, Si, and H_2O.

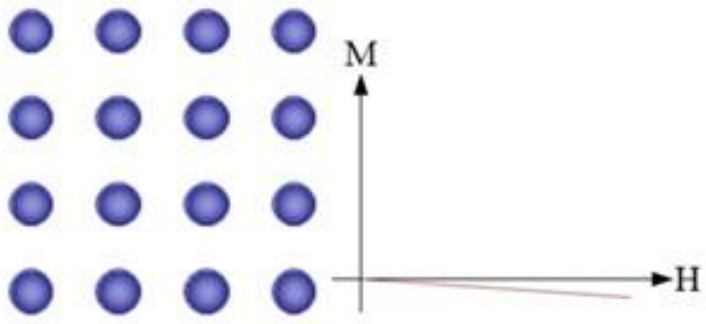

Fig.5. Diamagnetism, atoms have no magnetic moment. Susceptibility is small and negative.

1.2.2. Paramagnetism

The atoms in paramagnetic materials have a permanent dipole moment due to unpaired electrons. The dipole moments are randomised but align with an external field showing a positive susceptibility, seen in fig.6. In paramagnetism, the interaction between neighbouring dipoles is weak and the materials don't retain any magnetism once the applied field is removed. Thermal motion can randomise the spin orientations and only a small fraction of the spins are orientated. Some examples are Al and diatomic gasses such as O_2.

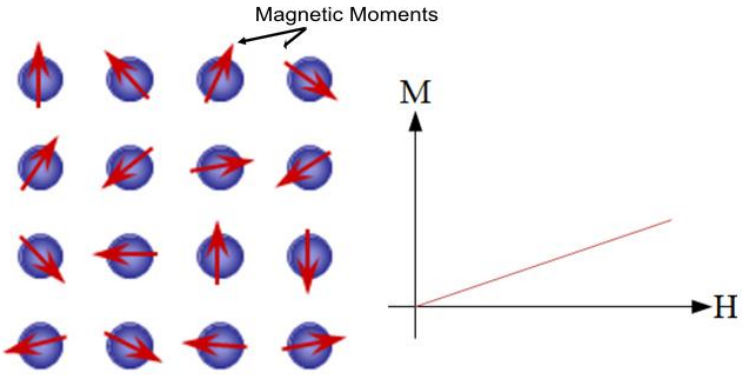

Fig.6. Paramagnetism. Randomly orientated magnetic moments, susceptibility is small and positive.

1.2.3. Ferromagnetism

Ferromagnetic materials exhibit long range ordering at the atomic level. Un-paired electron spins line up in parallel regions to form magnetic domains, which exist in the absence of an external field. This is known as the exchange interaction.

In ferromagnetic materials the magnetic dipoles align spontaneously and this gives rise to a spontaneous magnetization which exists in the absence of an external field, see fig. 7.

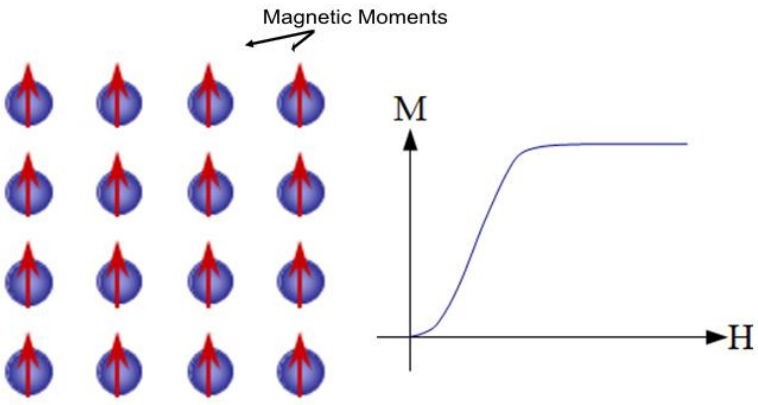

Fig.7. Ferromagnetism. Atoms have parallel aligned magnetic moments

The exchange interaction is related to the Pauli Exclusion Principle which states that two electrons with the same spin cannot occupy the same "position". When orbitals of outer valence electrons overlap with adjacent electrons from neighbouring atoms there is an exchange force between them. This allows electrons to exchange places between atoms, carrying with them information about the direction of the dipole moment which causes the tendency for spins to be aligned. This exchange energy can be either positive or negative. Increases in temperature in the system cause the alignment of the spins to be disturbed and magnetisation decreases. The temperature at which the magnetisation drops to zero is called the Curie point. The exchange energy is very sensitive to interatomic spacing and the diameters of unfilled sub shells. The Bethe-Slater curve plots the ratio of the interatomic spacing against the radius of the 3d sub shell, against the exchange integral, which is proportional to the exchange energy see fig.8.

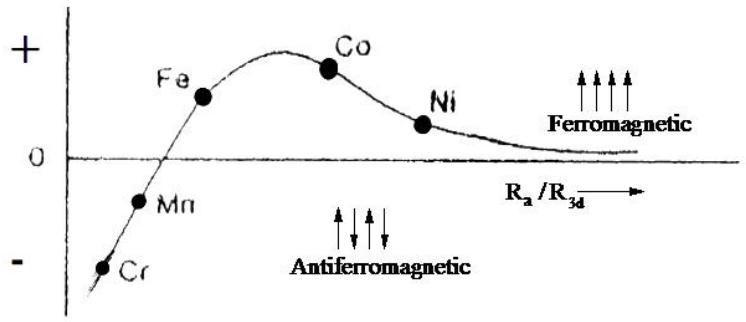

Fig.8. Bethe-Slater Curve.

Cr, Mn, Fe, Co, and Ni are shown on the Bethe-Slater Curve. The position on the curve relates to the strength of the exchange interaction and whether the element is ferromagnetic or antiferromagnetic. This depends on whether the exchange energy is positive; Fe, Ni and Co, or negative such as Cr and Mn, which are antiferromagnetic.

The effect of ferromagnetism is rare and is only exhibited by Fe, Co and Ni. (Gd exhibits ferromagnetic behaviour only at sufficiently low temperatures).

1.2.4. Antiferromagnetism

Antiferromagnetism is similar to ferromagnetism, as seen on the Bethe-Slater Curve, with exchange interactions causing ordering. However, due to the anti-parallel nature of the magnetic moments, the susceptibility is small and positive. Examples include Mn, Cr and many of their compounds such as MnO.

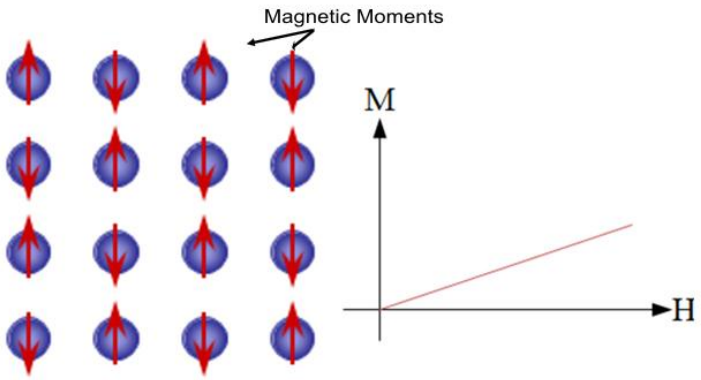

Fig.9. Antiferromagnetism

1.2.5. Ferrimagnetism

Ferrimagnetic materials exhibit spontaneous magnetisation. However not all of the moments are aligned. These materials have mixed parallel and anti-parallel moments. Where the opposing moments are not equal, susceptibility is large below the Curie temperature (Tc).

The Curie temperature is the point at which permanent magnetism changes to induced magnetism. Typical examples include $SrFe_{12}O_{19}(SrO{:}6Fe_2O_3)$.

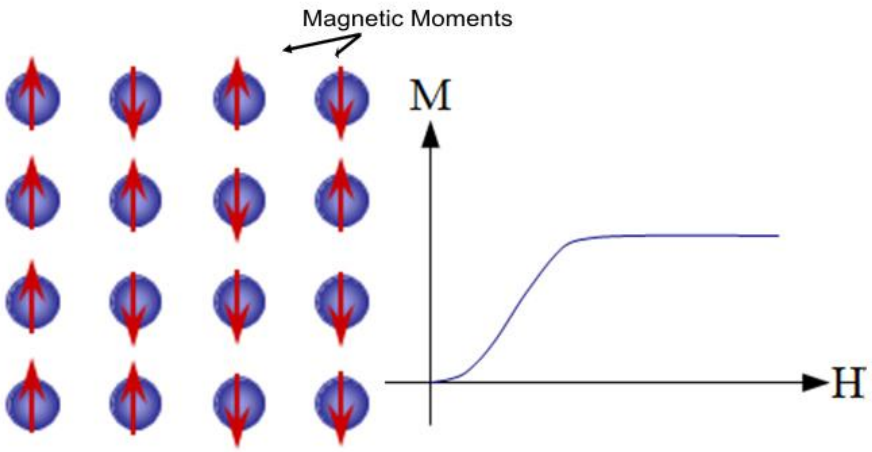

Fig.10. Ferrimagnetism atoms. They have mixed parallel and anti-parallel aligned magnetic moments.

1.2.6. Anisotropy

Anisotropy is the difference in the behaviour of a material dependent on direction. In the case of magnetic anisotropy the magnetic properties of a material are dependent on the crystal structure. Shape, stress and magnetocrystalline anisotropy all influence the coercivity, remanence and the shape of the hysteresis loop. Magnetocrystalline anisotropy is an intrinsic property and is dependent on the crystal structure. Other anisotropy effects can be influenced by microstructure and design.

1.2.6.1. Magnetocrystalline Anisotropy

Certain crystallographic orientations are preferred for magnetisation. This preference is called magnetocrystalline anisotropy. Magnetocrystalline anisotropy is caused by a coupling of the electron orbitals to the crystal lattice of the material, in the easy direction of magnetisation. This coupling is such that the orbitals are in the lowest energy state. The anisotropy field H_a (Equation 3.) is the field required to rotate all the moments by 90° as one unit in a single saturated crystal.

$$H_a = \frac{2K_1}{M_s}$$

K_1 = anisotropy constant.

M_S = saturation magnetisation at zero applied field.

H_a = Anisotropy field

Equation 3. Magnetocrystalline Anisotropy

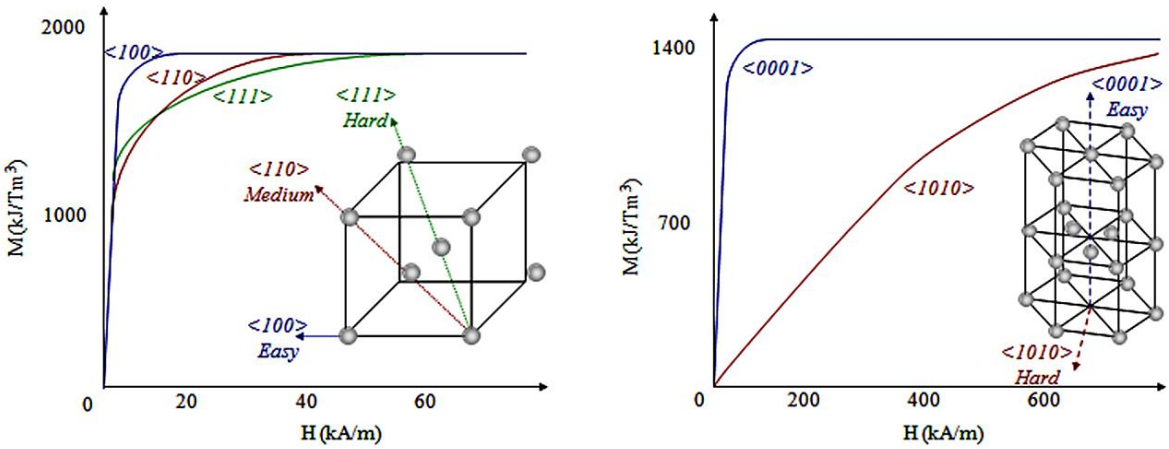

Fig.11. Preferred direction of magnetisation for Fe and Co.

Fig.11. shows the preferred direction of magnetisation for Fe and Co respectively. The easy and hard directions are shown. For cobalt the hexagonal crystal structure can be magnetised easily on the [0001] direction (the c axis), but has hard directions of magnetisation in the <1010> type directions (which lie in the basal plane, 90º from the easy direction).

1.3. Magnetic Domains

In 1906, Weiss proposed the existence of magnetic domains. A magnetic domain is a region within a material which has uniform magnetisation. Within this region all the magnetic moments are aligned in the same direction. The creation of domains reduces self-demagnetising fields by lowering the overall energy state of the system.

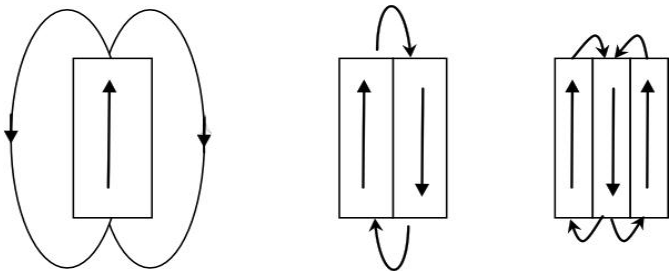

Fig.12. Reduction of the self-demagnetising field by the creation of additional domains.

If a material is uniformly magnetised there will be surface charges at the ends due to magnetisation, causing self-demagnetising fields. The energy associated with this is called magnetostatic energy. Magnetostatic energy can be approximately halved by splitting into two regions (domains), magnetized in opposite directions. This sub-division of the domains will further reduce the magnetostatic energy, up to a point, (shown in fig. 12).

The sub division and creation of domains requires the formation of a Bloch wall, named after the physicist Felix Bloch. The Bloch wall is a transition between two domains and has energy associated with it. The magnetostatic energy saved by the creation of the walls and the increase in the number of domains is proportional to the cube of the domain size, while the wall energy is proportional to the square of the domain size. So the net energy saved by the

reduction in domain size cannot continue indefinitely. There will be a point where the energy required to create another domain is equal to the energy required to create a domain wall.

The width of a domain wall depends on the two opposing energies that create it; the exchange energy and the magnetocrystalline anisotropy energy. Magnetocrystalline anisotropy favours thinner domain walls and is at its lowest when the magnetic moments are aligned in parallel. The exchange energy is reduced when the magnetic moments are aligned with a minimum amount of misalignment to one another, making the wall thicker. The domain wall thickness is at equilibrium between the two competing energies. This means that the domain wall has a finite surface energy and width.

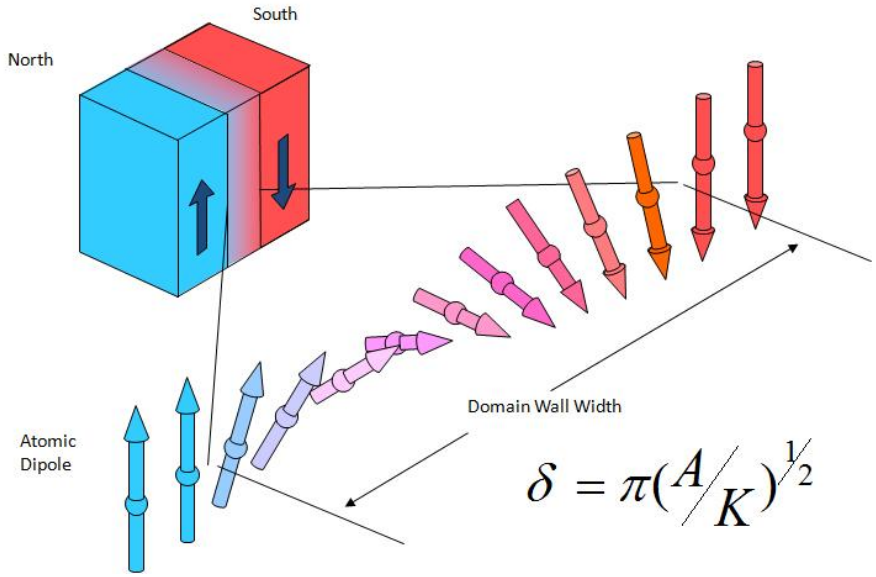

δ = domain wall width, A = exchange constant Jm^{-1}, K = anisotropy constant Jm^{-3}

Fig.13. Change in domain wall thickness, reproduced from

http://www.gitam.edu/eresource/Engg_Phys/semester_2/magnetic/domain.htm Accessed 10/05/14

The number of domains in a material depends on the physical size and shape of the sample and intrinsic magnetic properties such as magnetocrystalline anisotropy.

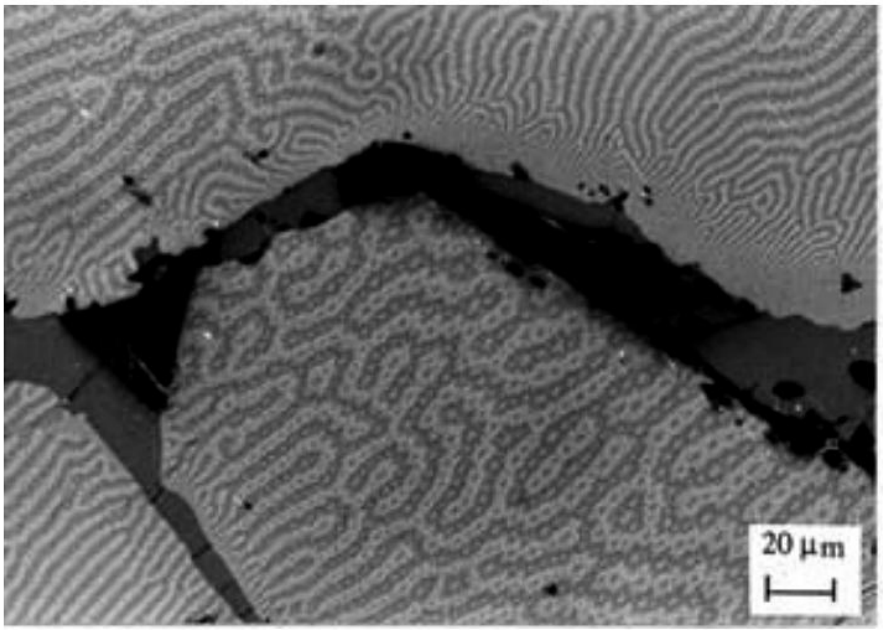

Fig.14. Kerr effect image of homogenised $Nd_{16}Fe_{76}B_8$ (showing domain patterns). Reproduced from (http://www.birmingham.ac.uk/Documents/college-eps/metallurgy/research/Magnetic-Materials-Background/Magnetic-Materials-Background-8-Domain-Observation.pdf) Accessed 04/06/14

When plane polarised light interacts with the surface of a magnetic specimen the reflected light is elliptically polarised. With the aid of polarising filters, this change in polarisation due to the interaction with the magnetic material generates magnetic domain contrast as observed in fig. 14.

1.3.1. Shape Anisotropy

If a sample is spherical the same applied field will magnetise the sample to the same extent in any direction. If the particle is non-spherical as in fig.15, the magnitude of this field will not be equal for all directions, creating one or more easy axes depending on the shape. It is easier to magnetise along the long axis than the short axis due to the influence of self demagnetisation.

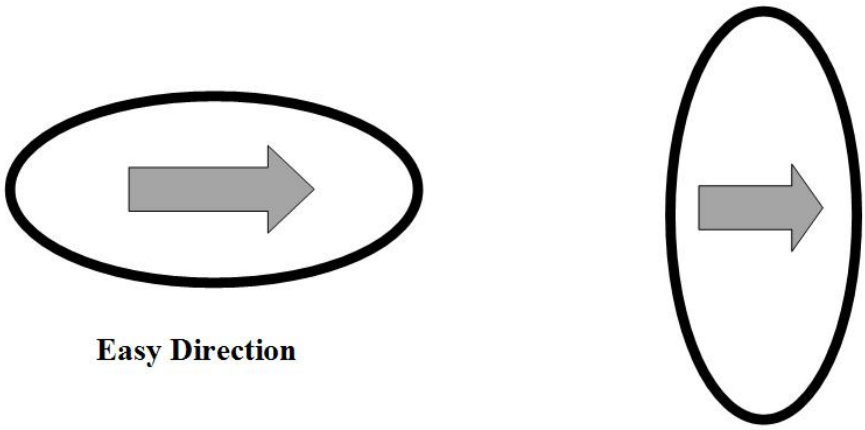

$H_d = NM$

H_d= Demagnetising field

N = Demagnetising Factor

M = Magnetisation

Fig.15. Influence of shape anisotropy on magnetisation.

1.3.2. Stress Anisotropy

Magnetostriction is a ferromagnetic material property which causes a change in shape or dimensions due to the application of a magnetic field. The inverse of the magnetostrictive effect, (Villari Effect) is the change in magnetisation when a stress is applied to a material and this depends on the crystallography of the material and the resulting change in susceptibility when the material is subjected to mechanical stress.

1.4. Magnetic Hysteresis

The hysteresis loop describes the behaviour of a magnetic material in response to an applied field.

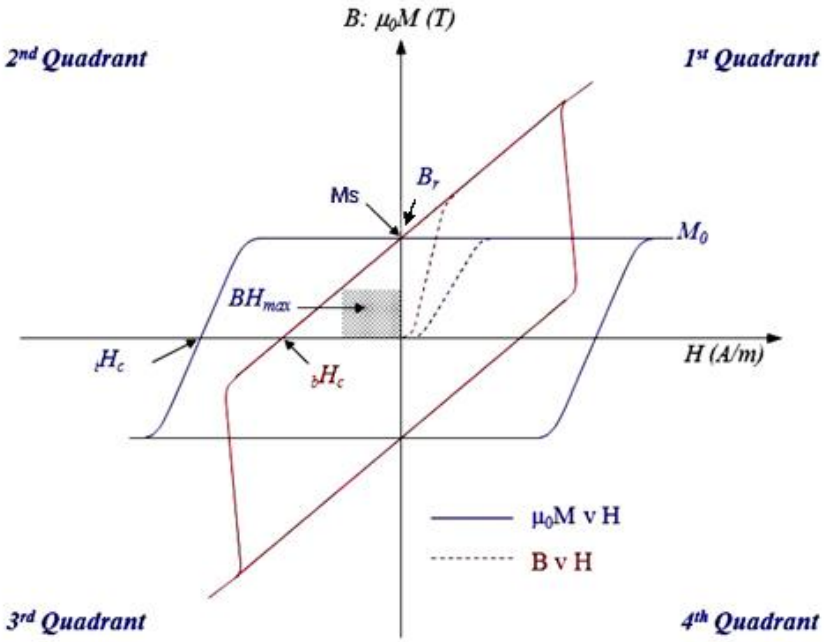

Fig.16. Typical hysteresis loop for a hard magnetic ferro or ferri-magnetic material.

For a typical hysteresis loop (fig.16) the red line describes the induction (B) where

$B = \mu_o(H + M)$. The blue line describes the polarisation (J) in response to an applied field (H). The two are related by ($J = \mu_o M = B - \mu_o H$) where μ_o is the permeability of free space. The saturation magnetisation (M_s) is the point on the blue curve when the applied field is zero. The saturation magnetisation is dependent on the volume of the ferromagnetic phase, ($Nd_2Fe_{14}B$ in the case of NdFeB-type magnets) and the crystallographic alignment of the ferromagnetic phase. The application of a demagnetising field causes rotation of the magnetic domains either due to nucleation and growth or rotation of domains. The field required to

reach a magnetisation of zero is called the coercivity, (intrinsic M = 0 or inductive B= 0). The coercivity can be influenced by modifying the microstructure.

1.5. Coercivity Mechanisms

The coercivity mechanism of a magnet depends on composition and microstructure. The three main mechanisms are pinning, nucleation and single domain. The direction of magnetisation in a ferromagnetic material is reversed by either a coherent rotation of all the magnetic moments or the growth and reversal of the directions of domains due to the movement of domain walls. If the process is purely due to the coherent rotation of magnetic moments, the field required to reverse the magnetisation should be equal to the anisotropy field H_a. Experimentally the field required is typically far lower than predicted. This is due to the nucleation and growth of reverse domains.

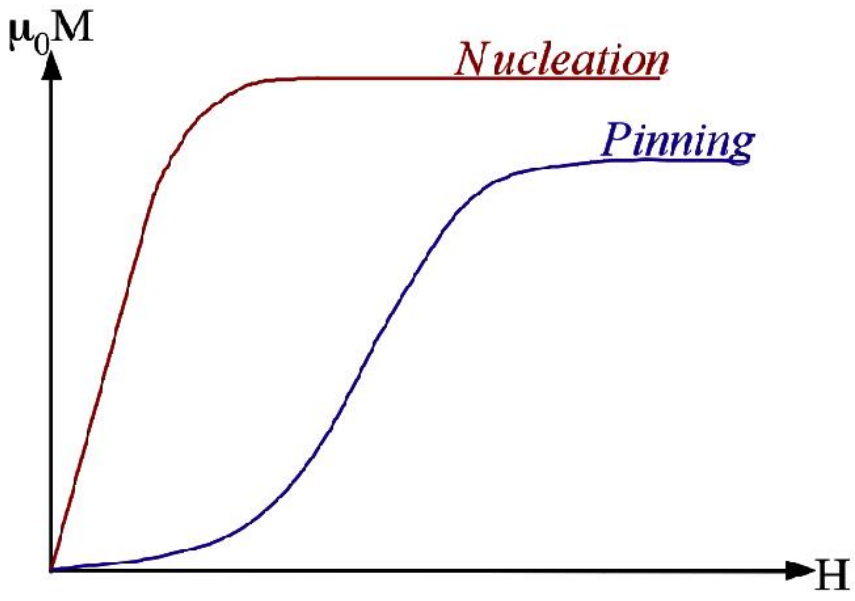

Fig.17. Nucleation and Pinning behaviour and the magnetisation of thermally demagnetised material

1.5.1. The Nucleation Type Mechanism

Reverse domains can nucleate at defects and triple points, causing anti-parallel domains, reducing the overall magnetisation. The nucleation mechanism requires the smoothing and isolation of grains with the aim of minimising the number of defects that can nucleate reverse domains. Isolating the grains can prevent domain reversal spreading throughout the material causing demagnetisation. The anisotropy field determines the applied field at which the nuclei for reverse domains will form. The shape of the initial magnetisation trace on a hysteresis loop of thermally demagnetised material (where the domains are randomised), is dependent on the coercivity mechanism of the material (Fig.17). This coercivity mechanism applies to NdFeB - type magnets.

1.5.2. The Pinning Type Mechanism

Defects, additional phases or precipitates can hinder the movement of domain walls increasing coercivity. Additional phases with differing magnetic properties to the matrix phase can impede the movement of domain walls by reducing the energy of the domain walls. Dislocations within a material can also impede the motion of domain walls, with the domain walls requiring additional energy to overcome the pinning barrier. The coercivity is controlled by the field required to overcome the pinning barriers (e.g. dislocations or additional phases). The initial magnetisation curve increases slowly until a field equal to the coercive field is applied and the movement of the domain walls can progress until saturation.

1.5.3. Single domain Particles

As the grain size decreases there will be a critical size where the grain cannot accommodate a domain wall. Due to the absence of domain walls the magnetization can only change by rotation which is an energetically difficult process. Large fields are required to rotate the

magnetisation from one easy direction through the hard and into the reverse easy direction. Materials utilising the single domain coercivity mechanism have high coercivities.

1.6. Microstructure of NdFeB-Type Material

The magnetic properties of NdFeB were discovered in 1984 simultaneously by General Motors in the USA (now Magnequench), and Sumitomo Special Metals of Japan. General Motors produced the magnetic $Nd_2Fe_{14}B$ phase using melt spinning. In the melt spinning process the molten alloy is rapidly quenched, (of the order of one million °C/s), on a rotating chilled wheel to produce a thin ribbon of material with very fine grain size (~ 50nm). The material is isotropic and is typically used for bonded magnets. Sumitomo Special Metals of Japan used a sintering route.

1.6.1. Sintered NdFeB Type Magnets

For sintered NdFeB-based magnets, the system typically consists of three equilibrium phases. According to the ternary phase diagram, these consist of the hard magnetic $Nd_2Fe_{14}B$ matrix phase, the boride $Nd_{1+\varepsilon}Fe_4B_4$ phase and the low-melting-point Nd-rich eutectic phase, (fig. 18). Additional non-magnetic or soft-magnetic phases can be present depending on the addition of dopants and the oxygen content.

There are various processing routes for NdFeB-type magnets, this project is focused entirely on sintered NdFeB. For the production of sintered magnets the composition used needs to be Nd-rich.

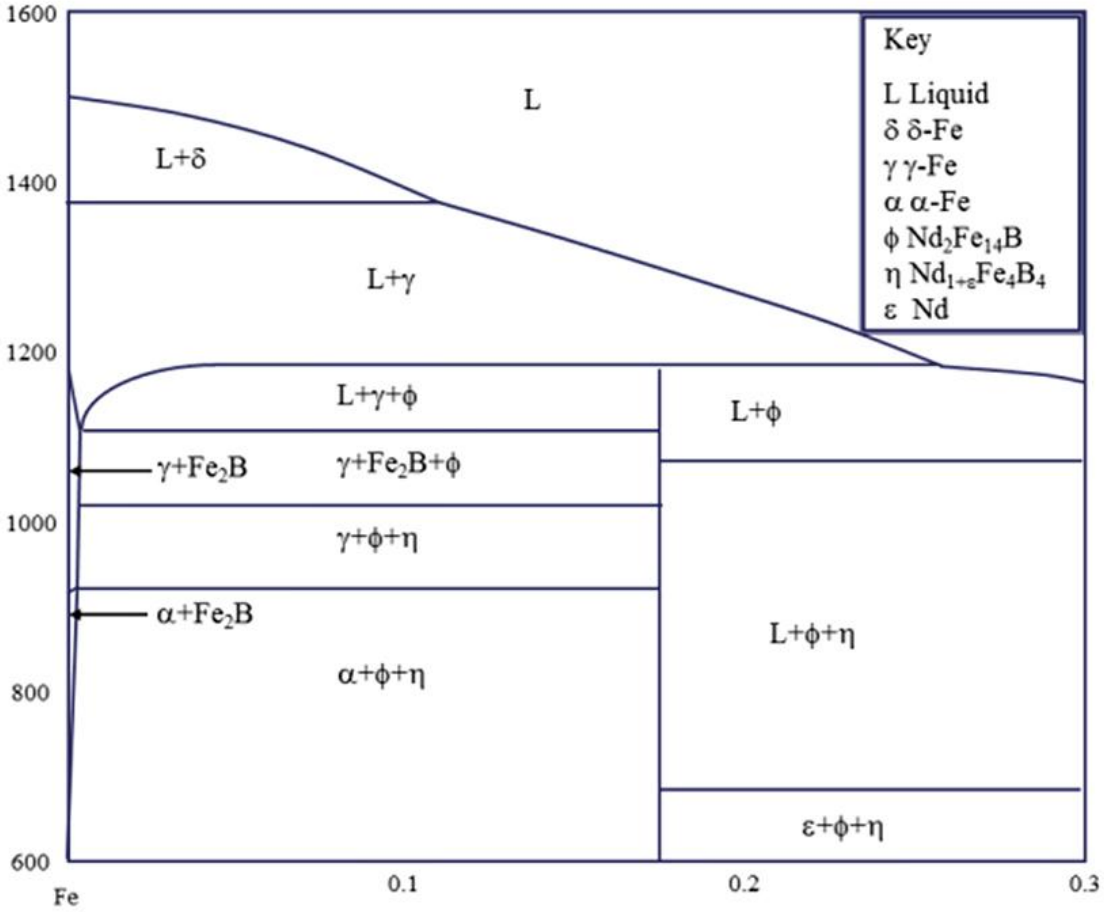

Fig.18. NdFeB isopleth showing phase formation during casting, Hua et al, (1987)

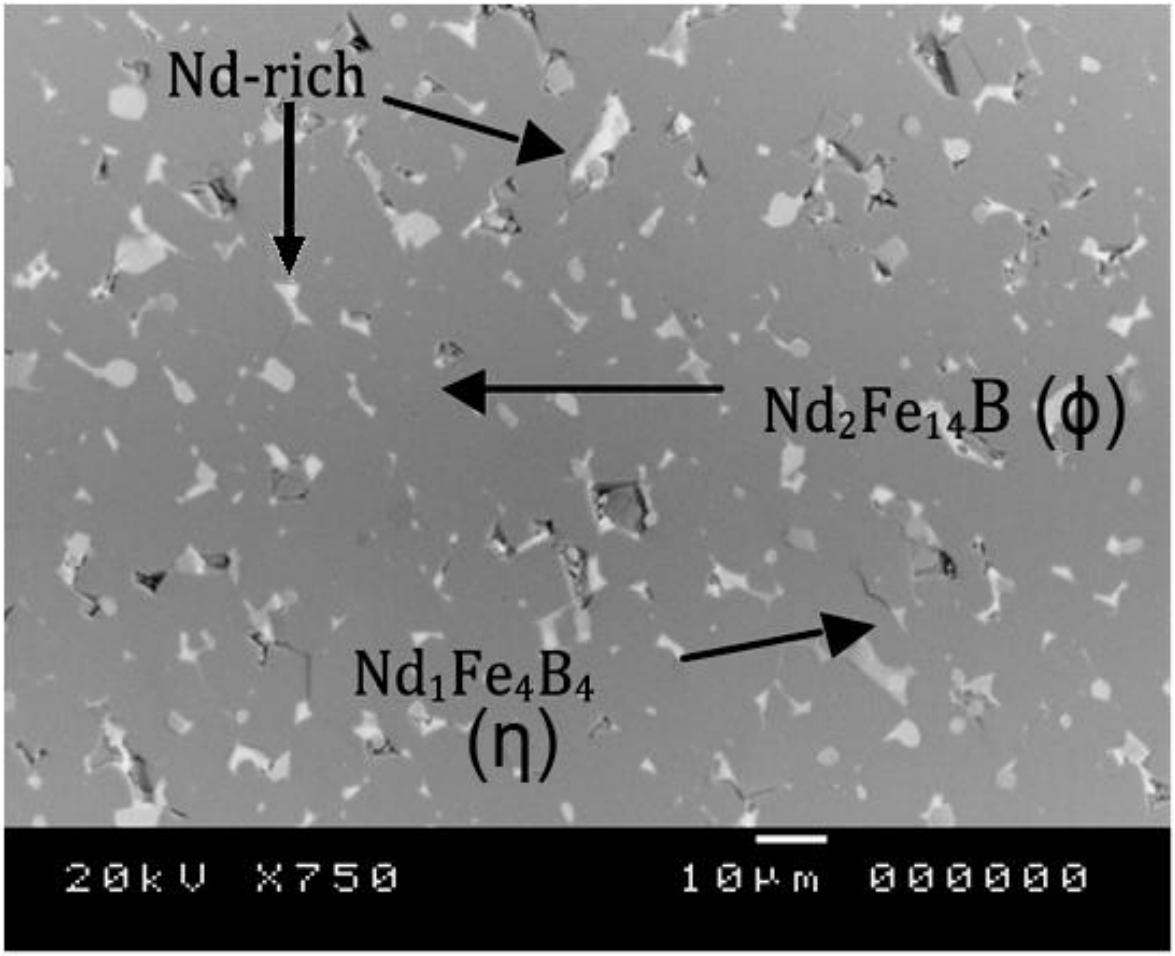

Fig.19. Typical microstructure of sintered NdFeB. Showing the $Nd_2Fe_{14}B$ matrix phase (dark grey), the Nd rich phase (light grey) and the paramagnetic NdFe4B4 phase at grain boundaries. Reproduced from Zakotnik et al, (2008).

1.6.2. $Nd_2Fe_{14}B$ Matrix Phase

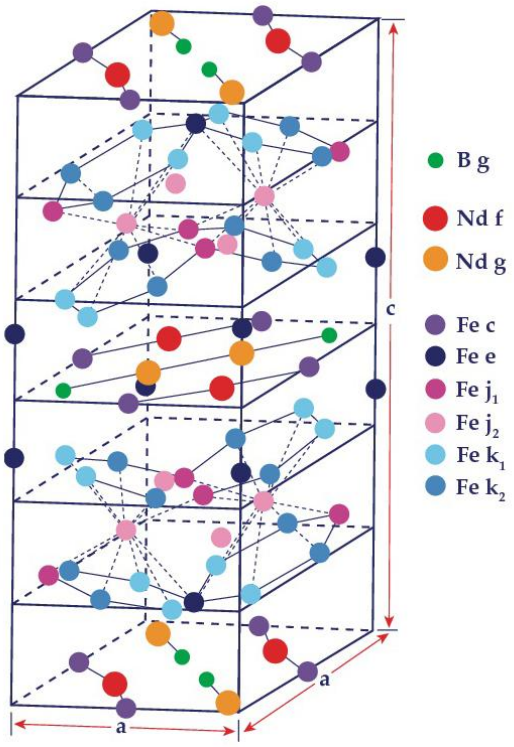

Fig.20. Unit cell of $Nd_2Fe_{14}B$ ($P4_2/mnm$ space group). Reproduced from Herbst et al, (1984).

In fig.20, the c/a ratio in the figure is exaggerated to emphasise the puckering of the hexagonal iron nets. The $Nd_2Fe_{14}B$ matrix phase, (Ø phase) is ferromagnetic and is responsible for the high saturation magnetisation of NdFeB-type magnets, (shown in figs.19 and 20). The structure was first determined by the use of neutron diffraction, (Givord et al, 1984) and (Herbst et al, 1984). $Nd_2Fe_{14}B$ can achieve a maximum saturation magnetisation as high as 1.57 T. Substituting Nd for Dy gives a lower maximum saturation but higher anisotropy thereby increasing the coercivity at the cost of remanence as the anisotropy field for $Dy_2Fe_{14}B$

[Ha = 15.0T] is much higher than that of $Nd_2Fe_{14}B$ [Ha = 7.6 T], (Givord et al, 1985) and (Abache et al, 1986). There are, however, drawbacks with the substitution of dysprosium for neodymium in that the cost of dysprosium is significantly higher than that of neodymium and there is also an associated reduction in remanence because the Dy moments are aligned anti-parallel to the Nd and Fe moments, (Boltich et al,1985).

1.6.3. The Nd-rich Phase

The Nd-rich phase plays a crucial role in the densification of sintered NdFeB-type magnets through the process of liquid phase sintering and melts at 655°C (fig. 19). Davies et al, (2001) used dilatometry to study the densification behaviour of green compacts over a range of temperatures and times. Their work showed that the Nd-rich phase plays a key role in the densification behaviour of green compacts and that increasing the effective Nd content resulted in greater densification at lower temperatures. The Nd-rich phase has also been shown to be crucial in the enhancement of magnetic properties of NdFeB- type magnets. This is reported to be due to improved magnetic separation between the $Nd_2Fe_{14}B$ grains with the aid of the non-ferromagnetic Nd-rich phase. It is also reported to be due to the reduction or removal of defects at the $Nd_2Fe_{14}B$ grain surfaces (Woodcock et al, 2012).

The Nd rich phase is mainly composed of neodymium but also includes iron and oxygen. Typically the oxygen is introduced during the processing stages. The crystal structure of the Nd-rich phase depends on the oxygen content and has been shown to be double hexagonal close packed (d.h.c.p) when the oxygen content is below 9 at.% . For the face centred cubic structure (f.c.c) it is between 11 and 43 at.% (Wenjian et al, 2008).

This agrees with the work by Shinba et al, (2005). Their work showed that the Nd-rich phase exists at grain boundaries in an fcc based structure and is amorphous when less than 2 nm thick. They report that a post sinter anneal is "effective in smoothing grain boundaries and encapsulating the $Nd_2Fe_{14}B$ phase by the Nd-rich phase" (Shinba et al, 2005). If the oxygen content exceeds 55 at %, the Nd-rich phase transforms to a hexagonal close packed (hcp) structure (Wenjian et al, 2008). Some oxygen in the Nd-rich phase of Nd-Fe-B- type sintered magnets has been shown to improve coercivity and corrosion resistance (Wenjian et al, 2008). It has been reported by Kim and Camp, (1996) that a small amount of oxygen is beneficial in preventing abnormal grain growth.

However, if the oxygen content in the Nd-rich phase increases to the point that the hcp structure is formed, the wettability of the Nd-rich phase is decreased and that "sintering density of magnets decreases when a large volume fraction of hcp structured Nd-rich phase exist" (Wenjian et al, 2008). As the ratio of Nd-rich phase increases the coercivity increases as the Nd rich phase is reduced the remanence increases.

1.6.4. The $NdFe_4B_4$ Phase

The $Nd_{1+e}Fe_4B_4$ phase (η) where e ~ 0.1 is usually described as $NdFe_4B_4$. The phase is not ferromagnetic and thus reduces the overall remanence of the material by diluting the effect of the $Nd_2Fe_{14}B$ matrix phase (fig.19).

1.6.5. Hydrogenation, Disproportionation, Desorption and Recombination

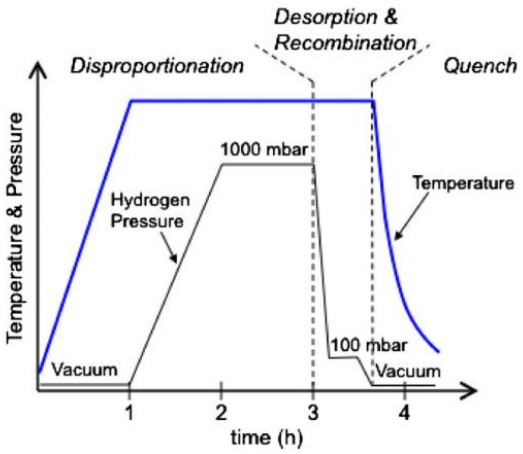

Fig.21. The HDDR process (reproduced from Sheridan et al 2012).

Another method for producing a fine grained material for bonded magnets is the hydrogenation, disproportionation, desorption and recombination (HDDR) route. The HDDR process can be used to make NdFeB powder with a grain size in the region of ~300 nm. Fig.21. shows the typical process route for HDDR. The HD stage is as described previously, (the matrix and Nd-rich phases are hydrogenated). During the disproportionation stage the $Nd_2Fe_{14}B$ phase breaks down into an $\alpha-Fe$, Fe_2B and NdH_2 as in equation 5. During the recombination phase grain refinement occurs and the $Nd_2Fe_{14}B$ reforms. The HDDR powder can then be mixed with a binder and used as bonded magnets.

$$Nd_2Fe_{14}B + 2xH_2 <-> 2NdH_{2x} + 12Fe + Fe_2B$$

Equation 5. The disproportionation reaction of the Matrix phase.

Chapter 2. The Production of Rare Earth Oxides and Metals

Rare earths are becoming increasingly important in the transition to a low carbon economy. Applications of the rare earths range from magnetic materials to phosphors for lighting, battery technology, catalysts and other applications such as sensors. Increase in the use of hybrid and electric cars, electric bicycles, wind turbines and the move towards more energy efficient lighting has pushed up the demand for and price of Rare Earth Elements (REEs).

REEs are relatively common in the Earth's crust and are also widely distributed. However, the concentrations are often low, or the REEs occur with high levels of radioactive materials. Rare earth mineral deposits usually contain both light and heavy REEs (Gupta and Krishnamurthy, 2005).

The most common mineral deposits are bastnaesite, monazite, xenotime and ion adsorption deposits. Most of the heavy REEs come from 'ion adsorption deposits'. The rare earth containing minerals can contain differing amounts of uranium and especially thorium so they are radioactive to differing degrees. The deposit monazite often has high concentrations of thorium (Long et al, 2010). The presence of radioactive materials increases the complexity of mining and the storage of the waste material. Due to the chemical similarity of the rare earths they are difficult to separate. Differences in the basicity of the REEs which influence the solubility of the salts, hydrolysis ions and the formation of complex species which can be exploited by fractional precipitation, ion exchange, and solvent extraction (Gupta, 1992), followed by step precipitation and electrolysis (Gupta and Krishnamurthy, 2005).

The processing of rare earths is energy intensive. Processes such as solvent extraction use large volumes of organic solvents which are not environmentally friendly. Due to the chemical similarity of the rare earths the processing can be time consuming and require multiple stages. REEs are often processed in batches. The electrolysis stage uses a large amount of energy to separate the rare earths from the oxygen.

2.1. The Production of Sintered NdFeB

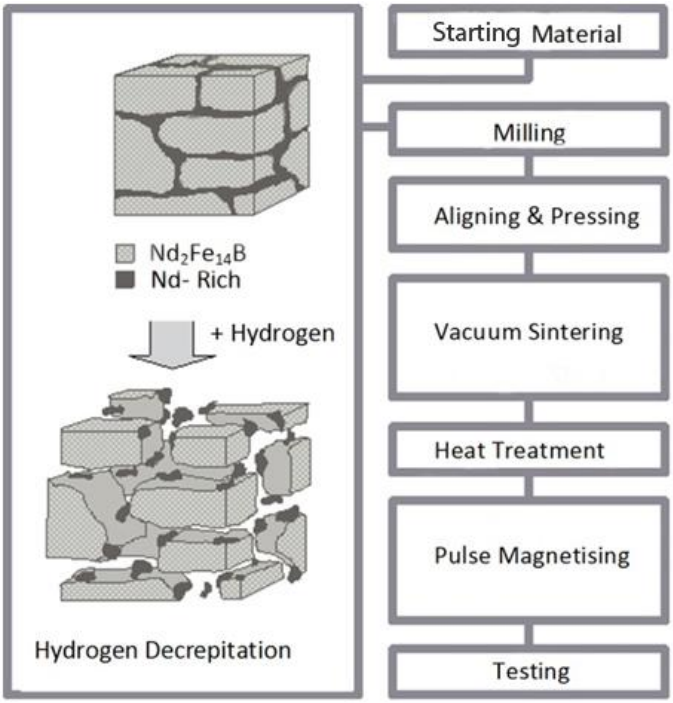

Fig.22. Processing route for sintered NdFeB - type magnets

For sintered NdFeB magnets the process route typically starts with cast material which can either be cast into a mould or cast using the strip casting technique (fig. 22). The strip casting process consists of a rotating water cooled Cu wheel. As the molten material hits the copper

wheel it cools rapidly (10^4 K/S), producing a fine grain size material, the fast cooling rates of the strip casting process can also limit the production of free iron, (see fig. 23).

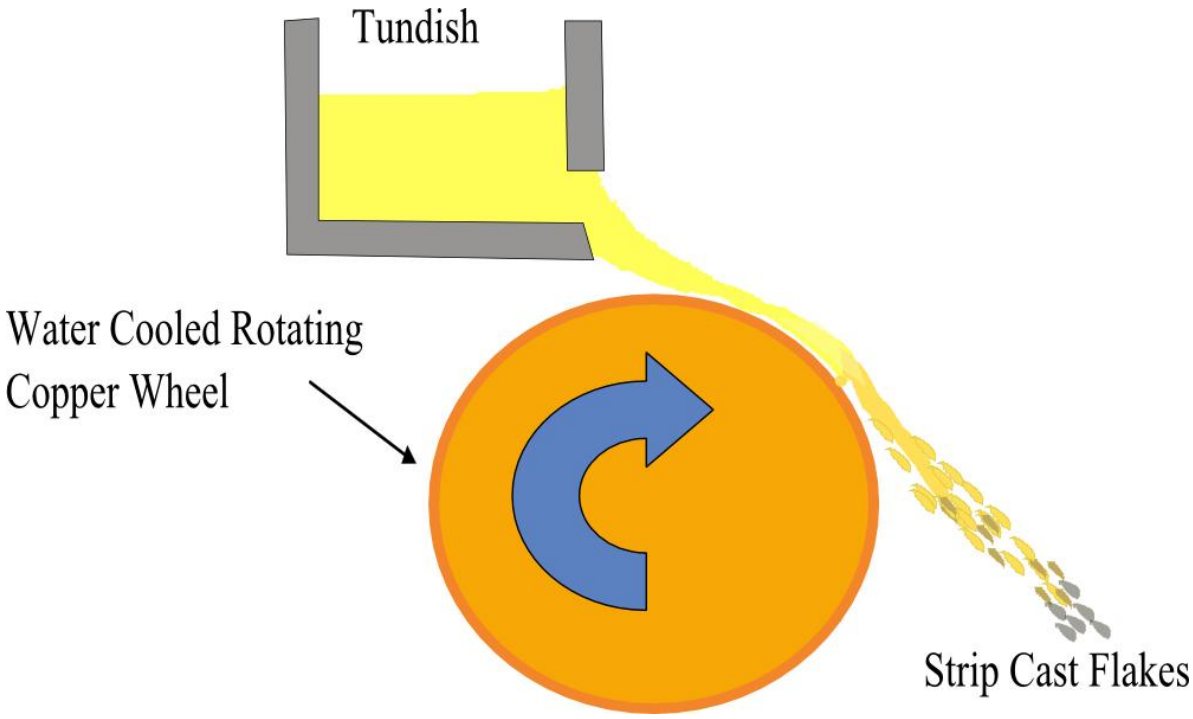

Fig.23. Strip casting process to produce flakes with a fine grain size.

Sintered NdFeB requires very careful control of the microstructure to achieve the required magnetic properties in the final sintered magnet. The coercivity of the final magnet is influenced by the grain size and density of the material. Work by Weizhong et al, (1990) showed that by decreasing the particle size, the grain size decreased. This was associated with a steady increase in coercivity, (H_c). To achieve the required grain size in the final sintered magnet the as-cast material therefore needs to be broken up to single crystal particles to make use of magnetocrystalline anisotropy. The reduction in particle size is achieved most conveniently by exposing the cast material to hydrogen (McGuiness et al, 1986). When exposed to hydrogen, the $Nd_2Fe_{14}B$ and the Nd-rich phase form a hydrogen solution and

hydrides respectively. The differential expansion caused by the difference in lattice expansion of the two phases generates stress in the material and the alloy breaks down further. This process is known as the Hydrogen Decrepitation (HD) process, (fig.22). A more detailed description of the interaction of hydrogen with NdFeB alloys and magnets is provided in chapter 3.

2.1.1. Milling of Hydrogenated NdFeB

After the HD process, the powder still needs to be further reduced in size. The most common processing route is jet milling. The jet milling process consists of near sonic confined jets of gas, (usually nitrogen), creating a vortex into which the HD powder is introduced. The high speed impact between the HD particles as they collide in the vortex causes a significant reduction in the average particle size.

In 2011, Guo et al carried out an investigation into the degree of hydrogenation of sintered NdFeB magnets and the effect on their microstructure and magnetic properties. The starting material was strip cast $Nd_{14.1}Co_{1.34}Cu_{0.04}Fe_{bal}B_{5.84}$ (at.%) alloy. This was then crushed to about 10-100μm and exposed to a controlled hydrogen atmosphere of 2 bar at room temperature. The hydrogenation of the alloy occurred at room temperature, (20 °C). They observed that the hydrogenation of the strips showed "features of intergranular fracture", which they suggested were due to the difference in the expansion rates of the two phases. They found that alloy strips without hydrogenation were easy to crush into “erose particles, (such as stick and sheet shapes), resulting in the non-uniform column grain size” (Guo et al, 2011). The particles obtained from hydrogenated strips due to the brittle fracture, produced sphere shaped particles. They found that "the hydrogenated strips are friable and much more readily milled than non-hydrogenated strips".

As discussed previously the grain size of material influences the magnetic properties. Work has been carried out on how the average particle size of the HD powder has an impact on the final magnetic properties of the sintered NdFeB-type magnets. For smaller scale laboratory processing, the reduction in the mean particle size of the HD powder can be achieved by ball milling in cyclohexane. The ball milling process consists of tumbling the powder in a liquid media with milling balls for a period of time. This method is used typically on smaller lab scale experiments. In 2000, Mottram et al reported that the ball milling time for cast material was 20 hours with 255g of milling balls. It was claimed that the hydrogenated cast material was "ball milled under cyclohexane for 20 hours and the powder produced by this means exhibited an average particle size of 3–7 μm.(Mottram et al 2000)"

The milling process has the potential to increase the oxygen content of the material. As the milling progresses, the surface area of the material increases making the powder more susceptible to oxygen. As discussed previously, the oxygen content has an influence on the crystal structure of the Nd-rich phase. It has been shown that increases in the oxygen content can reduce the ability for the Nd-rich phase to fulfil its role as a liquid phase sintering agent. This leads to lower densities and to increased porosity of the final magnet. The isolation and smoothing of the grains by the Nd-rich phase inhibits the nucleation of reverse domains on demagnetisation. Nothnagel et al, (1991) investigated the effect of the reduction of particle size on the coercivity of sintered magnets. They found that with the decreasing mean grain size, (which was varied by varying the milling time), the coercivity iHc of the final sintered material exhibited a maximum at a critical value of mean grain size, and hence, oxygen content. Subsequently, the coercivity decreased drastically as the powder and grain size dropped further. They showed that this abrupt deterioration of iHc was accompanied by a substantial change in the microstructure. From their results the critical mean particle sizes

were shown to be between approximately 1.5μm and 2.5μm, depending on the milling ball size used, (Nothnagel et al, 1991).

They conclude that the increase in oxygen content associated with the decrease in mean particle size resulted in the annihilation of the Nd-rich phase and as a consequence of this oxidation process, there was a negative impact on the liquid phase sintering. They stated that "the critical oxygen content increased with the RE content". They suggested that a further reduction in the Nd-rich phase may be due to the introduction of carbon arising from the milling liquid. They found that "the content of C increased with milling time". They proposed that, "for any given alloy, at a fixed oxygen content there existed a certain critical mean particle size associated with a critical oxygen content, thus limiting the development of the hard magnetic properties" (Nothnagel et al, 1991).

Namkung et al, (2011) also investigated the effect of the particle size distribution on the microstructure and magnetic properties of sintered NdFeB magnets. The starting powder was jet milled and then classified to obtain varying particle size distributions.

They stated that "the remanence and maximum energy product of the sintered magnet usually improved with the removal of fine particles, while the coercivity of the magnet increased by eliminating coarse particles. When the classified powder was too fine or too coarse however, the magnetic properties of the magnets deteriorated due to extreme grain growth for the former and poor densification for the latter". They also found that the magnets made with powder consisting of either mostly fine, or mostly coarse particles, exhibited lower density values. (Namkung et al, 2011).

Namkung et al showed that as the mean particle size and hence the grain size decreased, the coercivity increased. However, at a mean particle size of 3.35μm there was a drop in coercivity. They attributed this to abnormal grain growth due to a lack of the rare earth-rich

phase. They suggested that this was due to the increase in oxygen content with the reduction in the mean particle size. They showed that the powder with a mean particle size of 3.35μm had an oxygen content of 4000 ppm, compared with that of the starting powder of 2082 ppm. They suggest that due to the fact that the Nd-rich phase is sensitive to oxidation, there is a reduction in coercivity. Namkung et al, 2011 found that the "role of Nd-rich fragments for sintering can be reduced in the powder containing too much oxygen, which brings about a reduced density, and hence a poor insulation of the hard magnetic grains, thereby an abnormal growth of the grains."

The abnormal grain growth not only reduces the coercivity but also causes a reduction in the remanence due to the miss-orientation of the large grains.

Li et al, (2009) also investigated the origin of this reduction in the coercivity associated with the reduction of the particle and grain size. Starting with jet milled powder, they produced NdFeB magnets with various grain sizes. The mean particle sizes used were 2, 3 and 5μm, resulting in a grain size of 3, 4.5 and 7.5μm respectively, after sintering.

At a mean particle size of 3 μm and a grain size of 4.5 μm, an optimum coercivity of 17 KOe (1352.8 KA/m) was obtained. Subsequent reduction in the particle size resulted in a decrease in the coercivity. They concluded that their "microstructure investigations showed that the degradation of the coercivity below a critical grain size can be attributed to the oxidation of the dhcp-Nd phase to the NdO_x phase" and "the lack of the dhcp-Nd phase at the triple junctions would hinder the formation of the continuous thin grain boundary phase." They also noted that the nitrogen content was "substantially higher" in the 3 μm powder than in that of the 5 μm powder, Li et al, (2009). The increase in nitrogen in the 3 μm powder is likely to be due to the jet milling process.

2.1.2. Aligning and Pressing

After milling, the HD powder is usually aligned and pressed to form green compacts prior to sintering. There are two main pressing methods employed uniaxial pressing and isostatic pressing. With uniaxial pressing the powder is loaded and pressed in a die (slightly larger than the final component), in the presence of a magnetic field. This pressing method can achieve complex shapes. The other technique is the Rubber Isostatic Pressing (RIP) technique, innovated by Sagawa and Nagata, (1993). This technique consists of loading the powder into a thick rubber mould. Filling the powder into the mould is crucial as the density needs to be as high as the tap density and homogeneous throughout, (Sagawa et al, 2000). The powder is aligned in a magnetic field and isostatically pressed to produce the green compacts prior to sintering, (Sagawa and Nagata 1993). The isostatically pressed green compacts produce higher magnetic properties compared to uniaxial pressing.

2.1.3. Alloying Additions to NdFeB based Magnets

Additions of alloying elements to the NdFeB system can modify the magnetic properties and these can either be the result of direct substitution for the rare earths, for example the substitution of Dy for Nd, or the substitution of Fe for Co. Other alloying additions on the other hand, can interact with the rare earth rich phase to create improvements, for instance, the improved wettability of the liquid grain boundaries. Certain alloying additions can also pin grain boundaries with the intention of limiting grain growth and thus improving the coercivity. The use of intergranular alloying additions has the advantage of being able to target the intergranular regions. This has the potential of maximising the improvement in properties with a minimum of additions. The purpose of many of the alloying additions is to increase the coercivity. The methods used vary from limiting grain growth to modifying the Nd rich phase. Mottram et al, (2000) found that the blending addition of Co increased the

Curie temperature by 11 °C per at% Co in the range of 0 to 10 at% Co. The addition of Co also increased the remanence with a corresponding decrease in coercivity. It was found that with increasing cobalt content, the proportion of the grain boundary phase decreased and cobalt containing intergranular phases were observed.

They proposed that the increased remanence was attributed to the increased proportion of the $Nd_2(Fe,Co)_{14}B$ phase and the decrease in coercivity was attributed to the reduced magnetic isolation of the grains and the introduction of ferromagnetic, cobalt containing grain boundary phases, (Mottram et al, 2000).

2.1.4. Sintering of NdFeB- Type Magnets

The sintering stage is crucial to development of the properties of the final magnets. The sintering of NdFeB-type magnets relies on liquid phase sintering due to the Nd - rich phase which is liquid at 655 ºC and wets the $Nd_2Fe_{14}B$ matrix phase and aids densification (Davies et al, 2001). Careful control of the sintering temperature, sintering time and oxygen content is crucial. Increases in oxygen content can increase the possibility of the formation of Nd_2O_3 resulting in a reduction in density. If the oxygen content is too low abnormal grain growth can occur, both the density and grain size influence the magnetic properties.

The dwell time will affect grain growth. Ideally small grains of $Nd_2Fe_{14}B$ surrounded by the Nd- rich phase are required to achieve good magnetic properties. So the dwell time needs to be sufficient to achieve density, any further holding will result in grain growth.

McGuiness & Harris, (1988) and then McGuinness et al, (1989) showed that sintering at temperatures between 980 ºC-1040 ºC produced high coercivity magnets. Increasing the temperature resulted in excessive grain growth and a reduction in coercivity. The influence of

sintering temperature was also investigated by Davies et al, (2001). They investigated the influence of sintering temperature on the densification of NdFeB - type magnets

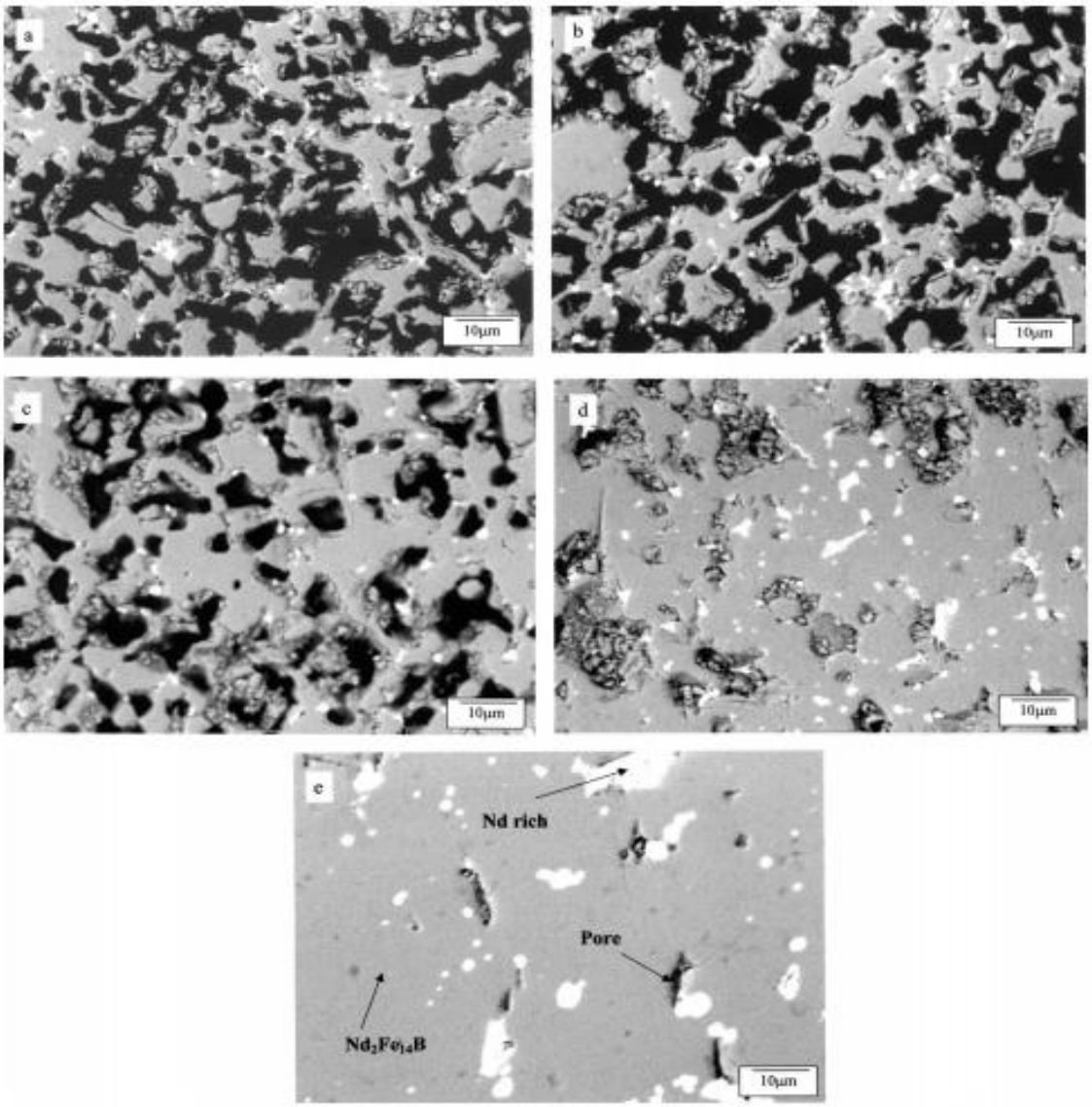

Fig.24. BSE pictures of samples sintered at: (a) 700, (b) 800, (c) 900, (d) 1000 and (e) 1100 ºC (1300X magnification).Reproduced from Davies et al, (2001).

Fig.24. shows the change in the microstructure of an alloy of composition $Nd_{16}Fe_{76}B_8$ (jet milled to an average particle size of 6μm), with sintering temperature. Davies et al showed

that significant densification occurs between 1000 and 1100 ºC. The density increased from 90 to 98% of the theoretical full density. They showed that "The sintering behaviour of $Nd_{16}Fe_{76}B_8$ magnets has been shown to change between 800 and 900 ºC. The densification of these magnets begins at 655 ºC as the grain boundary eutectic melts and increases linearly up to 800 ºC", (Davies et al, 2001).

They showed that liquid phase sintering did not start until 900ºC. They suggest that this could be due to the "formation of an oxide skin around the Nd particles at the powder processing stage". They suggestted that this would prevent the Nd-rich liquid wetting the matrix gains until a sufficiently high temperature was achieved to allow the Nd-rich phase to become mobile, (Davies et al, 2001). They also investigated the Nd-rich composition and showed that a rare earth lean composition of "$Nd_{13}Fe_{80.5}B_{6.5}$ required a higher temperature of above 1100 ºC to reach full density." Increasing the effective Nd content to "15at% by powder blending resulted in greater densification at lower temperatures (98% full density at 1060 ºC)".

The sintering stage can be followed by an annealing stage, which can increase the quantity of $Nd_2Fe_{14}B$ matrix phase due to the reaction of the Nd rich phase with the boride phase and excess free iron, (Holc et al, 1990). The annealing stage can also increase the degree of grain boundary smoothing.

Kim et al, (2012) investigated the use of cyclic sintering with the aim of increasing the magnetic properties of sintered $Nd_{13}Dy_2Fe_{79}B_6$ alloys. The cyclic sintering imposes compressive stress on the $Nd_2Fe_{14}B$ grain boundaries and triple junctions causing capillary forces which assist infiltration of the Nd- rich phase between the grains. These authors suggest that the process "may modify the grain boundaries of the magnets into well-defined, continuous and clean interfaces, which may result in increased intrinsic coercivity."

Zakotnik et al, (2008) showed that HD powder from recycled sintered NdFeB could be successfully re-sintered with the aid of neodymium hydride additions. In their work they used sintered the green compacts at 1080 ºC for 1 hour followed by furnace cooling.

Chapter 3. Hydrogen Absorption and Desorption

As described previously, NdFeB – type alloys can be processed in hydrogen to reduce the particle size. During sintering the hydrogen is desorbed from the material. The processes are described below.

3.1. Hydrogen Absorption in Pure Nd

Robert et al, (1955) investigated pressure, temperature and the composition of La, Ce, Pr and Nd hydrogen systems. They observed that increasing temperature facilitated the initiation of the reaction. However, the reaction would still proceed "at almost any temperature if enough time is allowed. Once started, the heat evolved raises the temperature of the metal, and the reaction velocity increases."

For Nd, the binary hydride covers a range of NdH_2 to $NdH_{\sim 3}$ (Yartys et al, 1997), (McGuiness et al 1988) and (McGuiness et al 1990).

$$Nd + xH_2 \rightarrow NdH_{(2+x)} \qquad \text{(Room temperature)}$$

Equation 6. Reaction of Nd +H_2 at room temperature.

3.2. Hydrogen Absorption in $Nd_2Fe_{14}B$-Type Alloys

Ryan and Coey, (1985) designed and built a miniature thermomanometer to study the absorption and desorption of hydrogen from samples such as $Nd_2Fe_{14}B$ as a function of temperature, with sample masses in the mg range. The thermomanometric analysis technique monitors the absorption and desorption of gas as a function of temperature using a pressure

gauge. The technique is complimentary to Differential Thermal Analysis (DTA) and Differential Scanning Calorimetry (DSC), providing similar information to thermogravimetry and temperature programmed desorption.

Ryan and Coey, (1985) suggested that the technique has the advantage that the apparatus required is simple and robust and in addition accuracy is potentially greater, since large changes in gas pressure are measured rather than small changes in weight. Their system consisted of a sealed volume with a piezoresistive pressure sensor used to continuously monitor pressure as the sample was heated at a constant rate.

Cadogan and Coey, (1985), showed that for the hydrogenation of $Nd_2Fe_{14}B$, the hydrogen absorption is activated at about 220°C but is followed closely by the desorption process which is almost completed by 650°C. They showed that the desorption process started at approximately 150°C and ended at approximately 600°C. They concluded that the tetragonal compound $Nd_2Fe_{l4}B$ readily absorbed hydrogen on heating in a hydrogen atmosphere of about 1 bar. This resulted in the formation of a stable Nd-Fe-B solution. They suggested that there was an associated increase in the lattice parameter of 1-2%.

Harris et al, (1987) also reported that the stoichometric $Nd_2Fe_{14}B$ alloy required elevated temperatures and showed that temperatures in the order of between 100 and 150°C were required to achieve hydrogen absorption.

$$Nd_2Fe_{14}B + H_2 \longleftrightarrow Nd_2Fe_{14}BH_x \text{ (Temperature range: 150 – 200°C)}$$

Equation 7. The reaction of $Nd_2Fe_{14}B + H_2$.

Andreev et al, (1985) investigated the hydrogenation of $Nd_2Fe_{14}B$ and $Y_2Fe_{14}B$.

Compound	Lattice parameter	
	a (nm)	c (nm)
$Nd_2Fe_{14}B$	0.8801	1.2205
$Nd_2Fe_{14}BH_{3.8}$	0.8919	1.2345

Table 1. Change in lattice parameter upon exposure to hydrogen, (Andreev et al, 1985).

Andreev et al, showed that the magnetic moment and Curie temperature increase as hydrogen is absorbed and that for sintered NdFeB- type magnets, hydrogen absorption "increases the specific magnetisation but the anisotropy and coercive fields H_A and H_C are greatly decreased." The lattice expansion seen in Table 1, gives rise to the decrepitation process, (Andreev et al, 1985).

3.3. Hydrogen Decrepitation of NdFeB -Type Material

Hydrogen decrepitation (HD) is the process patented by Harris et al, (1979). The process was first used on $SmCo_5$ and $Sm_2Co,Fe,Cu,Zr)_{17}$ alloys. During the HD process the alloy is exposed to H_2. Hydrogen is absorbed by the alloy causing a volume expansion which causes intergranular and transgranular cracking, resulting in the break-up of the material.

Harris et al, (1987) showed that a rare earth rich alloy of composition $Nd_{16}Fe_{76}B_8$ fully hydrogenated at room temperature when exposed to hydrogen. As discussed previously

hydrogenation of the $Nd_2Fe_{14}B$ stoichometric alloy requires elevated temperatures to initiate the hydrogenation reaction. The room temperature reaction observed by Harris et al, (1987) (on an alloy of composition $Nd_{16}Fe_{76}B_8$), shows that the reaction of the rare earth rich compositions is multi-stage, with the reaction of the Nd-rich phase initiating a further reaction of the matrix phase. Yartys et al, (1997) showed the exothermic nature of the hydrogenation of Nd, where the associated increase in temperature was $\Delta T = 65°C$. This local heating initiates the reaction of hydrogen with the matrix phase. DTA measurements also confirmed that the $Nd_{16}Fe_{76}B_8$ alloy readily absorbed hydrogen at room temperature along with an exothermic reaction (Harris et al, 1987).

Williams et al, (1991) investigated the hydrogen desorption behaviour of the following alloys; $Nd_{11.8}Fe_{82.4}B_{5.8}$ (formula unit $Nd_2Fe_{14}B$), $Nd_{15.5}Fe_{77.5}B_7$, $Nd_{12.5}Dy_3Fe_{74.5}V_3B_7$, $Nd_{12.5}Dy_3Fe_{69.5}Co_5V_3B_7$ and 95% pure neodymium. They found that "for the single-phase $Nd_2Fe_{14}B$ alloy the absorption of hydrogen was achieved by heating to 250°C and holding under hydrogen (approximately 1 bar pressure) for 1 h before cooling to room temperature. In the case of the other alloys and neodymium, absorption could be achieved at room temperature by exposure to hydrogen at about 1 bar for a time long enough to ensure complete absorption."

3.4. Hydrogen Decrepitation of Sintered NdFeB -Type Magnets

McGuinness et al, (1993) investigated the decrepitation behaviour of sintered NdFeB-type magnets with the composition $Nd_{16}Fe_{76}B$, isotropic (unaligned) and anisotropic (aligned) magnets were produced by isostatic pressing and sintering. These were subsequently decrepitated in a flowing atmosphere of argon / hydrogen gas.

Their results showed that the activation times for the samples varied significantly. The reaction rates were also different with the average reaction rate for the isotropic magnets 81 minutes and the average for anisotropic magnets 106 minutes.

McGuinness et al, (1993) also found that the decrepitation behaviour was different depending on the anisotropic or isotropic nature of the magnets. They found that the isotropic magnets "were attacked by the hydrogen at all points on their surface". The anisotropic samples were found to decrepitate exclusively from the ends of the rods.

Similar observations on the selective nature of anisotropic material were seen in the corrosion tests performed by McGuiness et al, (1993).

Further work on the anisotropic decrepitation behaviour of aligned sintered $Nd_{16}Fe_{76}B_8$ by Yartys et al, (1996) showed the process starting with explosive-like fractures. They describe plates of material being ejected from the ends of the sample. The second stage involves the hydrogenation of the $Nd_2Fe_{14}B$ phase and the Nd-rich intergranular material, resulting in a "continuous flaking away of layers of the magnet. With the exposure of increasing amounts of fresh surface the cylindrical sample began to break up into pieces, each of which decrepitate, until eventually, a roughly spherical shape is obtained which finally disintegrates into a powder" (Yartys et al, 1996).

McGuiness et al, (1990) showed that for decrepitated magnets the cracks tend to propagate intergranularly, although not to the extent whereby the material is reduced to particles of a single-grain size. They suggest that this could be related to the distribution of the Nd-rich material. They also showed that the hydrogen absorption initiated less rapidly in $Nd_{l6}Fe_{76}B_8$ magnets but then proceeded more rapidly. They suggest that this is probably due to changes in the Nd-rich phase and / or a reduction in grain size.

Luo, (2009) also investigated the decrepitation behaviour of sintered NdFeB- type magnets for the production of anisotropic powders from starting material, with a composition $(NdDy)_{15}(FeCoNbCu)_{79}B_6$. Hydrogen kinetics measurements were taken with a sample mass of 61.65mg. It was stated that "it appears impossible to hydrogenate these compounds at room temperature." This is at odds with the work reported by Williams et al, (1991) where rare earth rich alloys decrepitated at room temperature. The observed differences could be due to the small sample size (~60mg) used by Luo, (2009), which could have resulted in a reduced number of initiation sites.

Luo, (2009) showed that by subjecting the alloy to a heat treatment above 150 °C in a high vacuum (5×10^{-3} Pa), prior to hydrogenation, it enables the alloy to react at room temperature. The work also showed that the hydrogen decrepitation temperature had an influence on the fracture mechanism. The sample decrepitated at 50 °C showed both intergranular and intra-granular fractures. The sample decrepitated at 150 °C showed only intergranular fractures.

It was suggested that this was due to a larger hydrogen uptake in the 50 °C (HDT050) sample as compared to the 150 °C (HDT150) sample, "which results in a volume expand of the tetragonal phase in HDT050, larger than in HDT150" (Luo, 2009).

3.5. The Desorption of Rare Earths

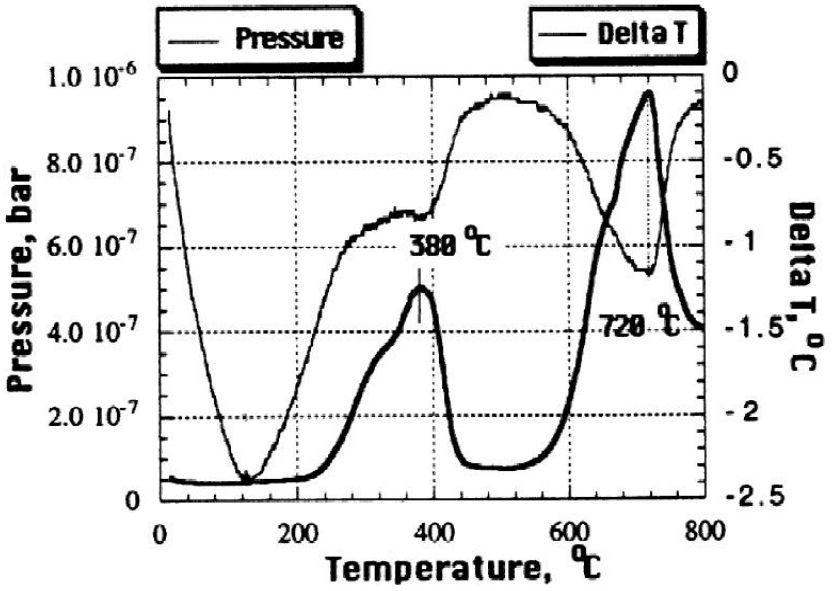

Fig. 25. A typical desorption trace of $NdH_{\sim 3}$ reproduced from Yartys et al, (1997).

Yartys et al, (1997) studied the desorption of a number of individual rare earth metals with masses of between 60 – 80 mg by heating the samples at 5 °C per minute, in a hydrogen atmosphere of 1 bar in a HDTA. The samples were then cooled to room temperature and evacuated before re-heating at 5 °C a minute, to a temperature of approximately 900 °C.

In fig.25. reproduced from Yartys et al, (1997), it can be seen that desorption of hydrogen from neodymium hydride occurs over two distinct temperatures. The first relates to the phase transformation of $NdH_{\sim 3}$ to NdH_2 and this occurs at the temperature range of 200 to 450 °C. This is followed by desorption of hydrogen from NdH_2 to Nd and this occurs generally over a range of 500 to 850 °C. For the light rare earth hydrides, the lattice structure is initially fcc

with the hydrogen initially, fully occupying all the tetrahedral sites. Excess hydrogen then sits in the octahedral sites, producing a "super stoichiometric rare earth dihydride", (Yartys et al, 1997). So we get an alloy with a typical composition of NdH_{2+x} where x is $0 \leq x \leq 1.0$.

Yartys et al, (1997) reported that in the case of the tri-hydrides of group I metals (Ce, Nd and Pr), "low temperature RH_{2+x} to RH_2 desorption consisted of two overlapping desorption events. A peak in the hydrogen desorption observed at 340–380 °C, was preceded at lower temperatures by a shoulder in the hydrogen pressure curve." This can be seenfor the desorption trace of Nd, (fig.25). Yartys et al, (1997) showed that the most pronounced effects were observed for Pr. Two low temperature peaks were observed with the main desorption taking place at 340 °C and a smaller, but clearly indicated second peak observed at 255 °C. In contrast, the low temperature desorption of the group II metals (Y, Sm, Gd, and Tb) consisted of a regular, single-peak with an approximate Gaussian-type distribution, (Yartys et al, 1997). This work by Yartys et al, (1997) did not explain the origin of the overlapping peaks.

Yoshihiro et al, (2006) also investigated desorption of various rare earth hydrides using a temperature swing column chromatography technique. The amount of hydrogen desorbed was quantified using thermal conductivity measurements. Desorption was monitored up to a temperature of 1000 °C. The desorption traces for all the 15 hydrides showed two main desorption events, as was seen by Yartys et al, (1997).

Yoshihiro et al, (2006) observed a difference between the low atomic number elements (La, Ce, Pr and Nd) and the higher atomic number elements. They observed that the shape of the first peak appeared broader for the lighter La, Ce, Pr and Nd elements.

The techniques used by both Yartys et al, (1997) and Yoshihiro et al, (2006) showed that desorption occurs over two distinct stages. Both Yartys et al, (1997) and Yoshiro et al, (2006)

claimed that desorption behaviour for the light rare earths La, Ce, Pr and Nd displayed a broad low temperature desorption peak. However, Yartys et al, (1997) suggest that this first peak is in fact two overlapping peaks and showed stronger evidence of this in the Pr desorption trace. The mass of samples used by Yartys et al, (1997) were in the region of 60 – 80 mg. The sample mass used by Yoshihiro et al, (2006) was unknown. Neither paper mentioned the mean particle size of the rare earths used prior to hydrogenation, or prior to the desorption processes and the origin of the overlapping low temperature peaks was not discussed.

3.6. The Desorption of Hydrogenated $Nd_2Fe_{14}B$

Harris et al, (1987) investigated the absorption and desorption behaviour of $Nd_{16}Fe_{76}B_8$ and $Nd_2Fe_{14}B$ using mass spectrometry. Desorption studies for $Nd_2Fe_{14}B$ alloy exhibited an initial peak that started at below 50 °C, peaking at approximately 150 °C, finishing at just over 300 °C. They suggested that the initial peak corresponded to the loss of hydrogen from the $Nd_2Fe_{14}B$ (matrix) phase, (Harris et al 1987). Further work by Williams et al, (1991) investigated desorption of an $Nd_2Fe_{14}B$ alloy using mass spectrometry.

The trace (seen in fig. 26), "consisted of a sharp peak centred on 150 °C followed by a broad shoulder which indicates a peak centred on approximately 250 °C".

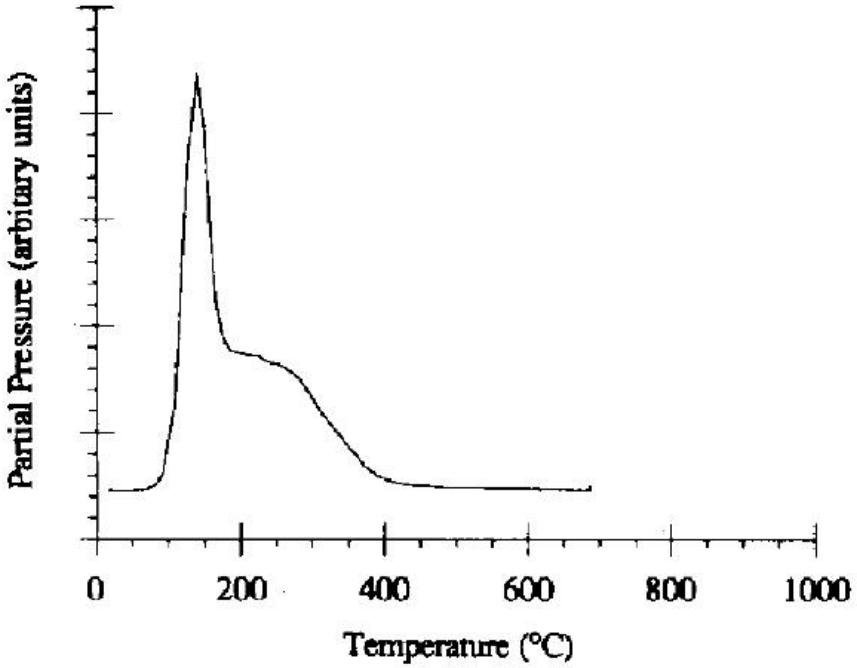

Fig.26. Mass spectrometer trace for $Nd_2Fe_{14}B$ phase (reproduced from Williams et al, (1991).

Due to the fact that the sample was a single phase alloy, they attributed this apparent dual stage process to the "desorption of hydrogen from different sites within the $Nd_2Fe_{14}B$ phase and / or to microstructural effects, such as the separate desorption of hydrogen from the grain boundaries and from the matrix". Williams et al, 1991).

3.7. Desorption of Hydrogenated NdFeB -type alloys

The desorption behaviour of NdFeB - type magnets is a combination of the desorption events from the matrix and the Nd-rich phase. Harris et al, (1987) investigated the desorption behaviour of a hydrogenated alloy of composition $Nd_{16}Fe_{76}B_8$. The alloy was vacuum degassed by heating at a rate of 5 °C per minute, up to a temperature of 1000 °C. The desorbed hydrogen was monitored using a mass spectrometer. Two distinct stages were observed, firstly from the matrix phase and secondly from the Nd-rich grain boundary phase. The relative amounts of hydrogen desorbed in these two stages agreed with estimates based on the amount of neodymium and $Nd_2Fe_{14}B$ phase in the $Nd_{16}Fe_{76}B_8$ alloy, (Harris et al, 1987).

The $Nd_{16}Fe_{76}B_8$ alloy was milled and then exposed to air containing moisture prior to degassing. Harris et al, (1987) demonstrated that the second stage peak was much reduced, to "1/10th of the value obtained from the material not exposed to the atmosphere." Harris et al suggested that this behaviour indicated that the oxidation and / or hydration of the grain boundary material resulted in a reduction in the amount of hydrogen desorbed from the Nd-rich grain boundary phase. They concluded that this confirmed the crucial role of the grain boundary phase in the activation process of the $Nd_{16}Fe_{76}$ B_8 alloy and that “matrix absorption could only be achieved readily at room temperature in the presence of the Nd-rich grain boundary material.”

Williams, McGuiness and Harris, (1991) investigated the hydrogen desorption of hydrogenated NdFeB-type alloys using mass spectrometry. They showed that the desorption behaviour of $Nd_{15.5}Fe_{77.5}B_7$ alloy consisted of two desorption events; one centred on 125 °C and one at 600 °C. They described the low temperature peak in terms of a pronounced

shoulder on the lower desorption peak on the high temperature side of the peak value (Williams et al, 1991). They suggested that the likely explanation for the increased shoulder height of the desorption peak of the $Nd_{15.5}Fe_{77.5}B_7$ alloy is "provided by the examination of the desorption curve for 95% Nd /5% Fe alloy and the disproportionated $Nd_{15}Fe_{77}B_8$ alloy which prior to desorption, is known to consist of $NdH_{2.9}$ (approximate composition), Fe_2B and iron.

These two curves are very similar and indicate clearly that desorption of hydrogen from $NdH_{2.9}$ is a two-stage process", Williams et al, (1991). From their mass spectrometry studies the final desorption peak shown for all the alloys, excluding $Nd_2Fe_{14}B$, occurred at approximately 600 °C. This is lower than the value of 720 °C observed by Yartys et al, (1997) and lower than the value of approximately 650 °C observed by Harris et al, (1987).

Chapter 4. Oxidation and Corrosion Behaviour of NdFeB

4.1. Oxidation and Corrosion

NdFeB magnets exhibit outstanding magnetic properties but are very susceptible to corrosion and oxidation. Significant differences have been shown between the reaction of NdFeB-type materials at temperature and in humid air. In humid air the reaction proceeds predominantly in the Nd-rich phase due to galvanic corrosion between the phases present in the NdFeB system. The reaction products cause expansion and grain pull-out, eventually forming a powder. Higher and drier temperatures (335 - 500 ºC) result in the formation of a dark grey surface layer and reaction zone.

4.2. Oxidation at Temperature

High temperature oxidation properties of a $Nd_{16.4}Fe_{75.7}B_{7.9}$ commercial sintered magnet were investigated by Edgley et al, (1997). The samples were exposed to a pure oxygen atmosphere of up to 500 ºC and in air between 350 ºC and 600 ºC.

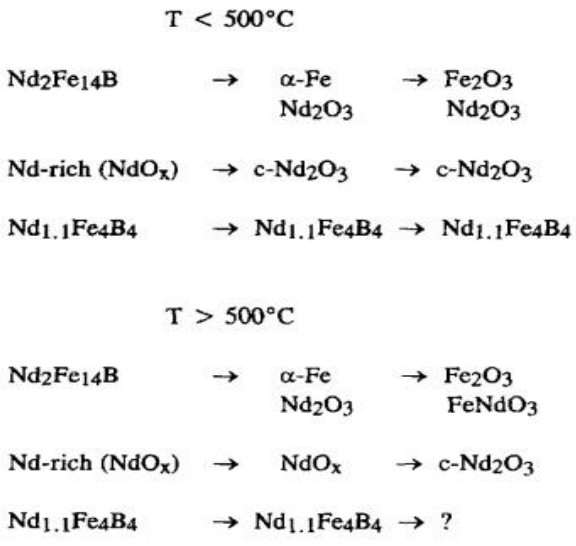

Fig.27. Schematic of oxidation behaviour of commercial sintered $Nd_{16.4}Fe_{75}.7B_{7.9}$, (Edgley et al, 1997).

Fig.27. shows Edgley et al's findings, (1997). The oxidation behaviour of NdFeB at temperature was produced from XRD data. They state that the main reaction is the dissociation of the $Nd_2Fe_{14}B$ matrix into a mosaic of α- Fe with nanocrystals of small precipitates of Nd oxides and undetermined compounds of boron. The products of the reaction form an adherent grey layer which grows transgranularly into the magnet, (Edgley et al, 1997).

Li et al, (2002) also investigated the high temperature oxidation of NdFeB. Their work showed that for higher temperatures in the range of 335 - 500 ºC, oxidation resulted in the formation of external scales of Fe_2O_3 and Fe_3O_4, with the principal degradation being the formation of an internal oxidation zone, agreeing with Edgley et al, (1997). This zone has been shown to increase parabolically with time and consists of α-Fe matrix containing dispersed (2 nm diameter) particles of NdO.

4.3. Corrosion of sintered NdFeB-type magnets

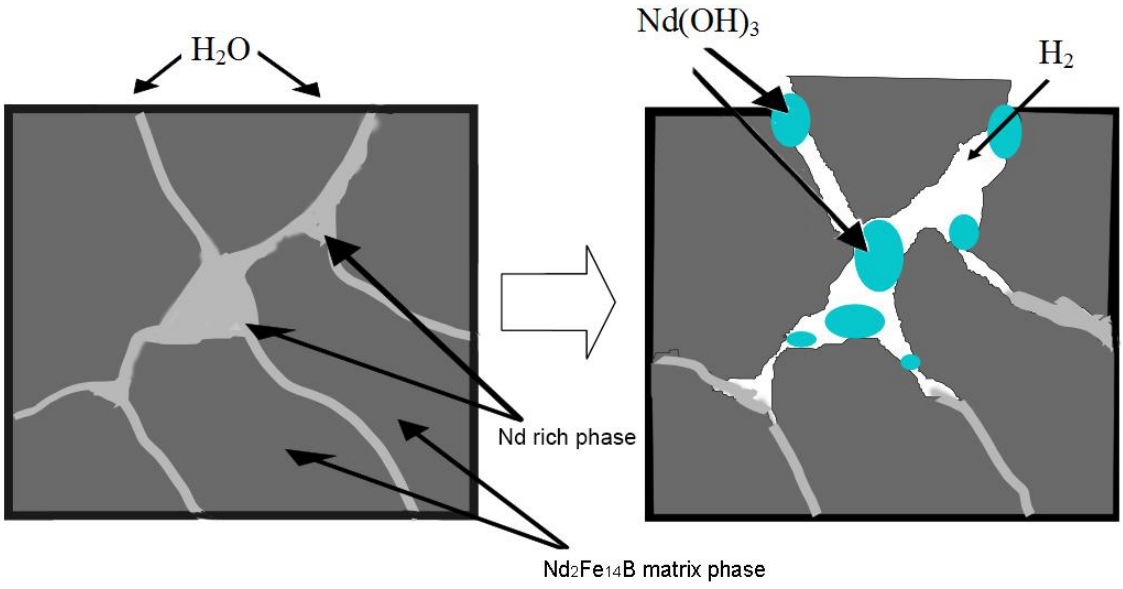

Fig.28. Corrosion of NdFeB at the grain boundaries

The corrosion process shown in fig.28 typically follows the equations shown below:

$$2\ Nd + 3\ H_2O > NdH_3 + Nd(OH)_3 \qquad \text{(Stage 1.)}$$

$$NdH_3 + 3\ H_2O > Nd(OH)_3 + 3\ H_2 \qquad \text{(Stage 2.)}$$

$$Nd + 3/2\ H_2 > NdH_3 \qquad \text{(Stage 3.)}$$

Equation 8. The corrosion of Nd FeB-type sintered magnets.

Katter et al, (2001) investigated the corrosion process of NdFeB-type alloys in hot and humid climates using a highly accelerated stress test (HAST).

They showed that, without the addition of Co, in hot and humid climates, conventional Nd-Fe-B magnets will corrode heavily. They stated that "In a highly accelerated stress test (HAST) at 130°C and 95% humidity, such magnets will lose more than 10 mg/cm^2 after a few days." With the addition of 3 wt% cobalt and some Cu, Ga, Al, "the weight loss is strongly reduced."

Katter et al, (2001) discussed the corrosion behaviour and stated that "the bigger the potential difference between the matrix and the intergranular phase of a magnet, the higher is the corrosion rate." They also showed that in a humid atmosphere, the reactions shown in Equation 8, stages 1-3 can occur with Nd-Fe-B magnets. "These reactions result in a fast decomposition of the intergranular phase by the reaction with the water vapour at higher temperatures (e.g. autoclave test at 130°C / 100 % humidity, 2.7 bar)", (Katter et al,2001).

They stated that "every water molecule which reacts with the intergranular phase accelerates the conversion of neodymium to Nd-hydroxide. The effect of this conversion is a marked volume increase of the intergranular phase which results in cracks forming along the grain boundaries," (Katter et al, 2001).

Katter et al concluded that, in hot and humid climates the corrosion mechanisms for NdFeB magnets consist of the formation of Nd-hydroxide and free hydrogen.

They suggest that "the hydrogen embrittles the remaining intergranular phase and together with the volume expansion caused by the formation of the Nd-hydroxide, matrix grains will peel off," (as in fig. 28).

As stated earlier, it was found that this reaction was much slower in magnets containing Co, Cu, Al and Ga. In these magnets, the intergranular constituents consist of $Nd_3(Co,Cu)$, $Nd_5(Co,Cu,Ga)_3$ and $Nd_6(Fe,Co)_{13}Ga$ compounds, all of which are more noble compared to pure Nd present in standard Nd-Fe-B magnets. Katter et al, (2001) observed that "the electrochemical driving force to form Nd-hydroxide is smaller in the new magnets, resulting in a reduction of the corrosion rate by a factor of about 1000."

The corrosion of NdFeB can be limited or prevented by a combination of techniques such as alloying additions, minimising the amount of the intergranular phase, minimising surface defects and cracks and minimising the surface area. Corrosion can also be limited by the addition of a barrier coating. Various coating methods such as metallic coating or polymer-based coating are employed, each with their own advantages and disadvantages.

4.4. Stability of HD Powder

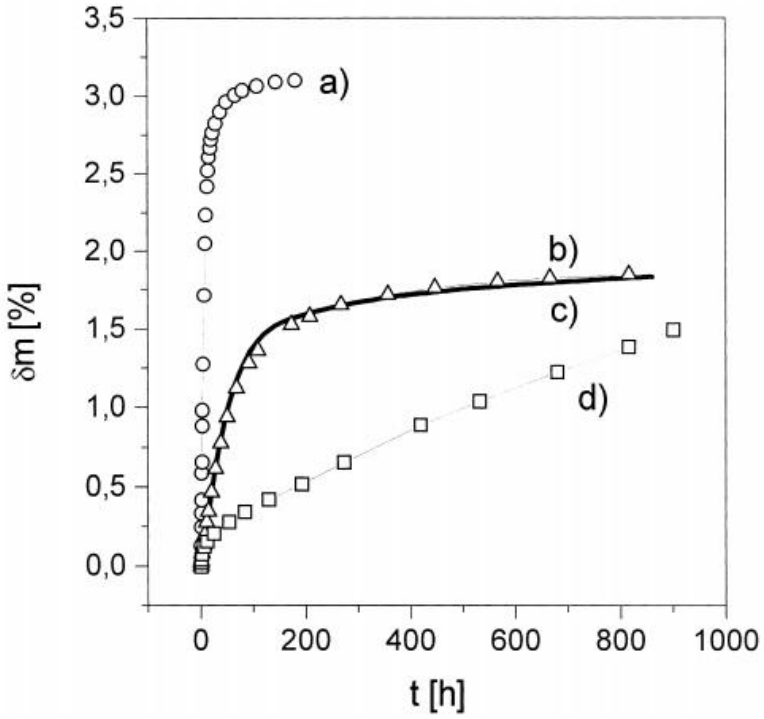

Fig.29. Comparison of the mass gain of fully hydrogenated NdFeB powder (a) partially hydrogenated powder (b) and mechanically milled powder (d), reproduced from (Liszkowski et al, 2001)

As seen from Equation 8, the corrosion of Nd with H_2O forms a hydride as an intermediate stage prior to the formation $Nd(OH)_3$. This intermediate stage was investigated further by Liszkowski et al, (2001). In their work they exposed hydrogenated NdFeB powders and mechanically milled powder to air for varying times, recording mass increases and recording phase changes with the aid of XRD.

A difference in mass gain was observed depending on the degree of hydrogenation. The fully hydrogenated powder showed a larger and far quicker mass increase as seen in fig.29. The difference in mass gain and the degree of hydrogenation of NdFeB-type powders was also observed by Chun-lin et al, (2004). For the hydrogenated powder Liszkowski et al, (2001) observed a "rise in intensity of the $Nd(OH)_3$ peaks accompanied by a drop in intensity of the

Nd peaks" as the reaction progressed. Liszkowski et al, (2001) suggested that the theoretical mass increase of the fully oxidised sample caused by the entire transformation of the intergranular Nd into $Nd(OH)_3$ should be 4%." and that this was in "good agreement with the experimental value" observed.

This agrees with the work by Verdier et al, (1994). They investigated the stability of NdFeB powders obtained by hydrogen decrepitation. Cast alloys were hydrogenated at room temperature under a pressure of 3 bar of hydrogen. The alloys were also either partially degassed or fully degassed in an autoclave. The powder was passed through a 150 µm sieve and was stated to have a particle size of 50 µm. 4 grams of powder was spread on dishes and the increase in mass with time was recorded.

Verdier et al, (1994) investigated the exposure of neodymium hydride to air. They reported that "the hydride formed at room temperature is very unstable and after an incubation time of around 10 minutes, the powder corrodes quickly and after one day turns to a reddish colour." They recorded the mass increase to a saturation value and for pure neodymium the mass increase saturated at 33 %. They suggest that after a saturation of 33 %, the remainder was $Nd(OH)_3$, which was confirmed by x ray diffraction.

They investigated whether partially degassing the neodymium hydride would influence the stability of the powder. They degassed the neodymium hydride powder at 560 °C and then exposed the powder to air. They showed that the partially degassed powder was stable for at least 700 hours. They suggest that "after this treatment, the powder is in the fully neodymium dihydride condition".

They also showed that for the composition $Nd_{15}Fe_{77}B_8$, the exposure to air had similar effects to those of the neodymium hydride. The mass increase was lower however at 2.9 % rather than the 33 % mass increase seen for the neodymium hydride. They stated that "the mass

saturation value for the hydrided powder (2.9 %) confirms the fact that only the neodymium rich material at the grain boundaries changes to $Nd(OH)_3$" (Verdier et al,1994).

They conclude that "the stability of the NdFeB powders in air is very dependent on the proportion of the Nd-rich grain boundary phase. The fully hydrided powders are very unstable on exposure to air and this is due to the rapid hydration of the $NdH_{\sim 3}$ to $Nd(OH)_3$." This is in agreement with the observations of Katter et al, (2001) who also stated that the corrosion mechanism involved the formation of a hydroxide phase.

They also concluded that "V additions lower the stability of the powder by increasing the proportion of the Nd-rich phase, whereas additions of Ga or Co improve the corrosion resistance by combining with some of the free Nd thus reducing the proportion of the Nd-rich phase."

This is in agreement with the observation of Katter et al, (2001) who stated that the addition of Ga or Co resulted in a reduction in the driving force to form Nd-hydroxide in the Nd rich phase.

Chapter 5. The Recovery and Recycling of NdFeB-Type Material

Recycling and the recovery of rare earths can mitigate some of the supply risks described previously and minimise some of the environmental impacts of mining and processing of REEs. Possible feed stock for a recovery and recycling process could be machining residue from the processing of magnets into final components. Another possible source could be redundant magnets of known compositions; the result of chipping or fracture of the final component or components rejected due to magnetic properties being out of the specification range / dimensionally inaccurate. In these cases the composition is likely to be known and recycled internally, but not much information on the processes have been disclosed (Bounds, 1994), (Tanaka et al, 2013) and (Ellis et al, 1994).

After the magnets go into service there is potential for recovery from scrap via urban mining at end of use. The potential sources of NdFeB-type magnets vary, from electronic devices such as hard disk drives (HDD), catalysts, motors in hybrid and electric vehicles and wind turbines. The different sources of scrap have different recycling and recovery potential. For example the larger scale magnets from motor assemblies or from wind turbines could be recovered for re-use or made into smaller magnets. Re-using is not always achievable as it depends on the final product magnet shape and design. For re-use, the magnets need to be easily recoverable and need to be economically worthwhile. Reduction in the size of electronic waste is often followed by a reduction in the REE content. Typically these sorts of products would be shredded. The recovery of REEs from shredded Waste Electronics and Electrical Equipment (WEEE) streams presents significant challenges, (Binnemans et al, 2013).

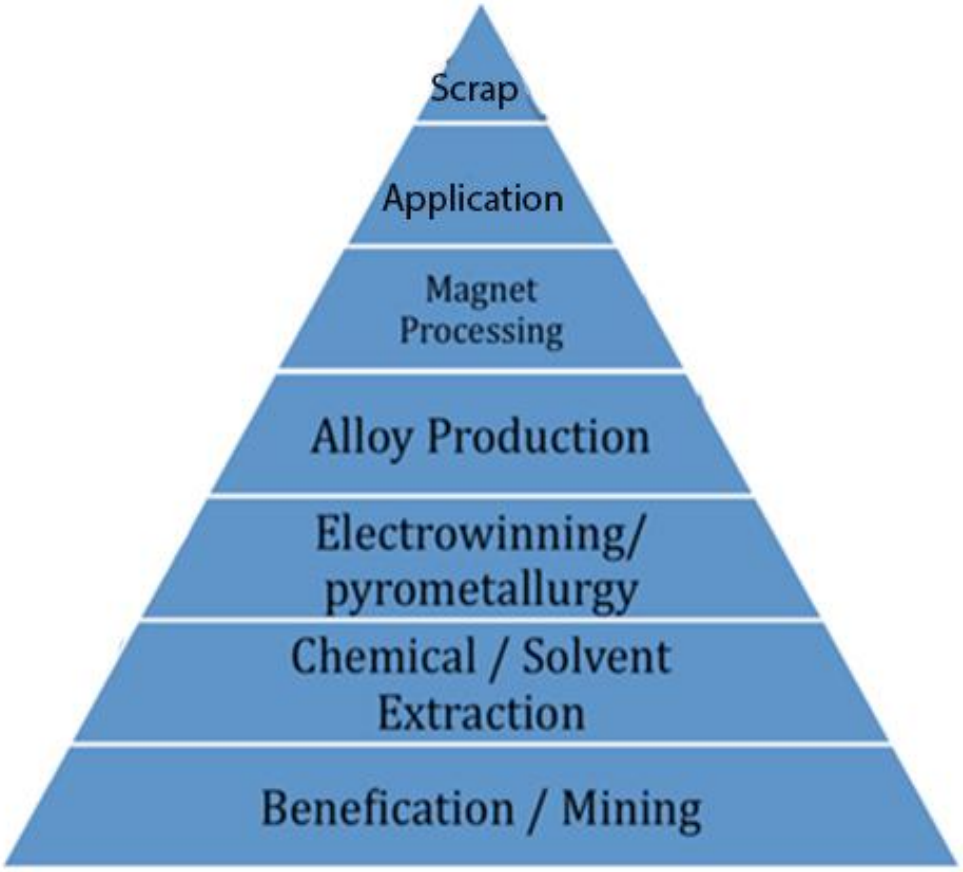

Fig.30. Stages of processing of rare earths for the production of magnets.

Fig.30. shows the stages of magnet production and possible recycling routes from scrap NdFeB type magnets. The scrap magnets can be re-introduced at various levels. A large number of papers discuss possible (lab scale) methods of recycling REEs, however commercially less than 1 % of REEs are currently being recycled (Meyer and Bras, 2011).

5.1. Chemical Solvent Extraction

It has been shown that 99 % of neodymium present in Ni coated sintered NdFeB magnets could be recovered using hydrothermal treatments. The magnets were subjected to a solution of HCl and oxalic acid and the neodymium formed a precipitate of neodymium oxalate. Koyama et al, (2009) showed that selective leaching of more than 80 % of neodymium and dysprosium could be achieved by exposing roasted NdFeB magnets to a HCl solution in an

autoclave at 180 ºC. They stated that less than 10 % of the Fe went into solution. The use of ionic liquids can improve the efficiency of solvent extraction. There is potential for ionic liquids to be safer due to their non-volatility (Binnemans et al, 2013). Wellens et al, (2012) have shown that ionic liquid extraction processes are feasible at a larger scale.

Tang et al, (2009) investigated the recovery of Nd_2O_3 from scrap sintered NdFeB using Na_2SO_4 double-salt precipitation and oxalate secondary precipitation. With the Na_2SO_4 double-salt precipitation, the product had a higher purity with a recovery of Nd_2O_3 of more than 82 %. The value of the oxide is lower than it would be if it were in the metallic form, as the oxide will need to be reprocessed (reduced and refined) which is energy intensive.

Shirayama and Okabe, (2009) showed that it is possible to selectively extract Nd and Dy into molten $MgCl_2$ from NdFeB magnet alloys. They showed that more than 80 % of Nd and Dy were extracted after 12 hours. Saito et al, (2006) investigated the recovery of rare earths from sludges containing rare earth elements. To recover the expensive Nd element from Nd-Fe-B sintered magnets, the NdFeB magnets were hydrothermally treated at 110 ºC for 6 hours in a mixed aqueous solution of hydrochloric and oxalic acid. More than 99 % of the Nd contained in the magnet was said to have been recovered. The drawback of this method is that only the Nd is recovered, resulting in the loss of the other elements.

The main disadvantage of the hydrometallurgical process is the need for large amounts of the chemicals required and the need for products to be converted into oxides (fluorides or oxides) before it can be reduced back to the metal (Binnemans et al, 2013).

5.2. Electrowinning / Pyrometallurgy

Pyrometallurgy routes can be used to recover rare earths from partly oxidised material using electroslag refining, (Ellis et al,1994). Scrap is either melted as an addition to a molten bath, or as an electrode. The material is held in the molten stage for some time to allow impurities to react with the slag. Finally the metal is poured into chilled moulds leaving impurities in the slag layer. The technique is not suitable for "swarf materials, due to their fine nature and high levels of contamination" (Binnemans et al, 2013).

The liquid-liquid extraction process can be used to recover rare earths. The process uses the selective dissolution of the rare earth by a liquid alloy. This method was investigated by Bayanov et al, (1966). Rare earths were separated from zinc-lead melts. The rare earths have a strong tendency to dissolve into the zinc-rich phase. The lead and zinc phases can be separated by density and the dissolved metals removed by distillation or sublimation, (Binnemans et al, 2013) and (Bayanov et al, 1966).

The process depends on the ease of the rare earths dissolving, "several transition metals have an even larger tendency to get dissolved in the zinc phase the zinc-lead system is not suitable for the separation of rare earths and transition metals," (Binnemans et al, 2013).

Other chemical methods investigated include the use of molten magnesium and diffusion to remove Nd from NdFeB magnet scrap. Xu et al, (1999) investigated the use of Mg melted over pieces of NdFeB scrap and held at temperatures in the region of 675-705 °C for 2-8 hours. The Nd was shown to diffuse into the molten Mg. The liquid Mg-Nd can be poured off leaving Fe-B particles behind. The advantage of the process is that the liquid metal solvent can be recycled and the waste stream minimised. The disadvantages are that the process typically requires high temperatures and high energy costs and the process cannot be applied to partly oxidised NdFeB scrap, (Binnemans et al, 2013).

5.3. Recovery of NdFeB Using the HD Process

Previous work at the University of Birmingham has utilised hydrogen to break up sintered NdFeB magnets into a powder using the HD process. The process has been adapted for use in the recycling of WEEE. Hard disk drives have been chosen as the initial feeds stock. 600 million are manufactured annually and typically contain 10-20 g of NdFeB each and the location of the sintered NdFeB is predictable. This equates to between 6000 and 12,000 tons of material which should have a reasonably consistent composition, (Walton and Williams, 2011).

The HDDs are sectioned with the coatings damaged. They are then loaded into a pressure vessel and exposed to hydrogen. The HDDs are then tumbled within the pressure vessel. The decrepitated powder falls into a collection port and is removed. The collected powder typically also contains nuts, screws, Ni flakes from the coating and parts of printed circuit boards. These can be removed by sieving the material prior to further processing.

Sprecher et al, (2014) investigated the energy and human toxicity cost associated with the recycling of NdFeB magnets from waste electronics using this method. They found that using this hydrogen assisted process used 88% less energy compared to the primary production process and scored 98% lower on the human toxicity baseline. They attributed this to the fact that this processing stage is very late in the NdFeB production process. They showed that "manual disassembly allows in principle for all magnetic material to be recovered, shredding leads to very low recovery rates (<10%)" Sprecher et al, (2014).

The recovered HD powder can be used at various stages on the flow diagram in fig. 31. for the production of magnets. This work focuses on the sintering route.

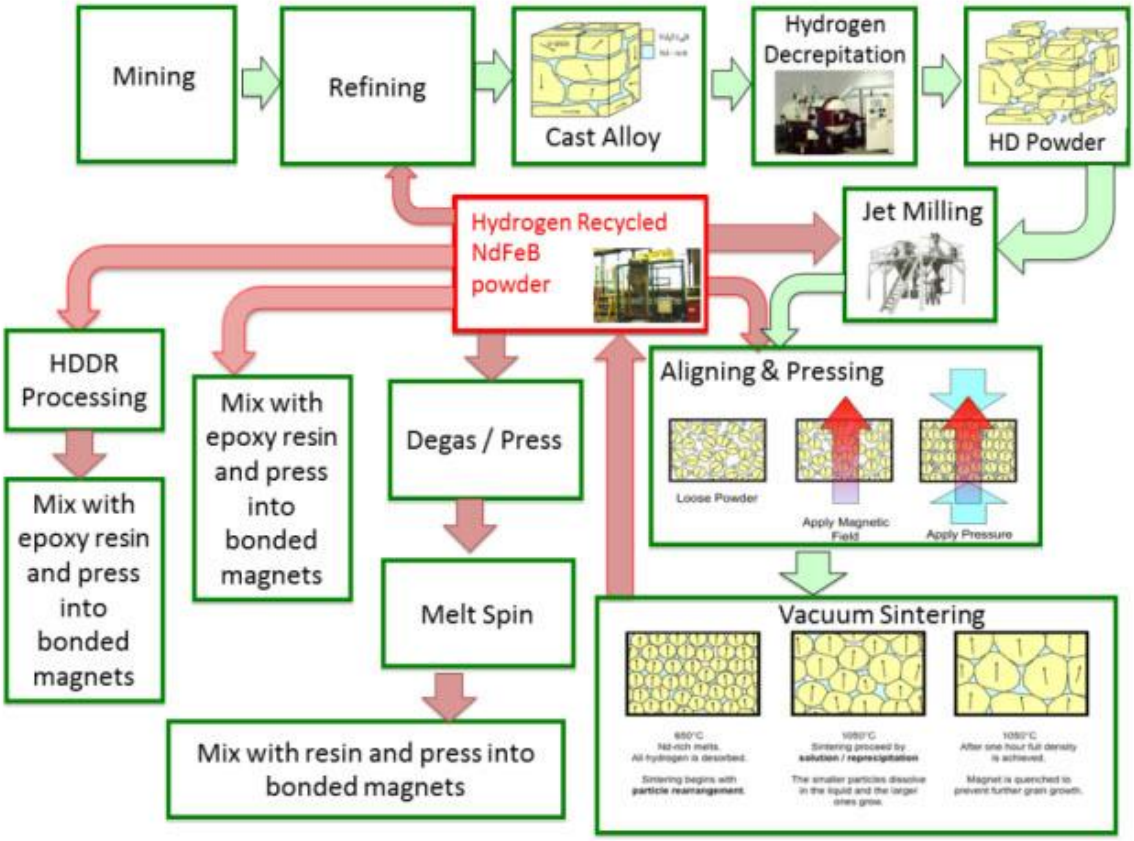

Fig. 31 Recycling routes. (Walton, 2012)

5.4. Re-sintering of NdFeB-Type HD Powder

Previous work has shown that sintered NdFeB magnets can be fully hydrogenated and the powder re-sintered. Zakotnik et al, (2007) investigated the recycling of fully dense sintered NdFeB-type magnets from voice coil magnets. They were subjected to the HD process to produce a powder that was further processed to produce permanent magnets. Sintered magnets were hydrogenated at various temperatures ranging from between 25 °C and 450 °C, and the cumulative masses were recorded. The data showed that the HD powder produced at 25 °C contained more fine powder (<250 μm) than that of the other sets of powders. However, the powder decrepitated at 25 °C had some larger particles (>500 μm).

Zakotnik et al, (2007) showed that increasing the processing temperature produced coarser powder. They suggested that, as the temperature increased, the solubility of hydrogen in the $Nd_2Fe_{14}B$ phase decreased rapidly.

They suggested that this lowering in the level of hydrogen absorption resulted in a lower volume expansion and, hence, greater penetration depth of the hydrogen occurs before sufficient stress is generated for fracture and therefore the formation of larger particles. This was clearly evident from the powder decrepitated at 300 °C and 450 °C.

Zakotnik et al, (2007) milled fresh HD powder for various times prior to aligning, pressing and sintering, to produce the sintered magnets.

Their best recycled magnet was produced by ball milling for 0.5 hours and sintering at a temperature of 1080 °C for 1 hour. The magnet exhibited remanence of 1240 mT, a coercivity (Hcj) of 830 kA m^{-1} and a maximum energy product $(BH)_{max}$ of 290 kJ m^{-3}. They also showed that full density could not be achieved after sintering the recycled powder. To achieve close to full density the HD powder had to be milled for 20 hours.

The recycled material had a lower remanence and a lower coercivity than that of the starting material. Zakotnik et al, (2007) suggested that the increased grain size and porosity were consistent with the decrease in the magnetic properties. They also commented that the magnet was produced from aligned, multigrain HD powder, so it was unlikely that the alignment in the recycled magnet could be greater than that of the starting magnet, which could also partly explain the decrease in the remanence.

The maximum energy product was 15% less than that of the starting material for the magnet milled for 0.5 hours and 1080 °C for 1 hour. The 20 hour milled powder sintered at 1080 °C exhibited a remanence (Br) of 1180 mT, coercivity (Hcj) of 780 kA m^{-1} and a maximum energy product ($(BH)_{max}$)of 260 kJ m^{-3}.

Zakotnik et al, (2008) also recycled sintered voice coil magnets multiple times. They investigated the blending of $NdH_{\sim 3}$ with the HD powder which was then milled for 0.5 hours and sintered at 1080 °C for 1 hour. They found that after subsequent recycling stages, the magnetic properties fell progressively with a reduction in loop squareness, remanence and coercivity. This was also accompanied in a marked fall in the density which was ascribed to progressive oxidation.

The addition of 1 at% Nd hydride to the recycled magnets recovered much of the initial magnetic properties. This blending was carried out in the 2nd and subsequent stages. From ICP analysis, Zakotnik et al (2008) found that there was a drop in Nd following subsequent recycling steps and a corresponding increase in oxygen. They pointed out that the increase in oxygen would reduce the amount of Nd-rich material by producing Nd_2O_3, but would not reduce the overall Nd content. Zakotnik et al suggested therefore, that the loss of Nd could also be due to a degree of volatilisation during the vacuum sintering treatment which had been reported in previous work.

Luo, (2009) investigated the decrepitation behaviour of sintered $(NdDy)_{15}(FeCoNbCu)_{79}B_6$ magnets. The magnets hydrogenated at 50 °C showed both intra-granular and inter-granular fractures. The sample hydrogenated at 150 °C showed only intergranular fractures. Increasing the hydrogenation temperature increased the amount of smaller particles compared to the room temperature sample. Luo states that this is due to the reaction occurring more vigorously at temperature. The decrepitated powder showed a large percentage of powder particles above 200 μm. This is similar to the results obtained by Zakotnik et al, (2008).

Luo, (2009) tried decrepitating the powder twice with the aim of further reducing the particle size. Sintered scrap was hydrogenated, followed by a desorption step and was again hydrogenated. Several desorption temperatures were investigated. The conclusion was that the

repeated decrepitation of the powder resulted in finer powder and a reduction in the percentage of larger particles. Luo, (2009) investigated the impact of oxidation on sintered NdFeB scrap samples. The sample was exposed to the outside environment for 3 days. This sample was compared to the original sample with fresh facture surfaces. They found that the hydrogenation process of the sample exposed to the outside environment absorbed less hydrogen than the sample that was not oxidised. They also saw that by 300 °C all the hydrogen had been desorbed.

They noted that the Nd-rich phase in the centre of the sample should not have been oxidised. The sample had finished desorbing hydrogen at 300°C.

5.5. Review of Project Aims

Maintaining a supply of rare earths will be important to achieve current environmental commitments. The recycling of rare earth magnets will be key in achieving this objective in the future. The aim of this research is to further knowledge on the processing of sintered NdFeB from recycled material. My research aims are as follows:

- Characterise HD powder from sintered magnets of a known composition
- Study the desorption behaviour and relate to the microstructure and magnetic properties.
- Study the desorption behaviour of sintered HD powder of a known composition exposed to air. Linking this to desorption behaviour and the microstructure and magnetic properties.
- Investigate the addition of neodymium hydride to HD powder of a known composition exposed to air for varying times.

Chapter 6. Methodology

6.1. The Experimental Method

The magnetic properties of sintered NdFeB can be tailored to match the specifications required by the end user. The magnets are graded with industry standard minimum specifications for each grade. The starting material used for this investigation consisted of two different types of uncoated sintered magnet blocks, provided by Arnold Magnetic Technologies, both differing in composition and magnetic properties.

The composition of the two different starting materials was determined using Inductively Coupled Plasma Mass Spectrometry (ICP) analysis. With this technique, the material was ionised to form plasma. Ions were then separated and quantified in a mass spectrometer.

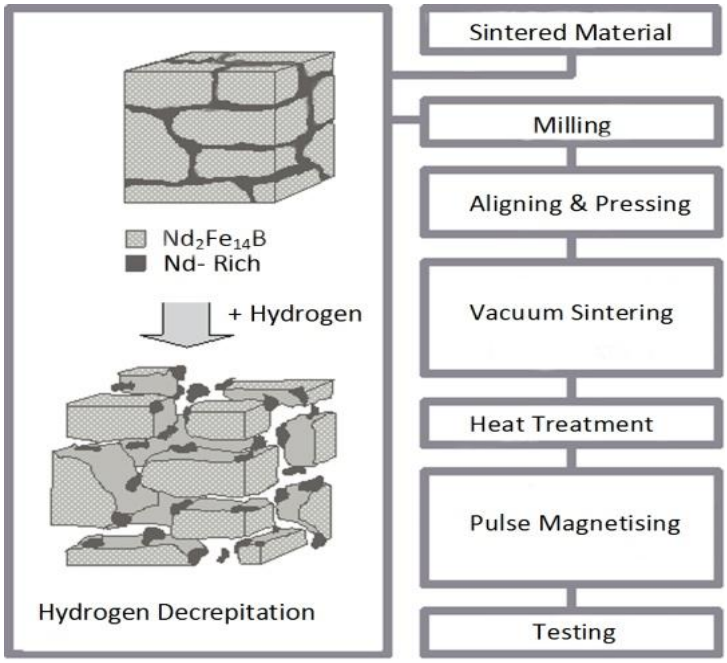

Fig.32. Overview of the processing of recycling sintered magnets.

6.2. The Hydrogen Decrepitation Process

Magnets of a known and consistent composition were fractured to produce a clean surface. The clean surface helps reduce the hydrogen decrepitation time as a result of the oxide layer on the freshly fractured surface being thinner. This enables the hydrogen to readily penetrate into the lattice of the sintered magnet.

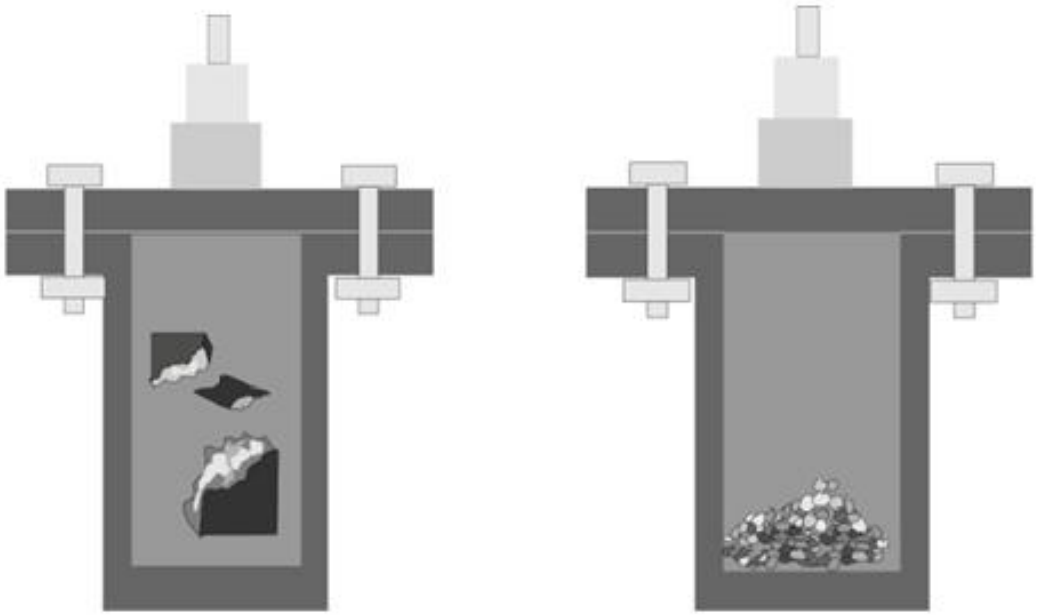

Fig.33. HD pressure vessel.

For each HD run, 100g of the fractured magnet was placed in a HD pressure vessel. The vessel was then evacuated and back filled with 4 bar of hydrogen. For all of the experiments the hydrogen decrepitation process was carried out at room temperature with the hydrogen pressure maintained manually at 4 bar. As the pressure fell due to hydrogen absorption into the sample, additional hydrogen was added. Once the uptake of hydrogen ceased, the HD pressure vessel was evacuated and (under vacuum) was transferred to a glove box for

unloading. The resultant HD powder was bagged and sealed in Kilner jars, in a glove box under an argon atmosphere with oxygen content of below 100 p.p.m (it is typically below 50 p.p.m). The oxygen concentration was monitored using an oxygen analyser which uses a fuel cell to monitor the oxygen content.

6.3. The Preparation of Neodymium Hydride

Neodymium hydride was added as an intergranular alloying addition, with the aim of supplementing the Nd rich phase lost during recycling.

Approximately 35g of lumps of neodymium (with any oxide layer removed by abrading), was loaded into a HD pressure vessel, in a glove box, under an argon atmosphere. The neodymium was then hydrided at room temperature at 4 bar, following the same procedure as the fractured, sintered magnets. Again the hydrided material was transferred to the glove box under vacuum. The resulting hydrided material was bagged and sealed in a Kilner jar.

6.4. The Ball Milling Of Powder

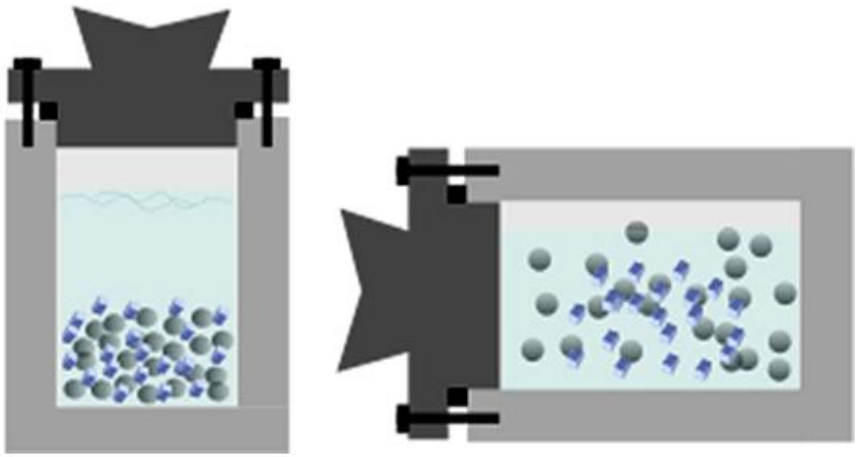

Fig.34. Milling pots and balls.

The neodymium hydride was then loaded into a milling pot in the glove box, with 250g of stainless steel milling balls (each milling ball weighed on average 2.25g) and 20 cm^{-3} of high purity cyclohexane. The milling pot was sealed with a rubber O- ring and then rotated at approximately 100 rpm for 20 hours. The action of the tumbling milling balls broke up the neodymium hydride into a fine powder. The milling procedure used was described by Mottram et al, (2000).

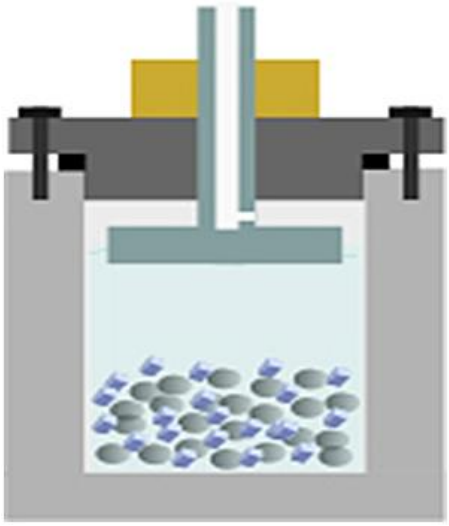

Fig.35. Milling pot with valve and tube and magnet.

After milling, the powder was dried. The drying was achieved by swapping the milling pot lid for one with a valve, shown in fig. 35. The milling pot was transferred to the transfer port and evacuated to remove the cyclohexane by evaporation. The dried powder was then bagged and sealed in a Kilner jar and stored in a glove box.

6.5. The Ball Milling of Sintered HD powder

The HD powder from sintered magnets was also ball milled. The ball milling process was the same as that for the neodymium hydride, however the milling times were reduced from 20 hours to 1 hour.

6.6. Burr Milling Sintered HD Powder

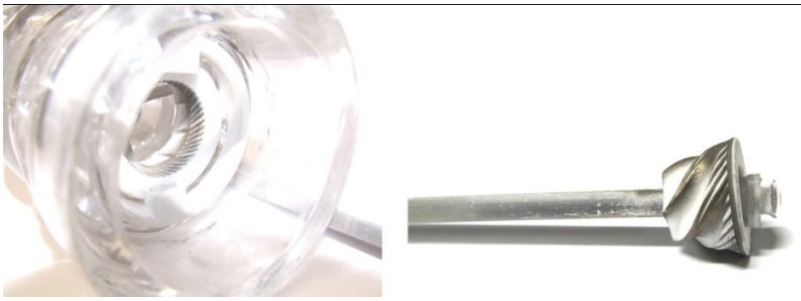

Fig.36. Salt burr mill

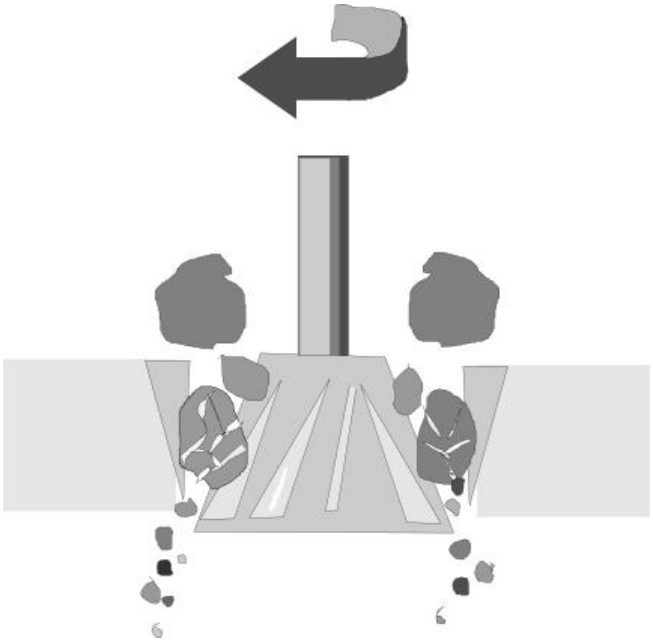

Fig.37. Bur Mill in action.

The HD powder from the sintered material was loaded into a hand operated burr mill, shown in fig. 36. The entire process was carried out inside a glove box. The burr mill used was a generic, hand operated, acrylic salt mill. The salt mill consisted of an acrylic casing with the key components being two alumina abrasive surfaces shown in fig. 37. One of the surfaces was fixed while the other rotated. The powder became trapped between the two surfaces and fractures. The fractured material fell through the gap between the two revolving abrasive surfaces.

6.7. Magnet Production

Each sintered magnet began with ~15.0g (±0.01g) of HD powder. All processing of the milled powder was carried out in a glove box under an argon atmosphere with an oxygen content of below 100 p.p.m.

For the magnets produced with the ball milled powder, ~ 15.0g (±0.01g) of powder was weighed and loaded into isostatic bags, tapped to settle the powder and then sealed. The tap density of the powder was calculated at approximately 3g/cc. For the magnets produced using the Burr milling process, the powder was sieved after milling, to obtain a powder with a known maximum particle size. 15.0g of the sieved powder was then loaded into isostatic bags and sealed. The isostatic bags consisted of neoprene tubes with a diameter of 15mm. The tubes were sealed with a rubber bung and taped within the glove box.

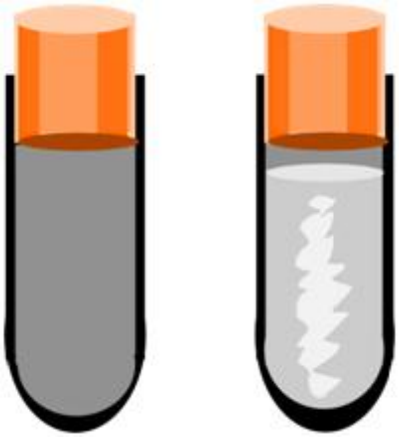

Fig.38. Isostatic bag empty and with powder, prior to aligning.

6.8. Alloying Additions

When alloying additions were added, the weights of the alloying addition and the weights of the milled HD powder were calculated to obtain in total, 15.0g of powder. Once weighed, the milled HD powder and the milled alloying additions were passed through a 90 μm sieve. This was repeated twice to ensure the intergranular additions were suitably mixed throughout the powder. To minimise the pickup of oxygen, this was carried out in the glove box.

6.9. Aligning and Pressing

The sealed isostatic bag was then transferred from the glove box for alignment. This was achieved using a capacitor discharge magnetizer which produced a pulsed field of 6T as the capacitors were discharged through a coil. The isostatic bag containing the HD powder sat within the coil. As the field was applied, the ferromagnetic particles in the powder rotated and aligned with the field. The amount of rotation (torque) of the particles for a given field depends on the size of each particle. The smaller particles see less torque than the larger particles. The pulse magnetizing process was repeated five times.

Once aligned, the powder was then transferred to an isostatic press. Care was taken to keep the powder in the isostatic bag in the same orientation to try to prevent misalignment. In the isostatic press it was pressed to 10 000 kg/cm^2. After pressing, the sample was removed from the isostatic bag and placed in a 321 stainless steel foil tube. The foil tube was then placed in the sintering tube. The process of loading the furnace took at most, thirty seconds. This was the only part of the process where the sample was subjected to the atmosphere and oxygen.

The system was evacuated and the data logger was started. Once the vacuum reached 6.8 x 10^{-2} mbars, the furnace ramp commenced. The furnace ramp rate was set at 7°C per minute to a dwell temperature of 1060°C. The furnace was held at this temperature for 1 hour and then cooled. The furnace remained over the furnace tube during the cooling stage in order to slow the cooling rate.

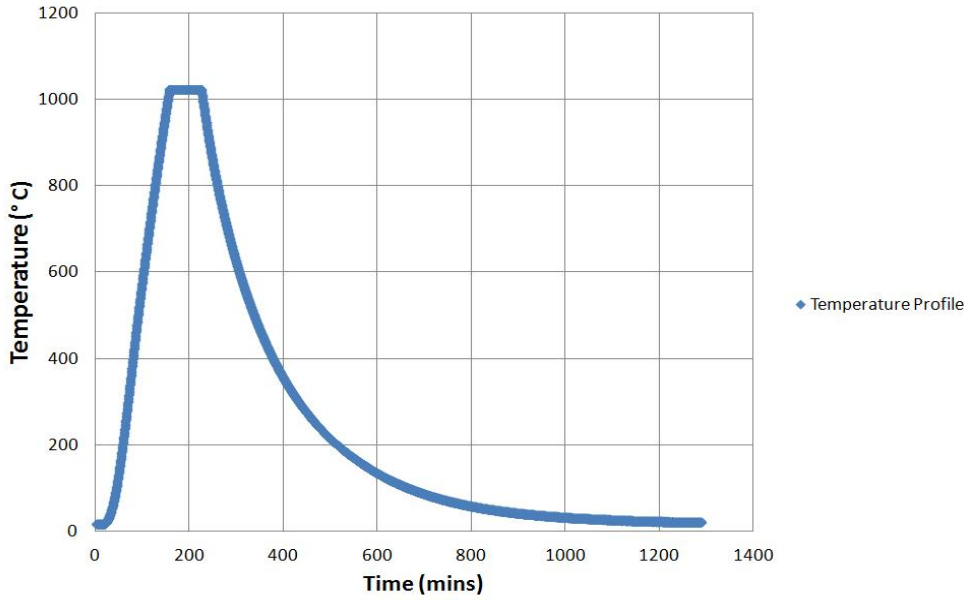

Fig.39. Heating and cooling stages.

6.10. Thermal Desorption Studies

To investigate desorption of hydrogen from the green compacts during sintering, a data logger was built. The data logger system consists of a Pirani gauge and a 945 Controller from Kurt J. Lesker Ltd and a thermocouple amplifier. These components are connected to an Arduino microcontroller which logged all the data as a CSV (Comma Separated Values) excel file to an SD (Secure Digital) card.

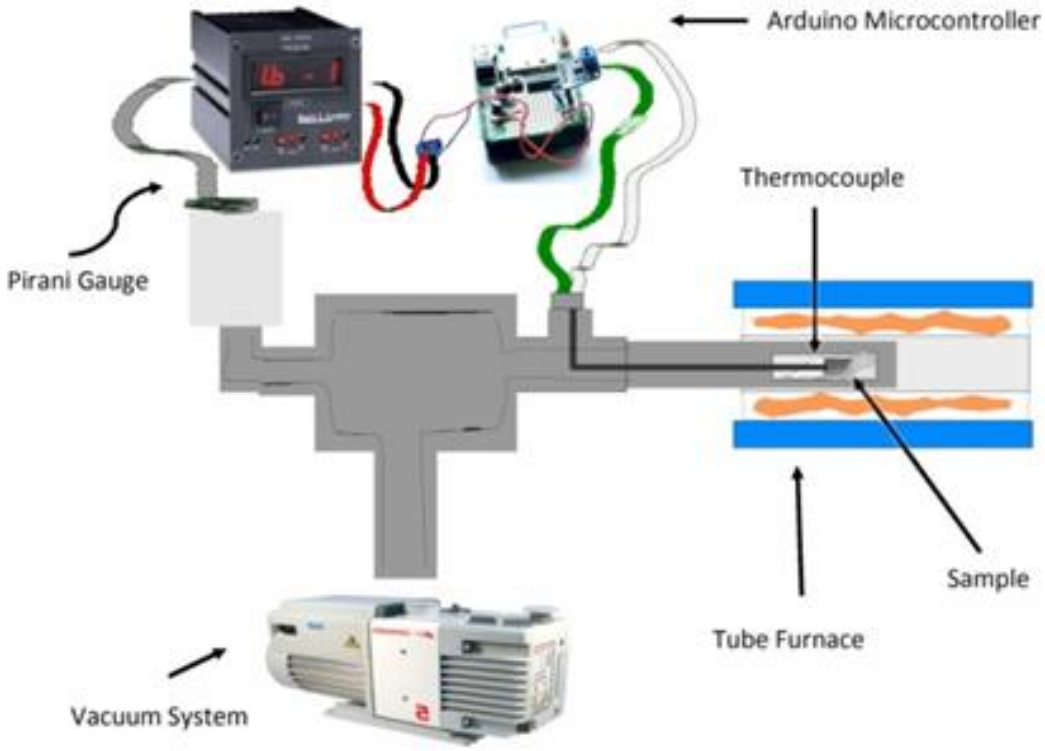

Fig.40. The data logging system.

6.11. Method and Construction

The Lesker 945 gauge controller has an analogue output. The output voltage varied depending on the pressure on the system monitored by the Pirani gauge. A type K thermocouple was placed inside the vacuum tube and in a location as close as possible to the green compact or powder during sintering. The microcontroller recorded the analogue signal from the pressure gauge controller, the temperature from the thermocouple amplifier and the cumulative time. The microcontroller used was an Arduino Duemilanove. The temperature was measured using a thermocouple amplifier and the data was stored on an SD card. The thermocouple amplifier chip used was a MAX6675 cold junction compensated K- type Thermocouple-to-Digital Converter. This outputs the temperature from a type K thermocouple as values in degrees centigrade, to the microcontroller over the Serial Peripheral Interface Bus. The thermocouple amplifier chip has a resolution of 0.25°C.

The microcontroller's analogue to digital convertor is 10 bit and in this work the range of voltages measured was from zero to five volts. This means that for a 10bit ADC, the analog voltage between zero and five volts is split into 1024 discrete units. This equates to a resolution of 5/1023 = 0.005 volts. The pirani gauge outputs an analog voltage between 0 and 3.2V. The data from the thermocouple amplifier and the analogue to digital convertor were saved to an SD card along with the cumulative time every twenty seconds. The values were saved in twenty second intervals as an Excel readable CSV file.

6.11.1. Limitations

There are limitations with the use of this technique for measuring the hydrogen desorption events. The main two limitations are that the gauge reader is calibrated for nitrogen and not for hydrogen. The second main limitation is that the voltage to pressure conversion from the gauge controller is not linear.

The voltage to nitrogen pressure table supplied by Kurt J. Lesker showed a certain range of voltages and corresponding pressures for Nitrogen, Argon and Helium.

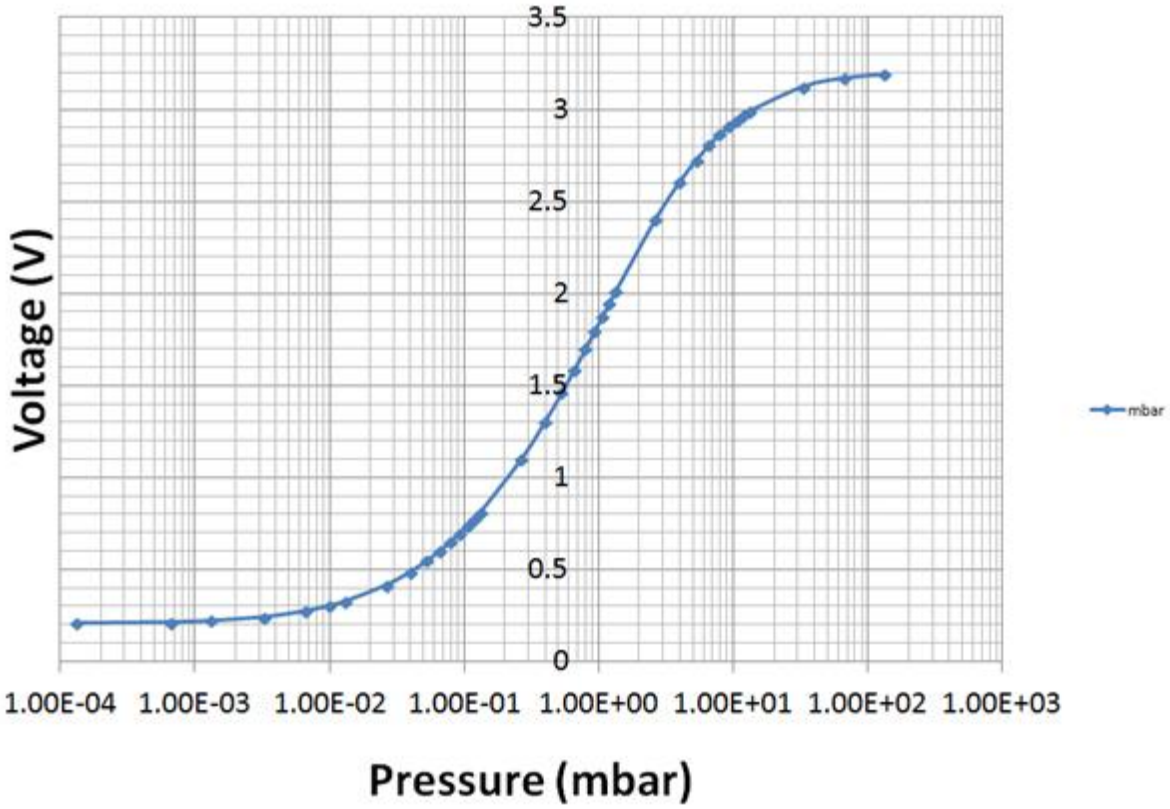

Fig.41. Graph showing the Non Linear voltage to pressure conversion from the Lesker data provided.

Fig. 41 shows the relationship between the output voltage from the gauge controller and the corresponding pressure in mbars for nitrogen. The data was taken from the voltage to pressure table provided by Lesker. Efforts were made to fit a single function to the entire curve but these were unsuccessful.

However, splitting the curve into discrete sections enabled functions to be fitted to the range of pressures of interest. This enabled any voltage in the range of the functions to be converted into a pressure value that mapped closely to the curve plotted in fig. 44.

The pressure range of most interest was that within the final peak of desorption, where $NdH_{\sim 2}$ transforms to Nd and H_2. The range over which this took place in the system outlined above is displayed in table 2.

Arb	**Volts**	**mBar**
68.20	0.33	1.33E-02
587.37	2.87	8.00E+00

Table 2. The pressure range of interest.

Table 2 shows the pressure range of interest obtained from the voltage to pressure data supplied. With arb corresponding to the calculated raw output from the data logger, which was effectively the zero to five volts, split into 1024 discrete values. Voltage multiplied by 204.8 gives the raw values from the data logger. The 204.8 value is 1024/5. Plotting the data provided over this range gives an exponential curve. The curve was split further into two, giving two functions that satisfy different regions of the curve.

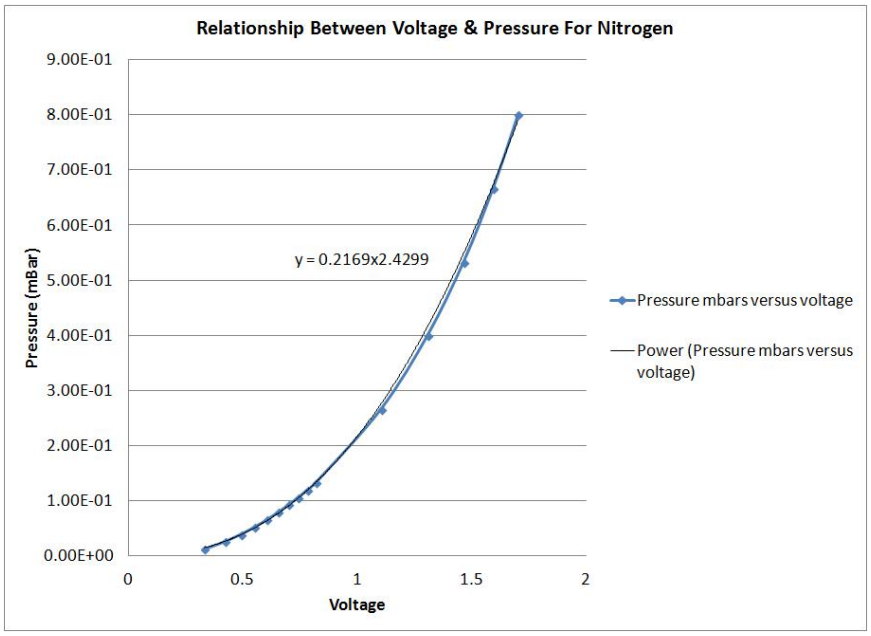

Fig.42. The relationship between 0.33 and 1.5 volts and corresponding pressures.

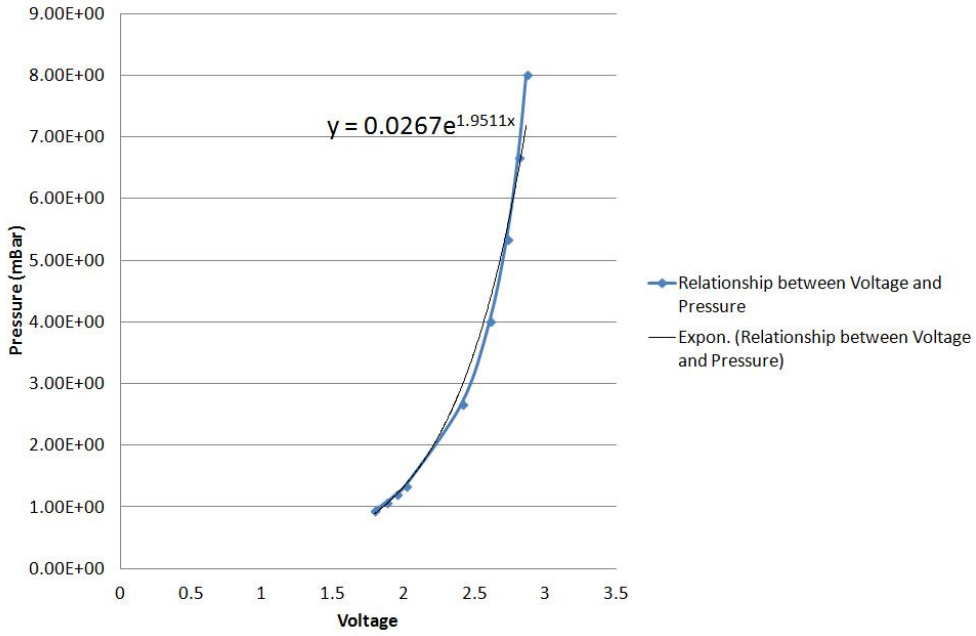

Fig.43. Relationship between voltage and pressure at up to 2.868 volts.

The two functions can be used to convert any voltage (in the range of 0.333 volts to 2.868 volts) to pressure values. Fig. 44 shows how the function fits compared to the data from the table provided by Lesker.

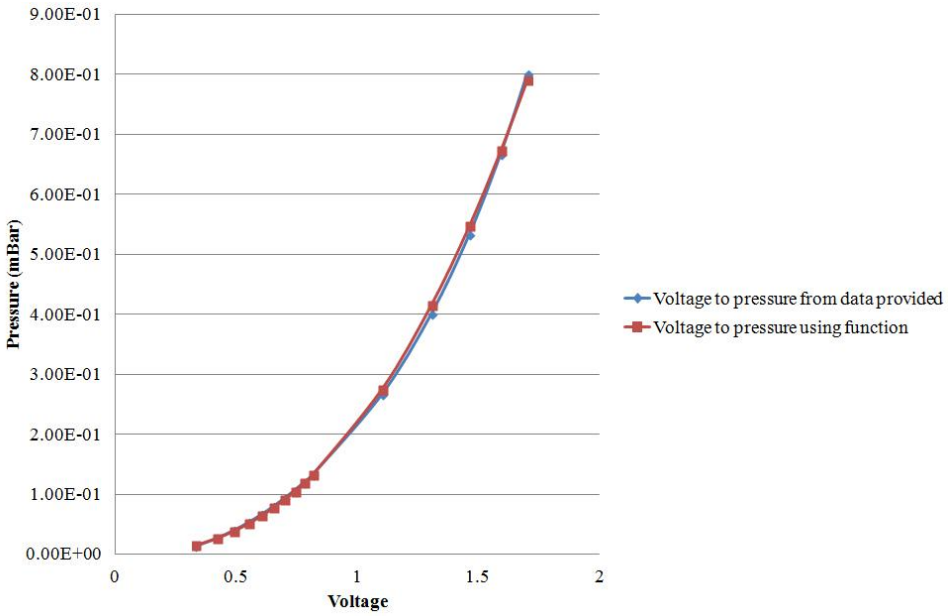

Fig.44 Data from the Lesker table compared to function.

6.11.2. Gas Calibration

Pirani gauges use the concept of thermal conductivity to calculate the pressure in a system. The gauge uses a heated filament that loses heat as gas particles interact with it. Any changes in the temperature of the wire correspond to changes in the wire's resistance. So as the number of gas particles reduces, (a reduction in pressure), the amount of particles interacting with the heated filament also reduces. This gives an indirect measurement of the pressure within a system.

The Pirani gauge relies on the thermal conductivity of the gases, so a change in thermal conductivity of the gas in the system, from the gas the gauge is calibrated for will affect the readout from the gauge controller. Unfortunately, the gauge controller used in this work was calibrated for nitrogen. The desorption gases being measured are most likely to be hydrogen. So the pressures indicated by the gauge controller will not be an accurate measure of the actual pressures inside the system.

6.11.3. Constant Volume

It is also important to keep in mind that what will be measured by the Pirani gauge will be the total pressure change in the vacuum system. This means that the volume of the system needs to be as close to constant as possible for each run.

The system is not a closed system as the rotary pump constantly operates removing gases from the system. It is assumed that the performance of the rotary pump is consistent over the pressure range and consistent between runs, so that the volume removed is consistent between runs.

By design, the Pirani gauge is in the exit path of the furnace tube so it should interact with any gases desorbed. Changes in the mass of the powder used will have an impact on the change in pressure within the system.

6.11.4. Other Potential Limitations

Another potential limitation is that the thermocouple amplifier on the system has a maximum temperature reading of 1024 °C. This is not a limitation for the desorption events but is somewhat inconvenient, as it prevents recording the maximum temperature reached when sintering at temperatures over 1024 °C. To counter this, a MyPClab USB data logger from Novus Automation was used to calibrate the sintering furnace. A newer model of the thermocouple amplifier chip (MAX31855) is now available enabling higher temperatures to be logged up to 1800 °C, with a resolution of 0.25 °C.

Because of the limitations discussed above, the changes in pressure due to desorption cannot be related to actual pressures. So the volume of hydrogen desorbed cannot be easily calculated.

6.12. Potential Variables During Desorption

6.12.1 Sample Mass

To compare desorption peaks, the mass of the green compacts needs to be as consistent as possible. This can be a challenge due to the method of production of the green compacts.

15.0 grams of powder was used to make the green compacts. The compacts were pressed as described earlier. There is potential for a slight loss of powder during removal of the green compacts from the isostatic bags.

6.12.2. The Heating Rate

Throughout all the desorption runs the heating rate was maintained at 7°C per minute.

6.12.3. Composition

The composition of the magnets will have an impact on the proportion of rare earth rich hydride phase compared to that of the $Nd_2Fe_{14}B$ hydride phase, which in turn should have an impact on the desorption peak heights.

6.12.4. Milling Conditions

Changes in the particle size distribution will have an effect on the desorption kinetics.

6.13. Particle Size Analysis

The particle size distribution of the HD powder and the milled powder was investigated using a variety of techniques.

6.13.1. Particle size Distribution of HD Powder

The unprocessed powder from the hydrided sintered magnets was subjected to a sieving process. Known masses of powder were sieved with varying sieve sizes. The mass of powder

that passed through and the mass remaining were recorded. The process started with a large mesh size progressing down to a 20µm size sieve. The process started with each sieving step using the powder that passed through the previous sieve. From this the cumulative mass percentage was calculated.

6.13.2. Particle Size Distribution of Milled Powder

The same cumulative mass achieved by the sieving process was used to characterise the milled powder. The sieving technique was found to be ineffective below 45µm mesh sieve size. There were potential problems with agglomeration occurring, making it difficult to establish the true particle size below 45µm. To investigate further the particle size of the sub 45µm powder it, was imaged optically using a Leitz optical reflecting light microscope. The image is captured using a Zeis Axiocam imaging system. Powder was distributed on a mirrored surface and a glass cover slide was placed on top and then viewed under the microscope. In this case, the mirror reflected the light back almost perfectly as it was perpendicular to the incident light, with the mirror showing up brightly. The powder however scattered the light, showing up as darker areas. The scattering was due to the various facets of the powder not being perpendicular to the incident light.

6.13.3. Agglomeration

Whilst imaging the sub 45µm powder it was observed that the powder had a tendency to agglomerate into large clusters. This made it difficult to identify the particle size of the powder.

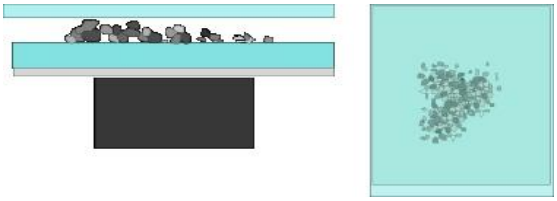

Fig.45. Imaging HD powder without an applied field.

To overcome this problem, a magnetic field was applied. The HD $Nd_2Fe_{14}B$ particles are ferromagnetic so they can be influenced by magnetic fields. By applying a field the particles aligned with the field, thus facilitating a better indication of the true nature of the powder particle size.

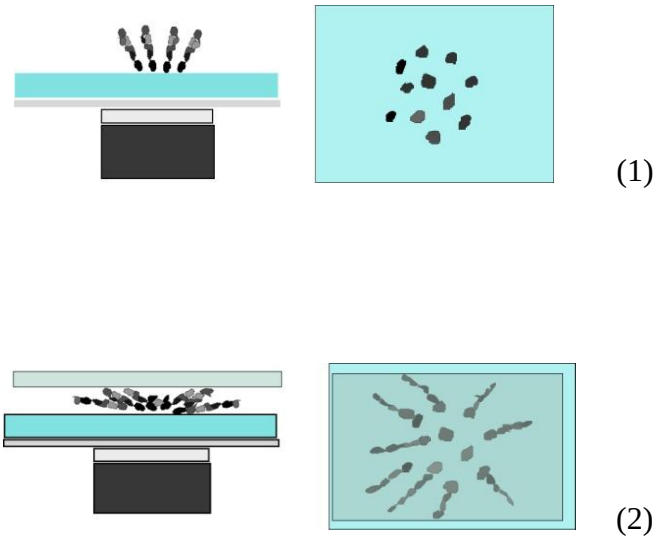

Fig.46. The imaging of powder, showing the effects of an applied magnetic field.

Fig. 45 and Fig. 46 show examples of the effects of the imaging technique with and without a magnetic field applied. You can see that the particles align with the magnetic field lines thus overcoming agglomeration Fig. 47. In this case the field was static and was supplied by a rare

earth magnet sandwiched between a steel block and the mirror. The strength of the field at the mirror surface was measured using a Hall probe and was ~200mT.

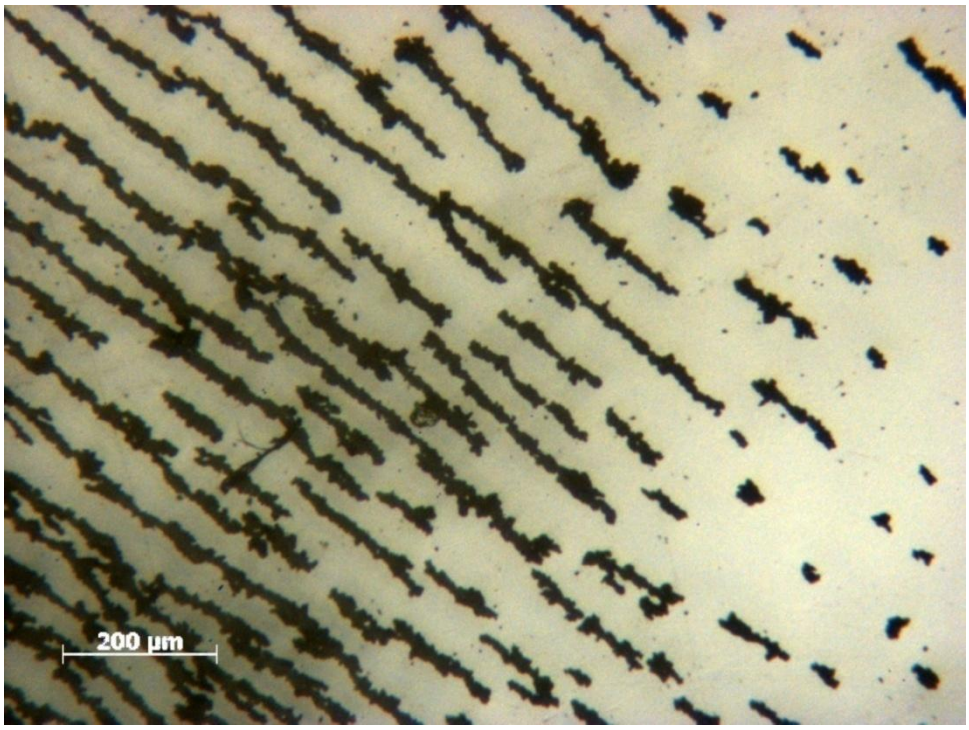

Fig. 47. Aligning the HD powder, (micron marker 200µm).

6.14. Reaction of HD Powder Exposed to Air

Powder was exposed to normal air for varying times. Powder was prepared using the Burr milling technique described previously. Powder with a particle size of less than 75µm was used for all the reaction runs. Batches of powder of approximately 15.2g were milled and then the milled powder was passed through a sub 45µm sieve and the mass fraction of powder greater and smaller than 45µm was recorded. The powder was then recombined using a 90µm sieve.

The mass used was 15.2g of powder providing enough reacted powder to make 15.0g of magnet for each run. The recombined powder was placed in a glass specimen tube and tapped to achieve a degree of compaction.

The tap density of the powder was calculated to be approximately 3g/cc. This was calculated from the mass of the powder and the diameter of the specimen tubes and the height of the powder within the tube after tap compaction. The tubes were sealed in the glove box and transferred into the atmosphere.

Cross Sectional Area (cm^2)	**Powder height (cm)** (± 0.01cm)	**Volume (cm^3)**	**Mass of Powder (g)** (± 0.01cm)	**Density (g/cc)** (±0.2g/cc)
4.08	1.28	5.21	15.2	2.92
4.08	1.29	5.27	15.2	2.89
4.08	1.28	5.22	15.2	2.91
			Average Tap Density	2.9

Table 3. HD powder density when exposed to air.

Once in air the specimen tubes were unsealed and the timer was started. The powder was exposed to the air for various times and then returned to the glove box to limit any further reaction prior to further processing.

This experiment has several drawbacks; the humidity of the air in the lab cannot be guaranteed to be constant and the temperature the samples will experience in the lab will vary. This is especially valid for the samples exposed for times exceeding 12 hours.

In an attempt to counter these problems, for each exposure time, two samples were exposed in unison. Humidity and the temperature experienced by both the samples should be identical.

After exposure to air one of the samples from the batch was processed aligned, pressed and sintered with the desorption events logged. The other sample from the batch had alloying additions added. The sample containing alloying additions and reacted powder was then processed and aligned and pressed into a green compact. The green compact was then sintered and the desorption events logged. The reacted powder from both samples should have the same humidity and temperature history as they were both exposed to air at the same time.

6.15. Adding Alloying Additions to Reacted Powder

After exposure, the powder in the specimen tubes was transferred to a glove box under an argon atmosphere, with an oxygen content which was always below 100 ppm, (typically ~50ppm). The masses of alloying additions were added to the exposed powder to make up 15g in total. The 15g of powder was subsequently passed through a 90µm sieve to combine and intimately mix with the powder. The sieving stage was repeated twice. The resulting powder was then added to an isostatic bag and then aligned, pressed and sintered, as described previously.

6.16. Machining of Sintered Samples

The sintered magnets were cut into two sections using a diamond cutting wheel. After slicing, the magnets were ground using silicon carbide paper to remove oxide coatings and to produce flat cylinders suitable for measuring.

6.17. Density

The density of the magnets was measured using the Archimedes principle. The samples were weighed in air (W_s) and in a liquid (W_l) of a known density (ρ_l) using an Ohaus balance, which is said to be accurate to 0.0001g. From this, the density of the sample can be calculated using the equation below. Prior to use, the sample was calibrated using a high purity copper sample. The errors associated with this measurement are ± 0.05gcm^{-3}.

$$\rho_s = \frac{W_s \rho_l}{W_s - W_l}$$

Equation 9. The Archimedes principle.

6.18. Characterisation

The magnetic properties of the samples were measured using a permeameter.

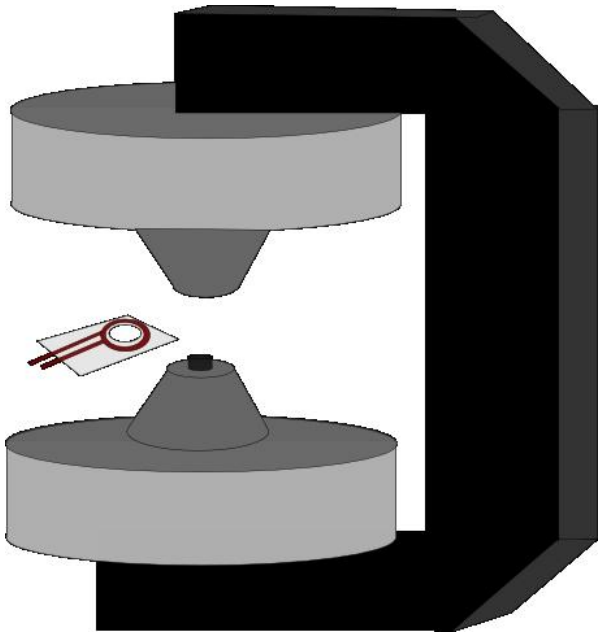

Fig.48. The permeameter system.

The permeameter system, (fig. 48) consists of two electromagnetic pole pieces which provide a closed circuit, changing field. The sample sits in the centre of the two pole pieces inside a set of measurement coils. The pole pieces are lowered and the sample is then subjected to a changing applied field. During a typical measurement operation, a sample of a known cross sectional area is pulse magnetised. The sample is then placed inside the coil, between the pole pieces and the pole pieces are lowered. Initially a demagnetising field is applied through the pole pieces. The measurement coils are connected to two integrated flux meters which measure the changing magnetic flux within the coils.

The permeameter is a closed loop system, so demagnetising fields from the sample can be ignored. With the sintered samples, the cross sectional area is obtained by measuring the diameter of the cylinder at various points. This was done eight times at various points around the sample. Care needs to be taken as the post sintered samples are not perfectly cylindrical. The permeameter was calibrated regularly with a Ni standard. Despite this, integrator drift, change in room temperature and sample positioning can all introduce errors. The cumulative errors for all of these was determined as Br±5mT, $_{i}H_{c}$ and $_{b}H_{c}$ ±5kAm^{-1}, (BH)max ±5kJm^{-3}.

6.19. Optical Microscopy

Samples were cut, mounted in Bakelite and polished for microscopy. Certain samples were etched using Vielas reagent. Others were etched using a 5 % citric acid solution.

The citric acid etch was developed during the course of the present work and was found to be very effective in revealing the grain boundaries. The etchants preferentially attack the grain boundaries, causing the grain boundaries to scatter light so that they appear darker when viewed with a metallographic optical microscope.

6.20. Kerr Effect Microscopy

A Leitz microscope was modified to make use of the polar magneto optical Kerr effect. The magneto optical Kerr effect employs the change in polarisation and intensity of light as it interacts with a magnetised material. A typical Kerr effect microscope makes use of two polarising filters.

The first filter polarises the light before it hits the sample. The light is then reflected off the sample and passes through another polarising filter and changes in intensity as it travels to the eyepiece and the camera. The result is changes in contrast, depending on the orientation of magnetic domains, allowing a qualitative judgement on the degree of alignment and size of magnetic domains and grains.

Image analysis was used on the microscopy images. All the images were taken using a Zeis Axiocam system, calibrated with a graticule at all magnifications. The analysis of the images was conducted using two different image analysis packages, J micro vision and image J.

Chapter 7. Characterisation of Starting Material

The starting material used throughout this project, was supplied by Arnold Magnetic and consisted of uncoated sintered blocks of NdFeB.

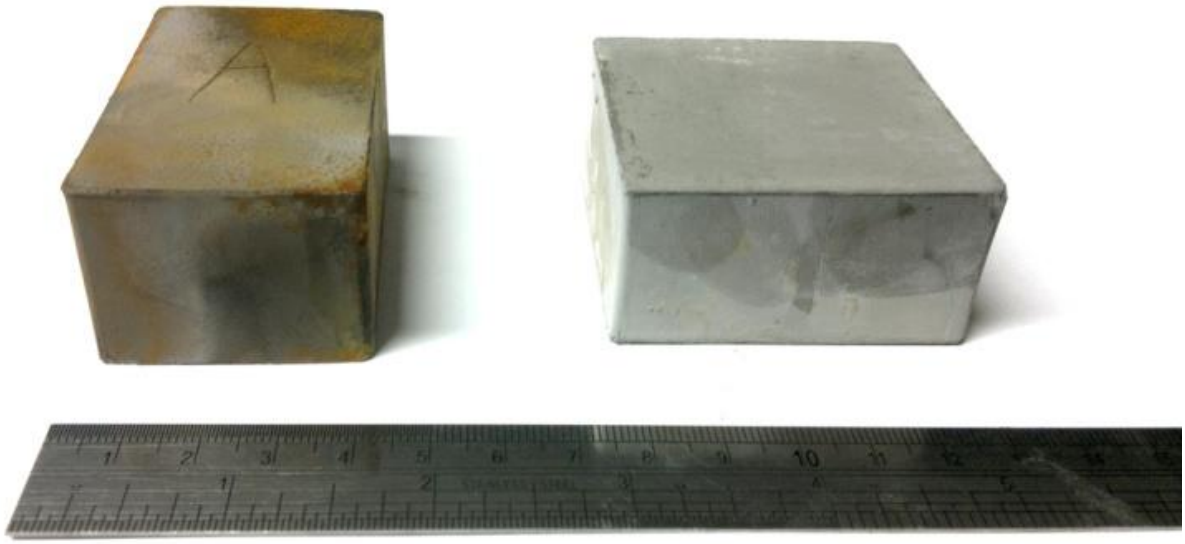

Fig.49. Starting materials; (uncoated sintered NdFeB), #R (64x39x29 mm) and #S (55x55x27 mm).

Two types of uncoated block were provided, as shown in fig. 49. The composition and magnetic properties of the two blocks were different. The two types of starting material will be referred to as #R and #S from now on. The majority of the work exhibited here was performed on the #R sintered blocks as the starting material. When there was a change in the starting material it will be indicated explicitly.

7.1. Composition of the starting material

The typical composition of starting material of the #R sintered block was obtained using ICP analysis.

ICP wt%	B	Fe	Nd	Dy	Pr	Al	Co	C	N	O	Nb
	%	%	%	%	%	%	%	Ppm	Ppm	%	%
#R	1.02	66.01	29.17	1.98	0.1	0.29	0.36	572.5	95	0.42	0.4
#S	1	58.16	25.95	4.21	0.34	0.34	4.22	671	222	0.41	0.83

Table 4. #R and #S composition. Errors ±0.01%

7.2. Density of Starting Material

Sintered Magnet # R	Density (g/cc)
1	7.54
2	7.52
3	7.47
4	7.56
Average	**7.52**

Table 5. Average density of the material was measured at 7.52 g/cc (±0.04g/cc).

7.3. Fracture surface of the starting material # R

The fracture behaviour of the starting material could provide an indication of the fracture behaviour of the hydrided material. To investigate the fracture surface of the starting material it was viewed with a Leitz reflecting optical microscope. Due to depth of field limitations, multiple images were taken and stacked to form a composite image so a greater proportion of the fracture surface was in focus.

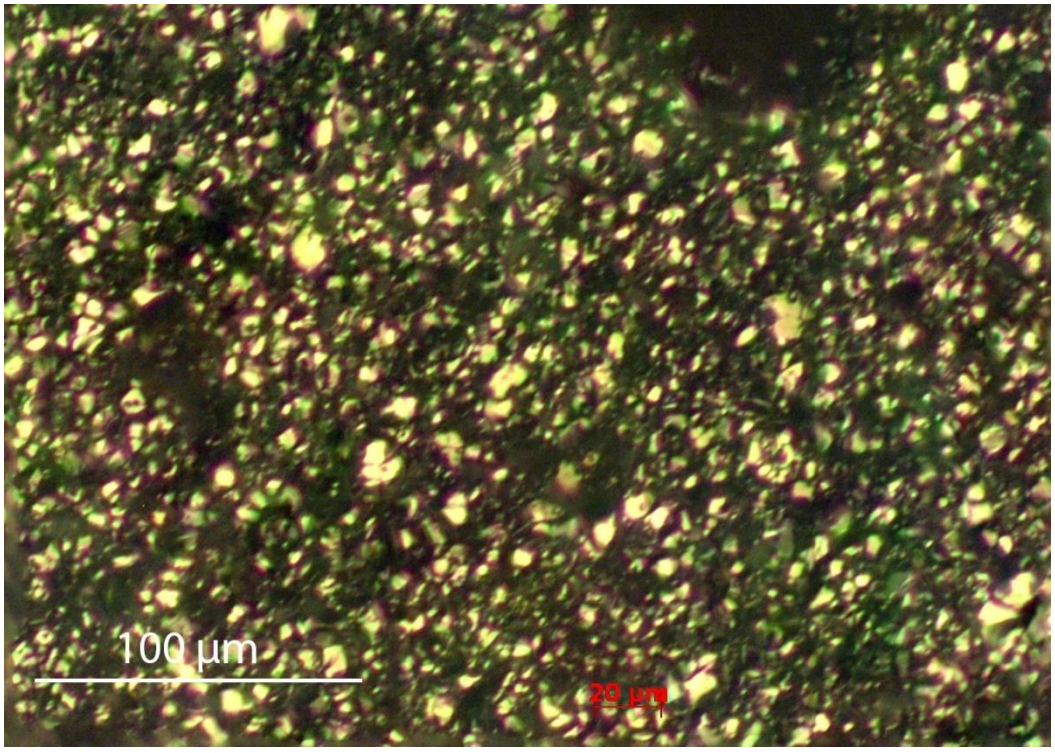

Fig.50. Fracture surface of the #R uncoated sintered magnet. Micron markers span 100 µm (20 µm).

Fig.50 shows fracturing on the surface of the sintered # R material, it appears to be intergranular. The lighter features in the image show the grain facets of the material. Jiang et al, (2000) investigated the fracture mode of sintered NdFeB. Their investigation showed that the fracture mode of sintered magnets is mainly intergranular, with cracks propagating along

the grain boundaries. They reasoned that the mechanism of the fracture "is the weakness of the boundaries". They suggest that this is due to the presence of the Nd rich phase at the grain boundaries.

7.4. Imaging of Polished Fracture Surface

Samples of the starting material where mounted in Bakelite, polished and then imaged using a Leitz optical microscope.

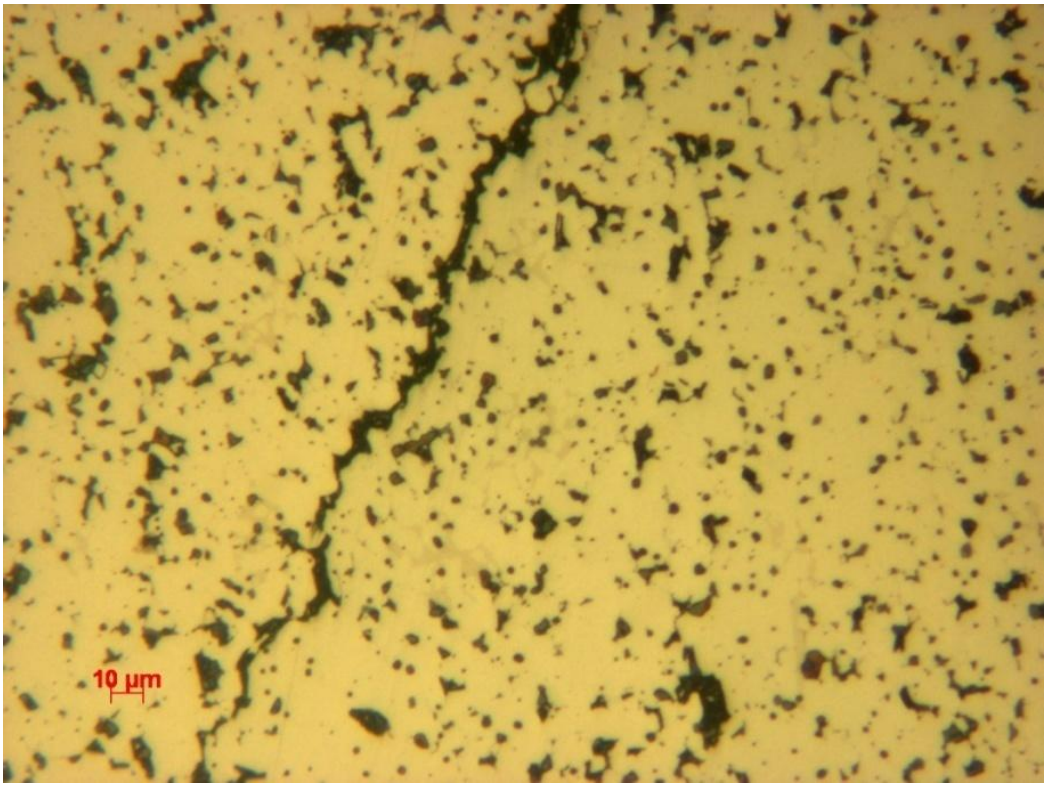

Fig.51. Crack propagation in sintered NdFeB.

Fig. 51 shows the path of a crack travelling through sintered starting material mounted in Bakelite and polished. The path of the crack starts at the top of the image and appears to snake around the grain boundaries towards the bottom left of the image.

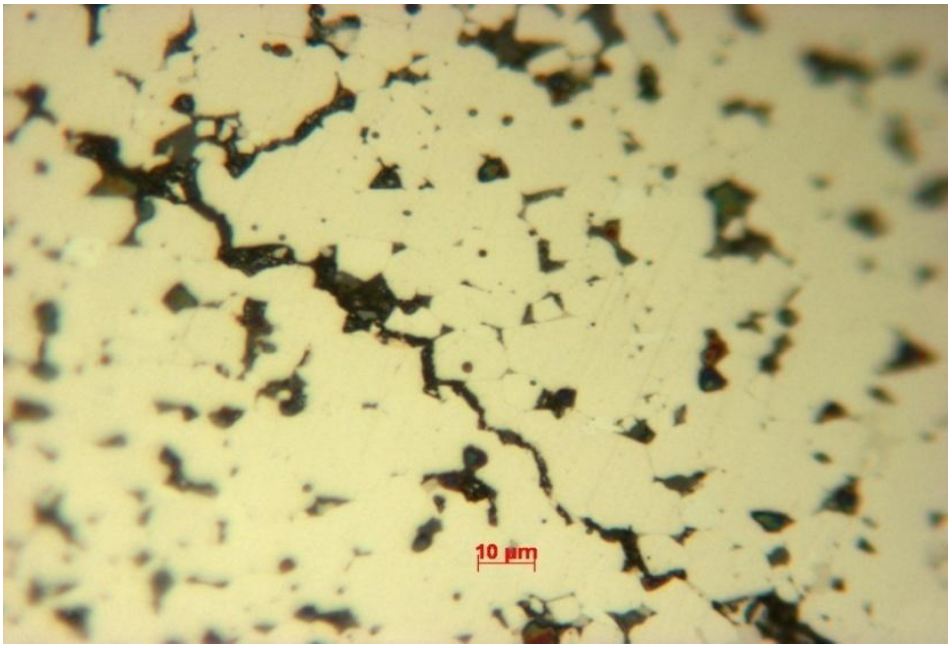

Fig. 52. Close up image of a crack propagating through the #R starting material.

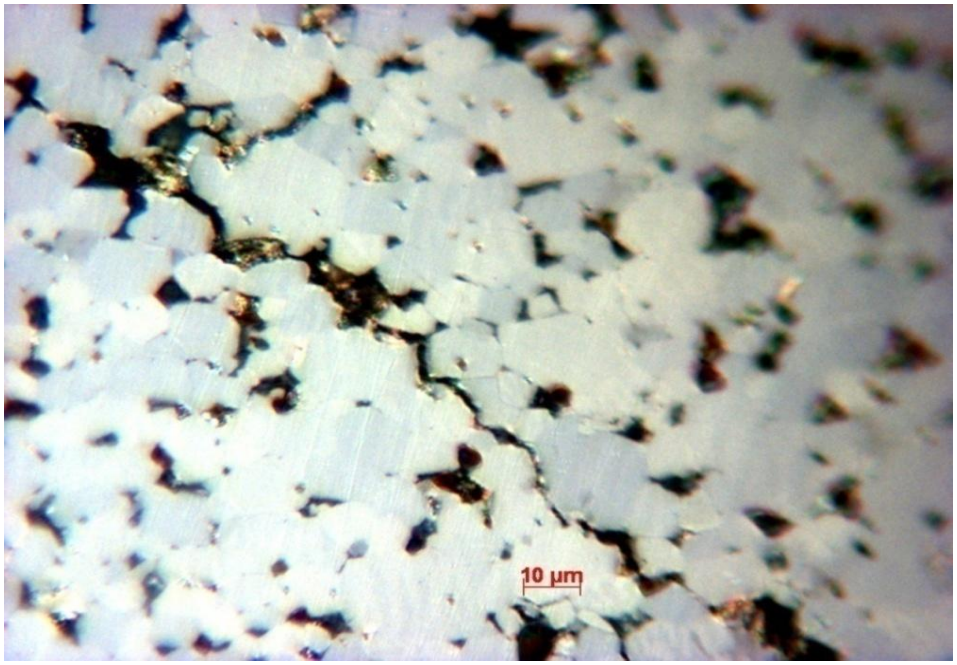

Fig.53. Same location, imaged using polar magneto optical Kerr effect to highlight individual grains.

It can be seen from fig. 51 that the crack path appears to be travelling along the grain boundaries of the sintered material. The fractures shown in fig. 51, fig. 52 and fig. 53 all seem to show that the crack path is following the grain boundaries of the material. This agrees with the view of Jiang et al, (2000) that the fracture mechanism of sintered NdFeB tends to be intergranular in nature. They argued that the fracture path tends to follow a path through the Nd rich phase at the grain boundaries which is lower in strength.

7.5. Fracture Surface

The three images in fig. 54 below show the fracture surface of the starting material, the facets have been measured using image analysis software.

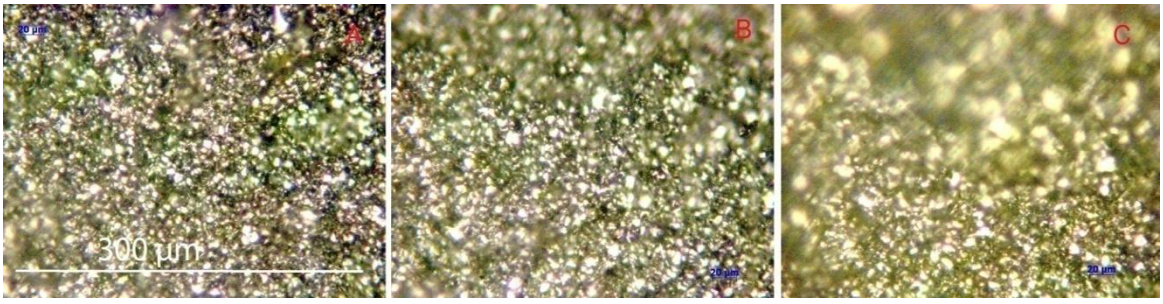

Fig.54. Fracture surfaces of #R sintered magnet. Span of micron markers 300µm.

Fracture Surface	Average (µm)	Max (µm)	Min (µm)	Median (µm)	Mode (µm)	SD
A	6	15	2	5	4	2.08
B	6	17	2	6	5	2.3
C	6	15	2	6	5	2.52
Combined (455)	6	17	2	5	4	2.26

Table 6. Fracture surface data. Measurement error ±2µm.

Table 6 shows the average, min, max and standard deviation of the grains. The lighter areas in fig. 53 show facets of grains perpendicular to the path of light. As light strikes the surface it is reflected. The parts of the sample perpendicular to the path of the light reflect light back up towards the eye piece, appearing bright. The areas of the sample that scatter the light appear darker. Table 6 shows image analysis data on the fracture surface of fig.53. All the diameters of the lighter facets were measured by hand so human error during measuring will be present. Only facets or features that were thought to be single grains were measured. Features where this was unclear were ignored.

Facets and grains are not always regular shapes, so the Feret's Diameter was measured. This is the longest distance between any two points, so in this case the maximum diameter for each facet or grain.

Due to the depth of field and relatively large changes in height of the fracture surface, only a low magnification could be used to image the surface. This meant trying to measure diameters that were very small relative to the area in view. This would have resulted in larger errors when trying to measure the diameters of the facets. In addition to this, smaller grains could be missed or inaccurately measured as the facet diameter got close to the resolution limit. Each pixel in an image corresponds to a micron value and, depending on the magnification, this value of microns per pixel changes. The fracture mechanism cannot be guaranteed to be entirely intergranular. There may be some transgranular cleavage fracture occurring and this could distort the measurements. The diameter measurements from the image analysis software were converted to whole numbers to try to mitigate some of these errors.

For the three fracture surfaces shown in fig. 53, and table 6, the values all seem similar and consistent. The standard deviations for all three are similar and the maximum, minimum and mode for A, B and C are similar also.

7.6. Optical microscopy of the Starting Material

Optical microscopy of the sintered starting material showed evidence of porosity. The darker areas in the image are evidence of porosity.

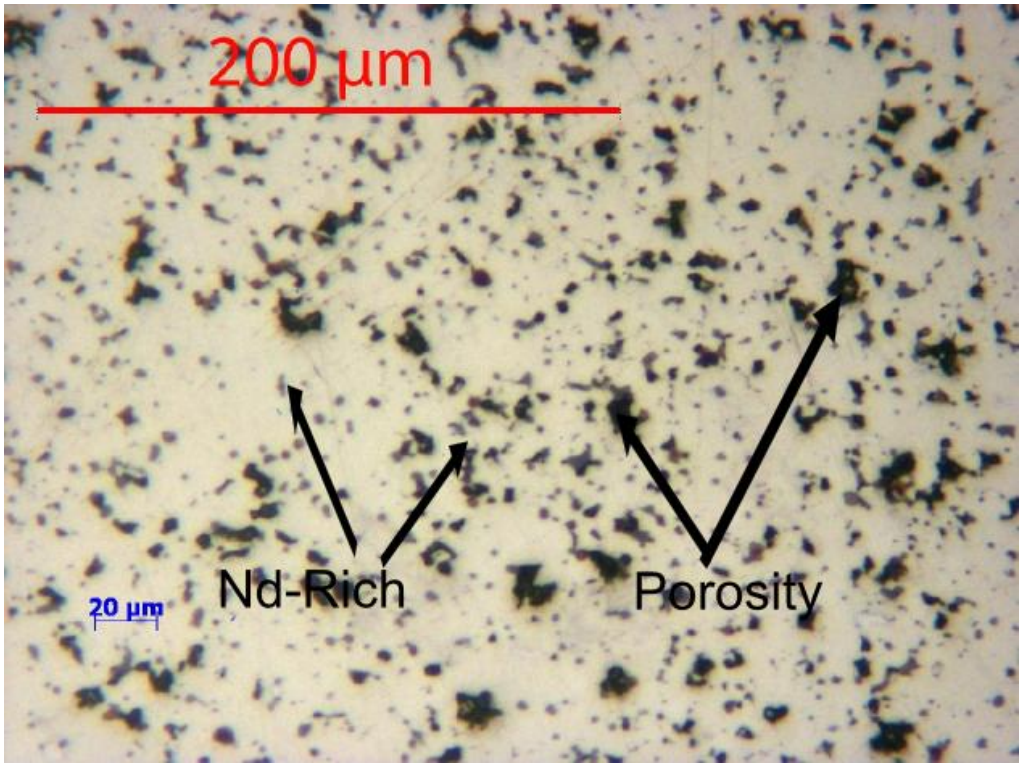

Fig.55. Optical microscopy of the starting material #R.

7.7. Optical microscopy of Polished and Etched Starting Material

The starting material was mounted in Bakelite with the sample surface perpendicular to the c axis. The samples were then polished and etched to reveal the grains. The etchant attacks preferentially the grain boundaries causing the boundaries to scatter the reflected light when viewed under a microscope. The etchant used in this case was Viella's reagent.

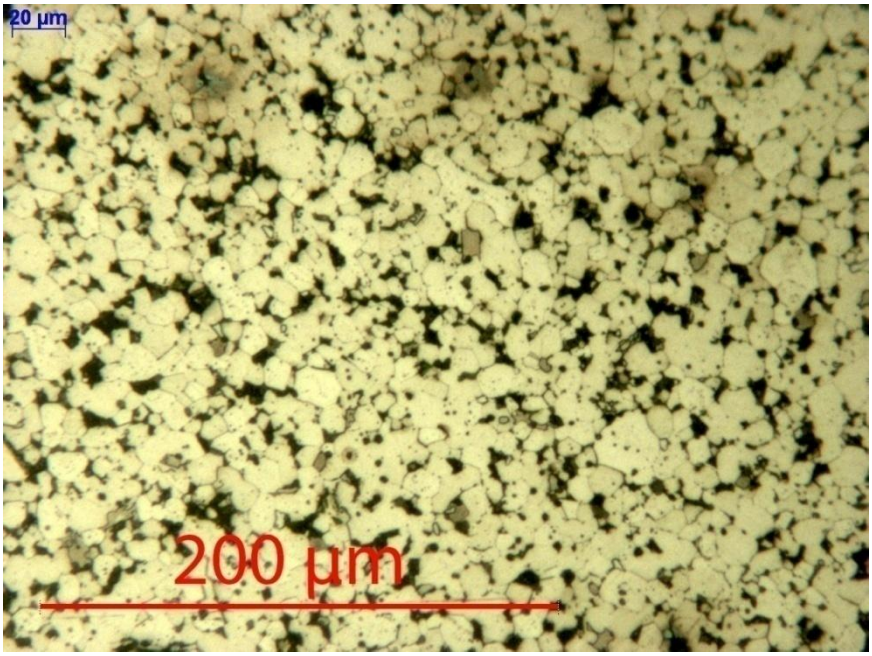

Fig.56. Polished, etched samples showing microstructure of the starting material.

Micron marker span 200µm.

Fig. 56 shows the grain size of the starting material. Micrographs were taken from three different samples with the grain size analyzed using image analysis software.

Etched	Average (µm)	Max (µm)	Min (µm)	Median (µm)	Mode (µm)	Standard Deviation
A	8.48	17	3	8	6	2.85
B	8.32	26	2	8	7	3.57
C	8.13	23	2	7	7	3.60
Total (540)	8.30	26	**2**	8	7	**3.37**

Table 7. Measurements of etched sample grain sizes. Measurement error ±0.5µm.

7.8. Etched Grain Size

Due to the fact that the samples are polished and etched, a more accurate measurement of the grain size can be obtained. This is partly because the outlines of the grains are clearer due to etching. It is also due to the fact that the sample is optically flat so higher magnifications can be used and the number of microns per a pixel can be reduced thus, giving a higher resolution. So the measurement error for the etched sample was calculated as ±0.5μm.

The grain size of the polished and etched samples varied from 2 to 26 microns with a mode value of 7 microns and an average of 8.3 microns.

7.9. Kerr Effect Images of the Starting Material

Samples were mounted in Bakelite with the c axis perpendicular to the polished surface. Instead of etching the sample to remove some of the grain boundary material the material was viewed using polarised light and the principle of the magneto optical Kerr effect (fig. 57). Polarised light striking the material interacts with the magnetic domains at the surface. This produces changes in polarisation as the light is reflected, which results in changes in intensity of the light measured by the imaging system. As with the etched sample, higher magnifications could be used as the sample was optically flat. The grain definition was also good. Under Kerr effect microscopy the Nd rich phase appears dark. The measurement error for the Kerr effect imaged samples is also plus or minus 0.5μm.

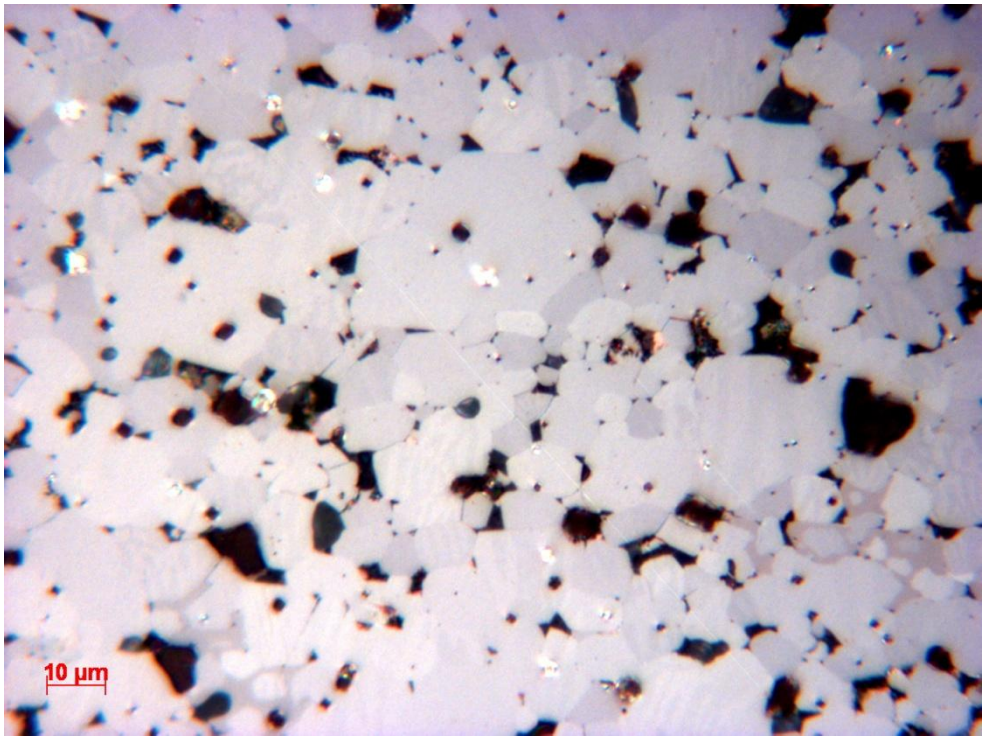

Fig.57. Kerr effect imaging of starting material. Span of micron marker, 10µm.

Kerr Effect imaging	Average (µm)	Max (µm)	Min (µm)	Median (µm)	Mode (µm)	Standard Deviation
A	12.09	33	5	11	11	5.66
B	11.03	32	5	10	9	5.26
C	12.42	28	5	11	10	5.00
Total	11.85	33	5	10.5	10	5.29

Table 8. Data from Kerr effect imaging - measurement of grains. Error ±0.5µm.

The grain size of the Kerr effect samples varied from 5 to 33 microns with mode values of 10 microns and an average of 11.85 microns.

7.10. Comparing Grain Size Measurement Techniques

Data	Average (µm)	Max (µm)	Min (µm)	Median (µm)	Mode (µm)	SD
Fracture (455)	6	15	2	5	4	2.08
Etched (540)	8.3	26	8	2	7	3.37
Kerr (568)	10.86	34	9	3	8	4.78

Table 9. Comparison of grain size in the #R starting material.

Table 9 shows data on the diameter of grains from the fracture surface and polished samples, imaged using the Kerr effect and also polished samples etched to preferentially remove grain boundaries. The number of data points for each measurement method is provided.

The data gives an insight into the grain size of the starting material. The etched and Kerr effect data proved to be the most reliable method of measuring the grain size, as when imaged, the grains were clearly delineated so a more accurate measurement could be taken. The fracture surface data can only infer the grain size of the material. In this case it seems that using the diameter of the facets gives lower values for the grain size of the starting material compared to the Kerr effect and etched methods.

For the etched and the Kerr effect samples, the mode and median values were close. The Kerr effect method showed a wider range of diameters (from 3 to 34 microns).

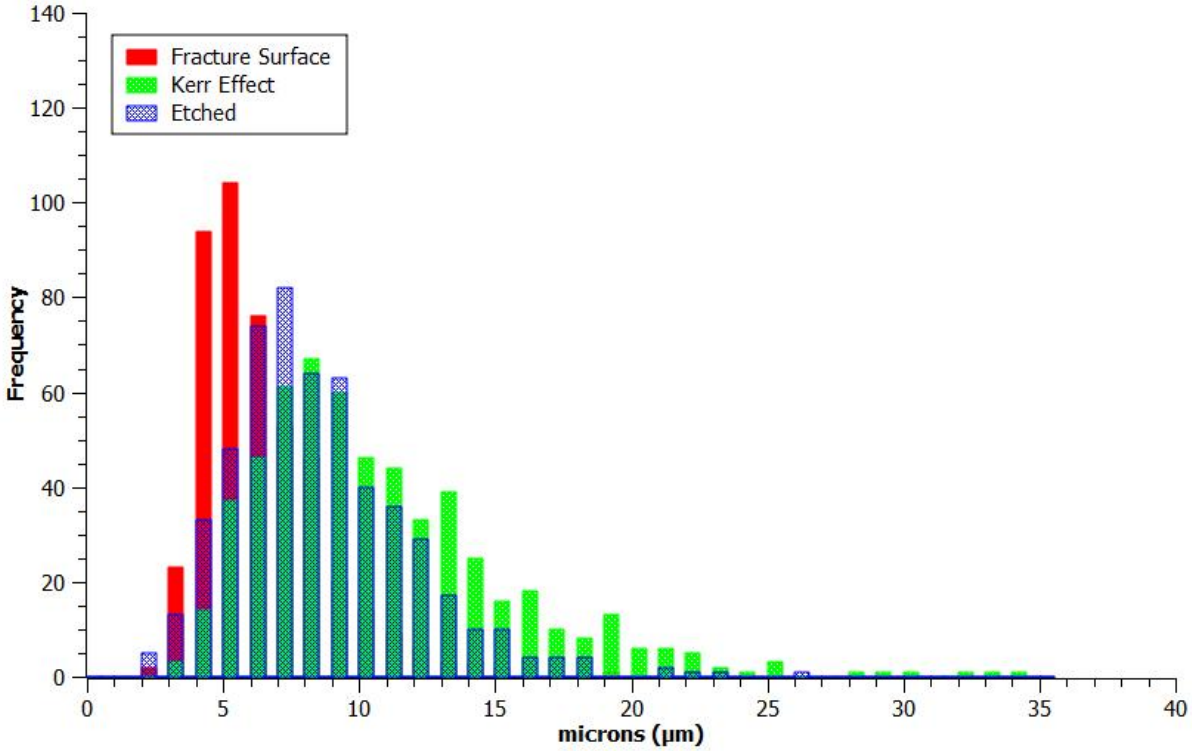

Fig.58. Histogram comparing grain size data.

The histogram in fig. 58 shows that the data for grain size, obtained using imaging of the fracture surface, appears to be shifted to the left towards smaller diameters. The Kerr effect and etched samples showed a very similar distribution.

7.11. Magnetic Properties of Sintered NdFeB # R

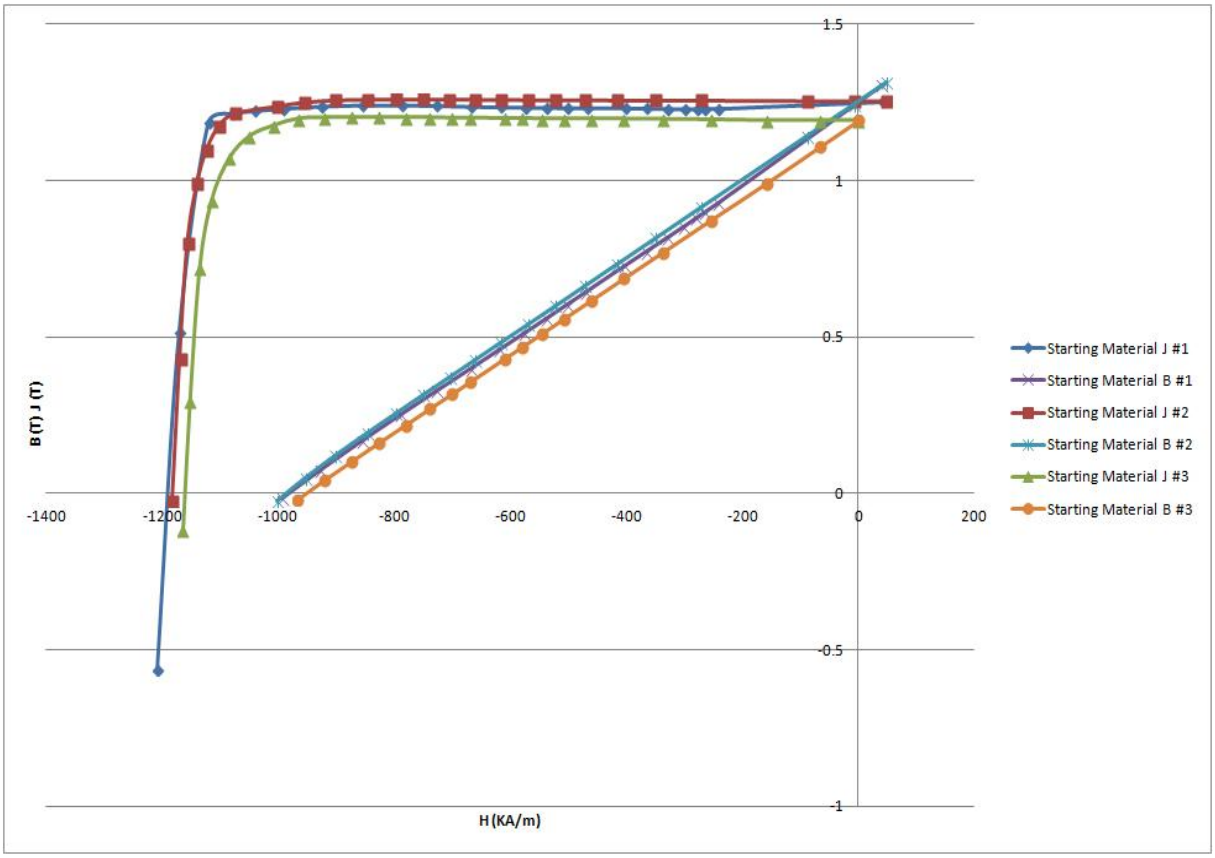

Fig.59. Typical demagnetisation curve for the # R sintered starting material.

	Mr(T) (±0.06T)	**Hci(KA/m) (±50 KA/m)**	**Hcb(KA/m) (±40 KA/m)**	**BHmax (KJ/m^3)(±50 KJ/m^3)**
#1	1.23	1208	993	302
#2	1.25	1182	1002	314
#3	1.19	1164	967	285
Average	1.23	1185	987	300

Table 10. Demagnetisation curve for three different batches of starting sintered magnet material.

7.12. Particle Size of the Hydrogenated Powder

Fig.60. Two partially hydrogenated blocks which started as fractured, rectangular, uncoated sintered magnets.

The starting material was hydrided partially at room temperature following the hydrogenated procedures described previously. In this case the hydrogenation was halted before the NdFeB magnets were fully hydrided. Fig. 60 shows a tendancy for the bulk material to spheroidise.

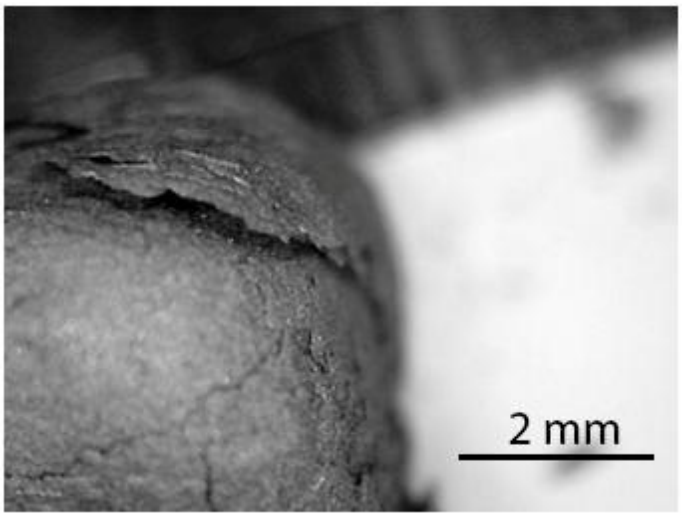

Fig.61. Close up of one of the partially hydrided magnets (b) in fig. 60.

Figs. 60 and 61 show close ups of partially hydrogenated magnets. You can see the fractures on the surface and the HD material is coming off in flakes. This is generally termed "onion skin" failure.

7.13. HD Powder Particle Size Distribution

Fully hydrided powder was passed through sieves with varying apperture sizes, starting at 850µm and ending with a sieve size of 20µm. The aim was to classify the HD-powder. The mass of powder between each sieve stage was recorded along with the powder passing through the sieve stage.

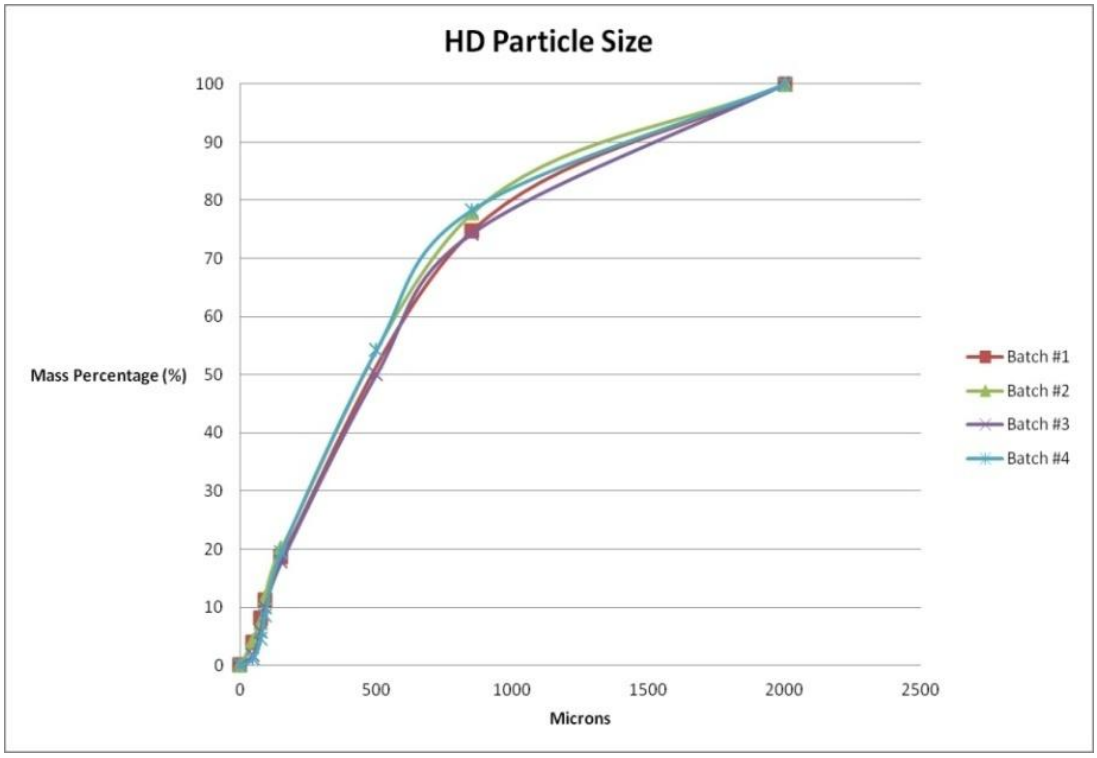

Fig.62. Cumulative mass of sintered material hydrided at room temperature.

Fig. 62 shows the cumulative mass percentage of four different batches of HD powder hydrogenated at room temperature and at a pressure of 4 Bar. By mass, between 70 and 80

percent of the HD powder is greater than 850μm in size, showing that the HD powder is relatively coarse, and only between 4 and 8 percent of the powder passes through the 75μm sieve. The plots for cumultive mass for four different batches exhibit good agreement.

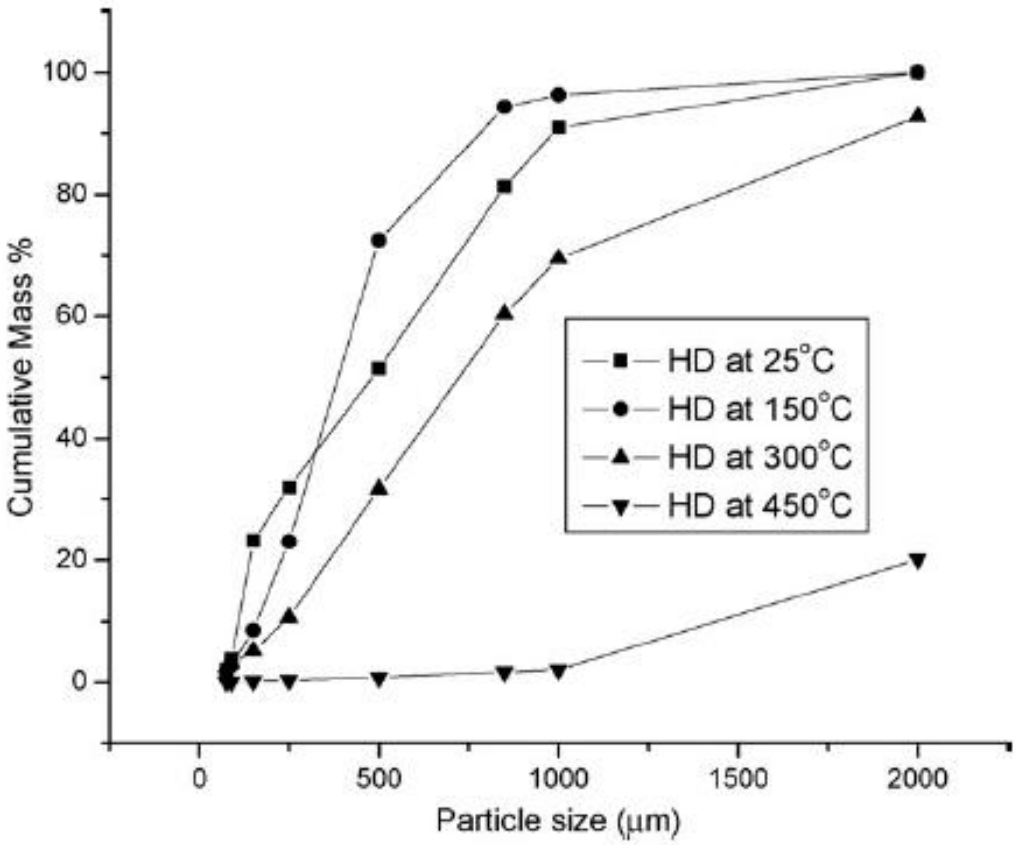

Cumulative mass % of sieve fractions of powders hydrogen decrepitated at a range of temperatures (as indicated in legend).

Reproduced From Possible methods of recycling NdFeB-type sintered magnets using the HD/degassing process
M. Zakotnik ⁂, I.R. Harris, A.J. Williams
Department of Metallurgy and Materials, University of Birmingham.Journal of Alloys and Compounds 450 (2008) 525–531

Fig.63. Cumulative mass of hydrogenated powder, reproduced from Zakotnik et al (2008).

The distribution in fig. 62 is similar to the results shown by Zakotnik et al, (2007) for sintered NdFeB hydrogenated at room temperature.

7.14. Microscopy of Fully Hydrogenated Powder

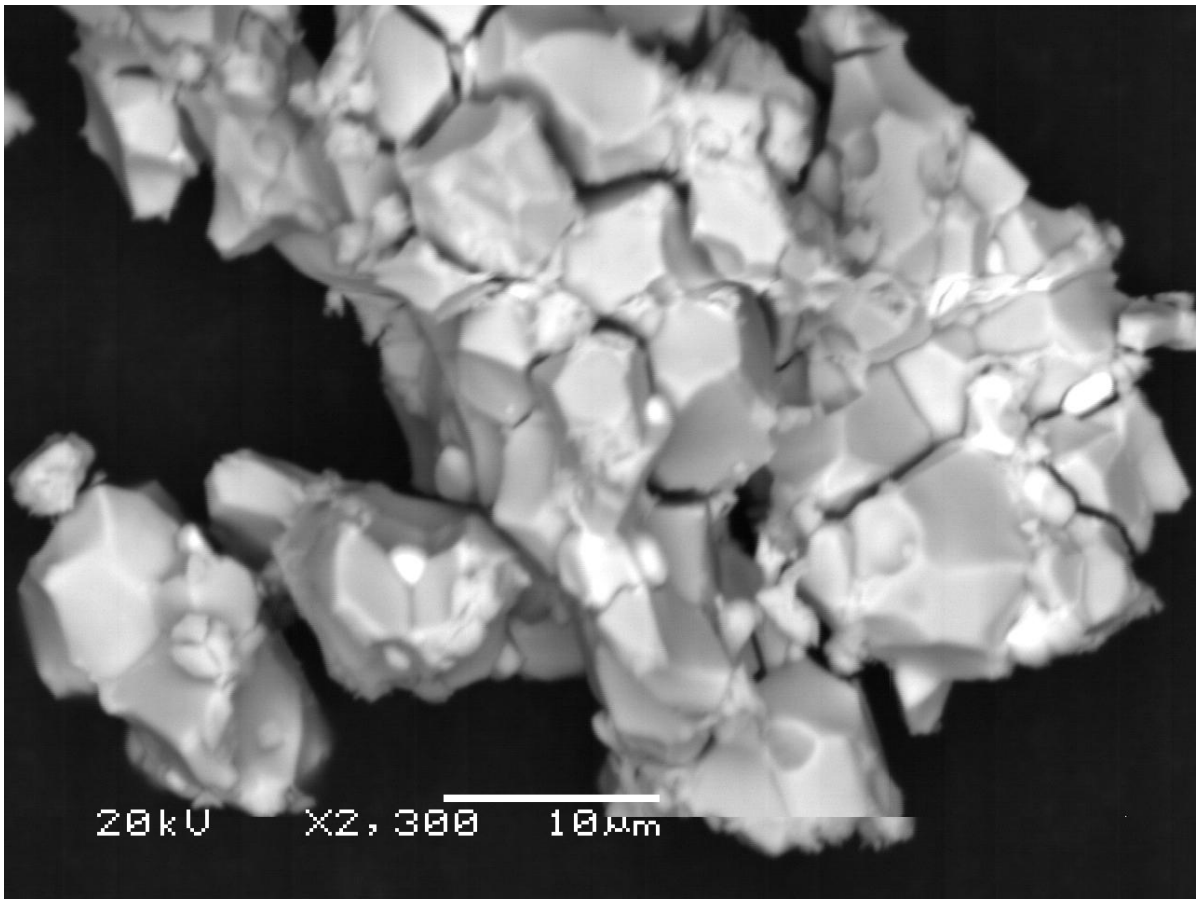

Fig. 64. Back scattered SEM image of HD powder.

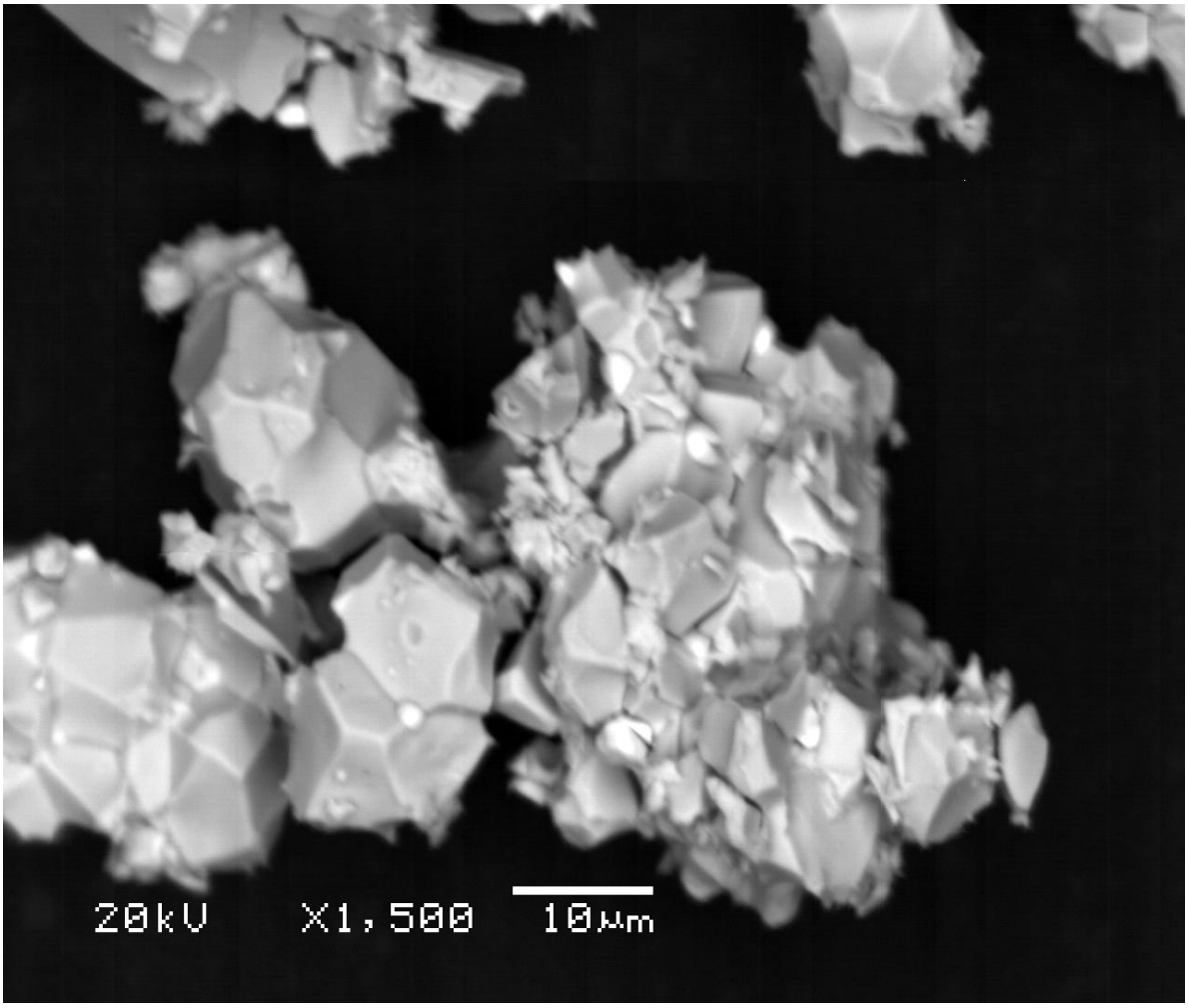

Fig. 65. SEM BSE image showing unmilled HD material.

To investigate the decrepitation behaviour further, samples were prepared by polishing the surface of sintered NdFeB to a finish of 1/4 µm. These samples were then magnetised and placed in a windowed HD chamber and reacted with 1bar hydrogen at room temperature. The reaction was allowed to fully complete resulting in fully decrepitated material. The experiment was repeated and the reaction was halted by evacuating the HD vessel just after the initial cracking phase. The sample was subsequently examined using an optical microscope. The sample was then returned to the HD vessel and the reaction resumed. Again

the reaction was halted to make observations of the microstructure. Finally, the sample was allowed to fully hydrodgenate.

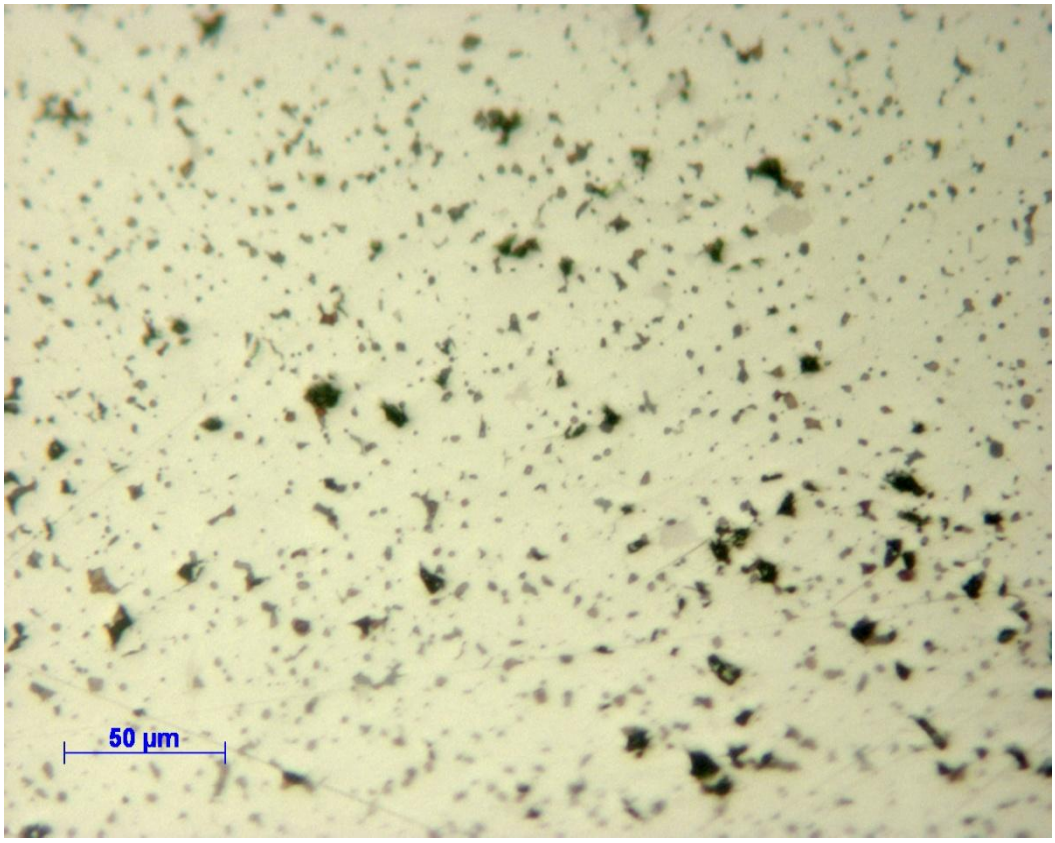

Fig.66. Starting microstructure of the sintered magnet prior to hydrogenation.

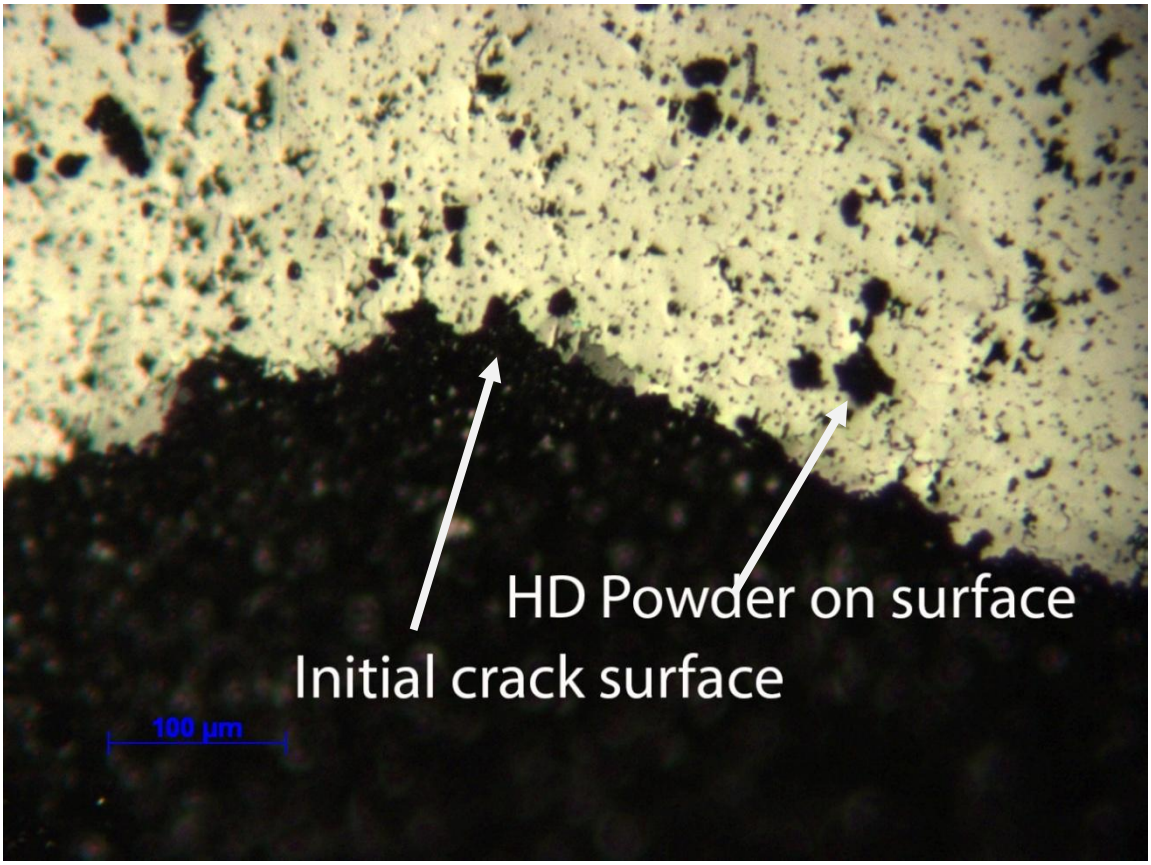

Fig.67. Sintered NdFeB exposed to 1 bar hydrogen. (Showing decrepitation just after initial cracking).

Fig. 67 shows the initial crack interface just after the initial fracture of the sample. The microstructure looks very similar to that of the starting material. The dark areas indicated are HD powder particles on the surface of the sample originating from the initial cracking.

The sample was returned to the HD vessel and exposed to hydrogen for a further 5 minutes to 1 bar, at room temperature, before it was removed and the microstructure examined. Fresh cracking was observed as seen in fig. 68. The new cracks started from the initial crack site and travelled into the main body of the material.

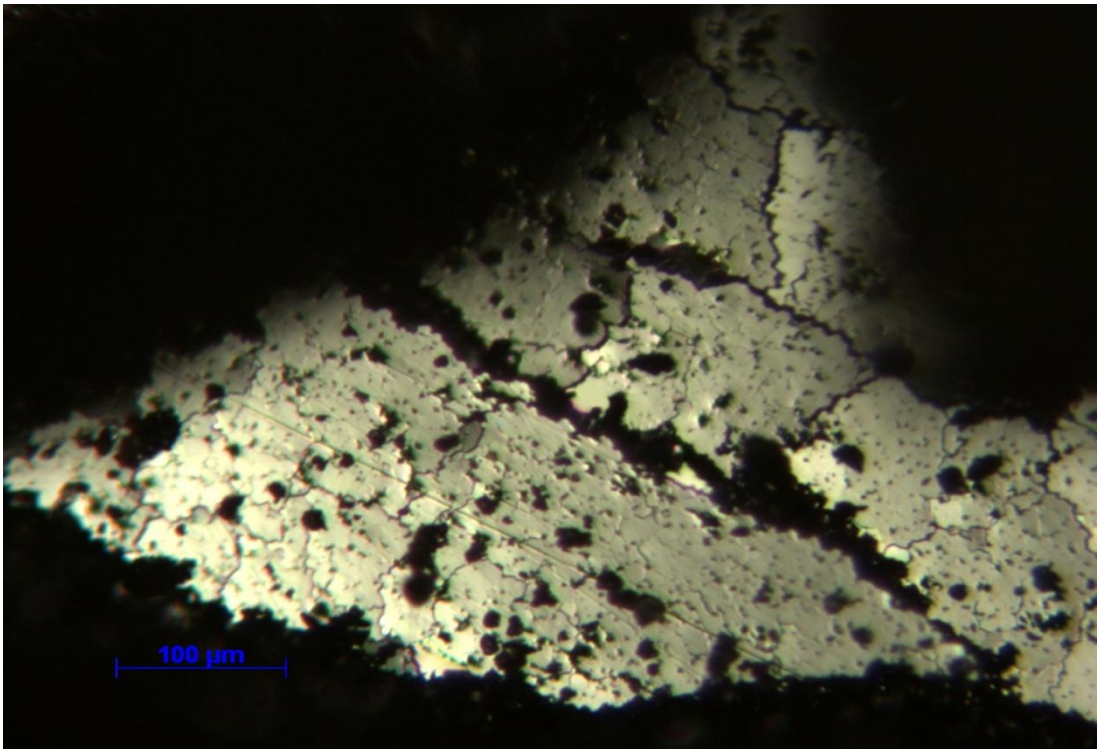

Fig.68. Sintered NdFeB after exposure to hydrogen, showing decrepitation, 5 minutes after initial cracking. The crack is clearly visible.

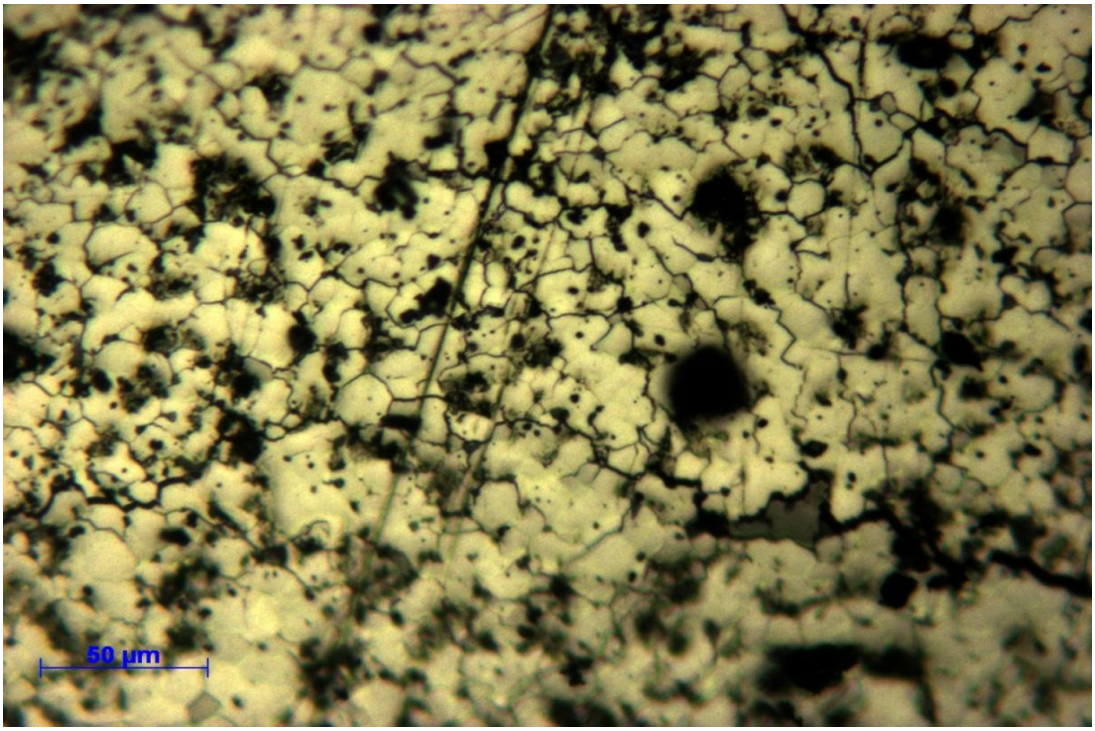

Fig.69. Microstructure of a fully hydrogenated sintered NdFeB sample (micron marker 50µm).

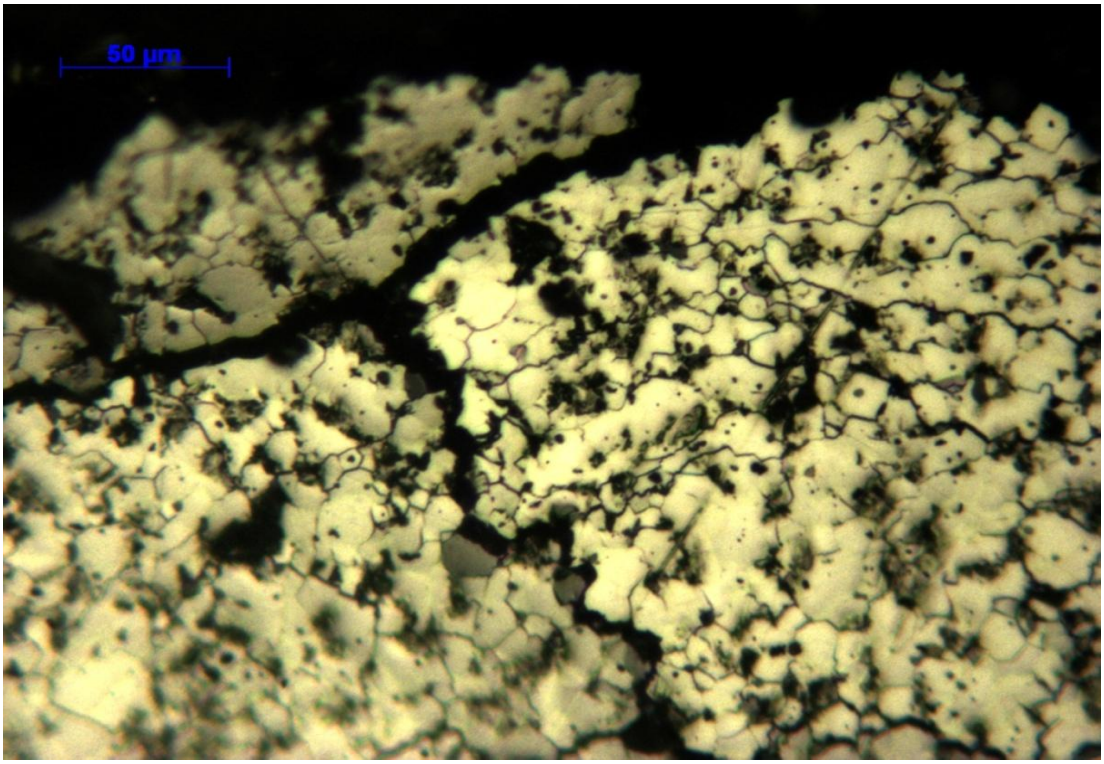

Fig.70. Fully hydrogenated sintered NdFeB. Intergranular cracks are clearly visible throughout.

From the initial crack, further smaller cracks propagated, heading towards the main body of the material as seen in figs. 67 to 70. This agrees with the work by Yartys et al, (1996) who observed an initial explosive - like fracture, followed by the flaking away of layers of material.

When allowed to fully decrepitate, the sample developed mainly intergranular cracking throughout. This shows that the reaction of sintered NdFeB-type magnets with hydrogen at room temperature does indeed fracture in a mainly intergranular manner, as reported in the literature of McGuiness et al, (1990) and Luo, (2009), who showed intergranular cracking and transgranular cracking for samples decrepitated at 50ºC.

7.15. Discussion

The grain size of the starting material was determined using etching and magneto optical Kerr effect microscopy. Both methods showed similar histogram distributions of the grain boundaries. Intergranular cracking was observed in the sintered NdFeB (Figs. 51 to fig. 53). as observed in the literature (Jiang et al, (2001) and Harris et al, (1998)).

Jiang et al, (2001) discussed the fracture mechanism of NdFeB and showed that for static bending the NdFeB magnets fractured in an intergranular manner. They suggest that the intergranular fracture is due to the "Nd-rich phase with O,whose strength is low". The low strength of the Nd-rich phase should lead to the HD process fracturing in a similar manner. Intergranular fracture was observed in BSE SEM images of the HD powder (fig. 64 and fig. 65) of sintered magnets decrepitated at room temperature at 4bar.

The HD process was also tracked at various stages from the initial cracking to the full decrepitation stage using optical microscopy on polished sintered NdFeB, fig. 66 shows the starting material prior to the HD process. Fig. 67 shows the image just after the explosive like fracture (described by Yartys et al, (1996)) producing an initial crack. After re-exposing the sample to hydrogen further smaller cracks were seen to propagate, heading towards the main body of the material as seen in fig. 68 to fig. 70. This agrees with the work by Yartys et al, (1996) these workers observed an initial explosive - like fracture, followed by the flaking away of layers of material.

In this current work the cracking was seen to progress mainly along the grain boundaries of the material. When the reaction was complete the sample showed a network of mainly intergranular cracks as seen in fig. 66 - fig.70. This agrees with the literature, in which the fracture mechanism is described as being mainly intergranular (McGuiness et al, (1990),

Harris et al (1998) and Jiang et al (2001)). Luo, (2009) showed intergranular cracking and transgranular cracking for samples of sintered NdFeB-type magnets decrepitated at 50ºC.

Some evidence of transgranular cracking was observed in this current work (fig. 65). The sintered #R material hydrogenated at room temperature was sieved and the fractions weighed, the data showed over 80 percent of the powder was larger than 850µm. The distribution was similar to those shown by Zakotnik et al, (2007) in fig. 63.

The fracture behaviour and the pressence of intergranular cracks in the HD powder means that the HD powder should easily break up with light milling to close to the starting grain size of the material.

7.16. Ball Milling of HD Powder From Sintered Source Material

Ball milling is a typical lab scale milling technique used for the HD powder. Prior to sintering, Zakotnik et al, (2007) used ball milling in cyclohexane to reduce the size of the HD powder made from sintered magnets prior to sintering. Zakotnik et al, (2007) made recycled sintered magnets from voice coil magnets based on the composition $Nd_{13.78}$ $Dy_{0.66}$ $B_{6.3}Al_{0.76}Fe_{75.51}$ $C_{0.32}$ $O_{1.84}$ (at%) composition. They suggested that the best results achieved were with milling for 0.5 hours and sintering at 1080 °C for 1hour. However, the HD powder ball milled for 1 hour showed a higher density and slightly lower magnetic properties compared to masses of the 0.5 hour milled powder. The coercivity is dependent on the microstructure of the material and can be increased by reducing the grain size and this has been shown by W.F. Li et al, (2008), Nothnagel et al, (1991) and Namkung et al, (2011).

The literature shows that at a critical mean particle size there is no longer an improvement to coercivity. It is thought that this reduction is associated with the increased oxidation of the Nd-rich phase as the particle size reduces. The Nd-rich phase is known to play a critical role

in liquid phase sintering and in isolating the $Nd_2Fe_{14}B$ grains. So the critical mean particle size is likely to depend on the composition of the material with the rare earth lean compositions likely to be more sensitive to the reduction in particle size, (Li et al 2008, Nothnagel et al 1991 and Namkung et al 2011).

To achieve magnetic properties close to that of the starting material the mean particle size of the powder would need to be smaller than the grain size of the starting material and close to the optimum particle size of approximately 3- 5μm. Having a similar or larger mean starting particle size is likely to result in a larger grain size and hence, lower coercivity due to grain growth during sintering.

NdFeB sintered magnets are susceptible to corrosion with the Nd rich phase readily reacting with moisture in the air, eventually causing the breakup of the sintered magnet. Yan et al, (1999) found that "Nd–Fe–B magnets can absorb hydrogen readily from moisture in the environment". In their work they found that the higher the density of the magnets the less hydrogen was absorbed.

The magnetic properties presented by Zakotnik et al, (2007) for the 0.5 hour and the 1 hour milled material were similar with the 1 hour ball milled powder, showing a higher density, albeit with slightly lower magnetic properties. It was decided that improvements in density were preferable and, for this reason, the 1 hour ball milling was investigated.

HD powder was milled for 1 hour in cyclohexane, then 15g batches of powder were passed through sieves of varying sizes and the masses of the powder greater and smaller than the sieve size were recorded.

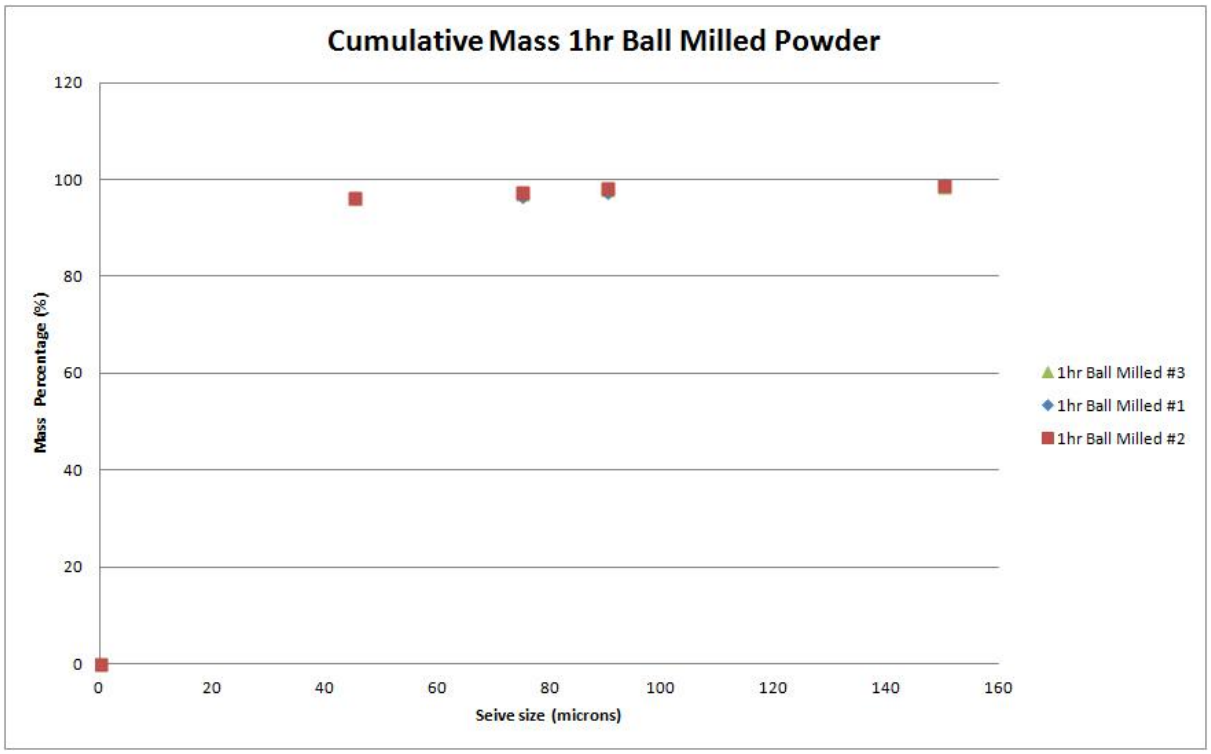

Fig.71. Cumulative mass of powder at various sieve sizes. (in microns µm)

Percentage Mass			
Diameter (µm)	#(1%)	#(2%)	#(3%)
2000>	100	100	100
500>	99.53	99.34	99.13
150>	98.87	98.74	98.33
90>	97.27	98.21	97.80
75>	96.54	97.54	97.13
45>	96.21	96.42	96.06

Table 11. Cumulative mass of HD powder hydrided at 4 bar at room temperature. Error ± 0.01g.

Table 11 shows the cumulative mass of powder, ball milled for 1 hour. As can be seen, the 1 hour ball milling resulted in over 96 percent of the powder passing through the 45µm sieve. The sieving technique became less reliable as the particle size dropped below 45µm. As the powder became finer, it tended to agglomerate making it difficult to pass through the final 20µm sieve, thus reducing the accuracy.

7.17. Sub 45µm Ball Milled Powder

From the graph of the cumulative mass versus sieve diameter in fig. 71, it can be seen that close to 96 percent of the powder is below 45µm in size. Samples from this powder fraction were then imaged using an optical microscope.

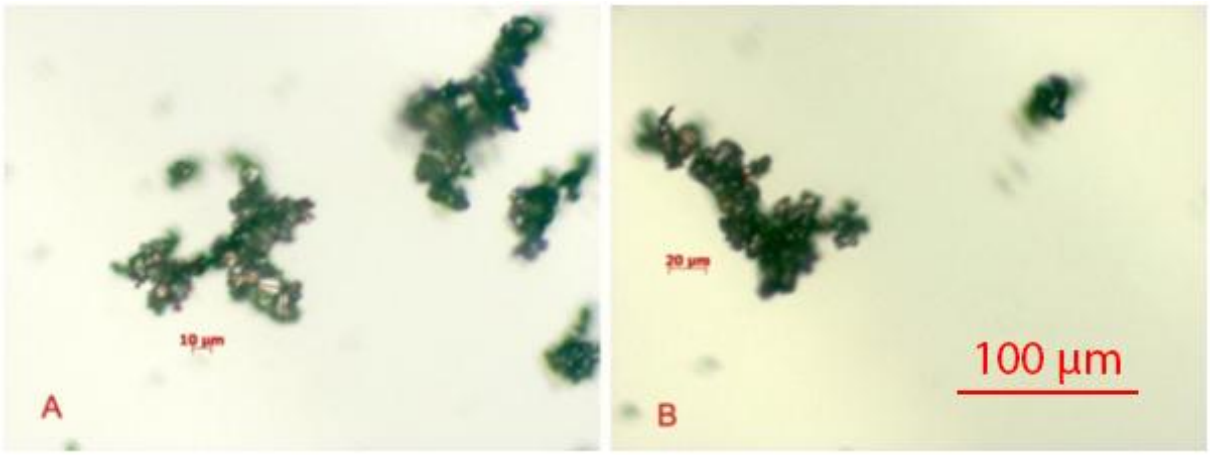

Fig.72. Powder passed through the 45µm sieve in the absence of a magnetic field.

Fig. 72 shows the powder that passed through the 45µm seive in the absence of a magnetic field. The red lines indicate the measurements used to calculate the values in table 12.

	A	B
Average (µm)	7	7
Mode (µm)	8	6
Median (µm)	7	6
Max (µm)	15	12
Min (µm)	2	3

Table 12. Particle size, assuming that the particles are agglomerated. Measurement error ± 0.5µm.

Fig. 72 shows the sub 45µm powder imaged on a mirror surface. The powder, could be polycrystalline and consist of larger particles, or they could be agglomerates. The facets of the crystals were measured assuming that the powder was in fact agglomerated and consisted

of single grains. To investigate the powder further, particles were imaged with the aid of a magnetic field as described previously.

7.18. Imaging HD Powder with the Aid of a Magnetic Field

This technique was developed by the author during the course of this project. The HD powder was still in the ferromagnetic state, albeit with a much reduced coercivity, so should interact with a magnetic field. Powder was placed on a glass mirror with a sintered NdFeB magnet underneath, providing a static field. The field at the mirror where the powder lay was~ 200mT, measured using a Hall probe.

7.18.2. 150 to 90µm Powder Under Influence of a Magnetic Field

To show that the magnetic field technique can be used to separate the powder particles, a coarse powder was employed. Sieved powder with a particle size of between 150 and 90µm was collected from the HD powder.

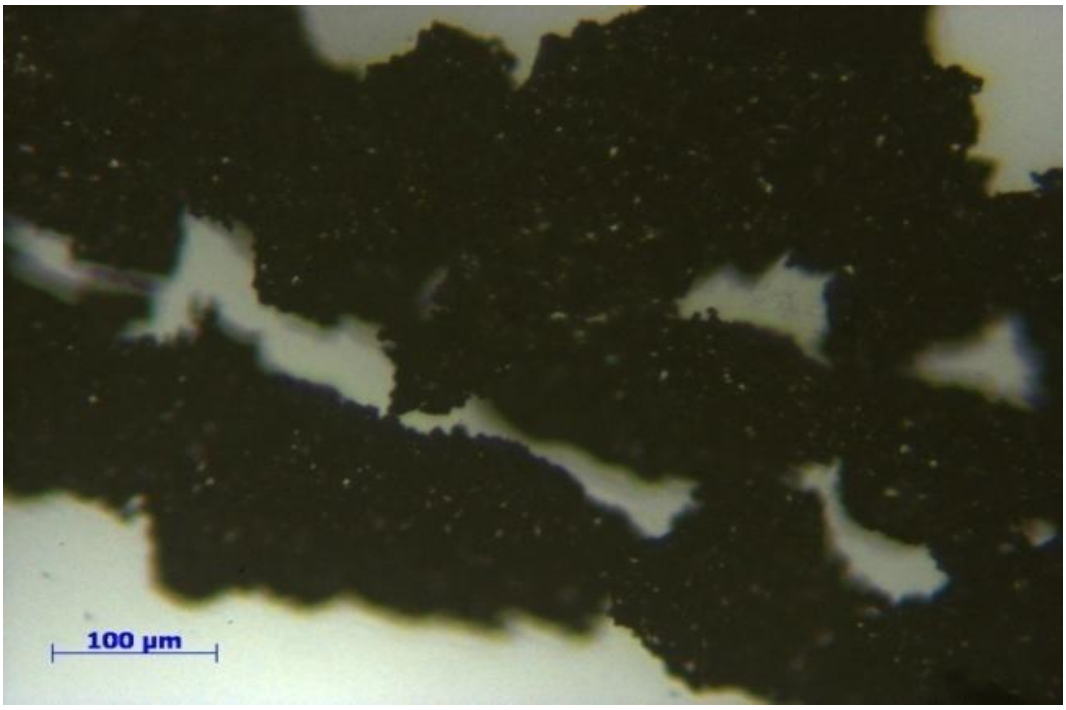

Fig.73. 150 – 90µm powder without the influence of a magnetic field. Particle size cannot be defined.

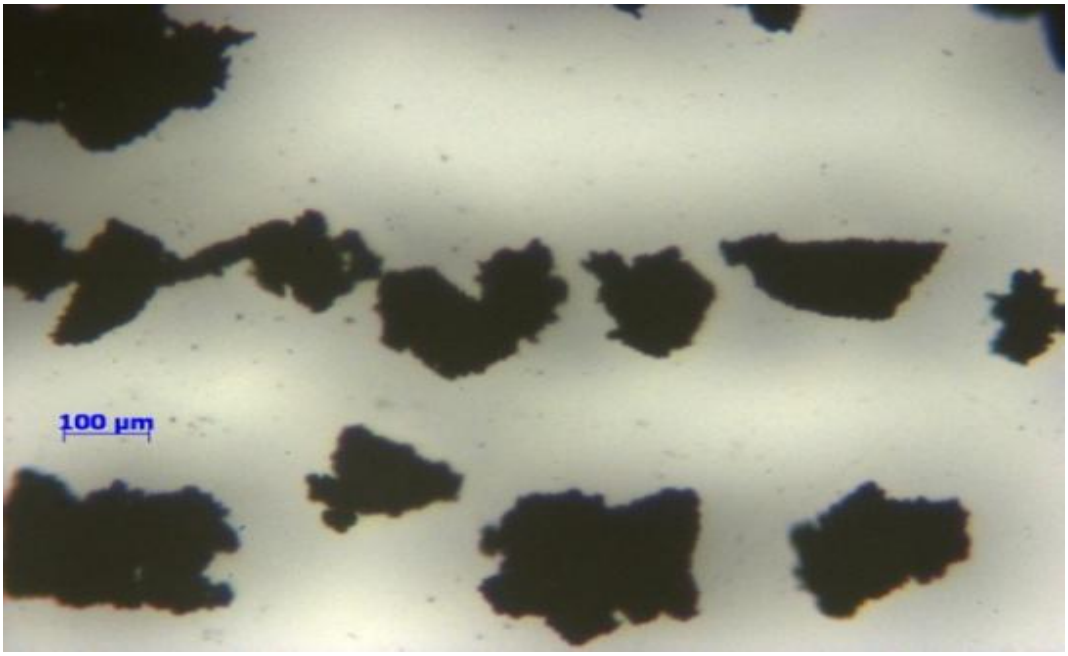

Fig.74. 150 – 90µm powder under the influence of a magnetic field.

Under the application of a magnetic field, the particles separate allowing individual particles to be seen rather than clumps or agglomerates. From the images it can be seen that, as expected, the individual particles are in the region of 150 to 90µm.

7.18.3. 1hour Ball Milled Powder Aligned With a Magnetic Field

The technique outlined above was then applied to the 1 hour ball milled powder. Over 96 percent of the 1 hour ball milled powder was found to be under 45µm in diameter, so a fraction of the sub 45µm fraction was selected for imaging.

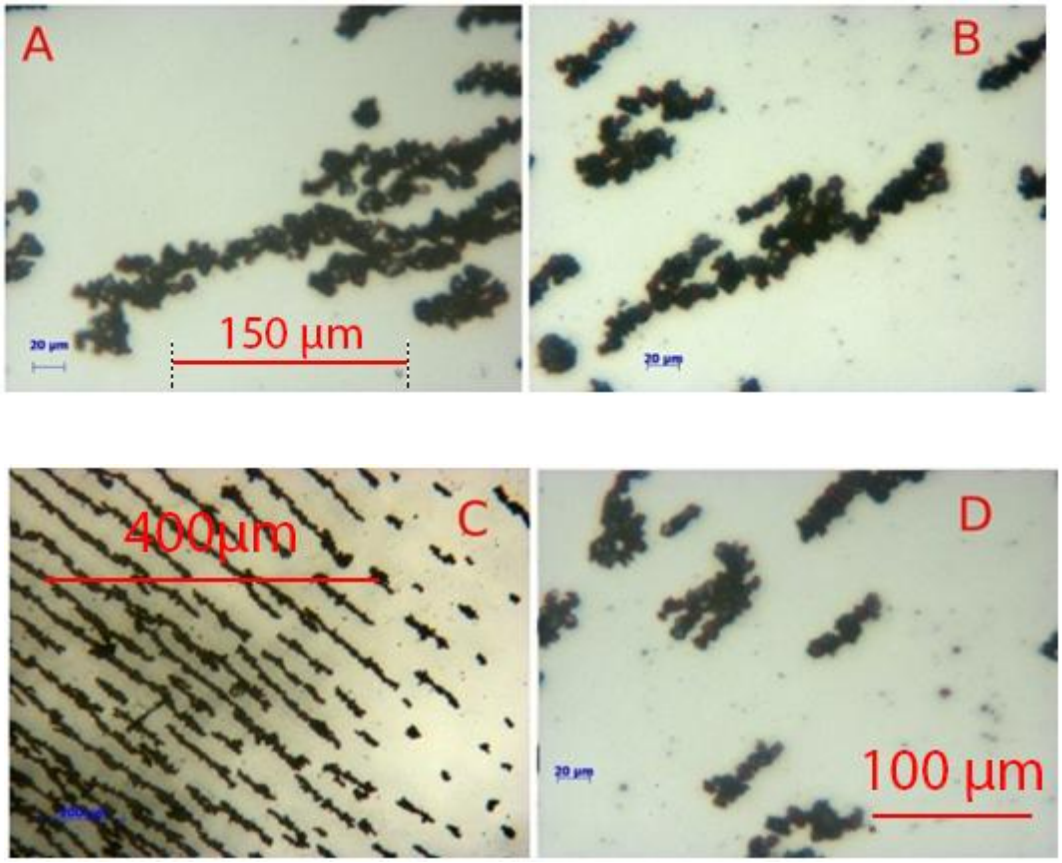

Fig.75. Aligned powder from sub 45µm fraction. (Red lines indicate measurements taken for image analysis.)

The measurement error for A, B and D is ± 0.5µm. For C the measurement error is ±1µm. From the images in fig. 75, it can be seen that the magnetic field has an influence on the ferromagnetic phases present in the HD powder. The aligned particles were measured manually using image analysis software and the error associated is plus or minus 0.5µm.

Ball Milled	Average (µm)	Max (µm)	Min (µm)	Median (µm)	Mode (µm)	SD
A	6.95	12	4	7	5	2.03
B	8.03	16	4	8	8	2.2
C	9.77	18	5	10	10	2.36
D	7.93	17	2	8	8	3.11
Combined (246)	**8.94**	**18**	**2**	**9**	**8**	**2.66**

Table 13. Grain size data for Ball Milled powders. Measurement error ± 0.5µm.

The powder influenced by the magnetic field is ferromagnetic so must be the $Nd_2Fe_{14}B$ based phase. The average particle size of the particles influenced by the magnetic field appears to be very similar to the starting grain size of the NdFeB starting material.

Source	Average (µm)	Max (µm)	Min (µm)	Median (µm)	Mode (µm)	Standard Deviation
Etched (541)	8.3	26	2	8	7	3.37
Kerr (568)	10.9	34	3	9	8	4.78
1hr Ball Milled (246)	8.9	18	2	9	8	2.66

Table 14. Grain size data from the starting material. Measurement error± 0.5µm.

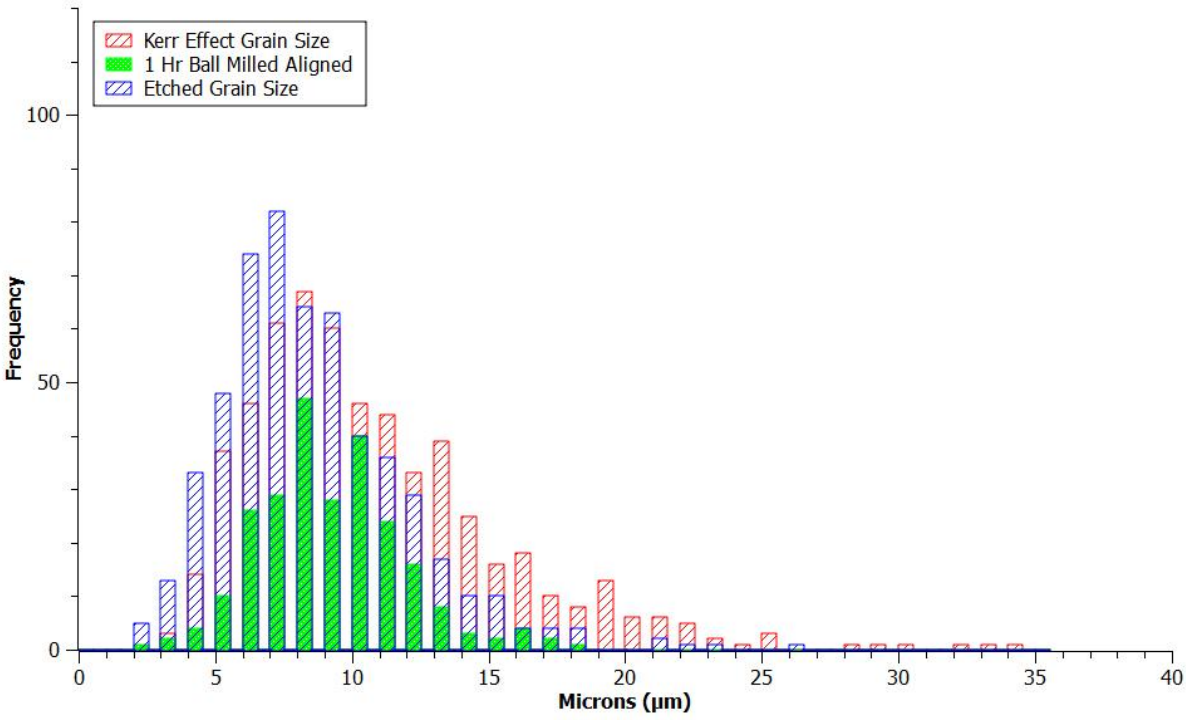

Fig.76. Histogram showing grain size of the starting material and the aligned powder.

In fig.76, the histogram shows the grain size of the starting material and the aligned, 1 hour ball milled powder. The bin widths start at zero to one microns, one to two microns and then subsequently increase by two-micron steps.

The mode of the grain size of the starting material and the mode for the aligned particles in the 1 hour ball milled powder are very similar. The histogram in fig.76 shows clearly the similarity of the distribution of the aligned powder with the starting grain size of the material.

7.19. Smaller Particles From 1 hour Ball Milled Powder

Additionally visible under the microscope were smaller particles that did not interact with the magnetic field.

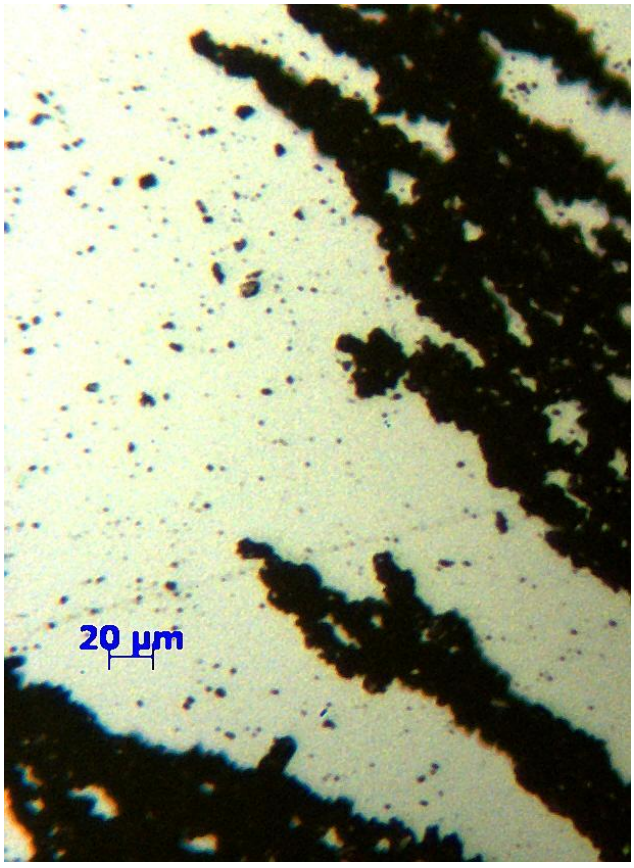

Fig.77. Close up of particles that are not interacting with the magnetic field.

Fig. 77 shows some particles are interacting with the magnetic field while others are not.

$$\tau = m \times B$$

Equation 10. The relationship between the torque observed by particles and an applied field.

The particles that do not interact with the magnetic field could either be Nd-rich particles ($NdH_{\sim 3}$), or attrition particles from the $Nd_2Fe_{14}B$ hydride phase. Equation 10 shows the relationship between the torque observed by particles and an applied field. The two variables that influence the torque observed by the particles are the applied field **B** and the magnetic moment of the particle **m**. As the particle size increases the magnetic moment of the particle increases. As the applied field increases the torque observed by the particle increases.

In this case the applied field was from a sintered NdFeB magnet underneath the mirror producing a static and a constant field of approximately 200mT at the mirror surface, where the powder sits. So the only variable affecting the torque on the powder will be the particle size of the powder. The smaller the particle, the smaller the magnetic moment of the particle; so the particle will observe less torque. The powder observed could be too small to be infleunced by the static applied field. This has implications when aligning the powder prior to compaction.

	Average (µm)	**Max (µm)**	**Min (µm)**	**Median (µm)**	**Mode (µm)**	**SD**
A (392)	2.87	10.41	0.64	2.45	0.64	1.96

Table 15. Data from particles not reacting to the applied field. (Error ± 0.5µm)

7.20. Errors Associated With the Non-aligning Particles

It is important to note that with optical microscopy the theoretical resolution limit is close to 0.5µm with the limit being dependent on the wavelength of light used. In this case the light source was from a halogen bulb. Some of the attrition particles being measured were approaching the limit of resolution for optical microscopy. Due to the diffraction limit, groups of these particles at, or smaller than 0.5µm may appear as one particle rather than as a cluster.

The actual measuring of the diameter of the particles was carried out automatically by software, so potential human error in accurately measuring particles will have been minimised. The recorded feret diameters (the longest distance between any two points), were measured to within two decimal places. A conservative error for the attrition particle diameter measurements is plus or minus 0.5µm.

The feret diameters of the attrition particles were measured by converting the images into binary form and then using Image J analysis software to analyze the particles.

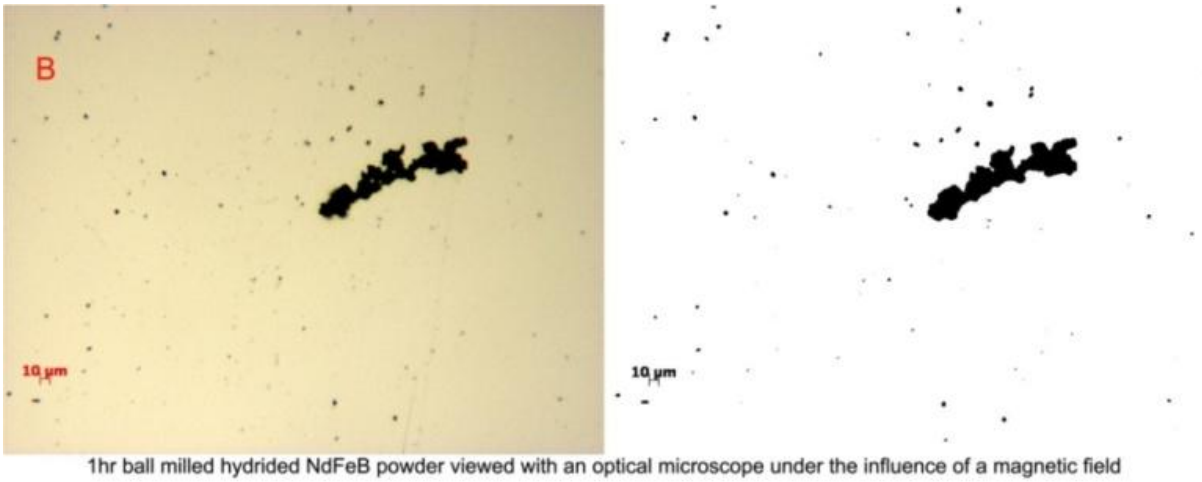

Fig. 78. Attrition particles from 1hour ball milled powder (micron marker 10µm).

	Average (µm)	Max (µm)	Min (µm)	Median (µm)	Mode (µm)	SD
B (76)	3.47	11.15	0.65	3.09	0.65	2.28

Table 16. Data from attrition particles from 1 hour ball milled powder.Error ± 0.5µm.

	Average (µm)	Max (µm)	Min (µm)	Median (µm)	Mode (µm)	SD
All (2079)	4.05	28.00	0.60	3.20	0.70	3.24

Table 17. The variance of particle size data points. Error ± 0.5µm.

Source	Average (µm)	Max (µm)	Min (µm)	Median (µm)	Mode (µm)	SD
Etched (541)	8.30	26.00	2.00	8.00	7.00	3.37
Kerr (567)	11.85	33.00	5.00	10.50	10.00	5.29
Particle Size (246)	8.94	18.00	2.00	9.00	8.00	2.66
Non aligned (2079)	3.38	9.9	0.50	2.9	0.70	3.24

Table 18. Comprison of the attrition particles to the aligned ball milled powder and the grain size of the starting material. Error ± 0.5µm.

To investigate further HD powder was milled for 20 hours and again imaged under the influence of a magnetic field, (fig.79).

Milling the HD powder for 20 hours showed an increase in the number of particles not interacting with the applied field. This shows that some of the particles present in the 1 hour ball milled aligned micrographs could also have been attrition particles from the $Nd_2Fe_{14}B$ particles.

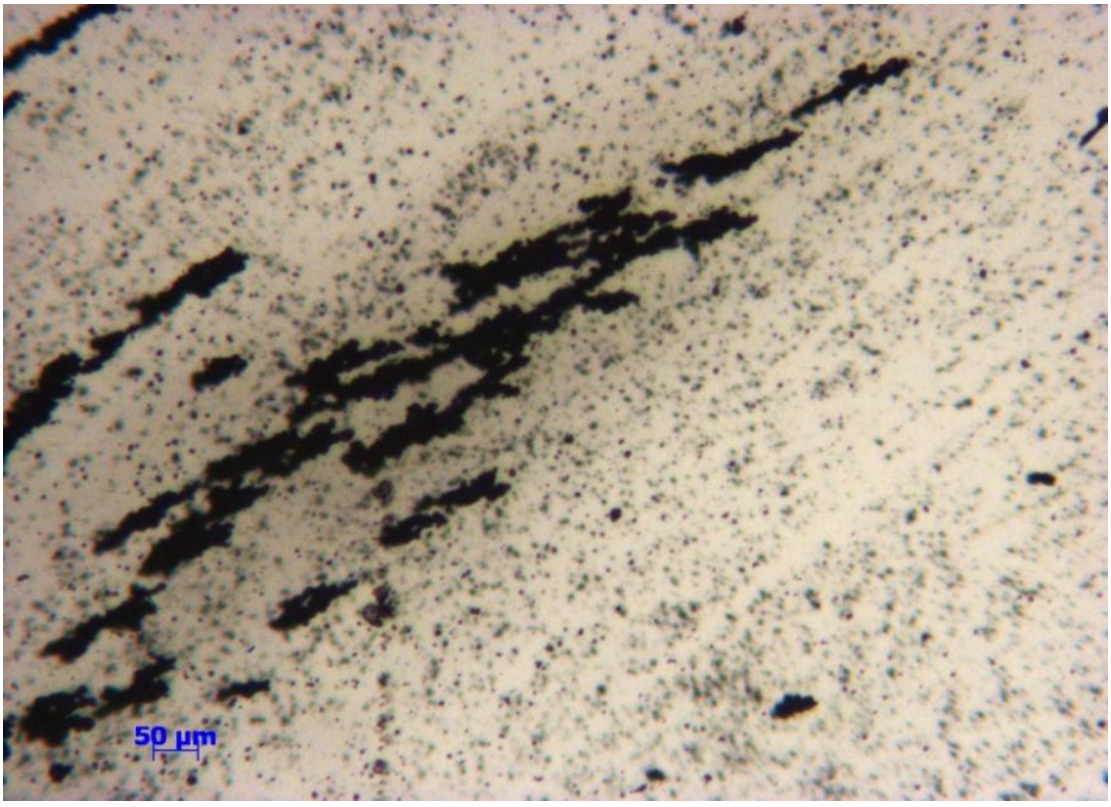

Fig.79. 20 hour ball milled powder under the influence of a magnetic field (micron marker 50µm).

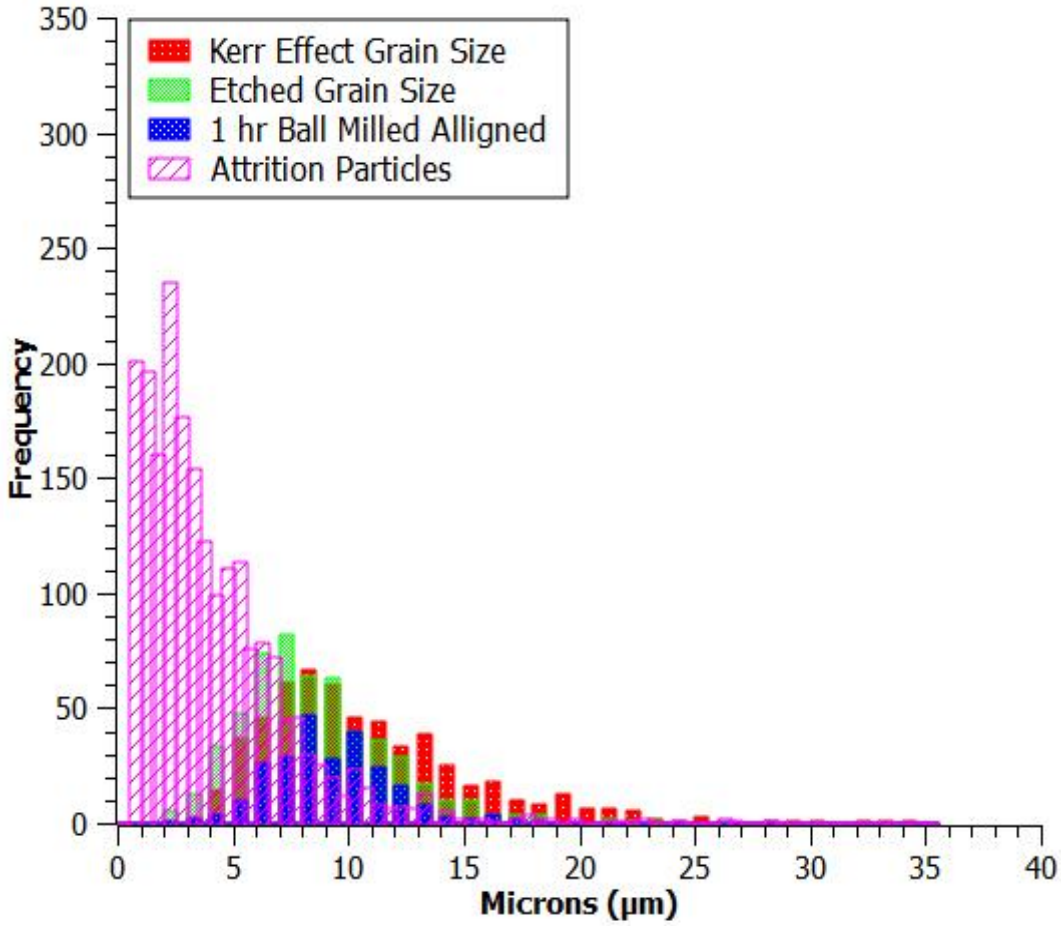

Fig.80. Histogram showing the grain size of the starting material and the aligned 1 hour ball milled powder compared with the attrition particles.

In fig.80, the bin widths start at zero to one micron, one to two microns and then subsequently increase by two-microns steps. From the histogram, it can be seen that the distribution of the potential attrition particles is shifted to the left. The mode of the these particles is 0.7µm, with many of the particles falling in the zero to two micron range. The median value for the attrition particles is 2.9 µm, showing a big reduction from the median

values of the grain size of the starting material and the median of the aligned particles (8,10.5 and 9μm).

The distribution of the attrition particles are shown to have shifted further to the left than that of the starting material grain size, thus confirming that these particles are likely to be attrition particles. Considering the mode value for these particles is 0.7μm, it is likely that the majority could be the result of attrition at the grain corners. The larger particles could possibly be due to intergranular fracture of the grains.

7.21. Discussion of Ball Milling

During light milling it is likely that the HD powder initially breaks up along the grain boundaries. It is possible that the single grained particles contain latent cracks from the HD-process. So there is potential for the particles to fracture further. It is likely that attrition of the single grain particles occured during milling.

The distribution in table 18 and the histogram of the aligned 1 hour ball milled powder show similarities with that of the grain size of the starting material. This agrees with the idea that the grain boundaries are weak points and the particles break up easily along the grain boundaries. Jiang et al, (2001).

The histogram data also showed particles with a particle size distribution similar to that of the distribution of the starting material grain size.

During the aligning of the ferromagnetic $Nd_2Fe_{14}B$ particles it was observed that not all the particles aligned with the field. These particles are likely to be a combination of $Nd_2Fe_{14}B$ hydride particles that are too small to be influenced by the applied field and the Nd-rich

phase. The quantity of these particles increased when the HD powder was milled for 20 hours, showing that these particles must include attrition particles.

Table 18 and the histogram in fig. 80 showed that these particles were smaller than that of the grain size of the starting material and the mode was also much smaller than that of the starting grain size. The existence of attrition particles will influence the mean particle size by causing an overall reduction in the mean particle size. The degree of this reduction is difficult to quantify.

Chapter 8. Burr Milled Powder

As seen previously with the low energy ball milling technique, the HD powder has a tendency to break up along grain boundaries. After 1 hour milling, the particle size distribution was shown, (with the aid of a magnetic field), to be close to the grain size of the original sintered starting material. The powder displayed a mean particle size which is likely to be lower than the grain size of the starting material. Much finer powder was also observed during microscopy. It is likely that some of these are attrition particles from fractured grains.

Due to the friable nature of the HD powder, burr milling the powder should achieve a similar reduction in particle size. The advantages of burr milling is that the whole process can be done inertly, in this case a glove box. The number of stages can be reduced and the use of solvents can be avoided thus providing an effective and cheaper alternative to ball milling. There is also a potential for contamination during the ball milling process either from the milling media or due to pick up of oxygen during the transfer of the sealed milling pots to the ball mill.

Nothnagel et al, (1991) suggest that a further reduction in the Nd-rich phase (alongside oxidation) may be due to the carbon arising from the milling liquid. They found that "the content of C increased with milling time". The HD powder was loaded in the mill and ground. The resulting powder was sieved and the powder that passed through a 75µm sieve was saved.

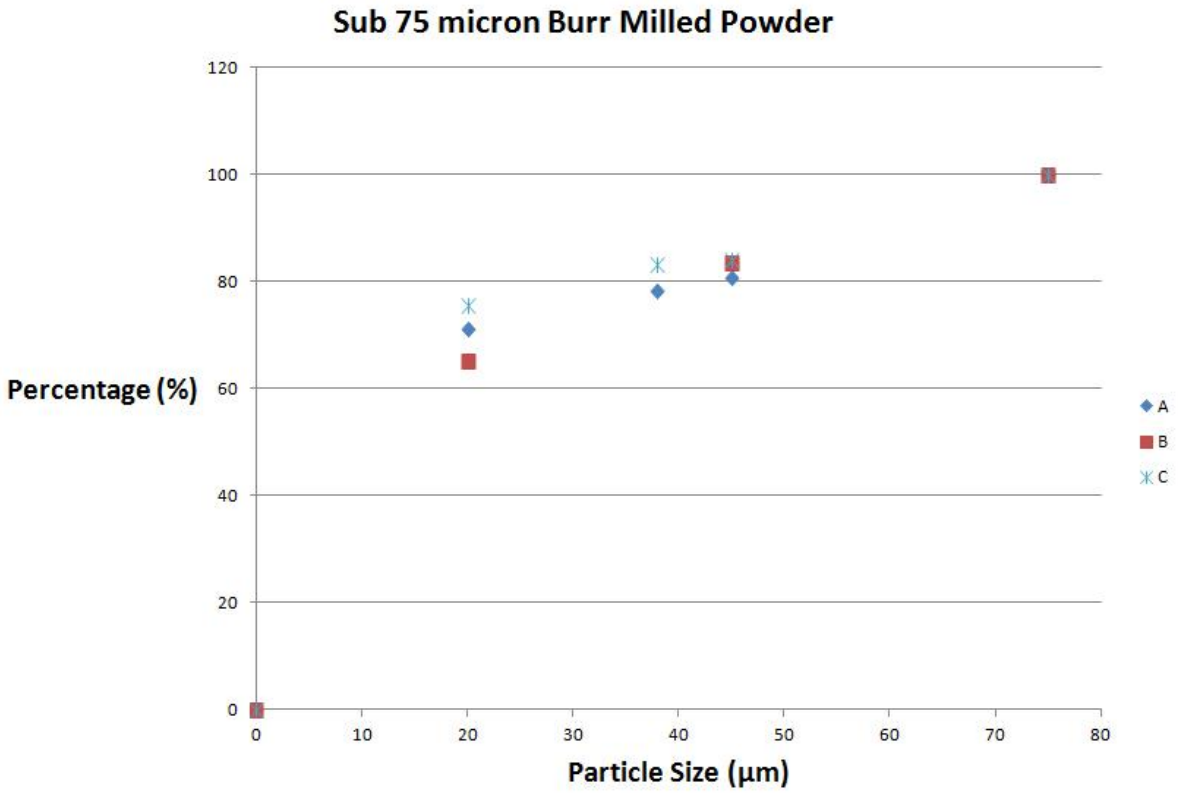

Fig.81.Three different cumulative mass plots for the sub 75µm powder while reducing sieve sizes.

Fig.81 shows the particle size distribution of HD powder, burr milled and sieved to a particle size of less than 75µm. Over 80 percent of the powder is less than 45µm in size, with the three tests showing close consistency. As the sieve size reduced, the sieving technique became more unreliable due to the agglomeration of the sub 45µm powder.

The agglomeration could be due to surface effects or the weakly coercive nature of the HD- $Nd_2Fe_{14}B$ phase within the powder.

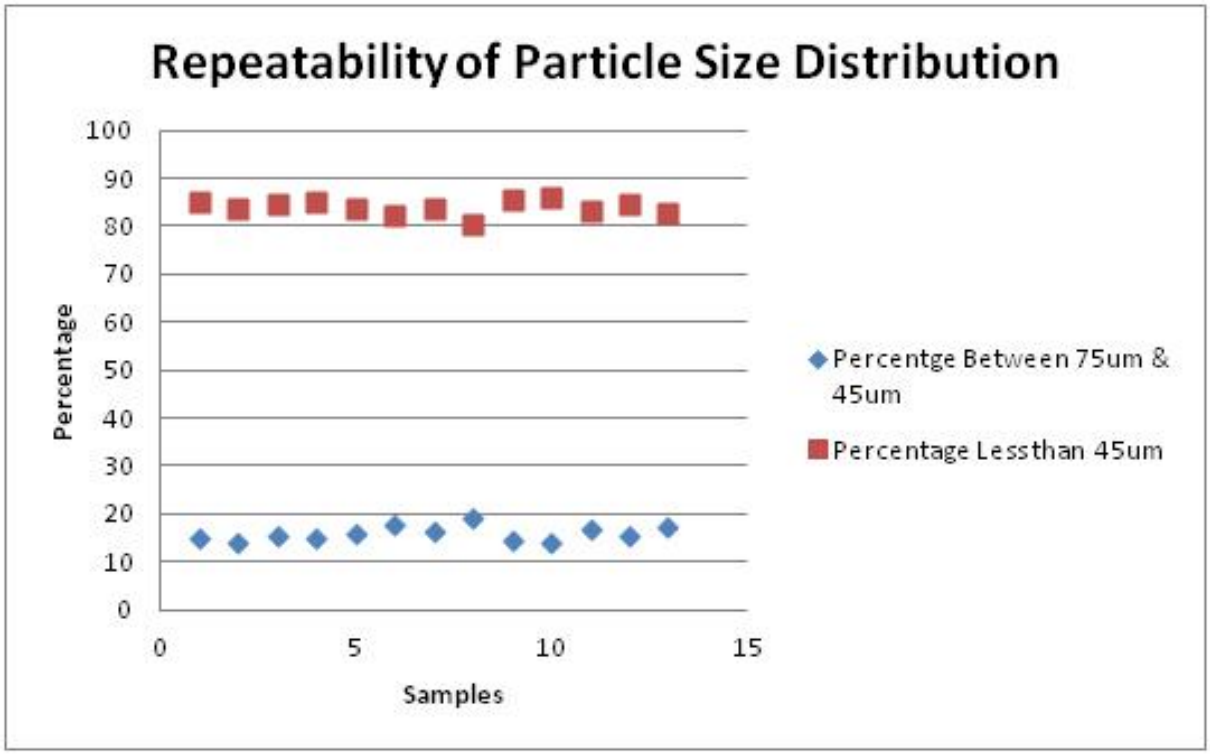

Fig.82. Cumulative mass distribution of the sub 75µm burr milled powder focusing on the percentage mass between 75 and 45µm and the percentage mass less than 45µm.

Fig. 83. A typical 15g batch of burr milled powder. The top left shows the powder between 75 and 45µm. The majority of the powder is less than 45µm.

In fig. 83 the majority of the sub 75µm powder tends to be less than 45µm. Fig 82 shows that this is consistently the case. After testing 13 different batches of powder, the sieved mass percentages remain similar.

To lessen cognitive bias errors in the sieving and weighing stage, the batch sizes were varied for a few of the samples from 15 to 25g. It can be seen that 80% of the powder that falls below 45µm is actually close to the grain size of the starting material and the investigation is discussed in this section.

The HD powder is crushed as the milling surface rotates. As seen previously, the HD powder is very susceptible to intergranular fracture and has been shown to contain latent cracks due to the HD process. The difference in volume expansion between the $Nd_2Fe_{14}B$ phase and the Nd rich hydride phase causes stresses at the grain boundaries causing the HD powder to break up along the weaker grain boundaries leaving mostly single grains, as seen by Luo, (2009).

Due to the nature of the burr milling process, there will be a gap between the rotating piece and the fixed piece. The 75 - 45µm particles are the result of approximately 15% of the powder falling through without interacting with the surfaces of the burr mill.

Fig. 82 shows the two mass distributions from a 15g batch of sub75µm powder. There is a visible difference between the two batches of powder. This indicates that there is likely to be a big difference in the particle size distributions.

8.1. Microscopy of the 75 to 45µm Fraction

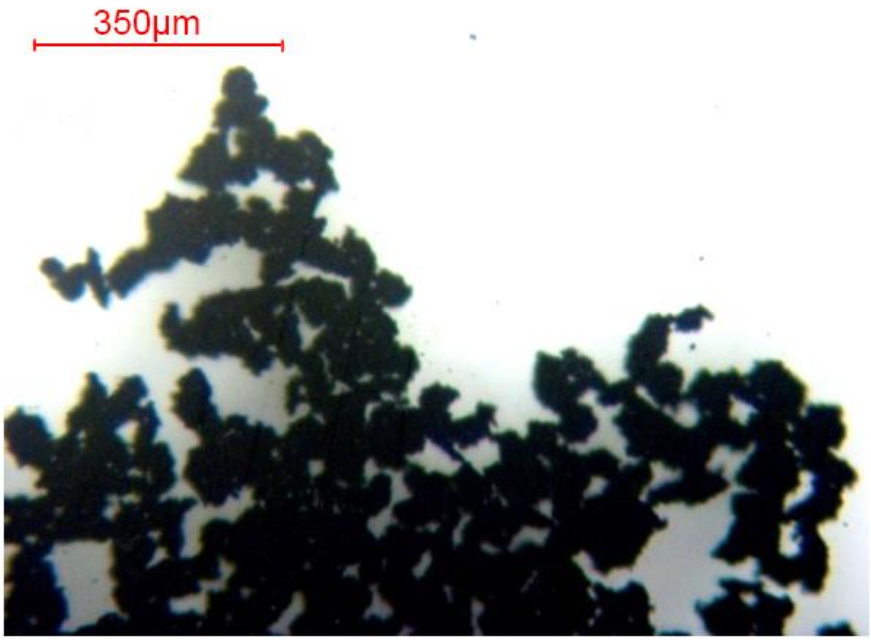

Fig.84. Microscopy of the 45 – 75µm fraction (no magnetic field applied).

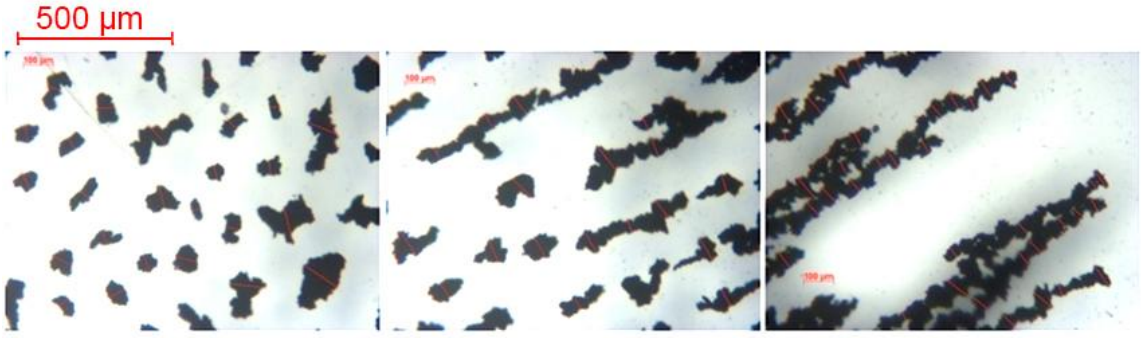

Fig.85. Microscopy of the 45 to 75µm fraction (with a magnetic field applied).

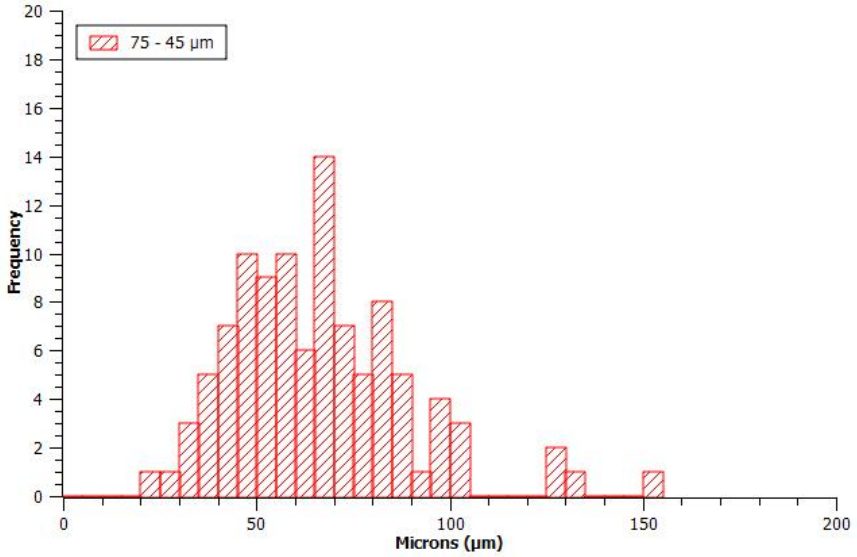

Fig.86. Histogram of the powder between 45 and 75µm. The bin widths are in 5µm steps.

75-45 µm Powder	Average	Max	Min	Median	Mode	Standard Deviation
Data Points (103)	65.56	151.00	24.00	64.00	48.00	22.94

Table 19. Data from the 45 – 75µm powder, error ± 1µm.

From the histogram in fig. 86 and data in table 19, you can see that there is a wide variance in the powder size distribution of the 45 – 75µm powder. The images in figs. 84 and 85 show the particles are irregular.

8.2. Imaging Sub 45µm Burr Milled Powder

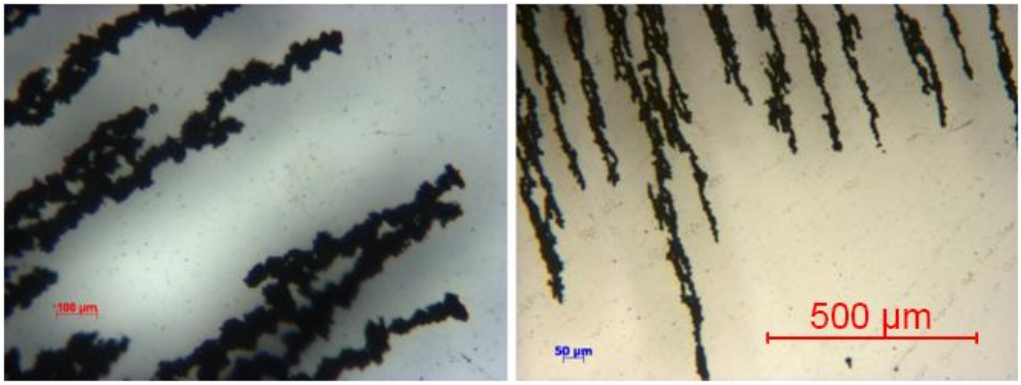

Fig.87. Comparison between the 75 – 45µm powder (left) and the sub 45µm (right) powder under the influence of a magnetic field both at the same magnification.

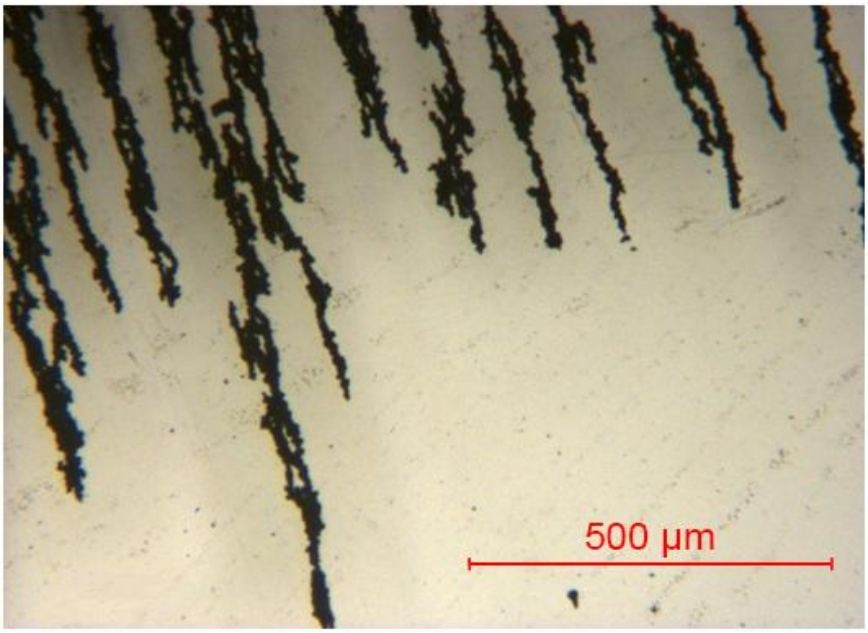

Fig.88. Aligned burr milled powder.

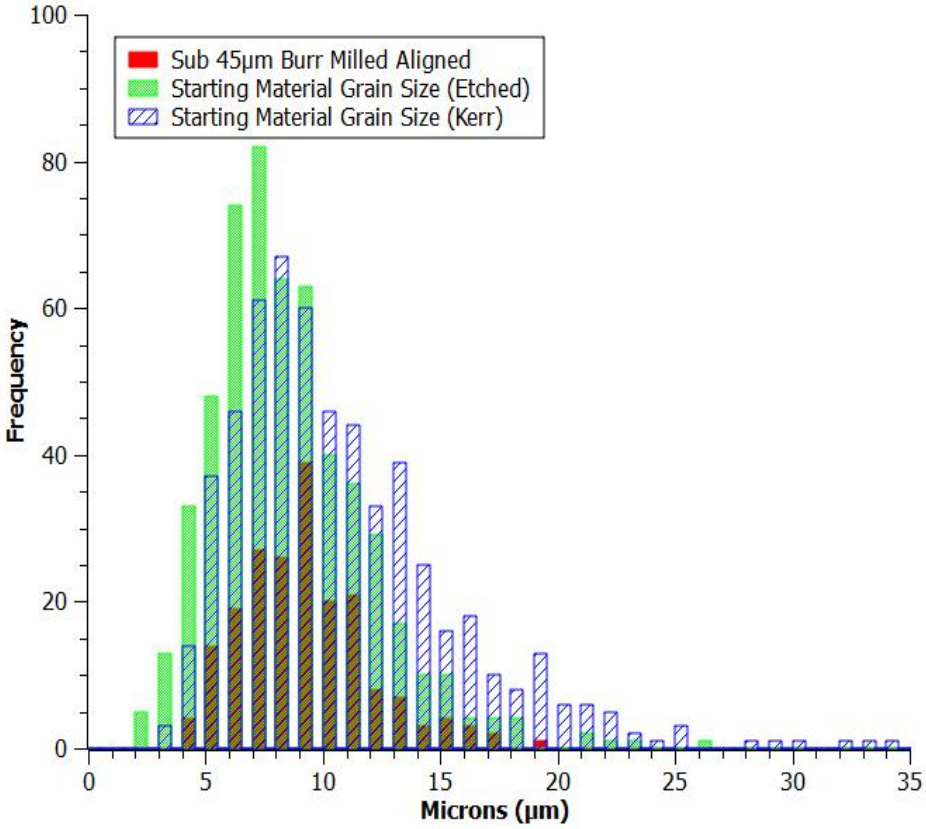

Fig.89. Histogram of aligned powder compared with grain size of sintered starting material.

Bin widths are 0.5 µm.

Sub 45µm Burr Milled	Average (µm)	Max (µm)	Min (µm)	Median (µm)	Mode (µm)	SD
Data Points (198)	8.93	19	4	9	9	2.77

Table 20. Data from the burr milled, aligned powder. Error ± 0.5µm.

Image analysis was carried out on various images of the aligned powder. Due to the nature of the images, the particle size estimation was performed manually. Table 20 shows the data. As with the ball milled data, the diameter values were converted to integers to minimise measuring errors. Errors are estimated at plus or minus 0.5µm.

8.3. Attrition Particles for Sub 45µm Burr Milled Powder

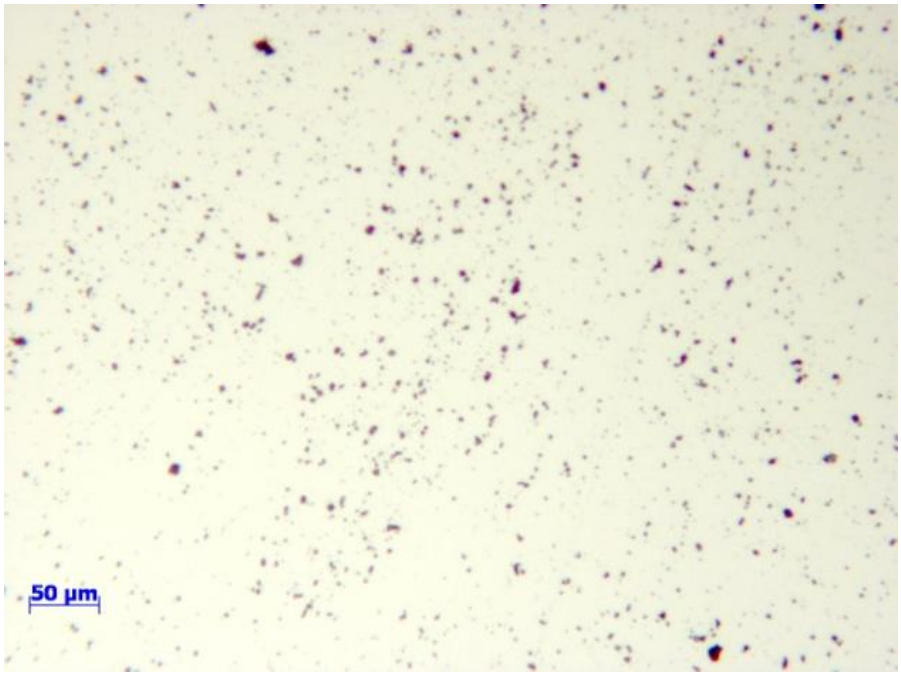

Fig.90. Attrition particles from Burr milled powder (micron marker 50µm).

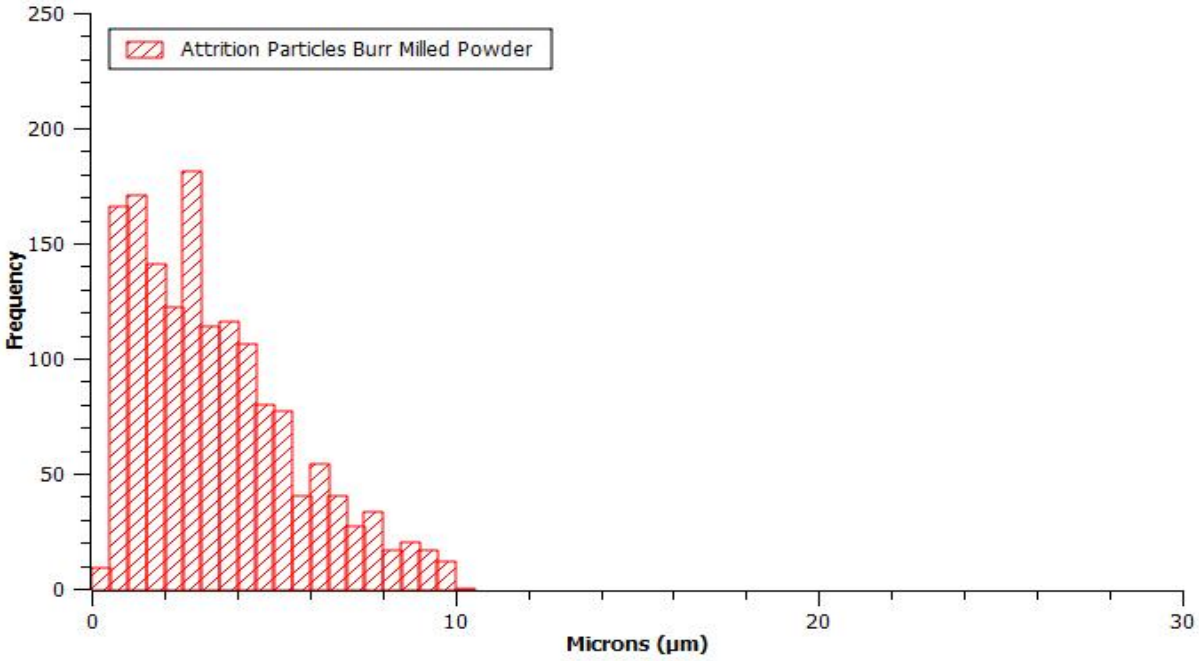

Fig.91. Histogram of attrition particles from burr milled HD powder. Bin widths 0.5µm.

Sub 45µm Burr Milled attrition Particles	Average (µm)	Max (µm)	Min (µm)	Median (µm)	Mode (µm)	SD
Data Points (1620)	3.85	24.5	0.35	3.18	0.7	3.04

Table 21. Data from sub 45µm burr milled attrition particles. error ± 0.5µm.

The diameter of the attrition particles was measured by converting the images into binary form and then using ImageJ analysis software to analyze the particles. The Feret diameter was used to represent the diameter. The Feret diameter values were then converted to two decimal place values.

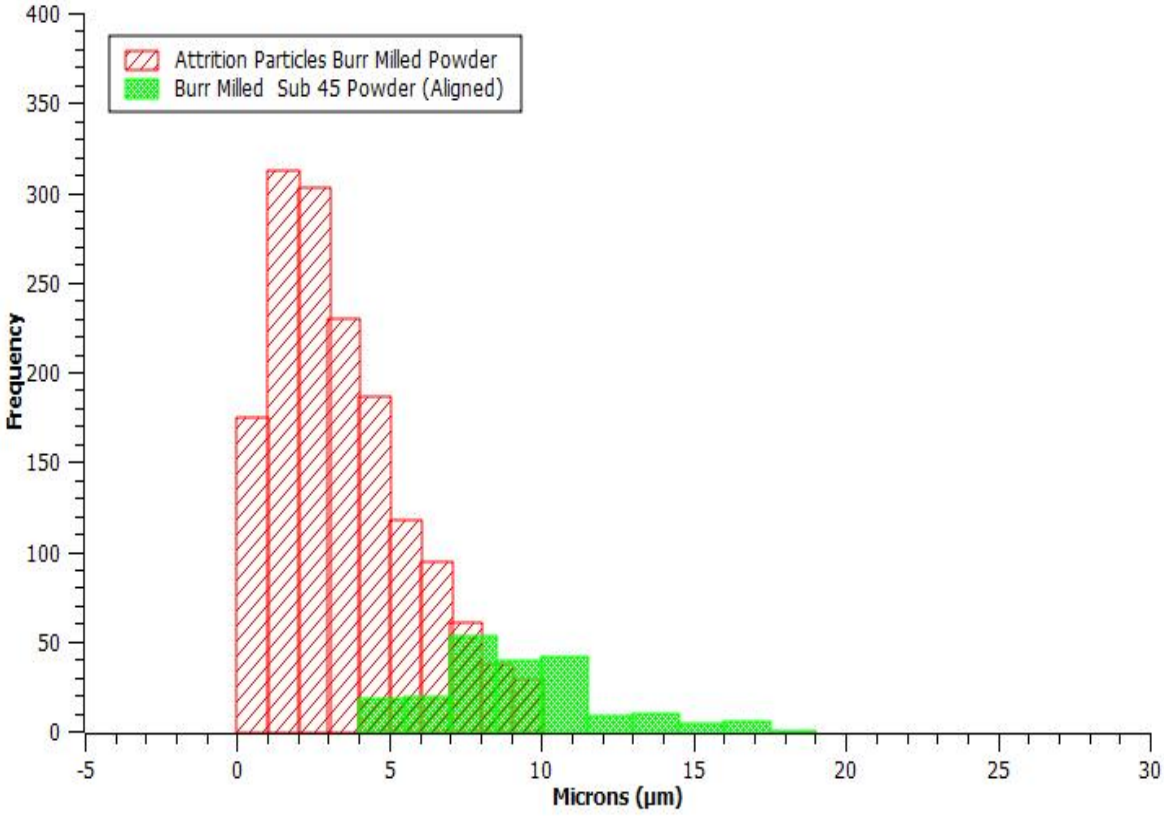

Fig.92. Comparison of histograms from burr milled powders. Bin widths 0.5 µm.

Sub 45 Burr Milled	Average (µm)	Max (µm)	Min (µm)	Median (µm)	Mode (µm)	Standard Deviation
Aligned (198)	8.93	19	4	9	9	2.77
Attrition (1620)	3.38	9.9	0.5	2.9	0.70	2.17

Table 22. Comparison of the 1 hour ball milled and the sub 45µm burr milled powder. Error ± 1µm.

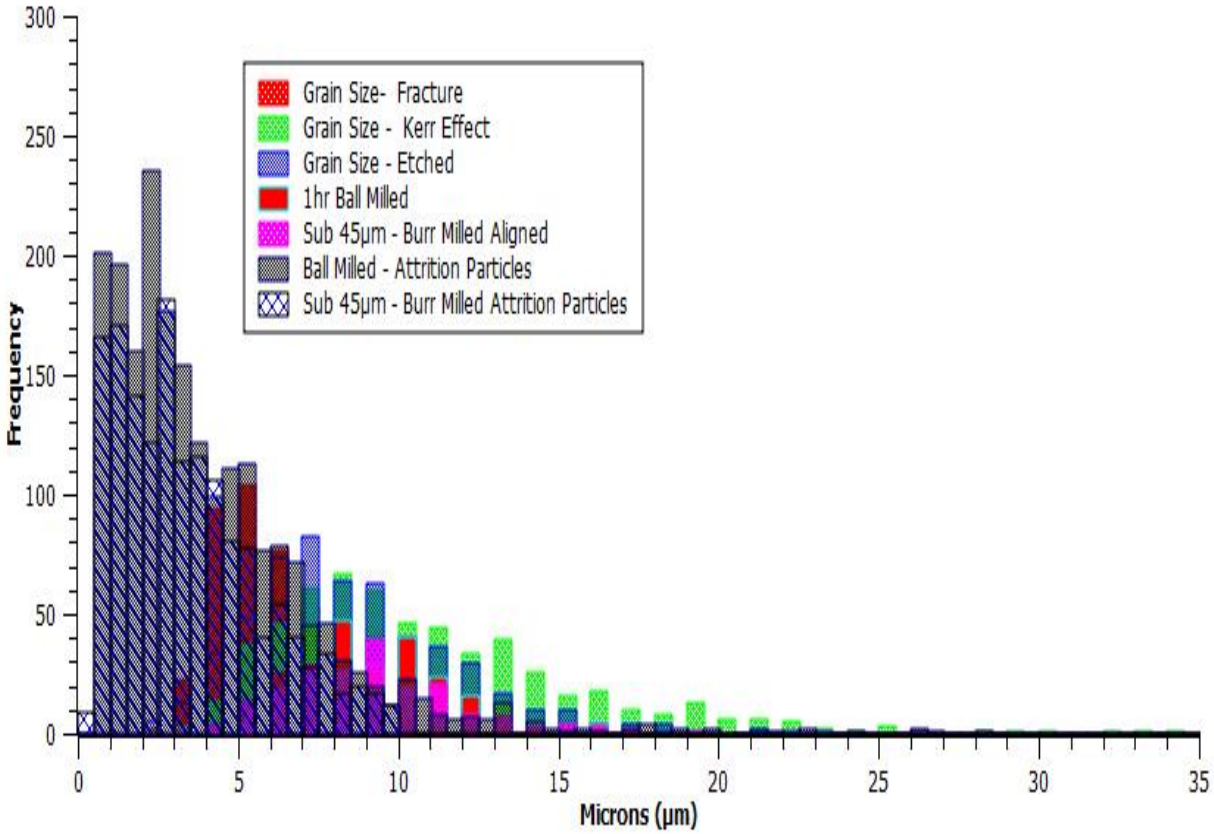

Fig.93. Comparison of all the histograms.

	Average (µm)	Max (µm)	Min (µm)	Median (µm)	Mode (µm)	Standard Deviation
Ball Milled Aligned (246)	8.94	18	2	9	8	2.66
Ball Milled Attrition (1941)	3.4	9	0.6	3.0	0.7	2.12
Burr Milled Aligned (198)	8.93	19	4	9	9	2.77
Burr Milled Attrition (1620)	3.4	9.9	0.5	2.9	0.7	2.17

Table 23. Data for comparison of milling techniques. (Error ± 0.5µm)

8.4. Comparison of Milling Techniques

The ball milling and burr milling techniques resulted in very similar particle size distributions and standard deviations for the aligned particles and attrition particles. Both the aligned and attrition particles had very similar mode and median values. The similarity is likely to be due largely to the nature of the fracture process of the HD powder, which tends to fail in an intergranular fashion. The expansion mismatch between the Nd-rich hydride phase and the hydrogenated $Nd_2Fe_{14}B$ phase is likely to encourage intergranular fracture.

From the data it seems likely that the particle size distribution of both the ball milled and burr milled powder is close to the grain size of the starting material. It is likely that increasing the ball milling duration will decrease the particle size further. Purchasing a burr mill with the ability to adjust the plate distances should also lower the mean particle size. The particle sizes obtained from both the ball milled and sub 45µm burr milled powder produced similar mean particle sizes, (9µm), slightly larger than that of the material produced by Mottram et al, (2000). In their work they milled cast material for 20 hours in cyclohexane and produced powder with an average particle size of 3 – 7µm.

The actual average of the ball and burr milled powder achieved here is likely to be lower than 8.9µm due to the attrition particles reducing the mean particle size. Further milling is likely to reduce the average further by increasing the proportion of attrition particles.

From the literature, the optimum particle size is in the region of 3µm, (Nothnagel et al,1991). The 9µm achieved by 1 hour ball milling and one pass through a burr mill could be optimised to further reduce the particle size.

Chapter 9. Desorption of Hydrogenated Recycled NdFeB

As discussed previously, during the sintering stage of NdFeB magnets, the hydrogen used for processing is desorbed. Investigating this desorption should provide information on the composition and information on the mean particle size of the green compact. As described previously by Ryan and Coey, (1985), the analysis of the change in gas pressure with temperature, described as the thermomanometric analysis (TMA) technique, can be used to investigate the desorption of gases from the HD powder.

Ryan and Coey (1985) used a piezoresistive pressure sensor and a sealed volume. The mass monitored was ~ 1 to 50mg. In the present work, a version of their technique was applied during the sintering process to monitor desorption of hydrogen from the green compacts as they densify. Instead of a piezoresistive sensor a Pirani gauge was employed to monitor the pressure change. It was a flowing system rather than at a constant volume. The mass of material measured was from 330mg to over 15g.

The system for desorption was set up as described previously. Gases desorbed during the heating of the samples were recorded using a Pirani gauge. This was logged alongside the temperature and the cumulative time. The values recorded by the data logging system consisted of the raw data in the form of a change in voltage from the gauge controller. The raw data was converted as described in the method section.

Arb	Volts	mbar
68.1984	0.333	1.33E-02
587.3664	2.868	8.00E+00

Table 24. Range over which the conversion functions from volts to mbar are applicable.

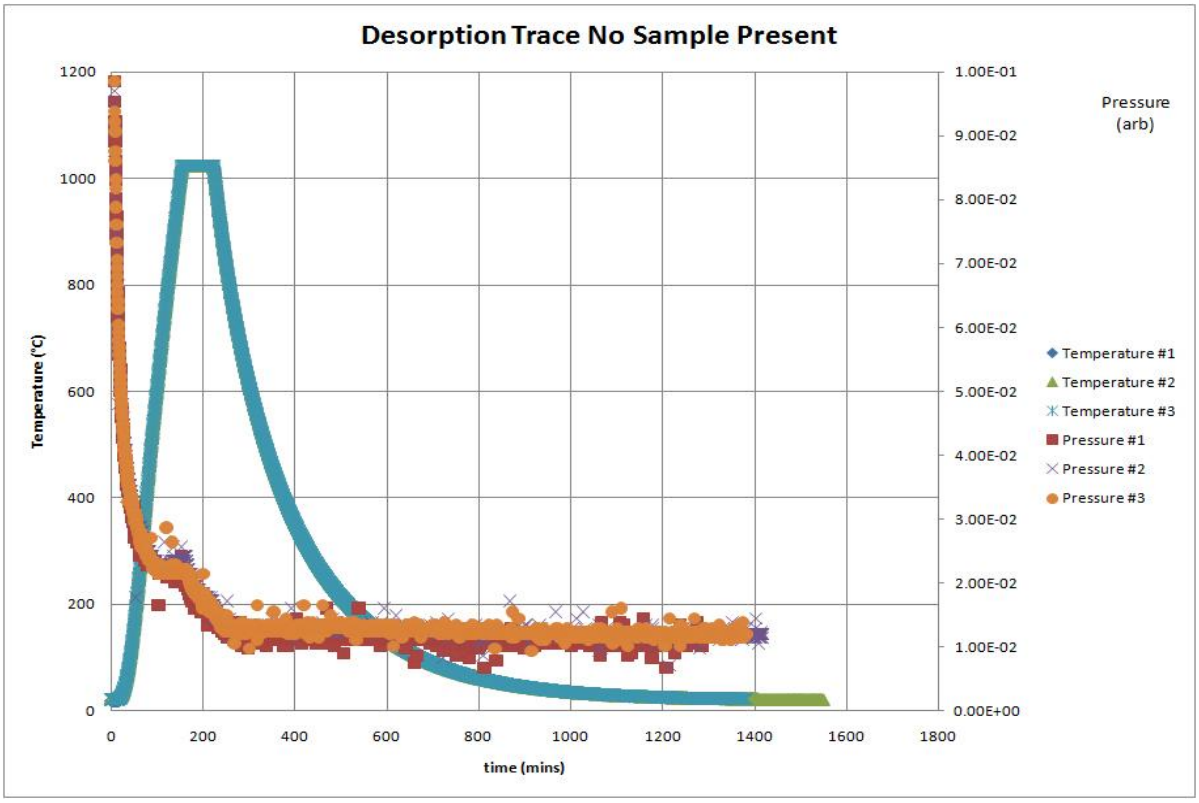

Fig.94. Three different sintering runs with no sample present.

The temperature, pressure and time were recorded every twenty seconds.

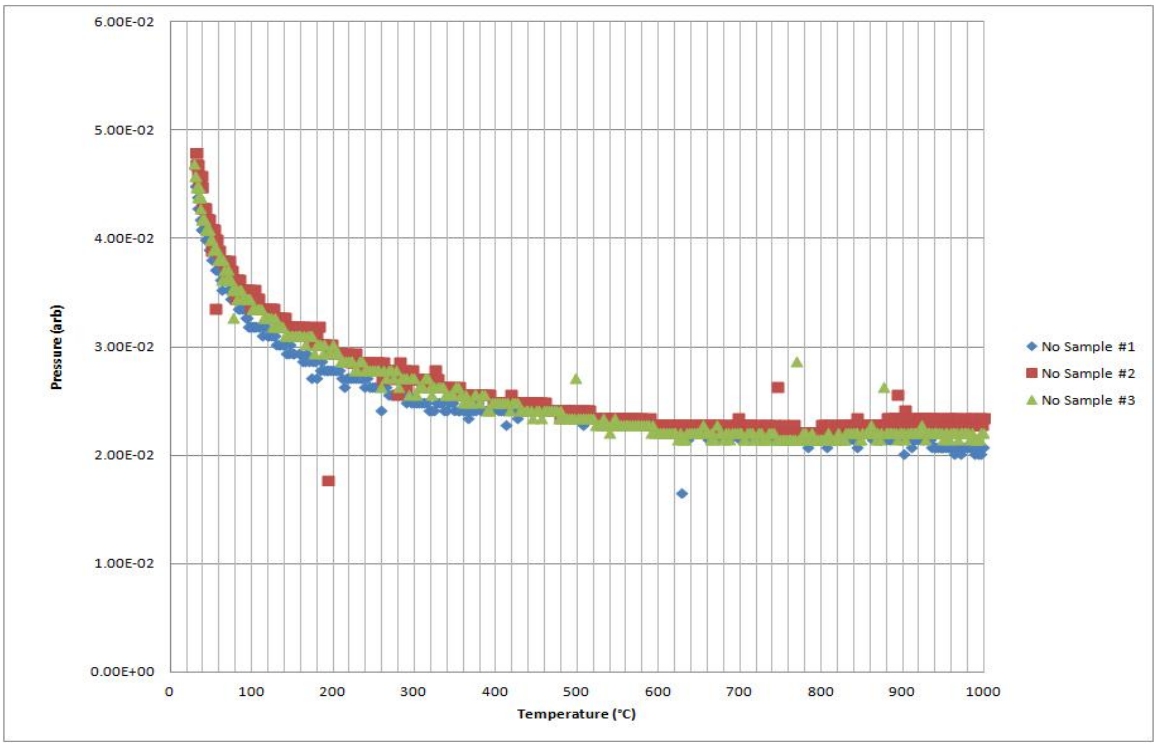

Fig.95. Pressure vs temperature up to 1000°C for the data shown in fig. 94.

It can be seen that, for the three different runs, the change in pressure with temperature is consistent and reproducible. In addition, the heating and cooling rates are consistent.

The range of interest for desorption of NdFeB is from approximately 100°C up to 900°C. From fig. 95, it can be seen that as the temperature increases, the pressure decreases and this is reasonably consistent over the three different runs. There are various deviations from the norm but the general trend of the data is repeatable and consistent.

9.1. Desorption of $NdH_{\sim 3}$

The literature, discussed the fact that during the hydrogenation process in the f.c.c. neodymium lattice, the hydrogen first fills the tetrahedral sites. This results in a composition of NdH_2 and excess hydrogen then partially fills the octahedral sites giving a composition of $NdH_{2+x,}$ where x is in the range $0 \leq x \leq 1.0$, (Yartys et al, 1997 and N. Yoshihiro, 2006). The value of x depends on the degree of occupancy of the octahedral sites and is dependent on the hydrogenation pressure. In this work the exact composition of the NdH_{2+x} is unknown so will be described as $NdH_{\sim 3.}$

Desorption of $NdH_{\sim 3}$ shown in the literature, consisted of two main events corresponding to desorption from $NdH_{\sim 3}$ to form NdH_2 and then finally from NdH_2 to form Nd and H_2.

The start peak and end points of desorption of neodymium hydride.

	Start (°C)	Peak (°C)	Finish (°C)
$NdH_{\sim 3} – NdH_2$	220	380	450
$NdH_2 – Nd + H_2$	550	720	800

Table 25. Data reproduced from (Yartys et al, 1997)

9.2. Desorption of $NdH_{\sim 3}$ Loaded in Air

Neodymium hydride was milled for 20 hours in cyclohexane and then dried under vacuum. Samples of the milled powder were desorbed in the vacuum sintering system to study the desorption behaviour. Three runs were performed, two with 330mg samples and one with a 660mg sample. The measurement errors associated with weighing the powders are ±5mg.

For all three runs, the material was loaded into 321 stainless foil tubes in the glove box and then transferred in air to the vacuum sintering system. The transfer time was estimated at less than 30 seconds. The heating rate was kept at a constant rate of 7°C / min throughout.

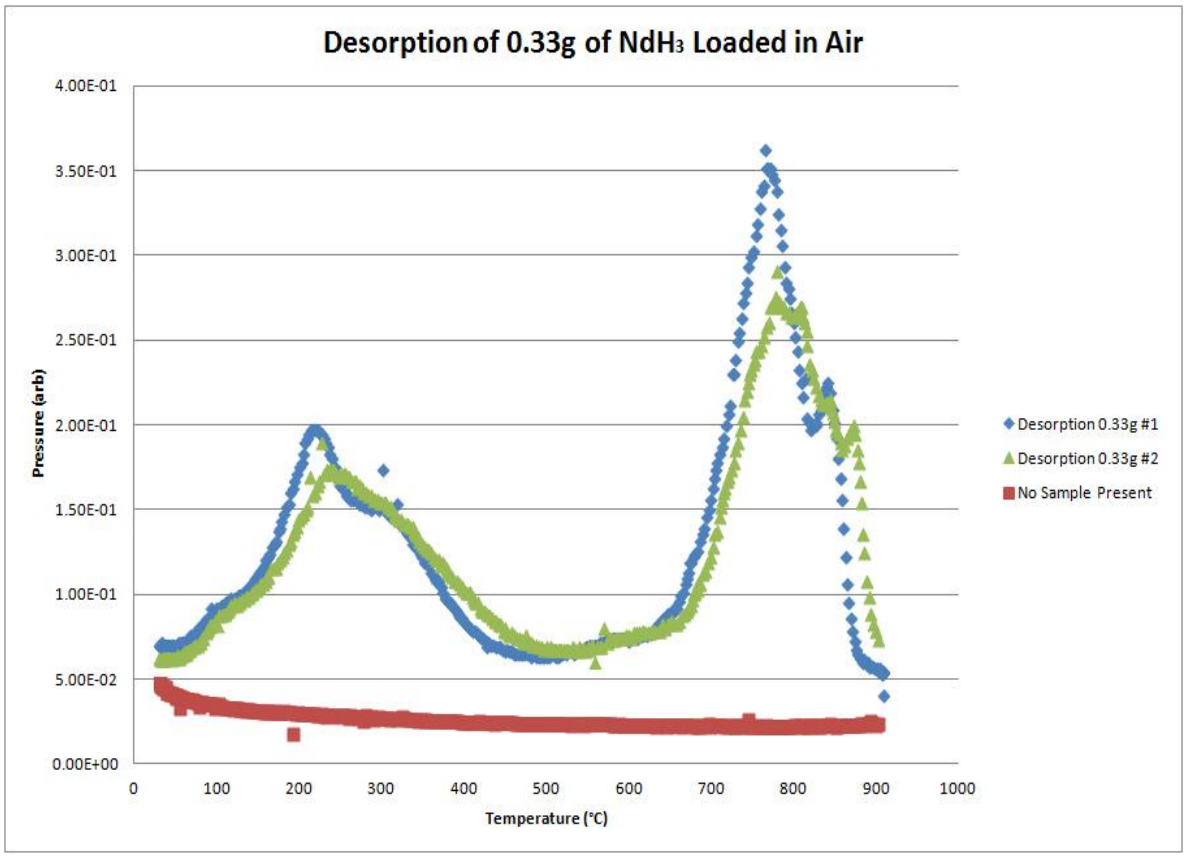

Fig.96. Desorption events for two samples of ~330mg (±5mg) of neodymium hydride milled in cyclohexane for 20 hours and dried under vacuum.

Desorption appears to start at approximately 80°C with a shoulder between approximately 100°C and 150°C, increasing to a peak between 217°C and 220°C and a shoulder at approximately 320°C, ending at approximately 460°C. The second event appears to start at approximately 650°C, peaking at between 765°C and 775°C, with the process finishing at 877°C and 890°C. The final desorption event seems to show various sharp peaks. Desorption was repeated with 660mg of powder.

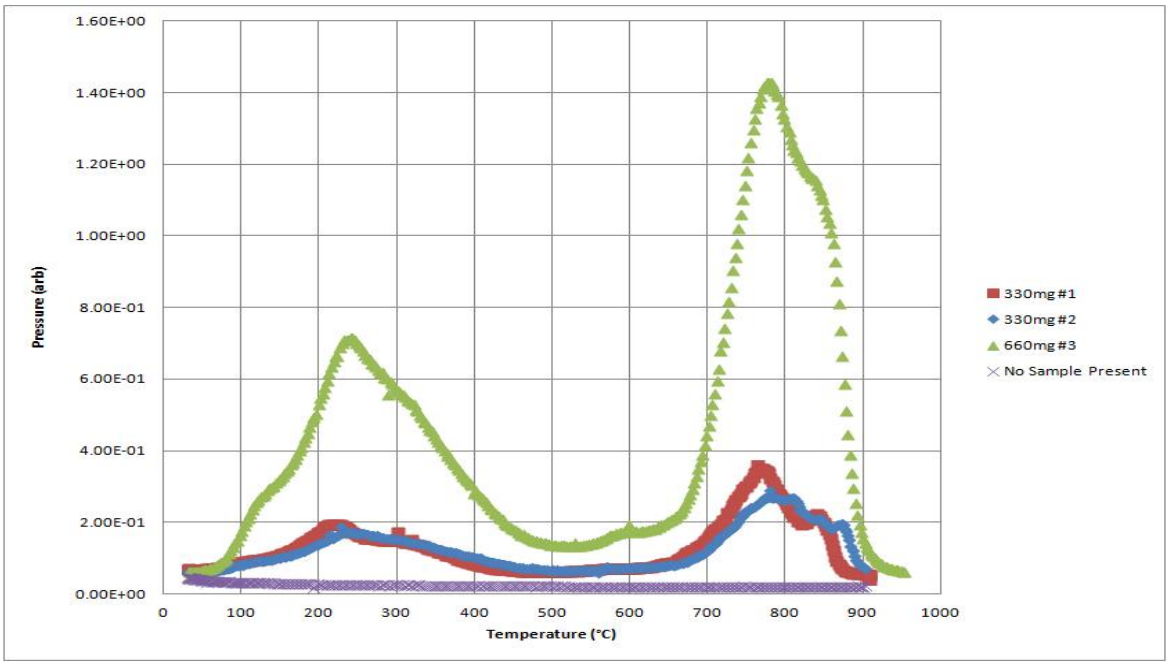

Fig.97. Desorption traces of $NdH_{\sim 3}$ for two runs, (330mg and 660mg). Milled in cyclohexane for 20 hours and loaded in air, (error ± 5mg).

The 660mg desorption follows a similar trace to those of the 330mg samples and the onset of desorption still starts below 100°C. The first desorption event peaks at approximately 230°C and finishes by approximately 460°C. There seems to be a very slight peak between 540°C and 620°C.

The final peak starts at approximately 650°C, peaking at approximately 774°C. Rather than the defined peaks seen on the 330mg desorption events, a shoulder is present. This shoulder is observed at approximately 815°C and 850°C.

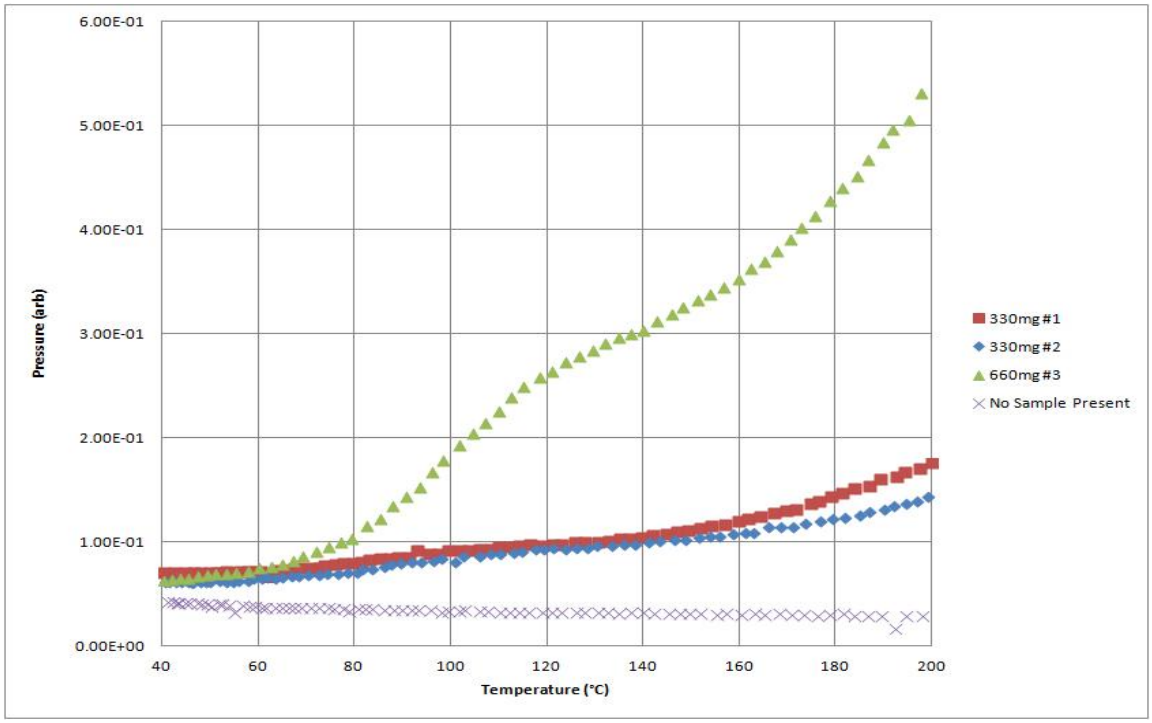

Fig.98. Initial low temperature desorption of milled neodymium hydride loaded in air.

9.3. Plotting Peak Height vs. Mass of Sample

The maximum peak height should relate to the amount of hydrogen released during the heating of the sample. Plotting the maximum peak height for known masses of $NdH_{\sim 3}$ should provide a reference point for the amount of Nd rich phase present in the sintered and hydrogenated NdFeB material of a composition described previously, (page 70). The final peak is the most suitable reference point as it is the conversion of the $NdH_{\sim 2}$ to Nd and H_2, whereas, for desorption of hydrogenated NdFeB, the first peak is a combination of the

desorption of the rare earth rich phase and the desorption of the matrix phase, as reported by Harris et al, (1987) and Williams et al, (1990).

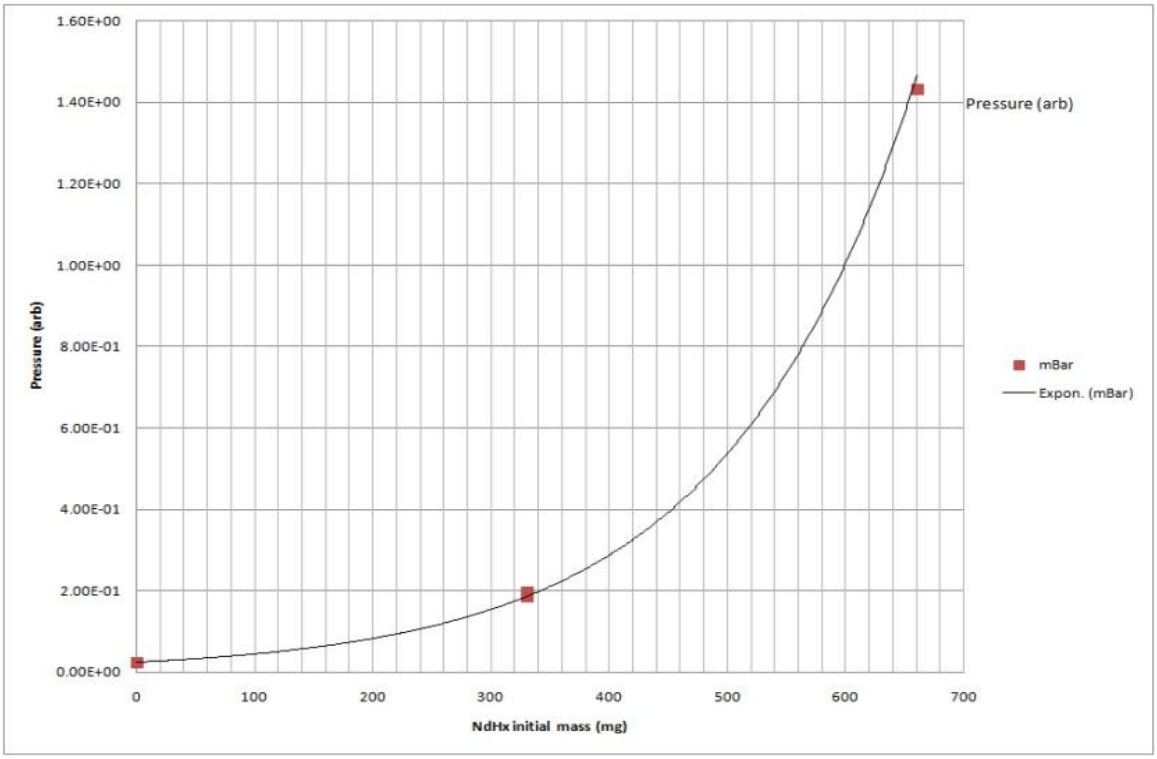

Fig.99. Peak height vs mass of powder desorbed.

Sample	Mass (mg) ±5mg	Pressure mBar
	0	2.28E-02
#1	330	1.85E-01
#2	330	1.95E-01
#1	660	1.43E+00

Table 26. Mass and maximum peak heights for the final desorption peaks shown in fig.99.

9.4. Inert Desorption of $NdH_{\sim 3}$

Oxidation or corrosion of the milled neodymium hydride powder will have occurred to the samples as they were loaded into the system in air, prior to evacuation and degassing. To limit the corrosion, hydrogenation material was loaded inertly into the furnace tube. The furnace tube and a ball valve assembly were transferred to the glove box in an argon atmosphere where the samples were loaded and the ball valve sealed. The sealed sintering tube was transferred to the vacuum sintering system which was evacuated prior to opening the valve.

The samples tested consisted of a single lump of 330mg neodymium hydride, (blue trace) and 330mg of coarse powder with a particle size of approximately 100µm – 200µm, (red trace). The approximate particle size for the coarse powder was determined using sieves.

The samples were not milled and were loaded inertly. The measurement errors were calculated at ± 5mg.

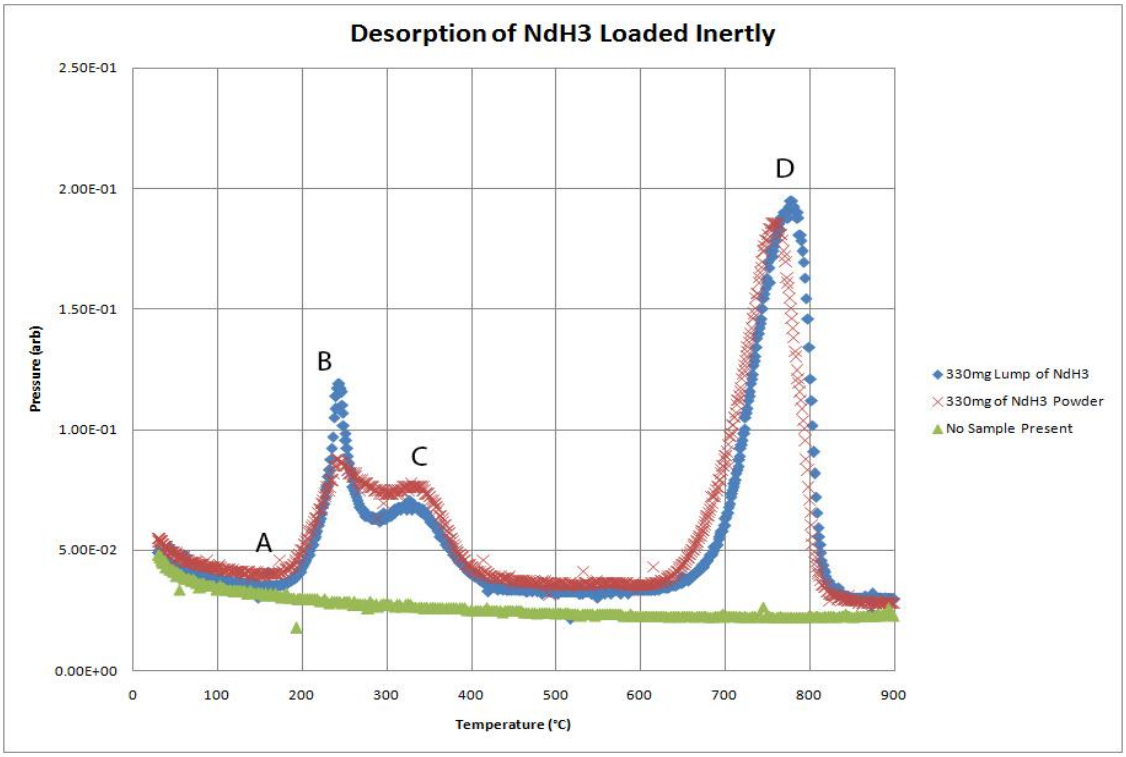

Fig.100. Two desorption traces for $NdH_{\sim 3}$ loaded inertly. The samples consisted of a lump of material and a desorption run of a coarse powder (100µm to ~200µm).

Inertly Loaded # Powder 330mg			
	start (°C)	Peak (°C)	Finish (°C)
Stage 1	181.5	+	422.5
1		242	
2		327	
stage2	639.5	759	816.5

Inertly Loaded # Lump 330mg			
	start (°C)	Peak (°C)	Finish (°C)
Stage 1	180.75		425.75
1		241.25	
2		322.25	
Stage 2	635	779.25	820.25

Table 27. Temperatures at which desorption peaks.

Both of the inertly loaded samples (fig.100), start desorbing at approximately 181°C, (A). There is a main peak at approximately 240°C, (B) with a secondary peak between 320°C and 330°C, (C). The first desorption event is finished by approximately 422°C to 426°C. There is a difference in the onset of desorption between the single lump of material and the coarse powder for the final desorption peak (D), The coarse powder starts desorbing at approximately 640°C, whereas the lump starts desorbing at approximately 665°C.

The powder peaks at 755°C and the lump material peaks at approximately 777°C. The inertly loaded samples finish desorbing at approximately 820°C. Neither of the inertly loaded samples shows the shoulder that was visible in the milled and the air loaded samples and neither shows multiple desorption peaks.

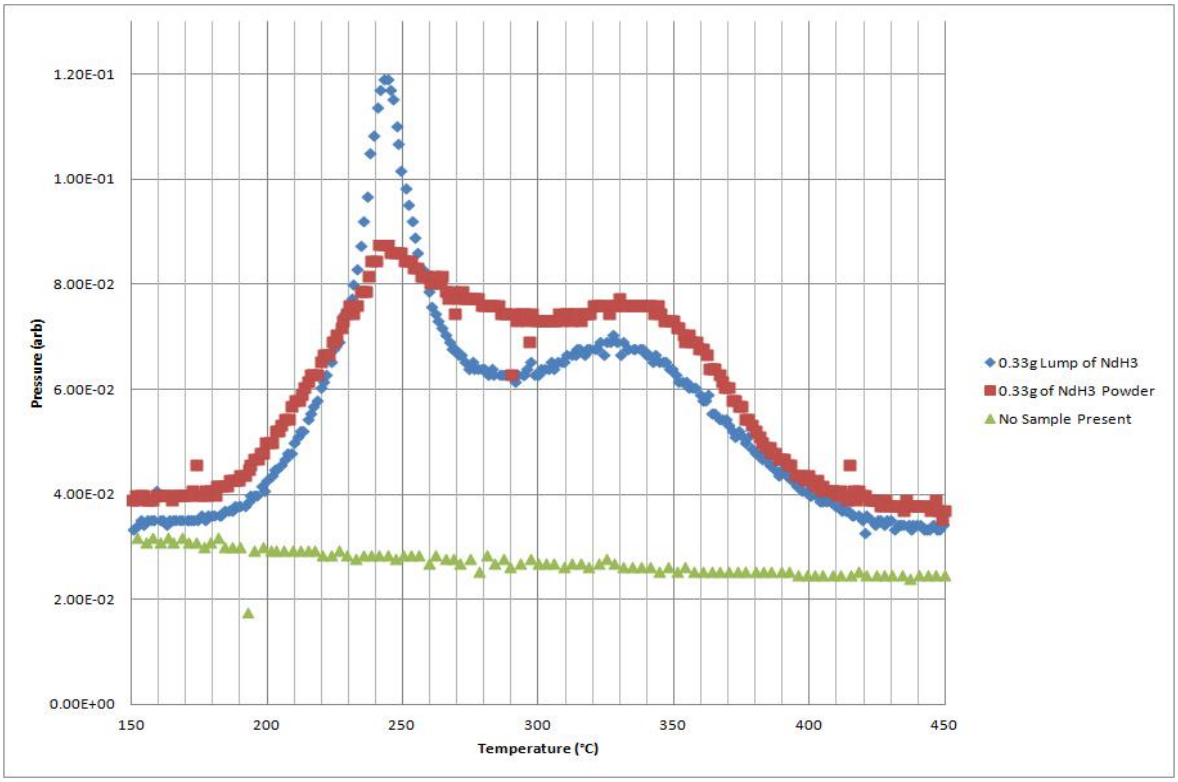

Fig.101. Graph detailing the first desorption event.

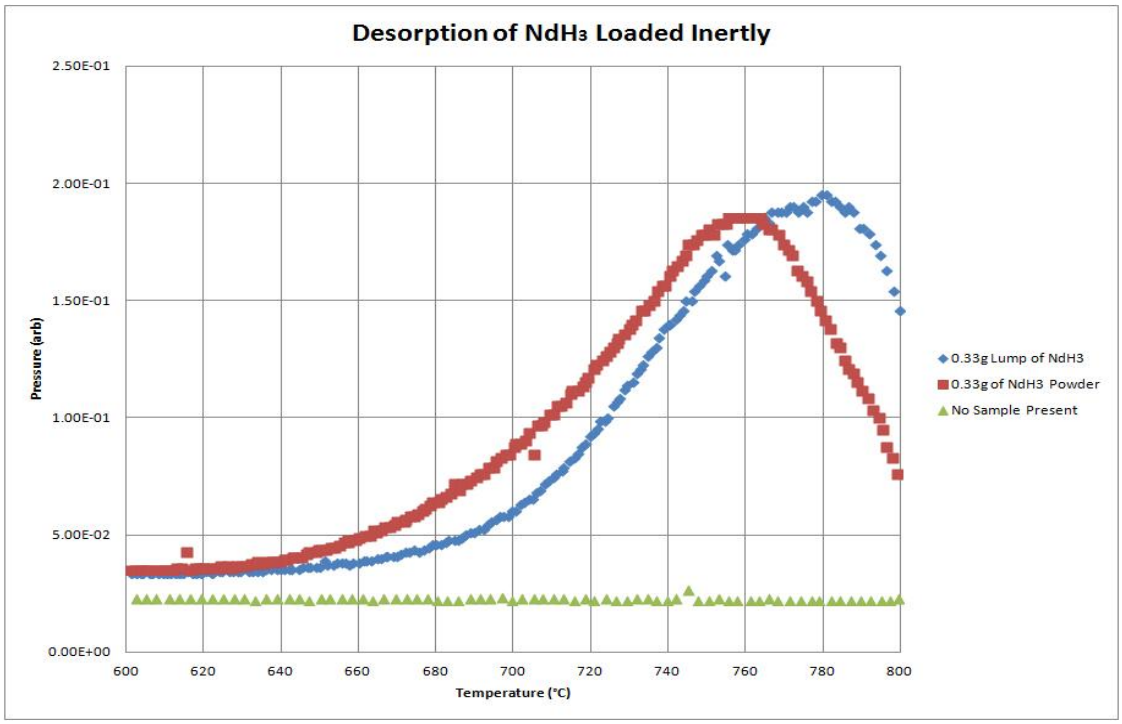

Fig.102. Temperature vs pressure for the final peak of the desorption traces shown in fig. 100.

Fig.102 shows that the powder starts desorbing before the lump of material. This is consistent with the increase in surface area which should improve the kinetics of the system.

9.5. Discussion on Desorption of Neodymium Hydride loaded in Air

The desorption traces of the neodymium hydride loaded in air indicated that the sample started desorbing at temperatures of approximately 70 to 80°C and exhibited a shoulder at between approximately 100°C and 150°C.

For two of the runs the desorption trace appears to show two peaks over the room temperature to the 450°C range. The first peak appears to be at approximately 220°C followed by a shoulder at 320°C. The second event appears to start at approximately 650°C peaking

approximately between 760°C and 770°C with the process finishing at between 870°C and 890°C. The final desorption event seems to show various sharp peaks for the 330mg samples. These extra peaks disappeared when the mass of powder was increased to 660°C. Yartys et al, (1997) showed that the start point for desorption of $NdH_{\sim 3}$ was in the region of 220°C. N. Yoshihiro et al, (2006) also showed that desorption of $NdH_{\sim 3}$ starts above 200°C.

The low temperature 70°C to 80°C desorption of the milled neodymium hydride is likely to be due to the formation of $Nd(OH)_3$ as discussed by, Verdier et al, (1994) and Katter et al, (2001). Verdier et al, (1994) discussed the exposure of neodymium hydride formed at room temperature. They concluded that the hydride formed at room temperature is "very unstable and after an incubation time of around 10 minutes, the powder corrodes quickly and after one day turns to a reddish colour. The saturation value of the mass increase (33%) reveals that the transformation of all the pure Nd is into $Nd(OH)_3$, which is confirmed by X-Ray diffraction". So it is likely that, either during the milling in cyclohexane or during the non inert loading of the powder (or both), corrosion of the powder occurs.

Bera et al, (1999) investigated the thermal decomposition of Nickel and Cobalt hydroxides using temperature programmed desorption (TPD), with the mass spectrometry analysis of the gases formed during heating. They showed that for the hydroxides tested (Ni,Co), water is lost in two stages. The first over 25-150°C, followed by loss of water at 225-500°C. The low temperature desorption peak observed from ~70°C in this work could be attributed to a low temperature desorption of water due to the presence of Nd-hydroxide in the $NdH_{\sim 3}$ powder in a behaviour similar to that observed by Bera et al, (1999). Further work needs to be done on desorption behaviour of neodymium hydroxides. Desorption of the inertly loaded, non-milled neodymium hydride started to exhibit desorption much later than the samples loaded in air.

The inertly loaded, non-milled samples started desorbing at approximately 180°C. This is much closer to the values quoted by Yartys et al, (1997) and Yoshihiro et al, (2006). This indicates that the initial low temperature (~70°C) desorption is likely to be related to the processing and / or the loading of the neodymium hydride powder in air.

The possible corrosion processes of the neodymium rich phase are:

$$2\ Nd + 3\ H_2O \rightarrow NdH_{\sim 3} + Nd(OH)_3 \quad (1)$$

$$NdH_{\sim 3} + 3\ H_2O \rightarrow Nd(OH)_3 + 3\ H_2 \quad (2)$$

$$Nd + 3/2\ H_2 \rightarrow NdH_3 \quad (3)$$

(Katter et al, 2001)

Equation 11. The corrosion process of the neodymium rich phase (in stages).

Neumann and Walter, (2005) investigated the thermal transformation of lanthanum hydroxide using a variety of techniques, including thermogravimetry. The general dehydration process for the lanthanides was described as:

$$Ln(OH)_3 \rightarrow LnOOH + H_2O \quad (1)$$

$$2LnOOH \rightarrow Ln_2O_3 + H_2O \quad (2)$$

Equation12. General equation for the dehydration process for rare earth hydroxides (ln = lanthanides)

Reproduced from Neumann and Walter, (2005)

Using thermogravimetry, Neumann and Walter showed that the dehydration process consists of two events. The first event peaked at 386°C with the second at 535°C corresponding to the formation of LaOOH and H_2O and finally to La_2O_3 and H_2O.

9.5.1. Discussion on Inertly Loaded $NdH_{\sim 3}$

The inertly loaded 330mg lump of neodymium hydride started desorbing at approximately 180°C. The onset of desorption for the inertly loaded material was closer to that reported in the literature but was still lower than the 220°C and 200°C observed by Yartys et al, (1997) and Yoshihiro et al, (2001).

The low temperature shoulders (at approximately 220°C and 320°C) observed on the traces for the powder loaded in air are even more pronounced compared to the inertly loaded samples fig. 97 and fig. 100.

These peaks were most evident in the inert desorption traces for a single 330mg lump of neodymium hydride. The traces for the inertly loaded single lump and the coarse powder start desorbing at approximately 180°C. There is a main peak at approximately 240°C, with a secondary peak between 320°C and 330°C. The pressure drops back to that of the starting pressure at approximately 420°C.

Yartys et al, (1997) discussed the presence of overlapping peaks during desorption of the light rare earth alloys. "For the group I elements, the low temperature NdH_{2+x} to NdH_2 reaction consists of two overlapping desorption events." They stated that "The most pronounced effects were observed for Pr which exhibited two low temperature peaks. The main desorption takes place at 340°C with a smaller but clearly indicated smaller peak at 255°C".

The two low temperature peaks observed in this work match closely those discussed by Yartys, (1997). The relative magnitudes of the peaks were different. In the present work, the lower temperature peak was greater than the higher temperature peak. This is opposite to the relative magnitudes observed by Yartys et al, (1997). The two-peak behaviour could be due to desorption of hydrogen from different sites within the material. The sharpness and magnitude of the low temperature peaks appears to reduce as the particle size reduces. This indicates the possibility that the differences in peak's height and broadness are related to the microstructure, possibly relating to the grain boundaries. The milled powder is likely to be closer to single grain powder.

The desorption behaviour displayed is the same as that reported by Yartys et al, (1997) and Yoshihiro et al, (2001). Desorption consists of two distinct events, consisting of desorption of hydrogen to form $RH_{\sim 2}$ and a final peak which relates to desorption to form the rare earth metal and hydrogen. The masses used previously, (Yartys et al, 1997) were in the region of 60 – 80mg, whereas the masses used in this work were 330mg (± 5mg), potentially more representative of the bulk material.

9.6. Desorption of $NdH_{\sim 3}$ Exposed to Air for 96 hours

To investigate the behaviour of the neodymium hydride exposed to air, the milled neodymium hydride was exposed for 96 hours with the aim of forming a significant amount of the hydroxide phase, with the intention of increasing the magnitude of the shoulders observed in the milled and air loaded samples. Approximately 260mg of the exposed powder was loaded into the desorption system and heated at a rate of 7°C per minute to 900°C. For the second run the mass of powder was ~266mg.

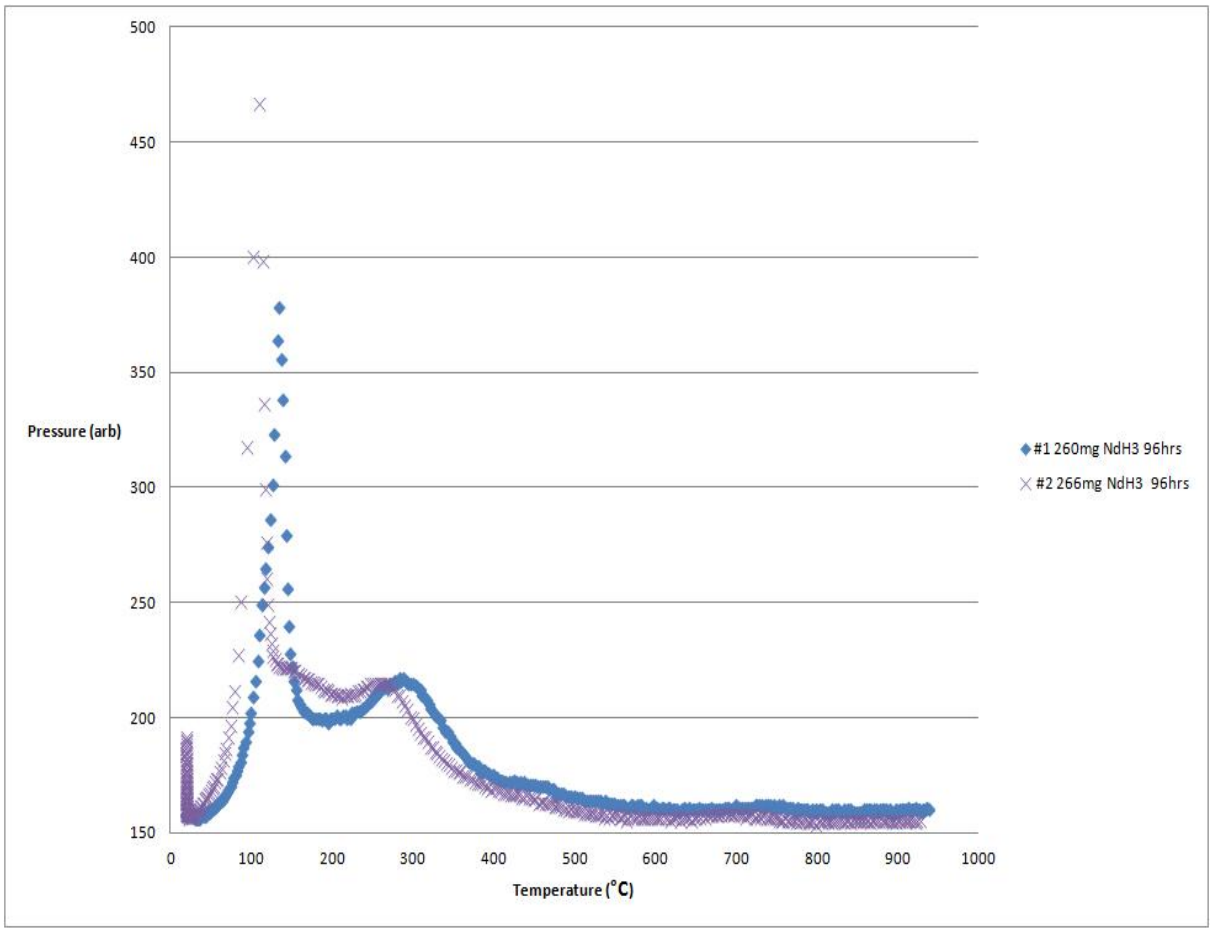

Fig.103. Desorption trace for ~260mg of milled $NdH_{\sim 3}$ exposed to air for 96 hours.

For sample #2 the first peak occurs at 134°C and is followed by a broader peak at 272°C. Sample #1 peaks at 110°C, followed by a broader peak at 252°C.

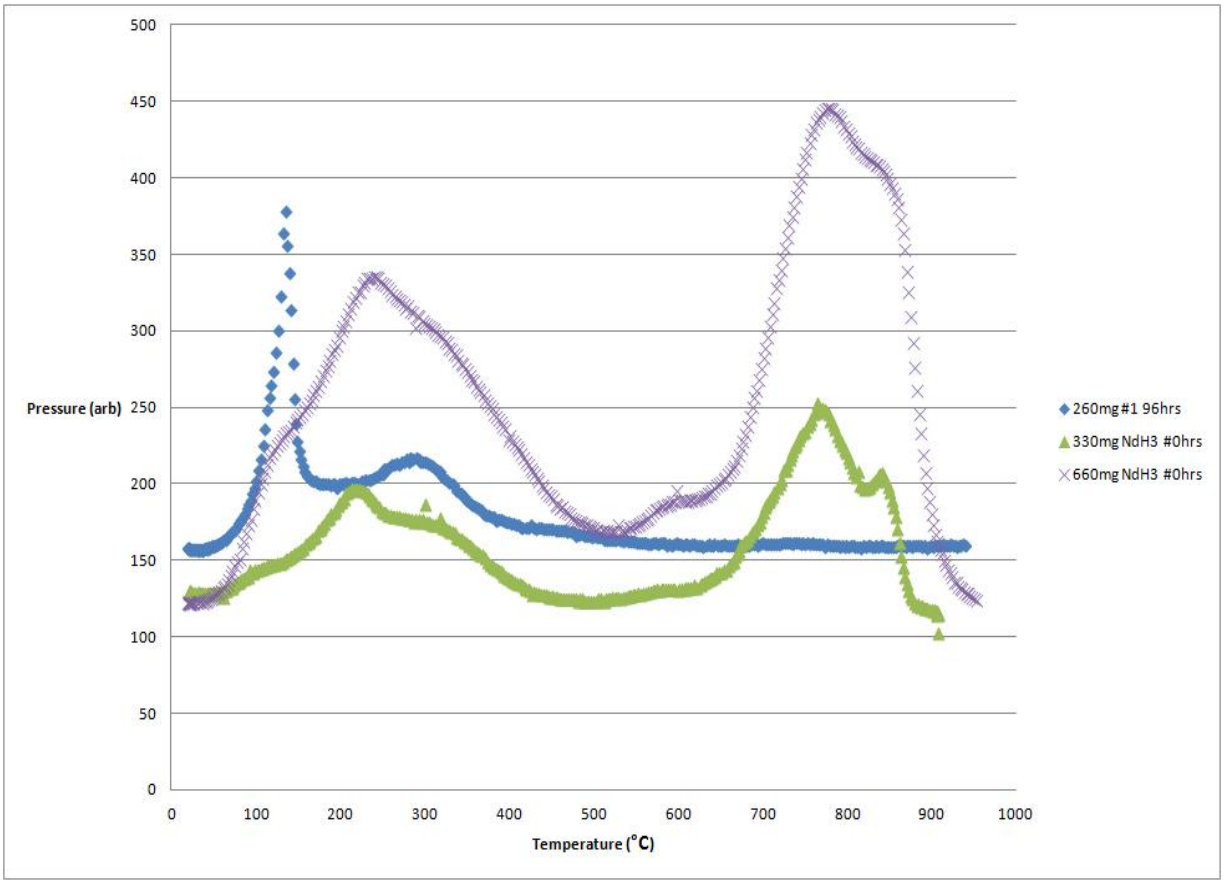

Fig.104. Desorption traces for neodymium hydride milled in cyclohexane and exposed to air for 96 hours and two runs with increasing mass of neodymium hydride with minimal exposure to air.

9.7. Discussion on $NdH_{\sim 3}$ exposed to air

The $NdH_{\sim 3}$ exposed to air for 96 hours showed two distinct peaks which are likely to correspond to the following:

$$Nd(OH)_3 \rightarrow NdOOH + H_2O \quad (1)$$

$$2NdOOH \rightarrow Nd_2O_3 + H_2O \quad (2)$$

Equation 13. $Nd_{\sim 3}$ exposure to air, stages (1) – (2).

The lack of a peak in the region of 700°C to 900°C shows that it is likely that the hydride phase is no longer present. The temperature at which the peaks for the desorption of the neodymium hydride exposed for 96 hours were much lower than for the peaks observed by Neumann and Walter, (2005) for Ni and Co hydroxides. For sample #2 the first peak occurs at 134°C and is followed by a broader peak at 272°C. Sample #1 peaks at 110°C followed by a broader peak at 252°C. This compares with 386°C and 535°C for La $(OH)_3$. This could be due to the difference in stability between Lanthanum and neodymium.

9.8. Desorption of Stoichometric $Nd_2Fe_{14}B$ H_x

The as cast alloy of $Nd_{11.8}Fe_{82.4}B_{5.8}$ ($Nd_2Fe_{14}B$) was annealed to homogenise the sample and was subsequently homogenised at temperature. The hydrogenated powder was transferred inertly to a glove box and then ball milled for 20 hours in cyclohexane and dried under a vacuum. 15.0g (± 5mg) of the hydrided powder was then vacuum desorbed at a heating rate of 7°C per minute up to 950°C.

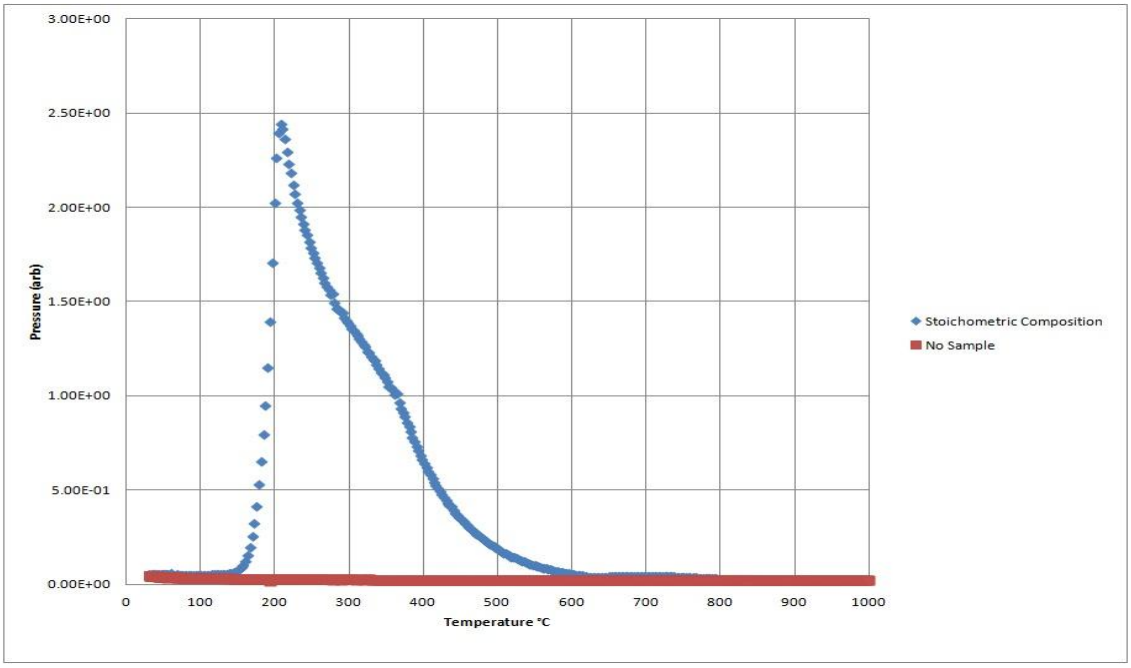

Fig.105. Desorption of 15g of annealed and hydrided $Nd_{11.8}Fe_{82.4}B_{5.8}$ ($Nd_2Fe_{14}B$) powder.

From the desorption behaviour shown in fig. 105 it can be seen that desorption starts with the onset of a rapid desorption at 150°C and peaks at 206°C with a shoulder at approximately 360°C and finishes at 610°C.

From the literature, it can be seen that desorption occurs as follows:

$$Nd_2Fe_{14}BH_{\sim 2.9} \rightarrow Nd_2Fe_{14}B + 1.45H_2 \quad \text{(Harris, 1987)}$$

Equation 14. Desorption.

Williams et al, (1991) showed that, for $Nd_2Fe_{14}B$ the desorption trace "consisted of a sharp peak centred on 150°C followed by a broad shoulder which indicates a peak centred on approximately 250°C. They suggested that this apparent dual stage "could be due to desorption of hydrogen from different sites within the $Nd_2Fe_{14}B$ phase and / or to microstructural effects such as separate desorption of hydrogen from the grain boundaries and the matrix."

The trace observed in the present work shows a similar sharp peak with a shoulder agreeing with the dual nature of the desorption process. In these results, the initial desorption starts at 150°C and peaks at 206°C with a shoulder at approximately 360°C.

There is approximately 50°C difference for the first peak and a 100°C increase in temperature before the second shoulder is observed. Harris et al, (1987) used mass spectrometry to observe the hydrogen desorption of $Nd_2Fe_{14}B$. The trace showed the desorption of the homogenised $Nd_2Fe_{14}B$ alloy starting at just under 50°C, peaking at approximately 150°C and ending at 300°C. The shift in temperatures observed in the present work could be related to oxidation of the powder during loading in air.

9.9. Desorption of Hydrogenated NdFeB Alloys

The published literature states that during the hydrogenation process, alloys with a Nd - rich composition should fully hydride at room temperature. (Harris et al, 1987 and Williams et al, 1991). The Nd - rich phase is said to initiate the hydrogenation of the $Nd_2Fe_{14}B$ phase. Their work showed that desorption of hydrogenated and milled cast material showed a combination of the desorption events that can be attributed to the rare earth rich phase and to the $Nd_2Fe_{14}B$ phase.

Harris et al, (1987) showed that "the hydrogen absorption process in the $Nd_{16}Fe_{76}B_8$ alloy is a multi-stage process reflecting the complex nature of the microstructure. The $Nd_2Fe_{14}B$ matrix absorption can only be achieved readily at room temperature in the presence of the Nd-rich grain boundary material."

The desorption traces for powder made from the sintered blocks with a composition of $Nd_{29}Fe_{66}Dy_{1.98}B$ wt% ($Nd_{13.6}Fe_{79}$ $Dy_{0.8}B_{6.3}$ at %) hydrogenated at room temperature at 4 bar powder, will comprise of two sets of desorption events. One set relates to desorption of hydrogen from the rare earth rich hydride phase and the other to desorption of the $Nd_2Fe_{14}B$ H_x phase. The rare earth-rich phase comprises mostly of neodymium.

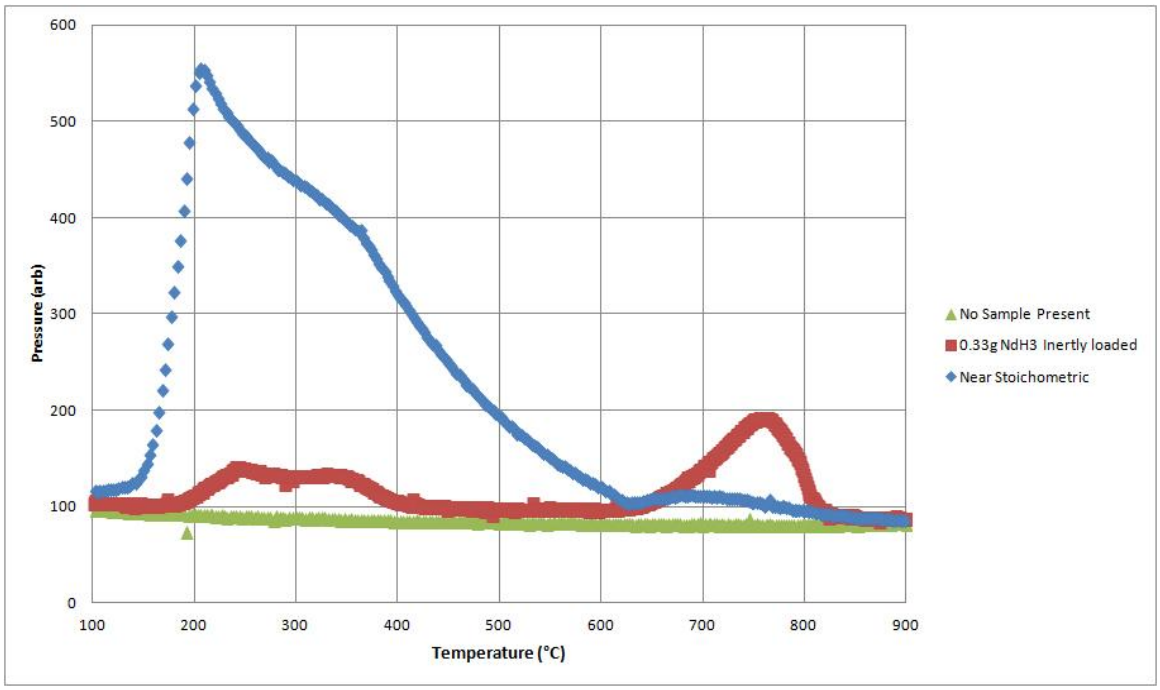

Fig.106. Raw data from for desorption of $Nd_2Fe_{14}B$ and the Nd rich hydride phases combined.

From fig.106 you can see that the primary neodymium hydride desorption peak coincides with that of the $Nd_2Fe_{14}BH_x$ phase.

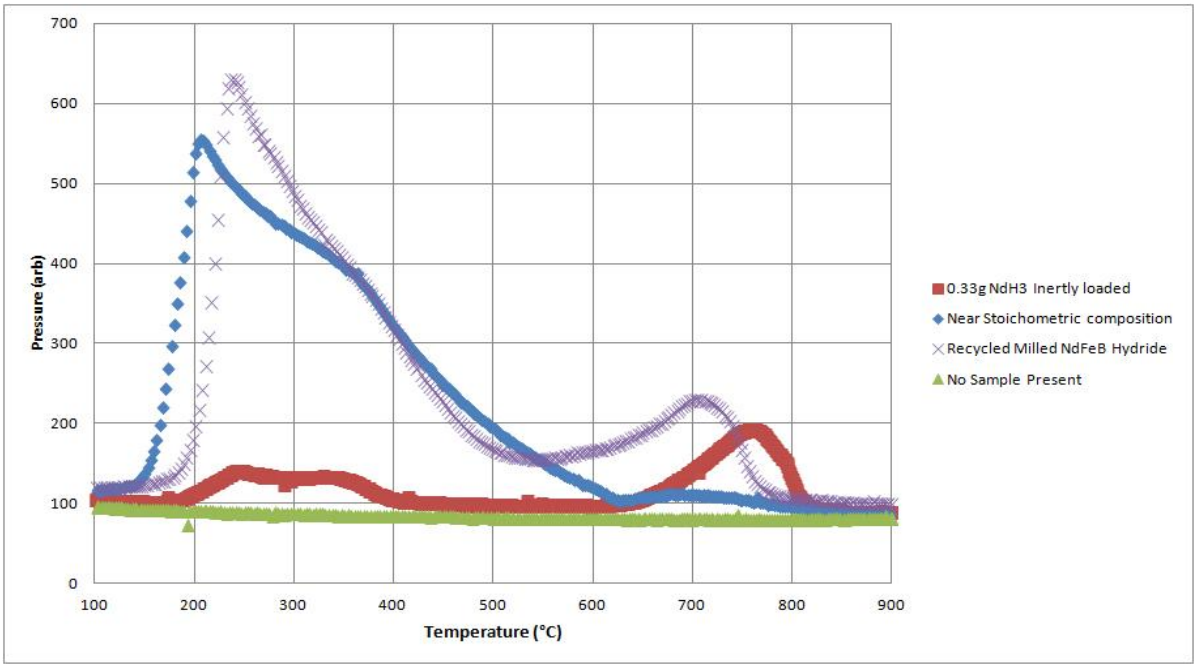

Fig. 107. Desorption of recycled burr milled HD powder and $Nd_2Fe_{14}B$ and Nd hydride traces.

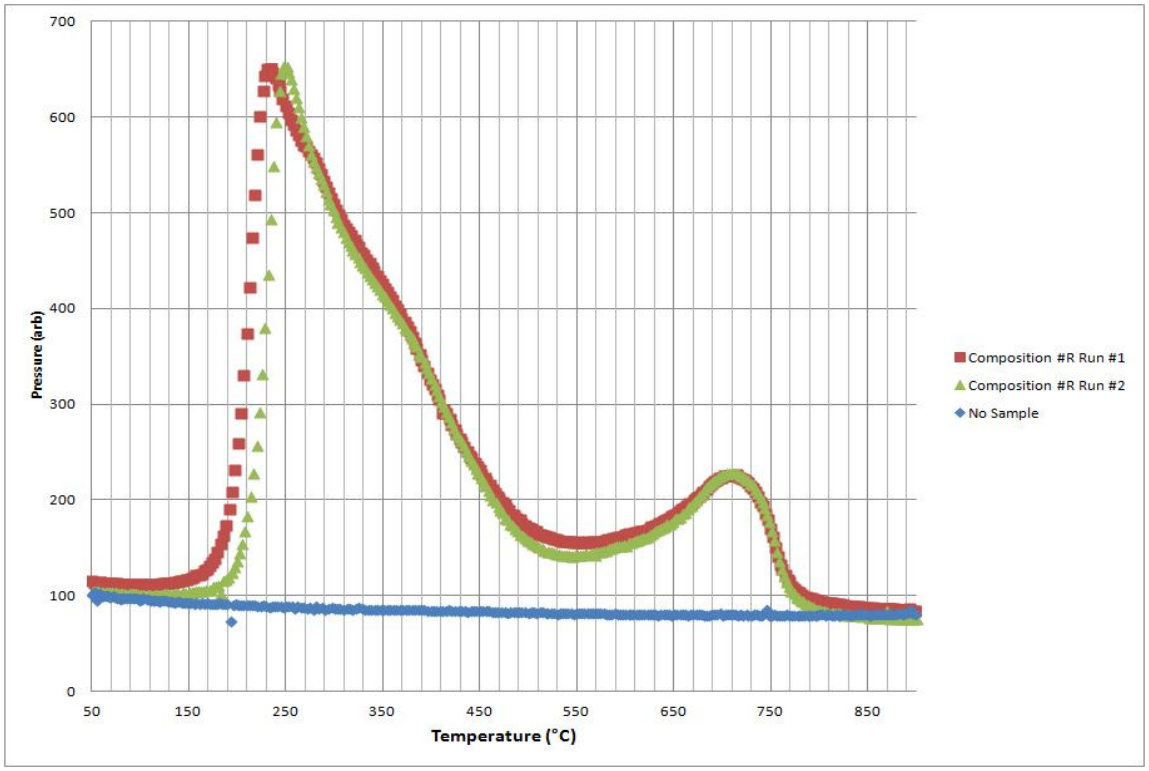

Fig.108. Two desorption traces of hydrogenated burr milled powder from the sintered starting material with a particle size of less than 45µm.

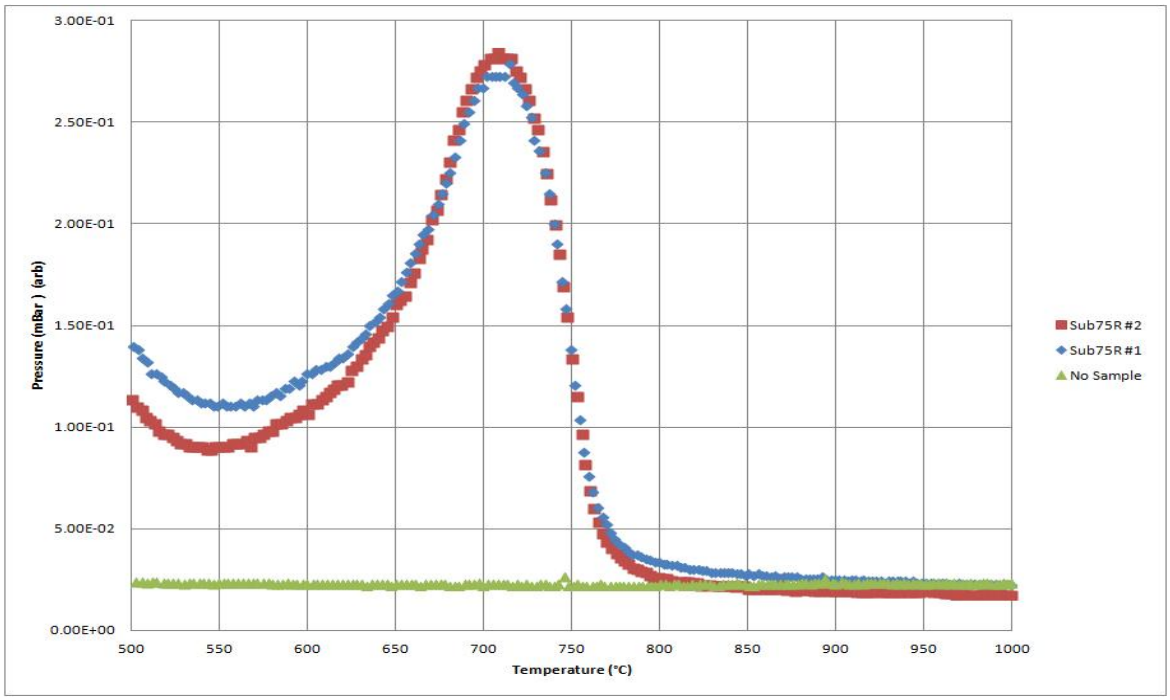

Fig.109. Final desorption event from $NdH_{\sim 2}$ to Nd plus hydrogen.

9.10. Discussion on the Desorption Behaviour of Sintered NdFeB

The desorption trace for the sintered magnet of composition $Nd_{29}Fe_{66}Dy_{1.98}B$ wt% hydrogenated at room temperature shows two peaks indicating that the $Nd_2Fe_{14}B$ phase is likely to have fully hydrogenated at room temperature at 4 bar pressure, thus confirming the work reported by Harris et al, (1987).

The HD powder from the sintered Nd-Fe-B magnet started desorbing at a higher temperature than the $Nd_2Fe_{14}B$ powder. The hydrided $Nd_2Fe_{14}B$ powder was ball milled for 20 hours so it was likely to have a much smaller mean particle size than the burr milled powder which was milled to a particle size of less than 75µm. Characterisation of the powder showed it consisted of 20% between 75 and 45µm, and approximately 80% less than 45µm. It has been shown in chapter 8 that the powder with a mean particle size less than 45µm is similar to the grain size of the starting material.

The shift in temperature for the $NdH_{\sim 2}$ to Nd peak is due possibly to the comparative difference in mean particle size. The inertly loaded neodymium hydride had a mean particle size in the region of 100 – 200µm. The burr milled HD powder was likely to have a mean particle size slightly larger than that of the starting material, (a mean particle size of approximately 10 microns).

This big difference in mean particle size is likely to be the cause of the reduction in desorption onset temperature for the burr milled alloy. Desorption of the burr milled HD material from the sintered starting material did not show the low temperature peak between 70°C and 150°C. This indicates it could be an artefact of the processing.

Results show that desorption of hydrogenated NdFeB, (including binary hydrides with masses of powder ranging from mg's to tens of grams), can be observed using a flowing system. The pressure is monitored using thermal conductivity pressure measurements from a Pirani gauge. The temperature versus pressure plots observed show agreement with traces observed in the literature (Harris et al 1987, Williams et al 1991, Yartys et al 1997, Yoshihiro et al 2001 and Ryan and Coey, 1985).

Chapter 10. Change in Desorption With Particle Size

The final desorption peak for desorption of the hydrogenated NdFeB magnet consists solely of desorption of $NdH_{\sim 2}$ to Nd as reported by Williams et al, (1990). They also reported that exposure to air resulted in a reduction of the final desorption peak. So any reduction of the rare earth rich phase either through corrosion and oxidation or the physical loss of the Nd-rich phase, should have an impact on the desorption behaviour of the final peak. Nothnagel et al, (1991), Namkung et al, (2011) and Li et al, (2009) showed that a reduction in particle size resulted in an increase in oxygen within the magnets produced.

Sintered magnets with a composition $Nd_{29}Fe_{66}Dy_{1.98}B$ ($Nd_{13}Fe_{76}$ $Dy_{0.78}B_6$) were hydrogenated at room temperature at 4 bar gauge pressure. The hydrogenated powder was transfered inertly into a glove box prior to processing. Three different particle size ranges were tested, (each size range was tested twice). The ranges chosen were powder with a particle size greater than 500µm, powder with a particle size distribution of less than 45µm and powder with a particle size distribution of between 150 and 90µm.

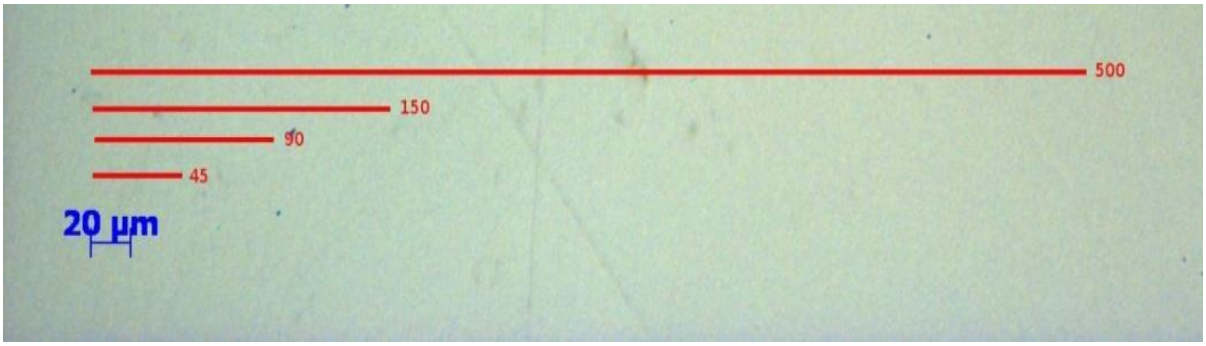

Fig.110. Relative scale of the particle sizes tested.

Fig.110 provides a guide to the relative differences in the mean particle sizes used. The difference in mean particle size between the greater than 500µm powder and the 150 – 90µm powder is much larger than the difference between the sub 45µm powder and the 150 – 90µm powder. However, as seen previously, the sub 45µm powder is likely to have a mean particle size of sub 10µm. The powders were loaded in air, so were exposed briefly to prior to loading into the vacuum sintering furnace.

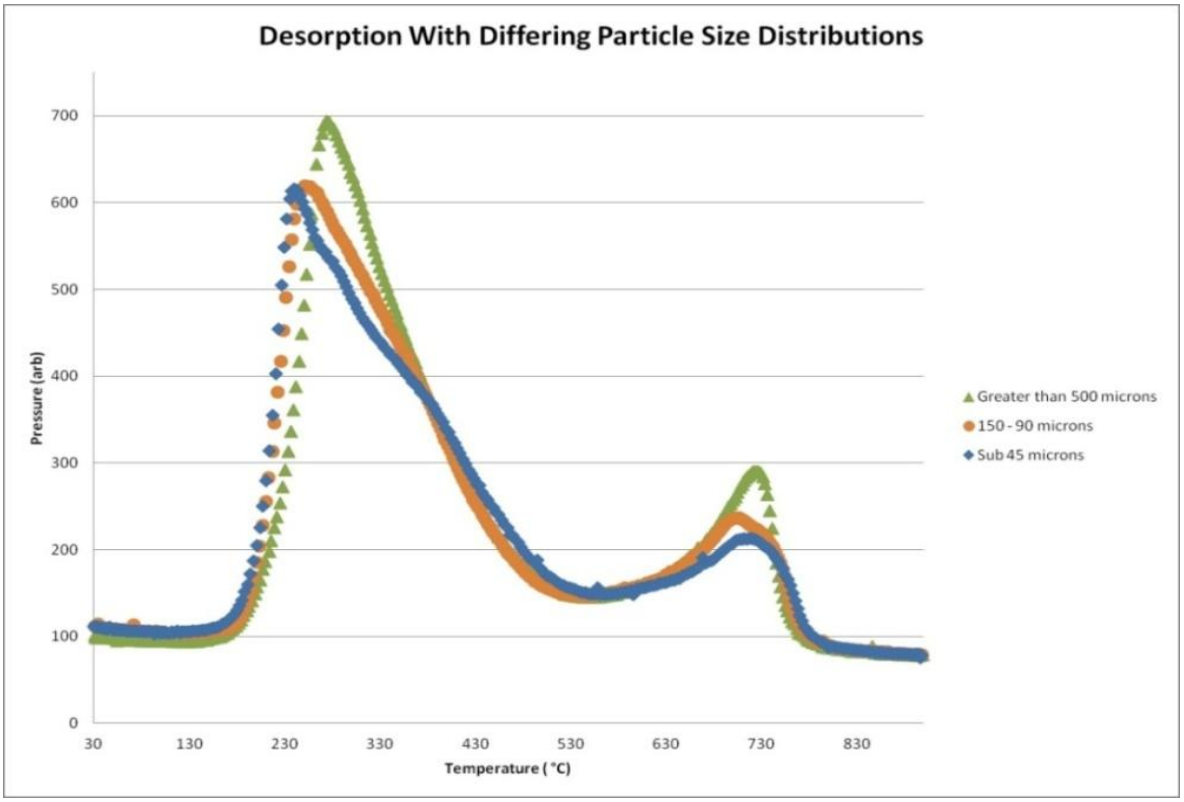

Fig.111. Desorption traces of HD powder from sintered magnets, (three different particle size ranges).

The traces in fig. 111 shows three desorption traces for powder with particle sizes greater than 500µm, between 150 and 90µm and less than 45µm. From this, it can be seen that the point at which desorption occurs happens earlier for the sub45µm powder compared with that for the powder greater than 500µm. The final peak shows a reduction in height as the particle size of

the powder was reduced. The broadness of the peaks seem to increase with the reduction in the particle size.

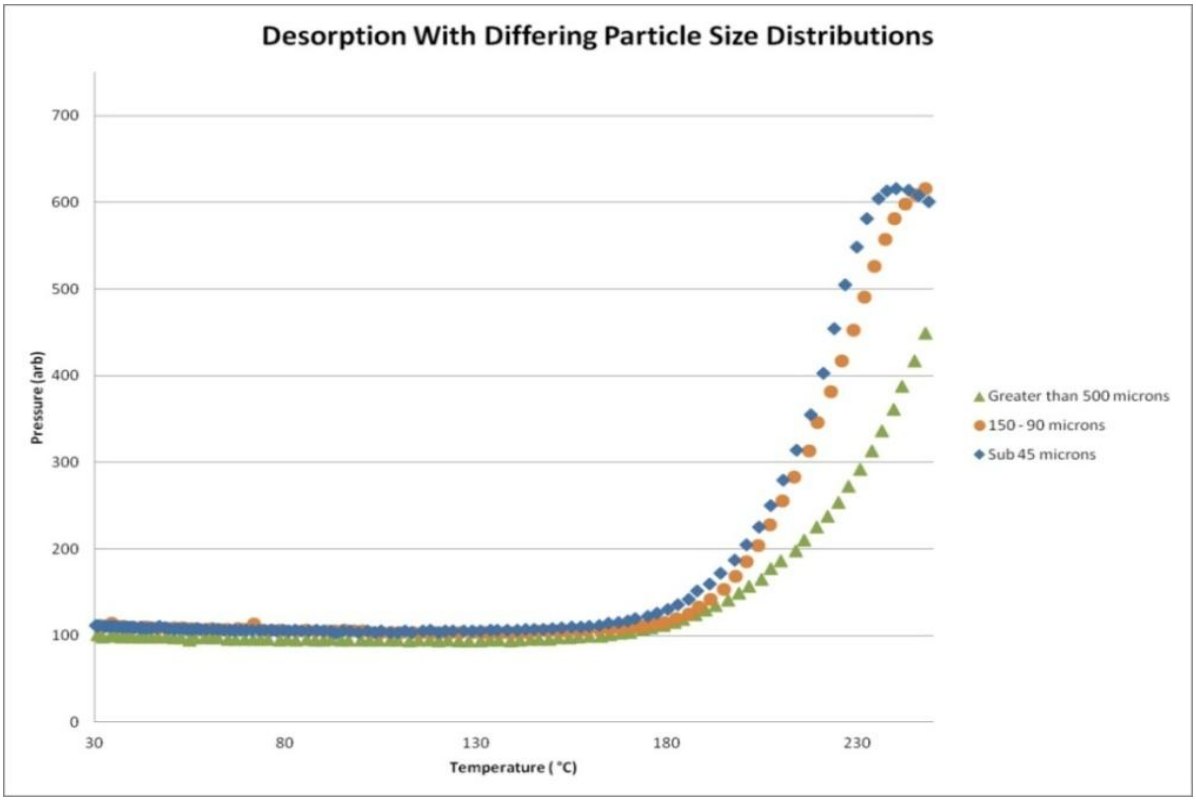

Fig.112. Onset of desorption for the three particles size ranges used.

As expected, the lower the mean particle size, the earlier desorption of hydrogen occurs. The sub 45µm powder and the 150 – 90µm powder have a closer mean particle size than the powder greater than 500µm and also show a similar desorption initiation temperature.

The powder greater than 500µm has a bigger difference in the mean particle size and also shows a bigger difference in desorption initiation temperature.

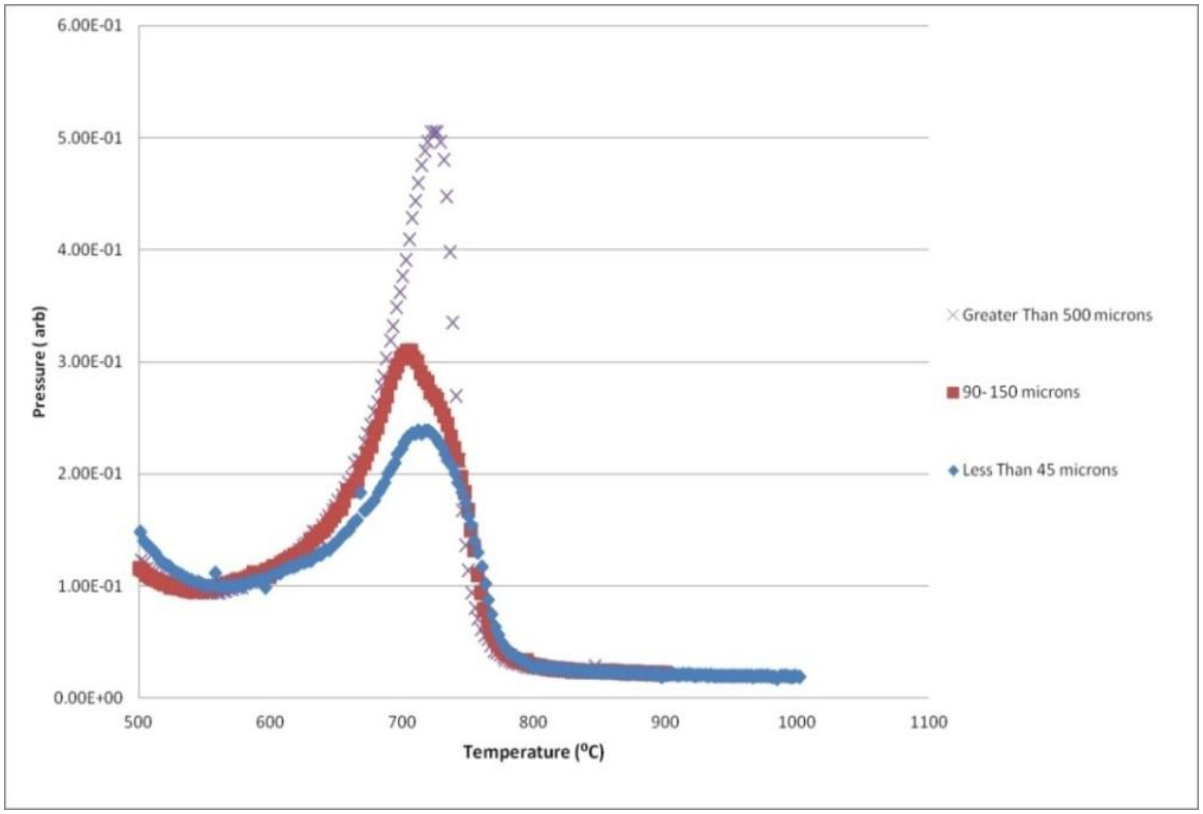

Fig.113. Final desorption peak with varying mean particle sizes.

In fig. 113 the final desorption peaks correspond to desorption of H_2 from the Nd rich phase. As the particle sizes reduce, so does the final peak height. The final peak corresponds to the transformation of $NdH_{\sim 2}$ to Nd and H_2.

Desorption of hydrogen from the different particle size distributions was repeated twice for each particle size range and the results recorded. The maximum peak heights on the pressure versus temperature plot for the final Nd rich desorption event were also recorded.

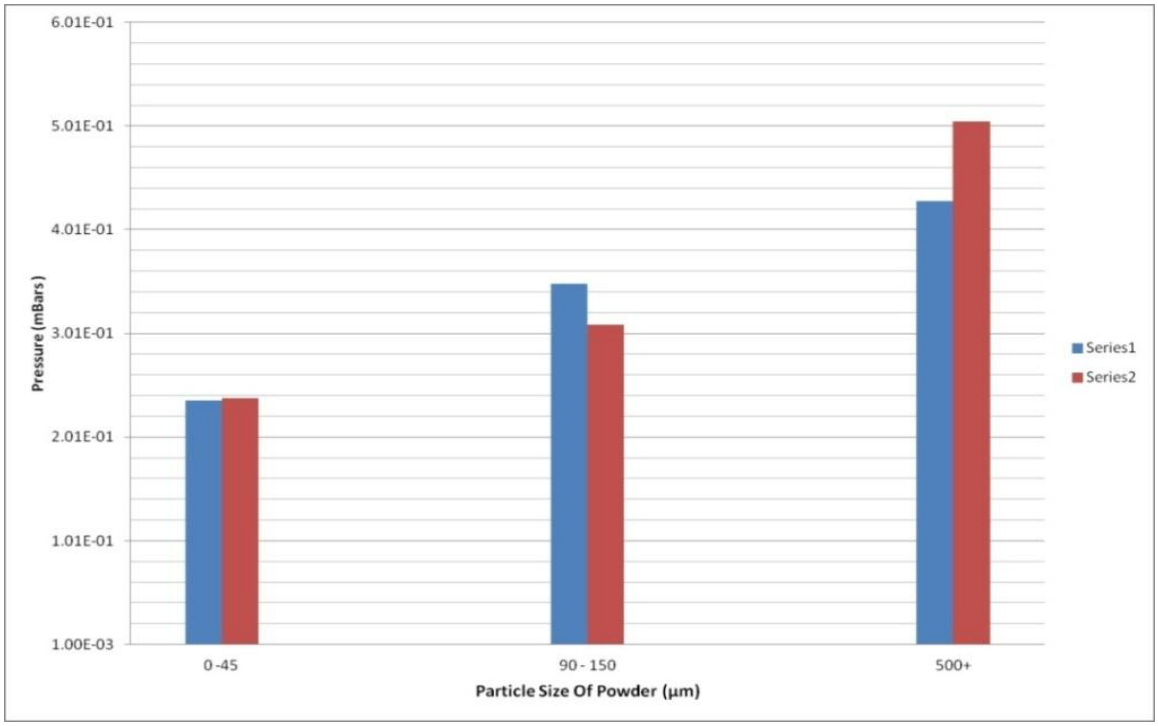

Fig.114. Maximum peak height for the final desorption event for the rare earth rich phase.

In fig.114 the results show a reduction in maximum peak height as the mean particle size is reduced.

10.1. Discussion on Change in Desorption Related to Particle Size

From the desorption traces obtained in this work, the powder with the lower mean particle size has an initiation temperature for desorption that occurs at lower temperatures than the powder with a greater mean particle size. The sub 45µm and 150 – 90µm powders exhibit similar initiation temperatures for the beginning of desorption, with the sub 45µm powder starting at a slightly lower temperature. Desorption from the powder greater than 500µm occurs at a higher temperature.

The powder was loaded in air so corrosion of the powder will have occurred during the process. The peak heights reduced as the mean particle sizes reduced. This is in agreement with the literature, for instance, Williams et al, (1990) showed that HD powder exposed to air showed a reduction in the height of the final peak when desorbed and analyzed using a mass spectrometer.

The literature discusses a reduction in magnetic properties as the particle size of the powder is reduced below a critical point. The consensus appears to be that, as the particle size is reduced, the oxygen content of the powder increases and this has been shown by Nothnagel et al, (1991), Namkung et al, (2011) and Li et al, (2009). The oxidation of the Nd rich phase is proposed to be the source of the reduction in magnetic properties. This ties in with the reduction in the Nd-rich peak observed in fig.114.

The sub 45μm powder shows very similar peak heights. The work on investigating the particle size distribution of sub 45μm powder showed that the particle size distribution of the powder is likely to be very similar to the grain size of the starting material. The narrow distribution of the particle size observed during characterization of the powder could explain the similar peak heights.

For the sub 45μm powder the mean particle size was observed to be approximately 9μm with a standard deviation of 2.77. The narrow particle size distribution of the sub 45μm powder could explain why the maximum peak heights are very similar. The powder with a mean particle size greater than 500 μm should have the greatest range of particle size and also show a bigger difference in maximum peak height.

The reduction in peak heights could also be due to the physical loss of the rare earth rich hydride phase during processing. During the HD process there is a difference in lattice

expansion between the Nd - rich hydride and the $Nd_2Fe_{14}B$ H_x solution phase (Cadogan and Coey, 1985). This expansion mismatch causes fractures and cracks to propagate through the material. It has been shown that the HD powder is likely to break up along the grain boundaries where the Nd-rich phase occurs. The average particle size of the Nd rich phase is in the order of sub-micron. Thus it is possible that some of the Nd-rich phase is physically lost during the milling process.

10.2. Desorption of HD Material Loaded Inertly in Relation to Differing Particle Size

To investigate further whether the reduction in the peak height is mainly due to corrosion or physical loss of the rare earth rich phase, the desorption system was modified and samples were loaded inertly.

HD powder was transferred inertly to the glove box and then either sieved to extract particles greater than 500µm or burr milled and then sieved to a particle size less than 45µm. The resultant powder was then loaded into a stainless steel foil tube and placed in a furnace tube with a ball valve assembly inside the glove box. The furnace ramp rate was 3 °C / min and the furnace was heated to 920 °C.

The ramp rate used here was different to that employed for the samples loaded in air and heated at 7°C per min. The difference in ramp rate was due to an error in checking the furnace program. Ideally the ramp rate should have been consistent throughout.

The addition of a ball valve section will have an impact on the desorption trace. To obtain results under comparable conditions, the volume of the system needs to remain the same, as changing the volume of the system will have an impact on the change in pressure monitored

by the Pirani gauge. For these reasons, desorption traces for the inertly loaded samples and those not inertly loaded, cannot be compared directly.

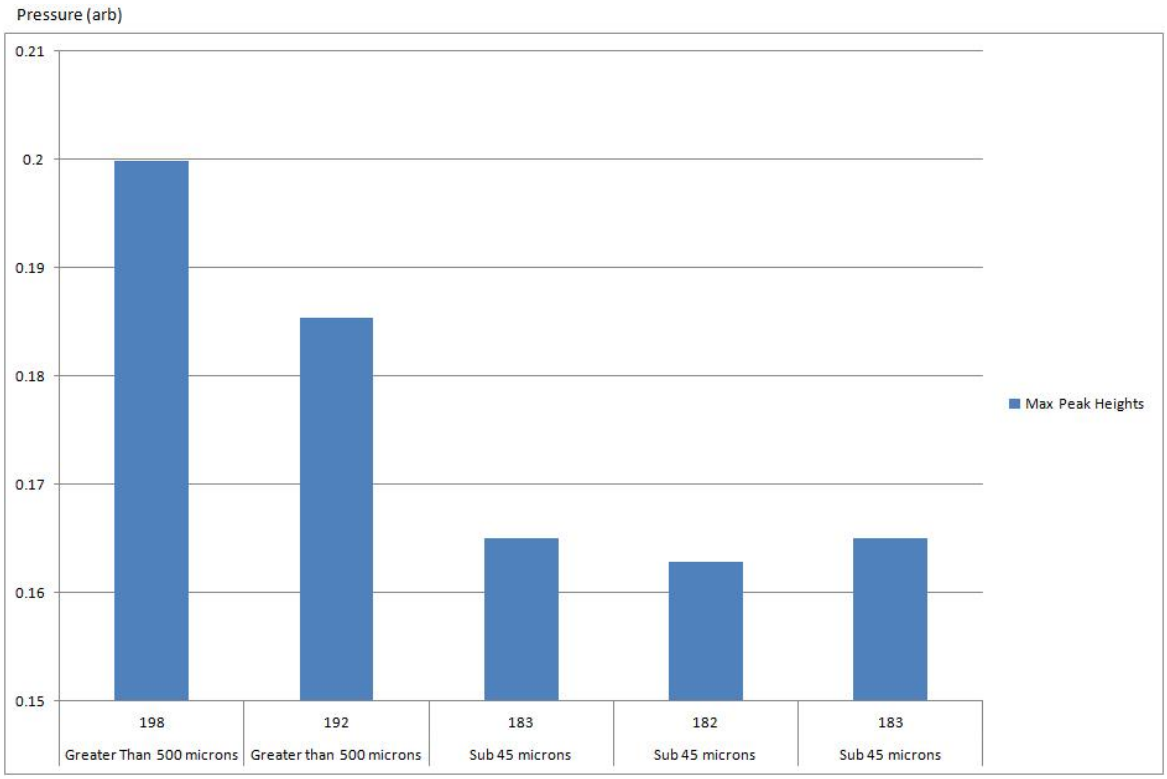

Fig.115. Reduction in the maximum peak height as the particle size is reduced.

10.3. Discussion on the Reduction in Peak Height

The reduction in peak height along with particle size (fig.115) is still significant, despite the samples having been loaded inertly. The oxygen content in the glove box was maintained below 100 p.p.m. The samples were loaded in the furnace tube inside the glove box and sealed using a ball valve assembly. The vacuum sintering furnace was evacuated to a pressure

of 6.8 $x10^{-2}$ mbar prior to opening the ball valve. The furnace was then ramped up when the vacuum recovered to 6.8 $x10^{-2}$ mbar.

To investigate further, 15g of powders with varying particle size distributions were sealed in rubber isostatic bags, aligned and pressed to 10000 kg/cm^2 and then returned to a glove box for loading inertly. The samples were heated at a rate of 3°C per minute and sintered at 1060°C for 1 hour then furnace cooled. Samples from these magnets were sent for ICP analysis, (to Less Common Metals).

10.3.1. Changes in composition with Particle Size

Inductively Coupled Plasma spectrometry is a form of mass spectrometry. Samples are ionised using inductively coupled plasma and the ionised particles are separated and quantified using a mass spectrometer. ICP measurements show the proportion of each element present. The fact that this method records the percentage of ions present means that the technique can establish how much of an element is present. It does not matter if the element was initially bound with oxygen or not so a significant reduction in the percentage of neodymium should signify a potential physical loss of neodymium rather than oxidation

	B	**Dy**	**Nd**	**Pr**	**Fe**	**O**	**N**
	%	**%**	**%**	**%**	**%**	**ppm**	**Ppm**
ICP Starting Material #1	1.02	1.98	29.17	0.1	66.01	4265	95
ICP Starting Material #2	0.97	1.57	27.92	0.09	63.64	2665	90
ICP Sintered Greater Than 500 µm	0.98	1.56	28.49	0.09	64.24	5080	125
ICP Sintered Less Than 45 µm	0.99	1.58	27.71	0.1	63.45	6620	361

Table 28. ICP analysis of two samples of starting magnet material - one made from powder with a particle size greater than 500µm and the other made from powder less than 45µm.

(More complete ICP supplied in Appendix 1.)

Table 28 summarizes the compositions of the starting materials, (two samples were tested and all samples were loaded inertly into the furnace). The compositions are very similar except for neodymium and iron. The neodymium is not homogeneously spread throughout the microstructure of the NdFeB magnet. As discussed previously, the grain boundaries contain higher concentrations than the matrix phase. This is likely to be why there is a difference in the neodymium and iron contents of the two sets of ICP starting materials results. This is probably compounded by the small sample size required for ICP.

The recycled sintered magnets with differing mean particle sizes were made using the same batch of HD powder so that the chance of a compositional variance between the starting sintered magnets should have been minimised.

10.4. Change in Oxygen and Nitrogen Content with Particle Size

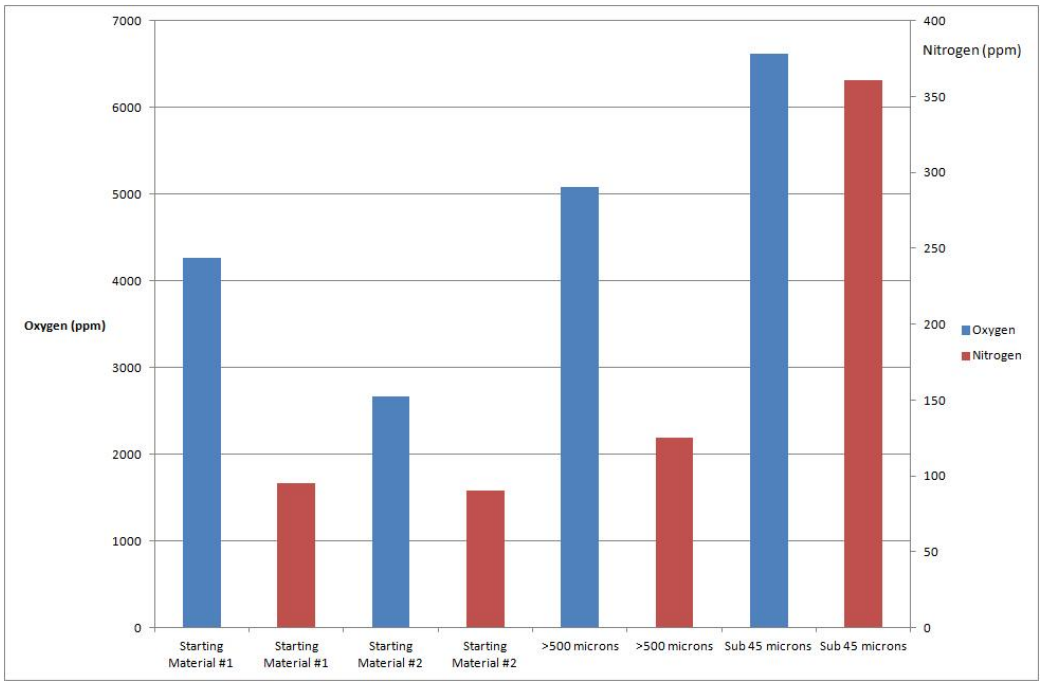

Fig.116. Oxygen and nitrogen content of the starting material and magnets made from powders with varying mean particle sizes.

All the sintered magnets were loaded into the furnace inertly. The nitrogen values are on the right and the oxygen values on the left. The results show a definite increase in the nitrogen and oxygen contents as the mean particle size is reduced.

10.5. Discussion on ICP Results

The ICP data showed a variance in the neodymium content of approximately 1 wt% between the two different starting material samples tested. Neodymium is not homogeneously spread throughout the microstructure of the magnet. As discussed previously the grain boundaries contain higher concentrations of Nd than the matrix phase. This could be why there was a difference between the neodymium content and the iron content given in the ICP results of the recycled magnets and the starting material. This is probably compounded by the small sample size required for the ICP analysis. The difference could also be due to a slight difference in composition between batches of magnets however this is less likely as the other alloying additions were very similar between the samples.

The recycled sintered magnets made from powders with differing mean particle sizes were made using the same batch of HD powder. The data shows a reduction in the neodymium content between the sintered magnets made with a mean particle size greater than 500µm and those made from powder less than 45µm.

An increase in oxygen and nitrogen content was also observed as the particle sizes were reduced (fig. 116). The increase in nitrogen with a reduction in particle size was observed by Li et al, (2009). They showed that, for powder with a mean particle size of 5µm, the nitrogen content was 250ppm. For a mean particle size of 3µm the nitrogen content rose to 940 ppm.

10.6. Discussion

The reduction in particle size of the HD powder was accompanied by a reduction in the final rare earth hydride desorption peak. The reduction of the peak is associated with oxidation or loss of the neodymium hydride phase. Williams et al, (1991) saw a similar reduction in peak height when HD powder was exposed to air.

The reduction in peak height and particle size also agrees with the work done by Li et al, (2009) who investigated the impact of the reduction in particle size on the magnetic properties. They showed that, as the particle size reduced, the oxygen and nitrogen content increased. They suggested that the oxidation of the rare earth rich phase was responsible for the reduction in properties.

The reduction in peak size was also observed when the powder was loaded inertly. If the reduction in peak height was purely due to the oxidation of the powder, it was expected that under these conditions there wouldn't be a noticeable reduction. The fact that a reduction was observed during inert loading leads to the possibility of the physical loss of neodymium during the processing of the powder.

The ICP results of magnets made from inertly loaded powder with varying mean particle sizes exhibited a reduction in the overall neodymium content of 0.78wt%. However, the neodymium content of the two starting material samples varied by 1 wt%. So whether some of the neodymium rich phase is lost during processing is uncertain. To gain a more definitive answer more samples need to be tested.

Chapter 11. Alloying Additions to Hydrogenated NdFeB

Sintered magnets with a typical composition of $Nd_{29}Fe_{66}Dy_{1.98}B$ ($Nd_{13.6}Fe_{79}$ $Dy_{0.8}B_{6.3}$ at %) were burr milled. The burr milled HD powder with a particle size of less than 75µm has been shown to produce reasonably consistent and repeatable particle size distributions, as seen previously in fig. 82. It was decided to use powder with a particle size distribution of less than 75µm because the combination of coarse and finer particles should lead to a better grain-density packing.

The ICP composition data for the powder with a particle size greater than 500µm and for the powder with a mean particle size of less than 45µm both show a composition close to stoichometry. The composition of the sub 45µm powder was $Nd_{13.5}Fe_{79.9}$ $B_{6.5}$ at% which is close to stoichometry $Nd_2Fe_{14}B$ ($Nd_{11.8}Fe_{82.4}B_{5.8}$ at %).

(wt%)	**B** **%**	**Dy** **%**	**Nd** **%**	**Pr** **%**	**Fe** **%**	**O** **ppm**	**N** **ppm**
ICP Starting Material #1	1.02	1.98	29.17	0.1	66.01	4265	95
ICP Starting Material #2	0.97	1.57	27.92	0.09	63.64	2665	90
ICP Sintered Less Than 45 µm	0.99	1.58	27.71	0.1	63.45	6620	361

Table 29. Compositional analysis of the starting materials.

The magnet made from sub 45µm powder exhibited higher oxygen and lower neodymium content that that of the starting material. Increases in oxygen content will reduce the effectiveness of the Nd rich phase for liquid phase sintering.

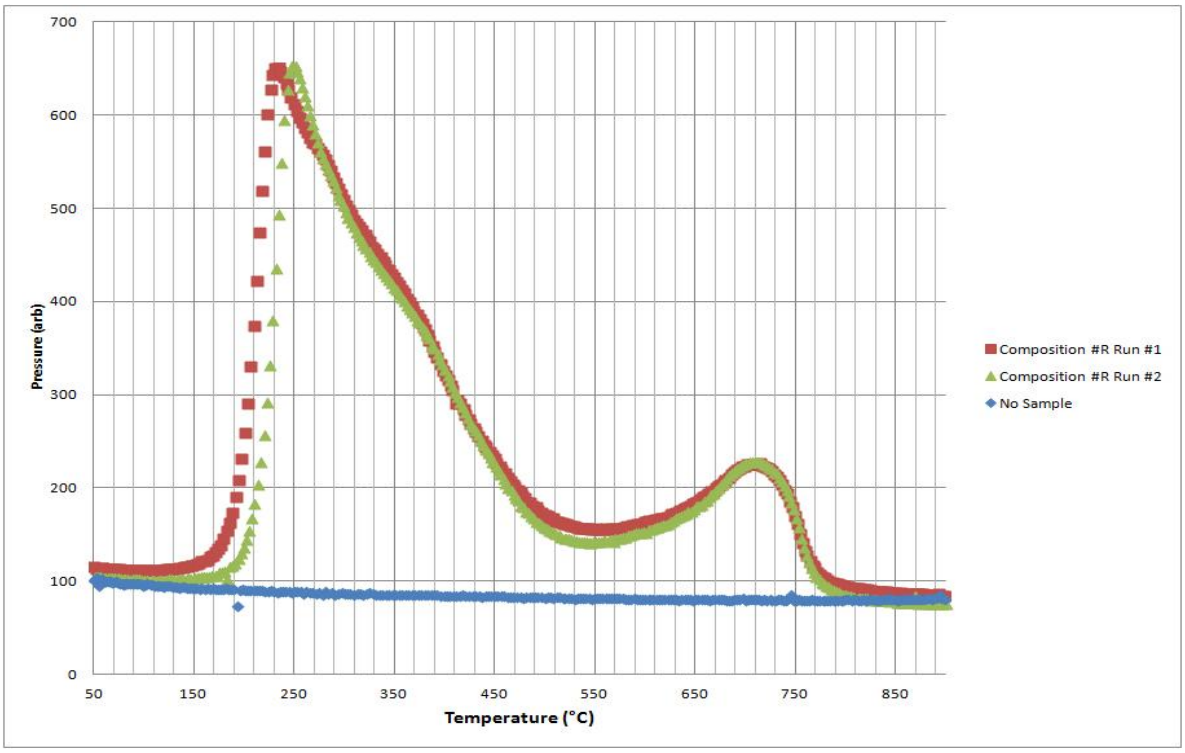

Fig.117. Two desorption runs of burr milled NdFeB with a particle size less than 75µm.

11.1. Microstructure

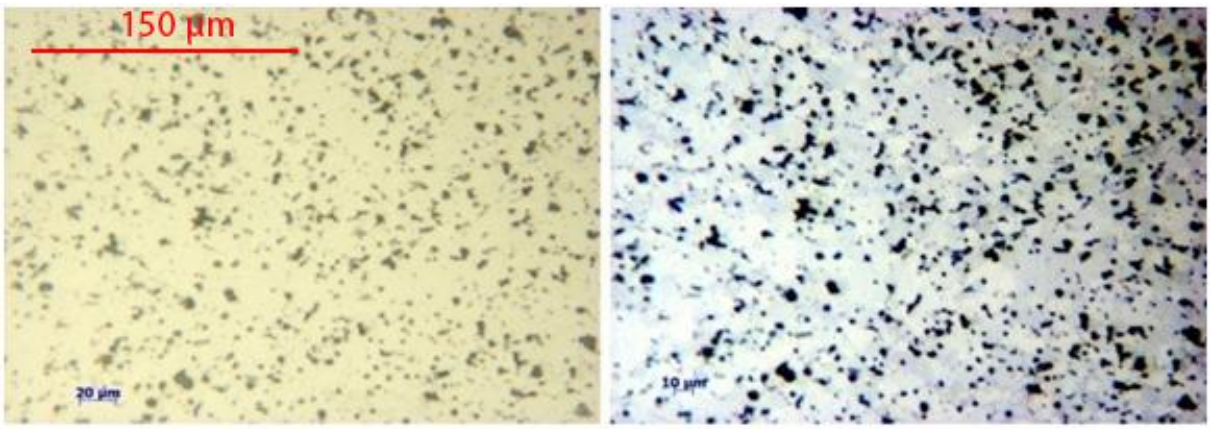

Fig.118. Microstructure of the starting material compared to that with no additions (Nd-rich phase appears dark purple when imaged with Kerr effect).

The black areas in the Kerr effect image (fig.18) show that the sintered starting material contains some porosity. The lighter purple areas are the neodymium rich phase.

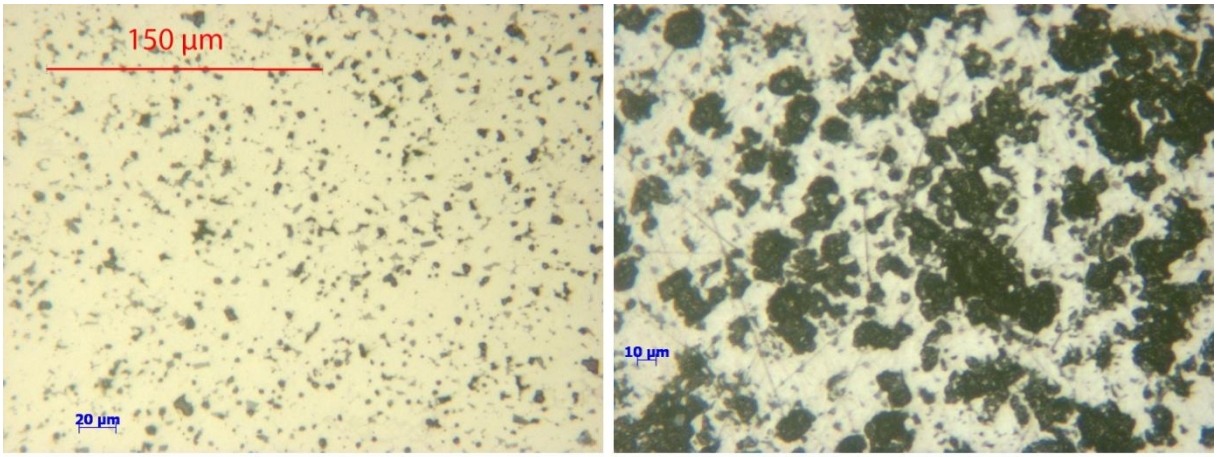

Fig.119. Micro structure of the starting material and the recycled magnet with no additions.

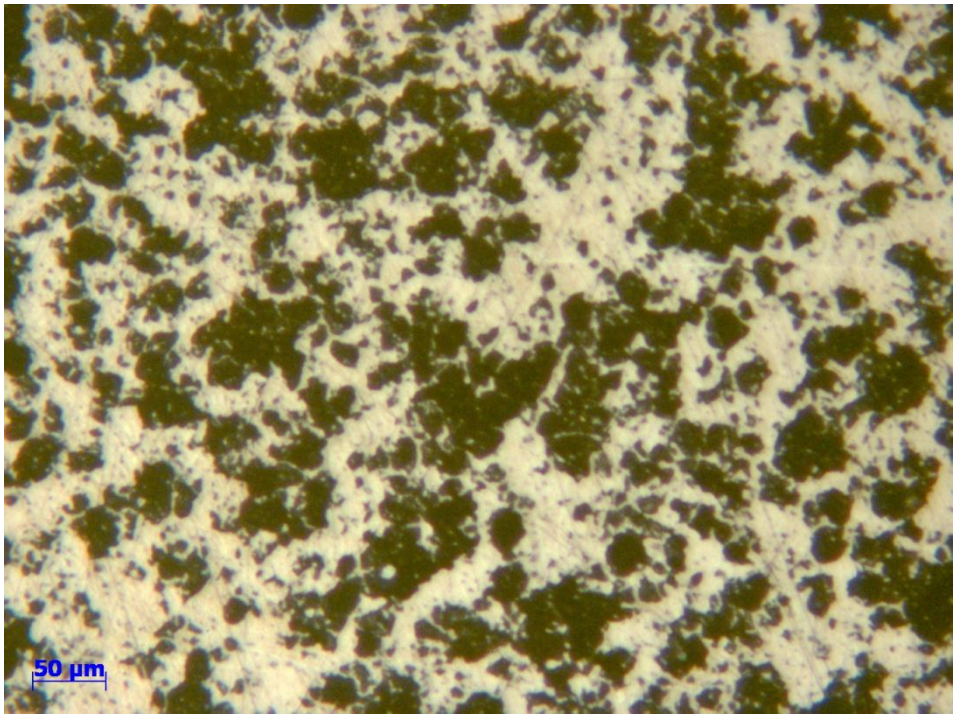

Fig.120. Microstructure of the recycled magnet with no additions (micron marker 50 µm).

The recycled material with no additions shows significantly more porosity, (figs.119 and 120).

11.2. Comparing Magnetic Properties

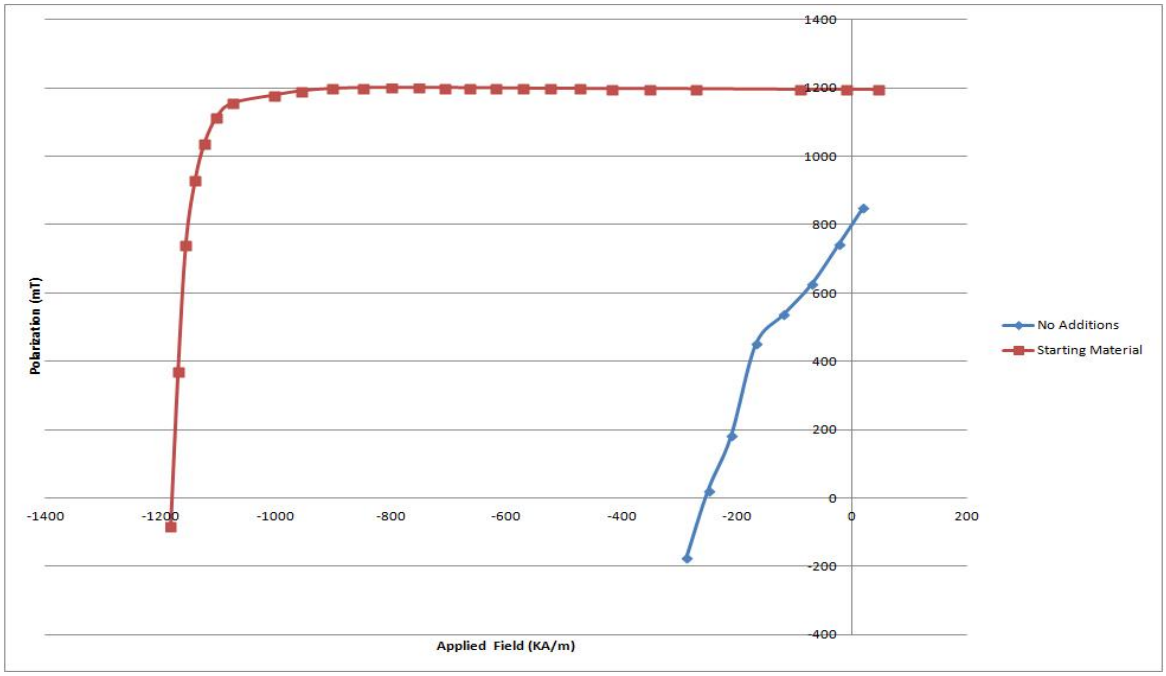

Fig.121. Comparison of demagnetisation curves.

	Density (g/cc) (±0.04g/cc)	**Coercivity** Hci **(KA/m) (±50)**	**Remanence Br (mT) (±0.06)**
Starting Material	7.53	1183	1195
Recycled No Additions	7.00	250	800

Table 30. Comparison of the starting material and the recycled material with no additions.

11.3. Discussion

The recycled magnets with no additions did not achieve full density. They only reached 7.0 g/cc (± 0.01g/cc) compared to the 7.5 g/cc of the starting material. Fig. 120 shows the typical microstructure of the recycled sintered magnets, significant porosity was observed.

The reduction in the density is likely to be due to insufficient Nd-rich phase present to form a liquid phase. The lack of the neodymium-rich phase is likely to be a result of corrosion. Fig. 120 shows the degree of porosity compared to that of the starting material.

Work done by Zakotnik et al, (2008) has shown that the addition of neodymium hydride recovered much of the magnetic properties of the recycled NdFeB sintered magnets.

Chapter 12. Neodymium Hydride Additions

Previous work has been carried out on the intergranular additions of neodymium hydride to HD powder from NdFeB, (Mottram and Harris1998). Zakotink et al, (2008) added 1 at % neodymium hydride to gain improvements to the recycled material from hard disk drive magnets with a composition $Nd_{13.78}$ $Fe_{75.51}Dy_{0.66}B_{6.3}$ at%. This composition is close to the composition of the sintered magnets being used in this work ($Nd_{13.6}Fe_{79}$ $Dy_{0.8}B_{6.3}$ at %).

As seen previously, sintering the recycled milled powder at 1060°C for one hour did not produce a fully dense magnet. To achieve full density neodymium hydride was added until the density increased to close to that of the starting material. The neodymium hydride was added in 1at% increments.

The $NdH_{\sim 3}$ additions should increase the amount of Nd-rich phase so increased densification occurs. The increase in $NdH_{\sim 3}$ should also lead to an increase in the magnetic properties of the sintered magnets. The $NdH_{\sim 3}$ was produced by hydriding at room temperature and then milling in cyclohexane for 20 hours. The milled powder was dried under a vacuum and stored in a glove box. The $NdH_{\sim 3}$ was added as an intergranular blending addition to the burr milled powder. It was added during the weighing stage and then both were passed through a 90µm sieve. The sieving stage was repeated twice to mix intimately the hydride with the burr milled powder.

As described previously, the samples were loaded into rubber isostatic tubes and sealed in the glove box. The samples were pulse aligned and then pressed. The green compact was then loaded in air into the vacuum sintering tube and the tube evacuated. The samples were heated at a rate of 7°C / min and then sintered at approximately 1060°C ± 5°C.

12.1. Desorption of Recycled Magnets with Increasing Additions

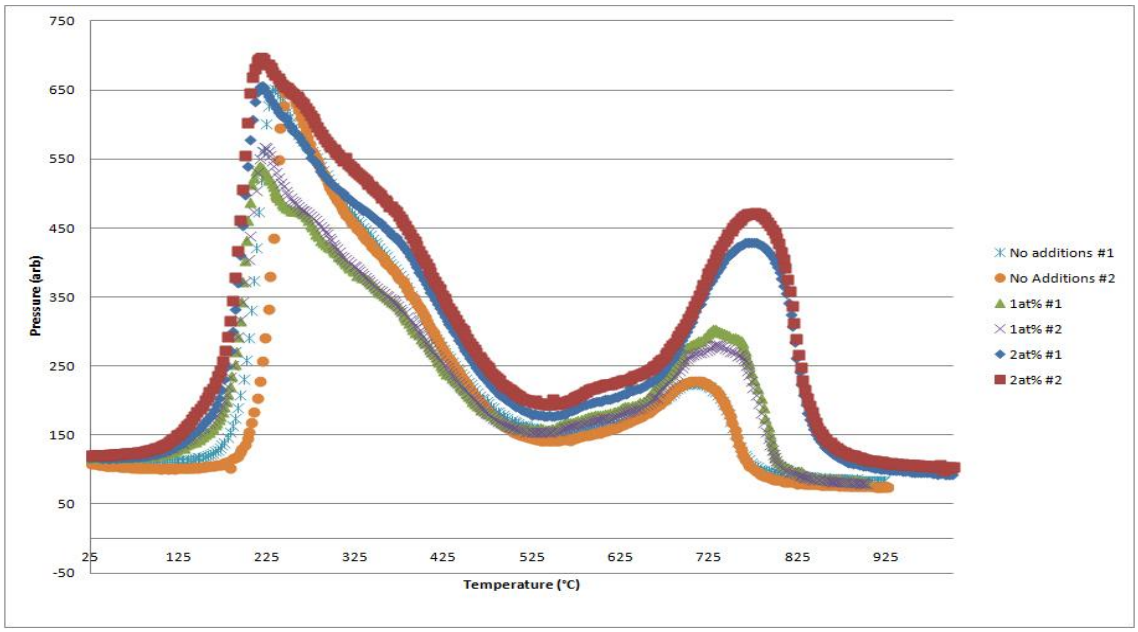

Fig.122. Desorption traces obtained with increasing alloying additions of $NdH_{\sim 3}$.

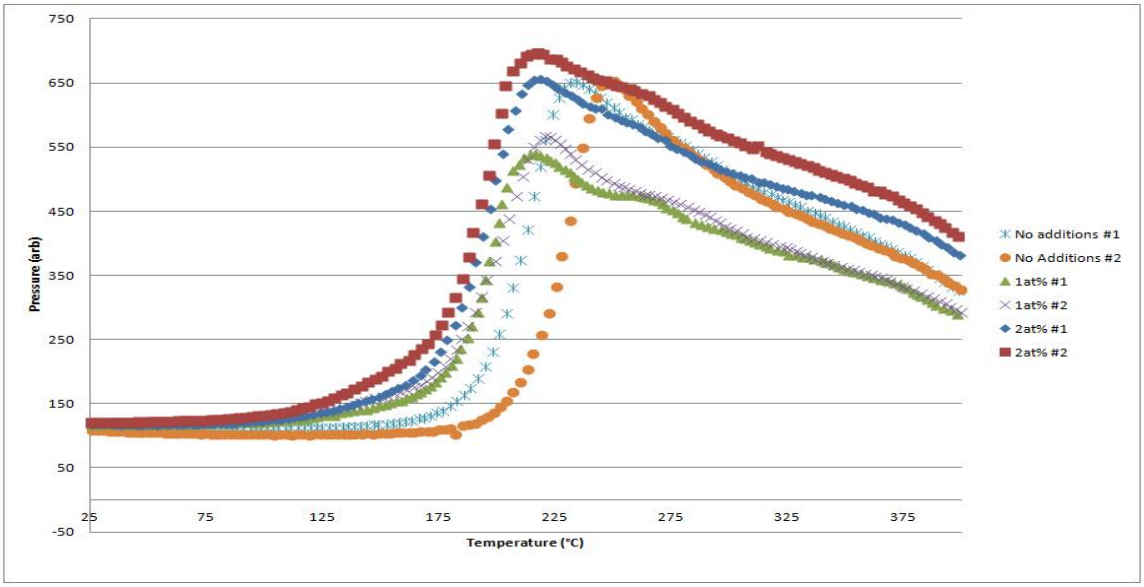

Fig.123. Initial desorption peak with increasing alloying additions.

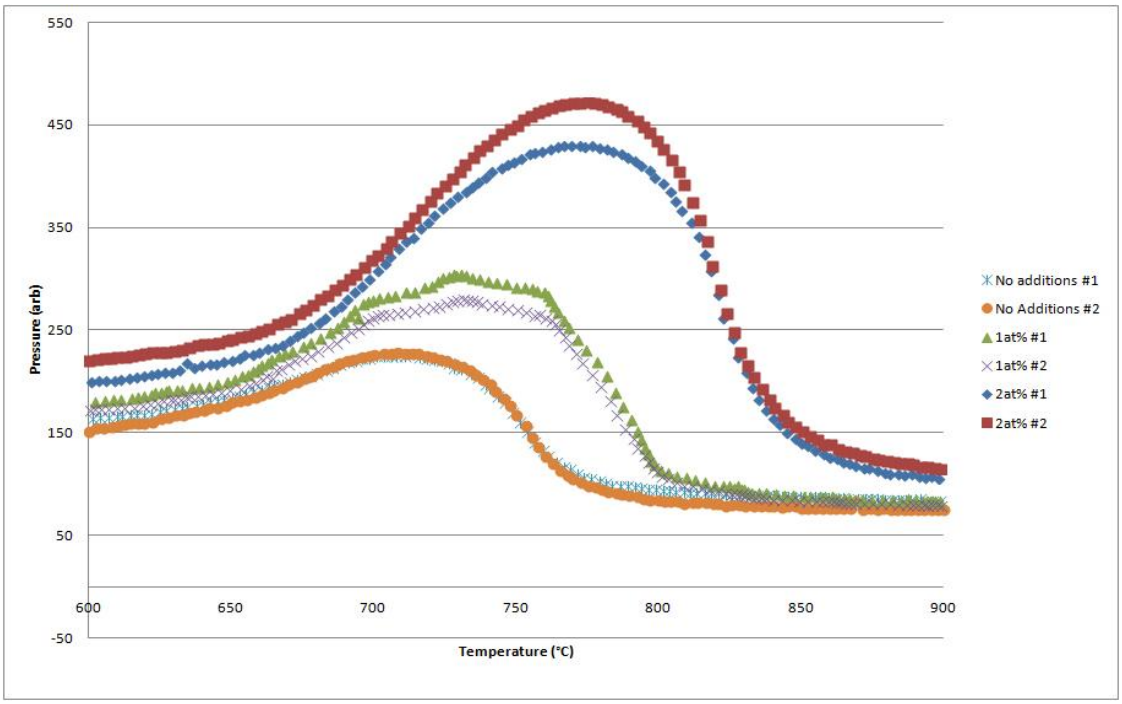

Fig.124. Increase in final peak height with increasing $NdH_{\sim 3}$ additions.

From Fig.124 it can be seen that, as the additions are increased, the magnitude of the peaks increase.

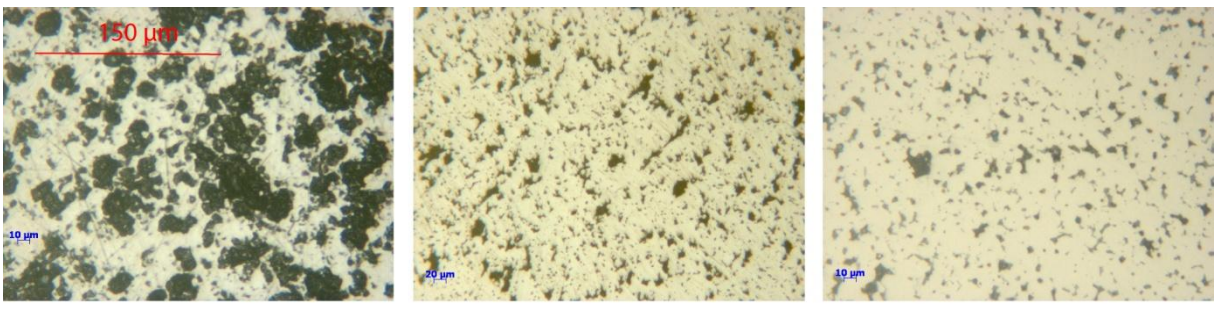

Fig.125. A reduction in porosity due to increasing alloying additions.

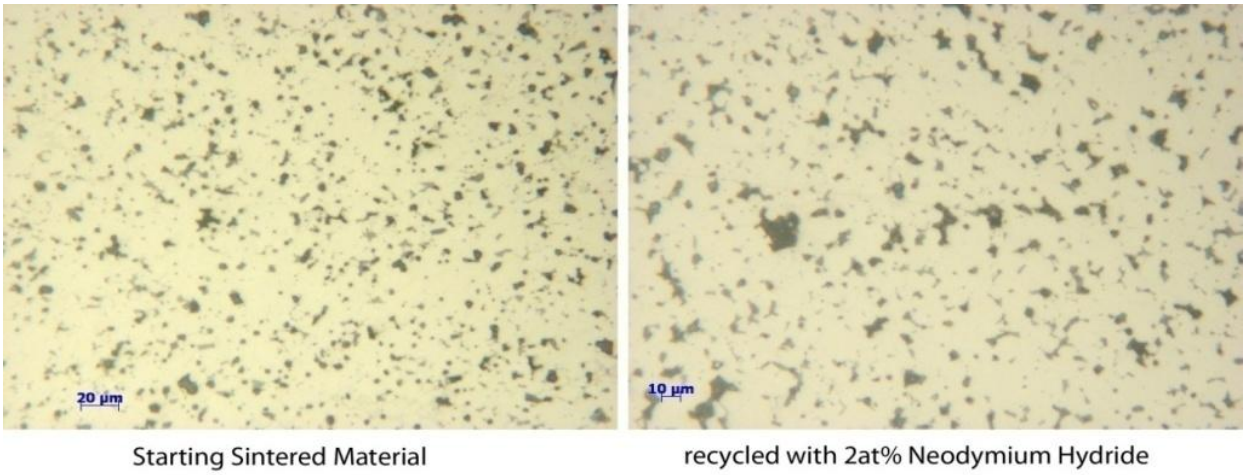

Fig.126. Comparison between the starting material and the sample with 2at% $NdH_{\sim 3}$ added, micron marker span 20µm and 10µm.

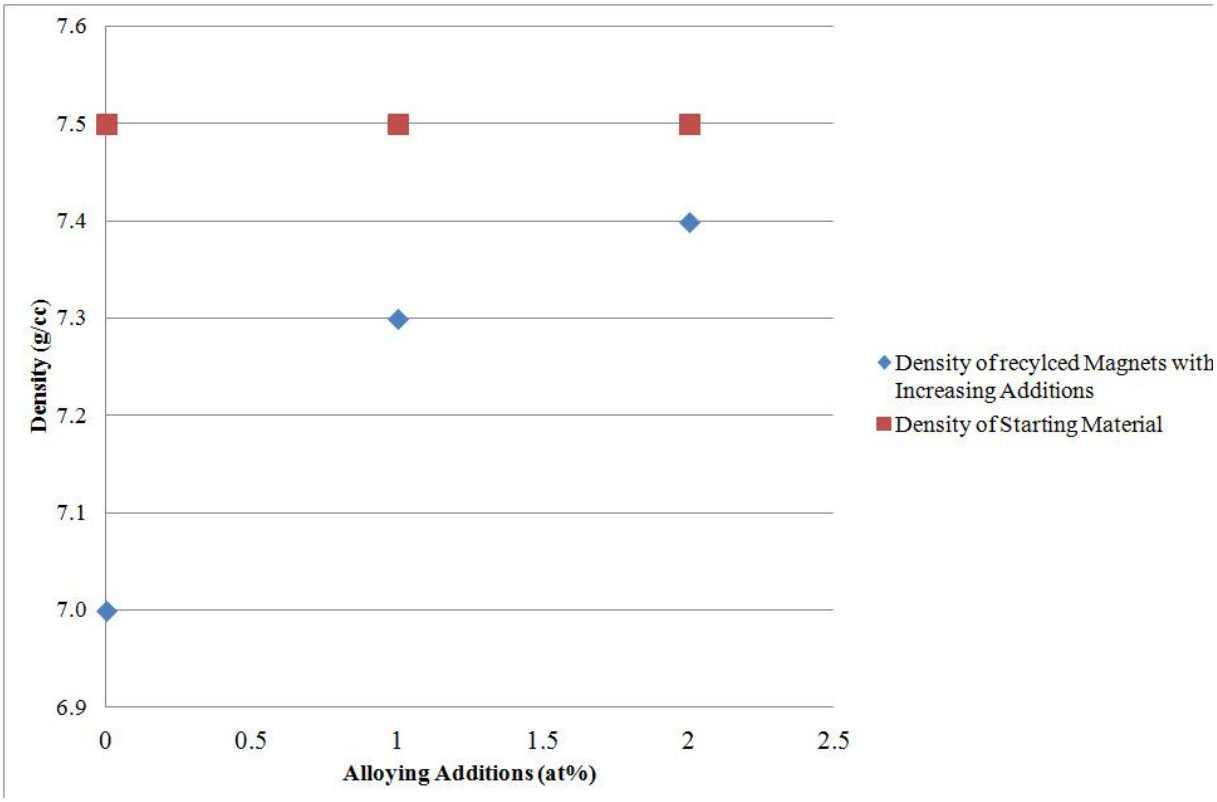

Fig.127. Density increase with alloying additions.

12.2. Improvement in the Magnetic Properties with $NdH_{\sim 3}$ Additions

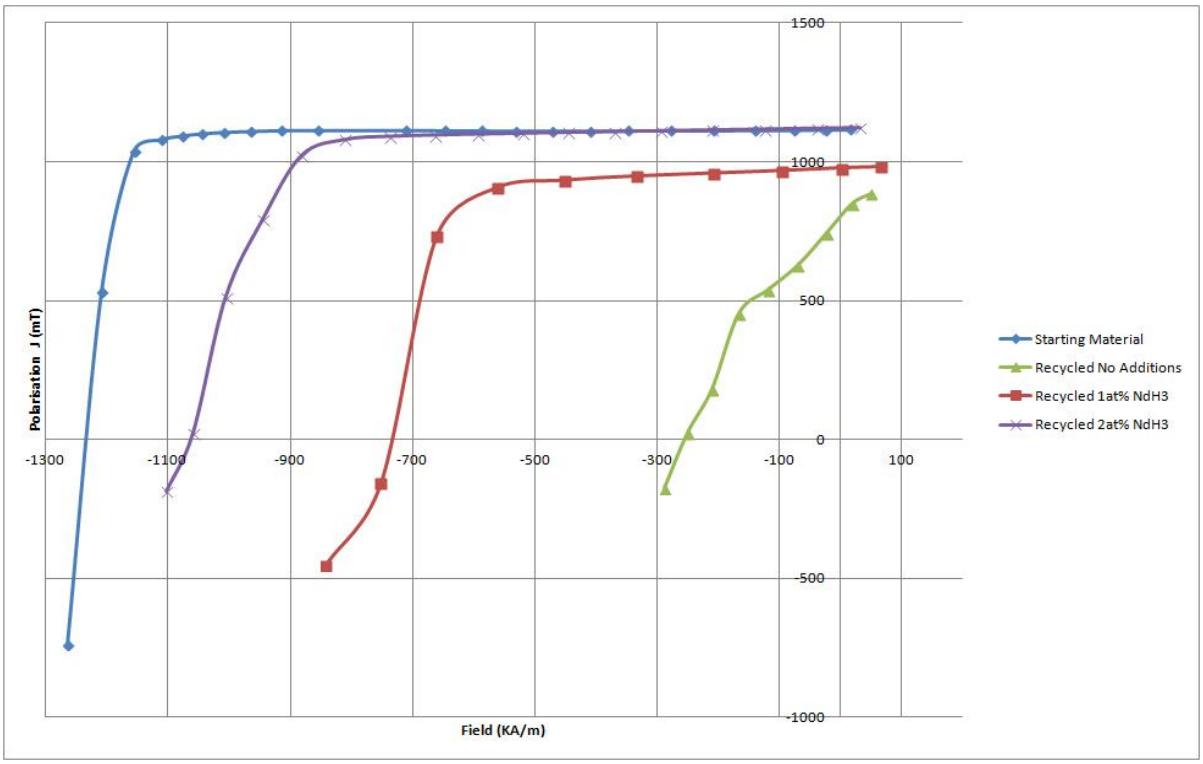

Fig.128. Demagnetisation curves with increasing alloying additions.

	Density (g/cc)	Coercivity iHc (KA/m)	Remanence Br (mT)
Starting Material	7.5	1183	1195
Recycled No Additions	7.0	250	800
Addition of 1at%	7.3	730	970
Addition of 2at%	7.4	1059	1123

Table 31. Samples comparison of density, coercivity and remanence. The errors associated are as follows Remanence: (mT) (±50) Coercivity (kA/m) (±50) Density (g cm^{-3}) (±0.05).

12.3. Discussion

The addition of intergranular $NdH_{\sim 3}$ had a definite impact on reducing the porosity. The increase in the magnitude of the final desorption peak in fig. 124 shows that more neodymium rich phase is present. The increase should lead to improved liquid phase sintering and mass transport, resulting in increased density. The increase in density and reduction in porosity can be seen in the microstructure. The recycled samples with 2at% neodymium hydride showed a similar degree of porosity to that of the starting material. The increase in density and reduction in porosity is in agreement with the work by Zakotnik et al, (2008). They showed that the addition of neodymium hydride improved the density of recycled sintered magnets that were recycled multiple times. The final desorption peak increases with $NdH_{\sim 3}$ additions and this is to be expected because the final peak is the transformation from $NdH_{\sim 2}$ to Nd + H_2. (Williams,1991)

As seen with the desorption of milled neodymium hydride, the desorption start temperature is much lower than those reported in the literature (Ryan and Coey 1985, Harris et al 1987, Williams et al 1991, Yartys et al 1997, and Yoshihiro et al 2001). The powder with no additions starts desorbing at 185°C and 200°C. This is much higher than the 70°C start temperature for the samples with added neodymium hydride, (fig. 122).

The observed increase in the evidence of the early peak is likely to be due to the formation of $Nd(OH)_3$ in the neodymium hydride, (Williams 1991, Verdier et al 1994 and Katter et al 2001). The difference in peak heights observed for the samples desorbed with intergranular additions is likely to be due to measurement errors in weighing the $NdH_{\sim 3}$ powder or possibly due to the formation of $Nd(OH)_3$ during loading. As expected, the increase in the Nd-rich phase improves the final density of the magnets. This leads to improvements in the magnetic properties, and these can be observed in fig. 128.

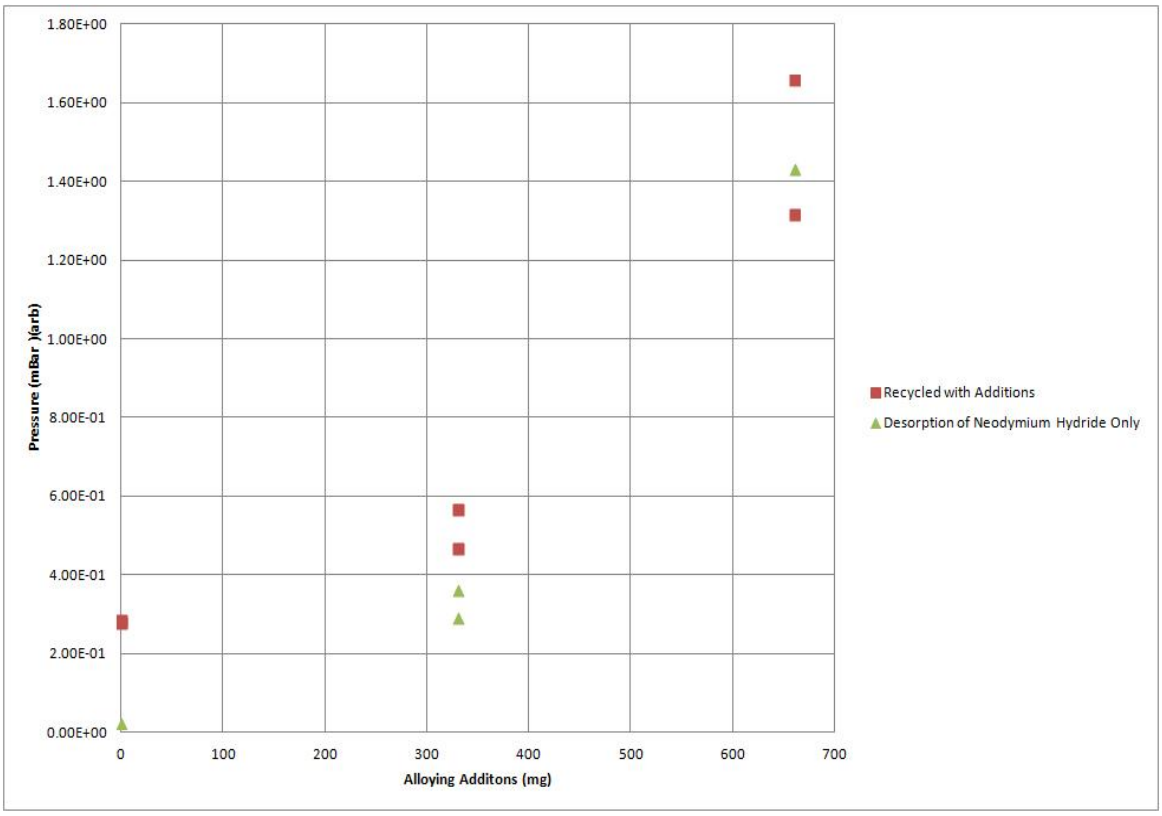

Fig.129. Maximum peak heights for samples with varying additions of $NdH_{\sim 3}$ and 15g green compacts with the corresponding amounts of $NdH_{\sim 3}$ added. The two sets of data increase at a similar rate.

Recycled With Additions			
Mass of Additions (mg)	**Pressure (arb)**	**Pressure (mBar)(arb)**	**Temperature (°C)**
0	227	2.79E-01	713.75
0	229	2.85E-01	708
330	304	5.66E-01	728.25
330	281	4.68E-01	731.25
660	430	1.32E+00	766.75
660	473	1.66E+00	775.25

Table 32. Correlation between the maximum peak height and mass of $NdH_{\sim 3}$ added to milled HD powder.

Desorption of Neodymium Hydride Only			
Mass of Powder (mg)	**Pressure (arb)**	**Pressure (mBar) (arb)**	**Temp (°C)**
0	81	2.28E-02	
330	253	3.62E-01	764.5
330	231	2.91E-01	778.75
660	445	1.43E+00	774.75

Table 33. Maximum peak heights for the desorption of $NdH_{\sim 3}$

Fig.33 shows the maximum peak height for varying additions of $NdH_{\sim 3}$ and 15g green compacts with the corresponding amounts of $NdH_{\sim 3}$ added. The two sets of data increase at a similar rate. The recycled material tends to show slightly higher peak heights than the maximum peak for neodymium hydride only. It would have been expected that a slightly higher peak would have been observed for the hydrogenated powder plus additions. This is because the HD powder with no additions still shows a peak, indicating a presence of the Nd-rich phase. The lower than expected peak height for the HD powder plus additions could be due to discrepancies during weighing the powder. Reactions with air could also be the cause of the lower than expected peak heights. The results show that it should be possible to infer the amount of Nd-rich phase present from the maximum peak height or the integral of the NdH_2 to Nd and H_2 desorption peak.

12.4. Increase in Coercivity

The intrinsic coercivity of the material with additions of 2at% $NdH_{\sim 3}$ was lower than that of the starting material. It is likely that the reduction in coercivity could be due to some grain growth during sintering. To investigate further, the sample was etched using 5% citric acid solution and subsequently image analysis was performed.

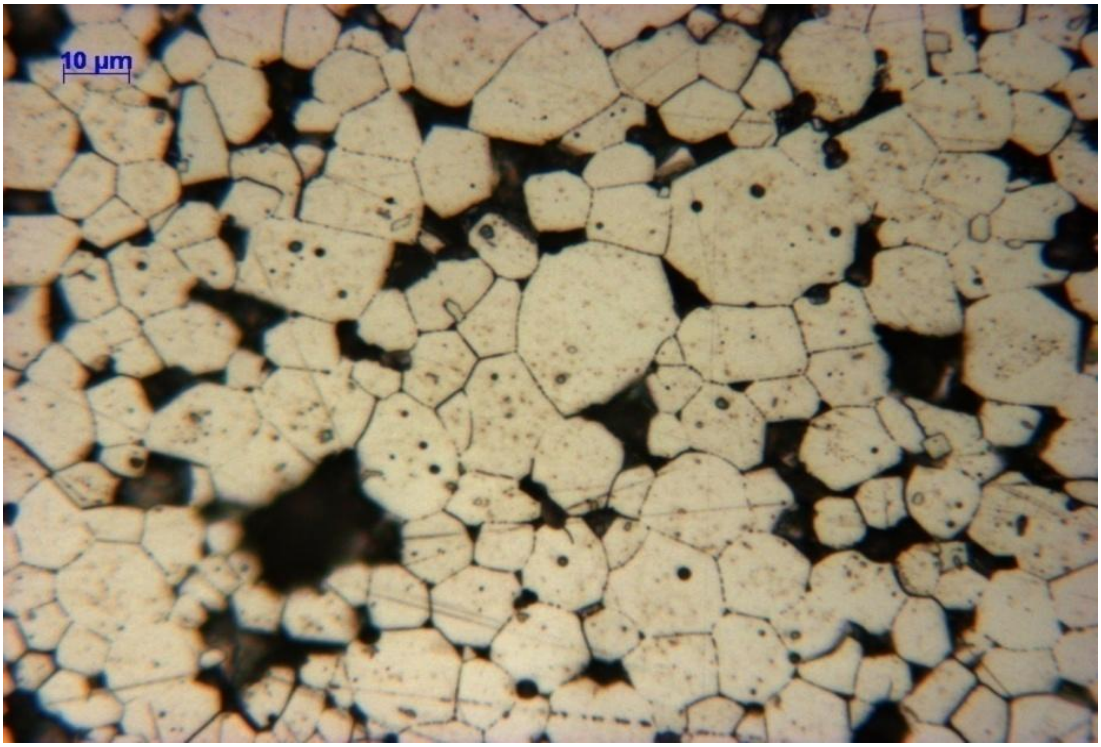

Fig.130. Typical etched sample showing grain size from sintered magnets with 2at% Neodymium Hydride Additions. The larger dark patches indicate porosity. The smaller dark patches likely to be as a result of removal of the Nd rich phase.

	Average (µm)	**Max (µm)**	**Min (µm)**	**Median (µm)**	**Mode (µm)**	**SD**
Starting #R (541)	8.3	26	2	8	7	3.37
0hrs 2at% (712)	11.29	32	2	11	10	4.88

Table 34. Comparing grain size in different samples, ±0.5µm.

Image analysis of the grain size data shows an increase in the mean grain size from approximately 8.3µm of the starting material to 11.29µm. The mode has also increased from 7 to 10µm.

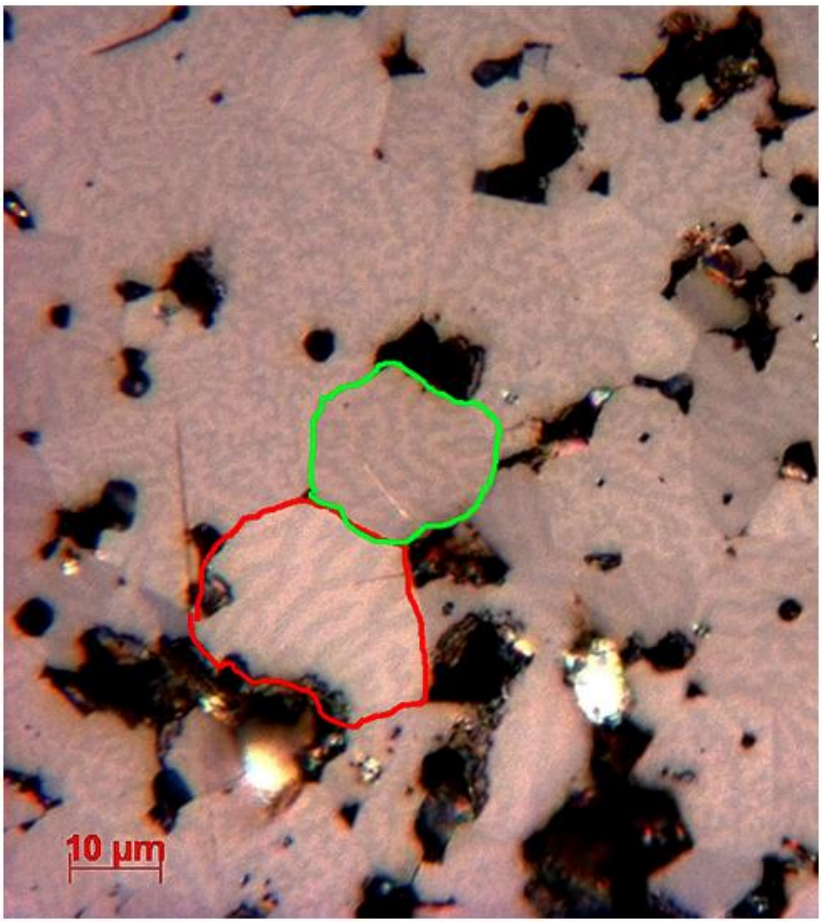

Fig.131. Kerr effect imaging showed evidence of misalignment of grains.

Prior to sintering the powder was aligned in a magnetic field. During alignment the powder particles should rotate and align with the field so that the c axis is parallel to the applied field. If the powder consists of single grains the individual grains should align with their c axis parallel to the applied field. In the case of polycrystalline particles consisting of multiple grains, they should all be aligned in the original magnet and hence become aligned in the presence of a magnetic field.

With polycrystalline particles the degree of alignment will depend on the number of grains with similar alignment and the size of these grains. For example, a polycrystalline particle

might consist of five grains, three of which have similar alignment and two with a greater degree of misalignment. Under an applied field the whole particle will rotate to align the three particles similarly aligned with the field, at the expense of the two grains with a greater difference in alignment from the other three. However the degree of alignment of magnets made from polycrystalline powder is likely to be lower than those made from single grain particles.

Kerr effect microscopy shows the magnet surface perpendicular to the c-axis. In fig. 131, a cog wheel pattern should be visible for grains imaged perpendicular to the easy axis of magnetization, (the c-axis). In grains that are parallel to the easy axis, the domains are seen as stripes. If there is perfect alignment, all the grains should show the cog wheel pattern. The presence of grains with stripes or a distorted cog-wheel would show that there is a degree of misalignment. Any misalignment of the grains leads to a lowering of the remanence.

12.5. Overall Discussion

The additions of neodymium hydride to the HD powder prior to sintering showed an increase in the final desorption peak that relates to desorption from the neodymium rich phase. As seen with the milled neodymium hydride, the desorption start temperature was much lower than the values reported in the literature (Yartys et al,1997). The increase in the area of the early peak is likely to be due to the formation of Nd $(OH)_3$ in the neodymium hydride additions (Williams 1991, Verdier et al 1994 and Katter et al 2001).

The powder with no additions starts desorbing hydrogen at a higher temperature, fig. 123. The difference in peak heights observed for the samples desorbed with intergranular additions is likely to be due to measurement errors in weighing the $NdH_{\sim 3}$ powder. Increasing the amount of intergranular neodymium hydride resulted in an increase in the magnitude of the final peak.

The density of the magnets increased with increased $NdH_{\sim 3}$ additions and the microstructure of these magnets also displayed a reduction in porosity. The increase in density and accompanied reduction in porosity is in agreement with the work reported by Zakotnik et al, (2008). They showed that the addition of neodymium hydride improved the density of recycled sintered magnets and that these were capable of being recycled multiple times. The magnetic properties were also improved by the intergranular addition of neodymium hydride. The best results achieved were with the intergranular addition of 2at% neodymium hydride.

	Density (g/cc)	**Coercivity iHC (KA/m)**	**Remanence Br (mT)**
N30 Grade (minimum values)		955	1120
N33 Grade (minimum values)		955	1170
Starting Material	**7.5**	1183	**1195**
Recycled No Additions	**7.0**	250	**800**
Recycled 1at%	**7.3**	730	**970**
Recycled 2at%	**7.4**	1059	**1123**
Recycled 2at% Annealed	**7.4**	1182	**1127**

Table 35. Comparing recycled magnets with commercial magnet grade specifications. Errors associated are as follows Remanence: (mT) (±50) Coercivity (kA/m) (±50) Density (g cm^{-3}) (±0.05).

Table 35. shows the coercivity and remanence obtained from the recycled nominal specifications for N30 and N33 grade NdFeB magnets. NdFeB magnets are graded by properties with minimum and nominal properties to provide a specification for customers. As the magnet grade increases the magnetic properties of the magnet increase.

From the table it can be seen that the magnetic properties of the recycled magnet with 2at% additions are greater than the values for the minimum properties to be classified as grade N30.

It should be noted that this has been achieved without a post sintering annealing treatment which should result in an additional improvement, (Vial et al, 2002).

To investigate the potential improvements on annealing, the sample with 2at% additions shown in table 35 was annealed at 520°C for one hour. This resulted in an increase in coercivity of approximately 120 KA/m (~12 % increase).

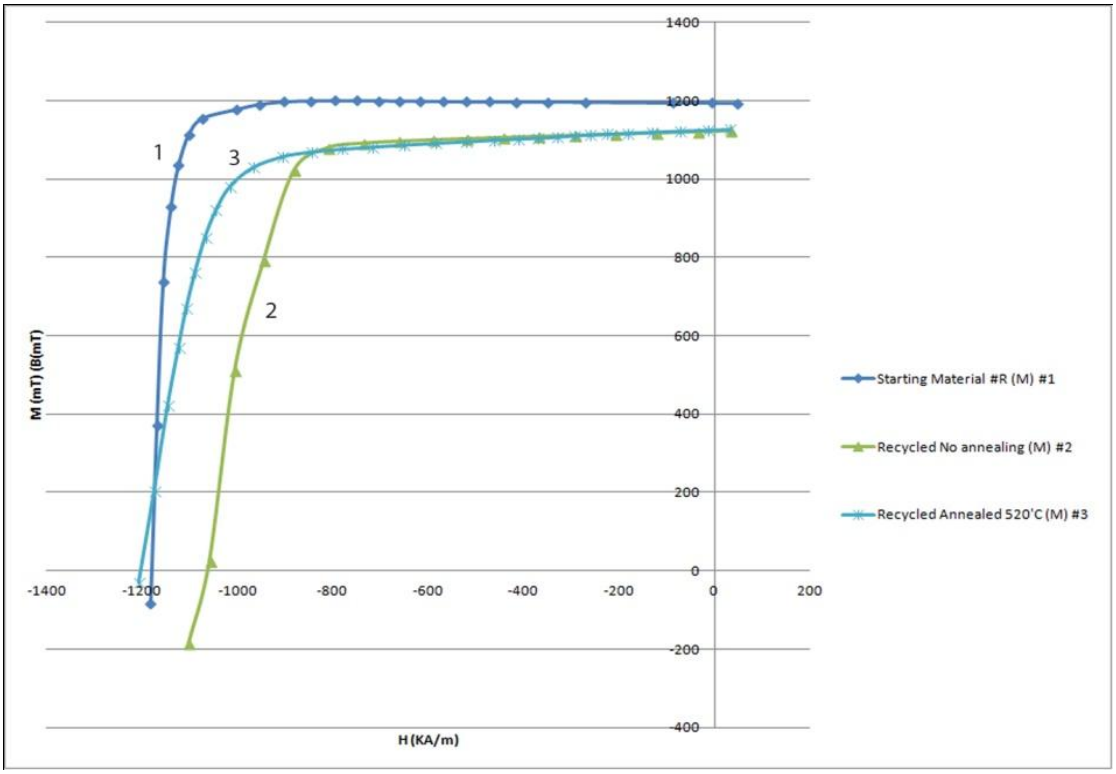

Fig.132. An increase in intrinsic coercivity, resulting from annealing for 1hour at 520 °C.

There is potential to improve the magnetic properties further by calculating an optimum annealing profile (Vial et al, 2002). The grain size analysis of the magnets with 2at% additions showed evidence of grain growth and an increase of the mean grain size from approximately 8µm for the starting grain size to approximately 11µm. Reducing the mean particle size further would lead to a smaller average grain size, further increasing the intrinsic coercivity.

Plotting the final peak height with additions and comparing this with desorption height for known masses of neodymium hydride (fig. 129), showed that generally, the maximum peak heights for a given mass of additions were higher than the peak height of desorption of neodymium hydride alone.

However it would have been expected that the alloying addition plots would be higher, as they would have started out with more neodymium rich phase present. The discrepancy could also be due to reaction with the air or measurement errors in weighing the neodymium hydride (± 5mg). The remanence could be increased by improved alignment of the powder and this could be achieved either by optimizing the particle size distribution and / or by increasing the aligning field.

The addition of 2at% $NdH_{\sim 3}$ achieved a density of 7.4g/cc, very close to that of the starting material (7.5g/cc). The remanence of the samples with 2 at% was very close to that of the starting material 1123mT and 1195mT respectively. Further additions of neodymium hydride would reduce the remanence, due to time constraints further additions of NdH~3 were not added.

Chapter 13. Exposure of Hydrogenated NdFeB Powder to Air

Burr milled powder from hydrogenated sintered magnets with a composition of $Nd_{29}Fe_{66}Dy_{1.98}B_{wt\%}$ ($Nd_{13.5}Fe_{79}$ $Dy_{0.8}B_{6.3\ at\%}$) was exposed to air for varying times to investigate the impact of exposure to air on the final desorption peak. Alloying additions were added to investigate the potential for the recovery of the properties of the powder exposed to air.

It has been seen that a reduction in the particle size resulted in a reduction in the peak height for the $NdH_{\sim 2}$ to Nd and H_2 desorption event. Alloying additions have been shown to improve the density and magnetic properties. It is thought that the improvement in properties is due to the increase in liquid phase (Zakotnik et al, 2008).

Two sets of samples were exposed at the same time for each air-exposure to ensure that the exposure environment was the same for the powder with and without alloying additions. So the same temperature and humidity profile will have been observed by both sets of powder.

13.1. Exposure of HD Powder over Time

Powder was exposed to air for varying times and each 15g batch of powder was pressed into green compacts and then sintered with desorption of the hydrogen monitored using the thermomanometric system. The samples were sintered at approximately 1060°C for 1 hour. The ramp rate for the samples was set at 7°C per minute. All the samples were furnace cooled so they will have experienced the same cooling rate.

The HD powder was processed, as described previously using the burr milling technique. The powder was loaded into specimen tubes for exposure. The calculation of the density of the powder based on the volume of the specimen tubes is calculated below.

Specimen tube Radius (cm)	Cross sectional Area (cm^2)	Powder Height (cm)	Mass Of Powder (g)	Density (g/cc)
1.14	4.08	1.25	15	2.94
1.14	4.08	1.26	15	2.89
1.14	4.08	1.30	15	2.83
Average Density	(g/cc)	2.9		

Table 36. Comparison of densities of powders exposed to air.

Specimens were exposed to air for the varying times. Ideally, the exposure process could have been more controlled but, unfortunately there is no data on the humidity experienced by these samples during exposure and no accurate data on the range of temperatures the samples observed. Some of the samples were exposed for over 24 hours and the temperature is likely to have varied over that time period. One of the two samples was degassed and sintered with no additions, the other had additions of $NdH_{\sim 3}$ added prior to aligning and isostatic pressing. Both samples would have seen the same temperature and humidity so should have had the same level of exposure.

Once the exposure time was complete, the samples were transferred into a glove box under an argon atmosphere. The oxygen content of the glove box was always below 100 ppm and typically at 50 ppm. One of the samples was loaded in an isostatic bag and aligned and pressed and sintered as described previously. The other sample was blended with 2 at% $NdH_{\sim 3}$ prior to aligning and pressing. None of the samples were loaded inertly. The intergranular additions added were in the form of $NdH_{\sim 3.}$

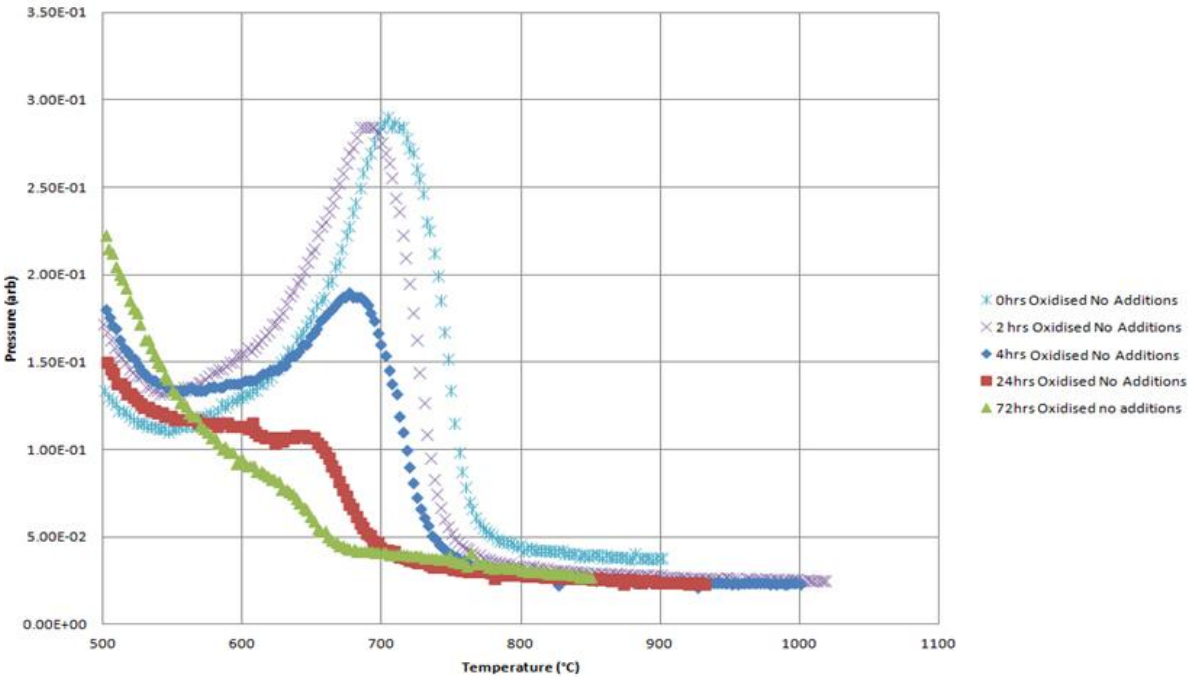

Fig.133. Reduction in the final desorption peak with oxidation time.

As the exposure time progresses the magnitude of the final peak reduces such that, by 72 hours virtually no peak is visible.

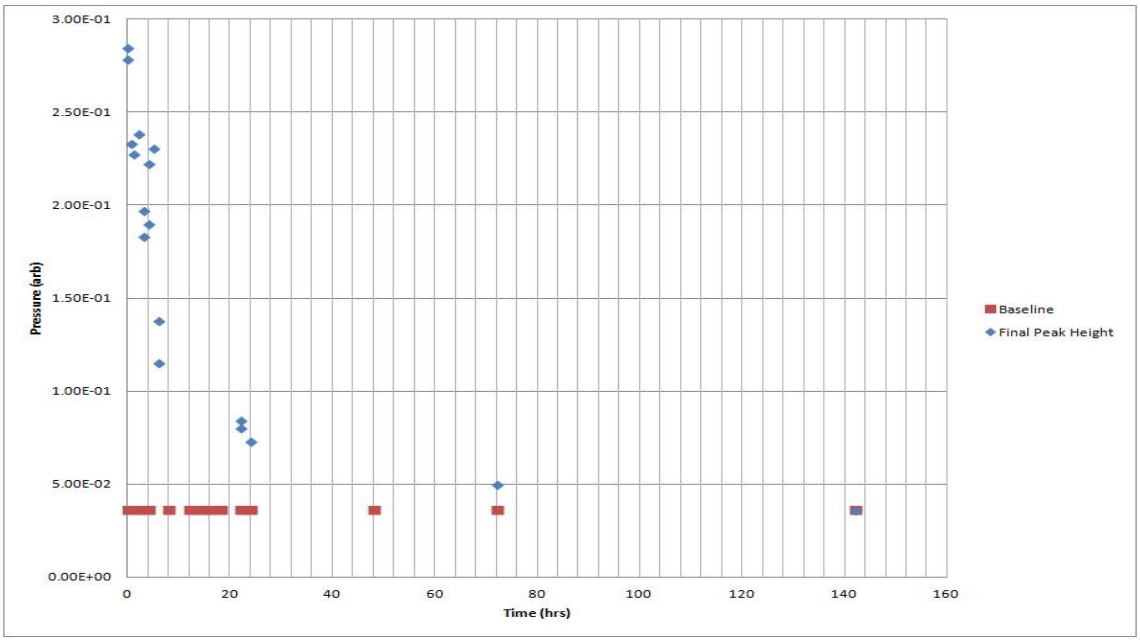

Fig.134. Reduction in maximum peak height with oxidation time.

The maximum peak height decreases with time, such that by 72 hours, the final peak has almost disappeared.

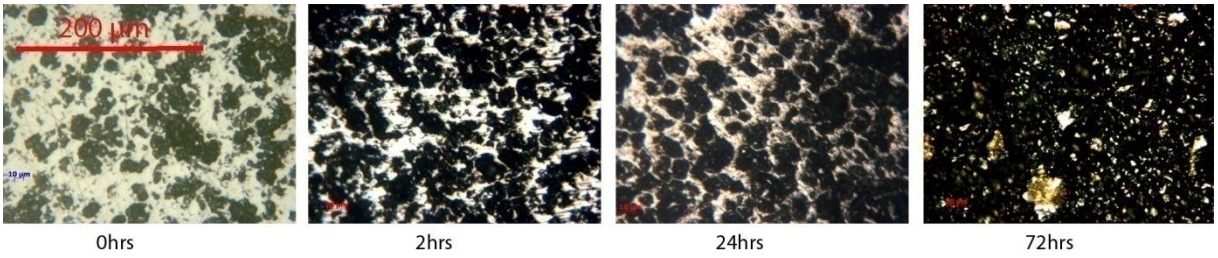

Fig.135. Increase in porosity with increased exposure times (magnification 20x).

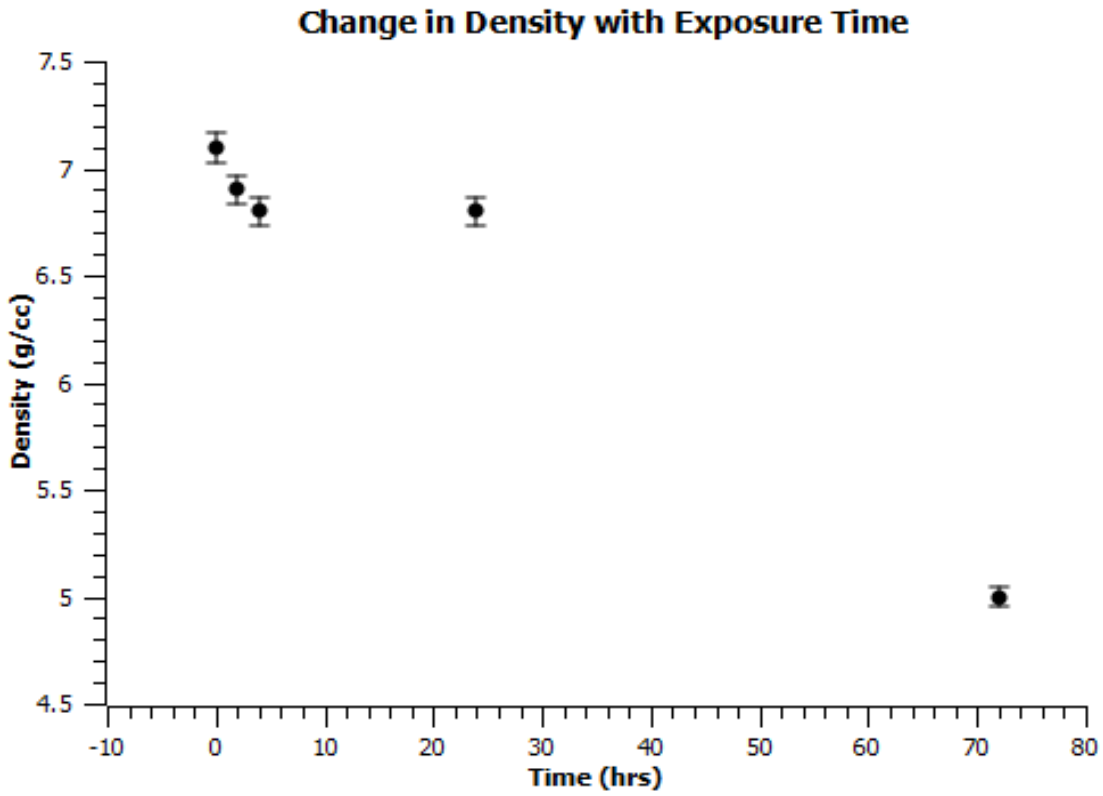

Fig.136. Density vs. exposure time graph.

No Additions			
Exposure Time (hrs)	Coercivity iHc(KA/m)	Remanence Br (mT)	Density (g/cc)
0	378	880	7.1
2	122	400	6.9
4	18	447	6.8
24	0	0	6.8
72	0	0	5

Table 37. Data showing effects associated with differing exposure times. Errors associated are as follows Remanence: (mT) (±50) Coercivity (kA/m) (±50) Density (g cm^{-3}) (±0.05).

13.2. Discussion on Desorption Behaviour of Hydrogenated NdFeB Powder Exposed to Air

The desorption of the powder exposed to air with a composition $Nd_{29}Fe_{66}Dy_{1.98}B$ wt% ($Nd_{13.5}Fe_{79}$ $Dy_{0.8}B_{6.3}$) shows a clear reduction in peak height with exposure time. This can be seen in fig. 133 and fig. 134. Complete loss of the final peak was observed to have taken place by around 75 hours. This is in broad agreement with Verdier et al, (1994). They exposed fully hydrogenated alloys based on composition $Nd_{l5}Fe_{77}B_{8,}$ to air and recorded the mass increase. They showed that the increase in mass ended at between 50 and 100 hours.

They also repeated this experiment for pure neodymium hydride and again, there was no subsequent mass increase at between 50 and 100 hours.

The desorption data shows that the hydrided Nd-rich phase is not very stable in air, transforming from NdH_3 to $Nd(OH)_3$. The images of the microstructure in fig. 135 show that the porosity of the material increases as the exposure time increases. The density measurements support this statement, with a reduction from a starting density of 7.1 g/cc to

5g/cc at 72 hours. As discussed previously the Nd-rich phase is key for liquid phase sintering to occur. The reduction in the density and the lack of Nd-rich phase isolating the $Nd_2Fe_{14}B$ grains results in lowering of both the density and the magnetic properties.

Chapter 14. Additions of Neodymium Hydride to Powder Exposed to Air

Intergranular additions of neodymium hydride by Zakotnik et al, (2008) have been shown to improve the properties of mildly corroded powder. To investigate whether the same improvements in density and magnetic properties can be seen for powder exposed to air for a prolonged period, intergranular alloying additions were blended with the powder.

As described previously two batches of the HD powder observed the same environmental profile. The amount of neodymium hydride added to the powder exposed to air was kept at a constant 2at% throughout. The total mass of powder including additions was approximately 15.0g.The powder and the additions were passed through a 90µm sieved twice to intimately mix the powder.

14.1. Powder Exposed to Air for 2 hours

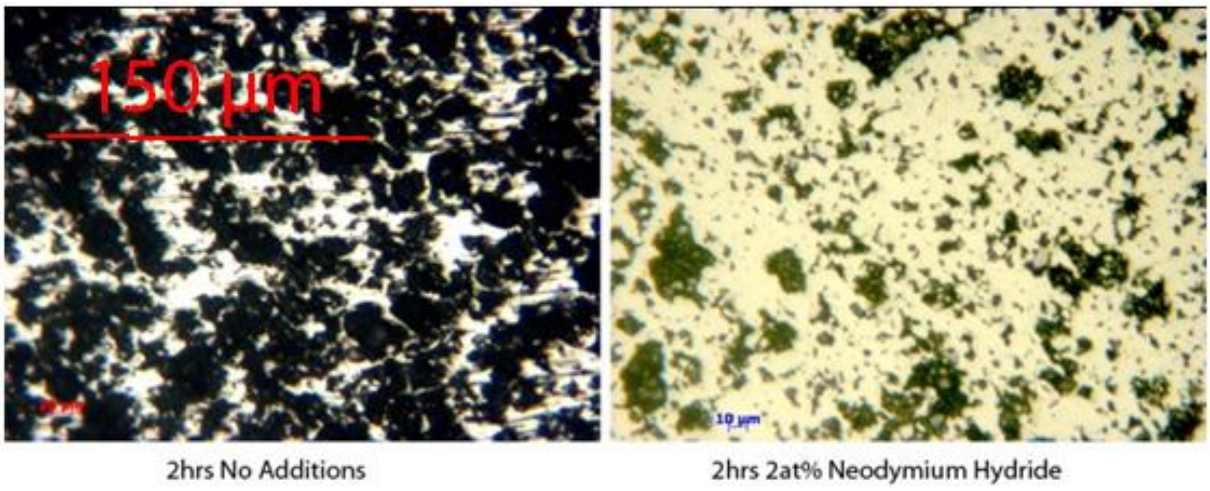

Fig.137. Comparison of sintered magnets made from powder exposed to air.

14.2. Powder Exposed to Air for 24 hours

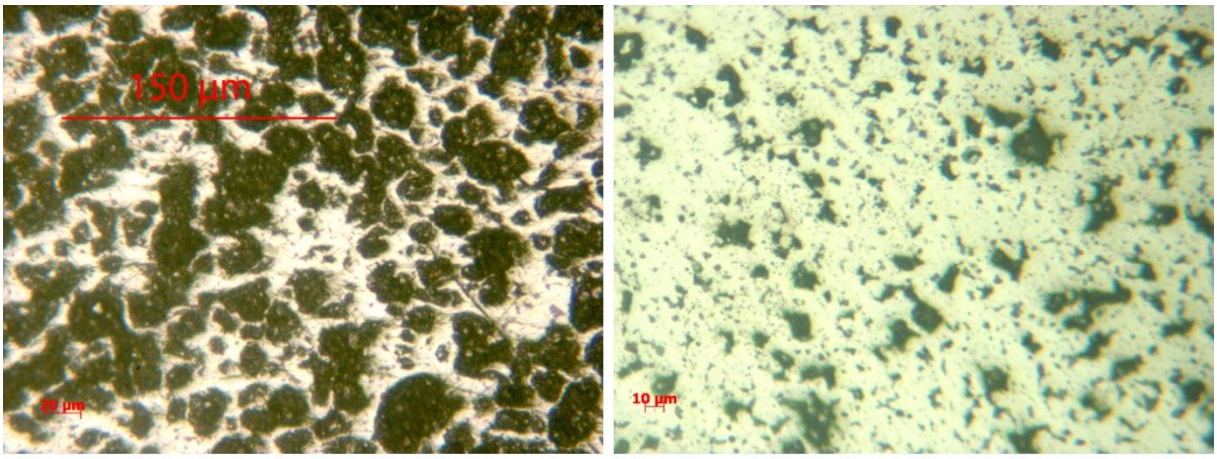

Fig.138. Sintered magnets made from powder exposed to air for 24 hours without and with additions.

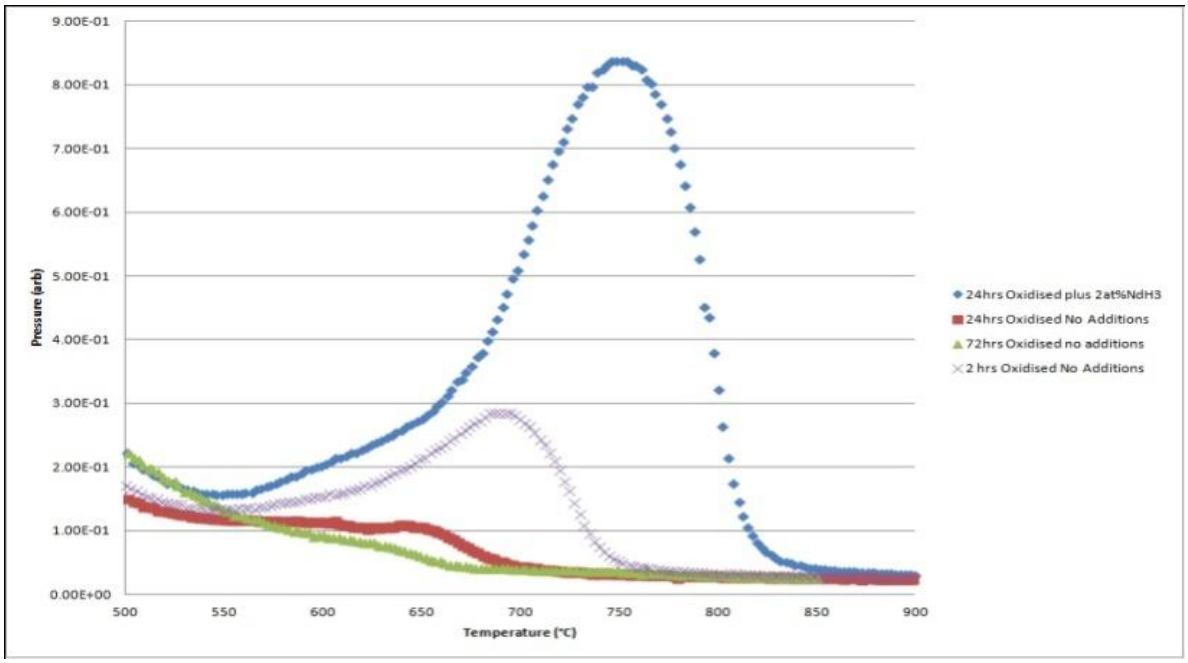

Fig.139. Increase in final peak with the addition of 2at % neodymium hydride for the 24 hour exposed powder.

Time (hrs)	Coercivity (KA/m)	Remanence Br (mT)	Density (g/cc)
0hrs No Additions	378	880	7.1
0hrs With Additions (2at%)	**1063**	**1256**	**7.43**
2hrs No Additions	122	400	6.9
2hrs With Additions (2at%)	**1135**	**1077**	**7.3**
4hrs No Additions	18	447	6.8
4hrs With Additions (2at%)	**1054**	**1116**	**7.29**
24hrs No Additions	0	0	6.8
24hrs With Additions (2at%)	**900**	**1138**	**7.3**
72hrs No Additions	0	0	5
72hrs With Additions (2at%)	**122**	**650**	**6.8**

Table 38. Data comparison of samples with differing time exposures. Errors associated are as follows: Remanence (mT) (±50) Coercivity (kA/m) (±50) Density (g cm^{-3}) (±0.2).

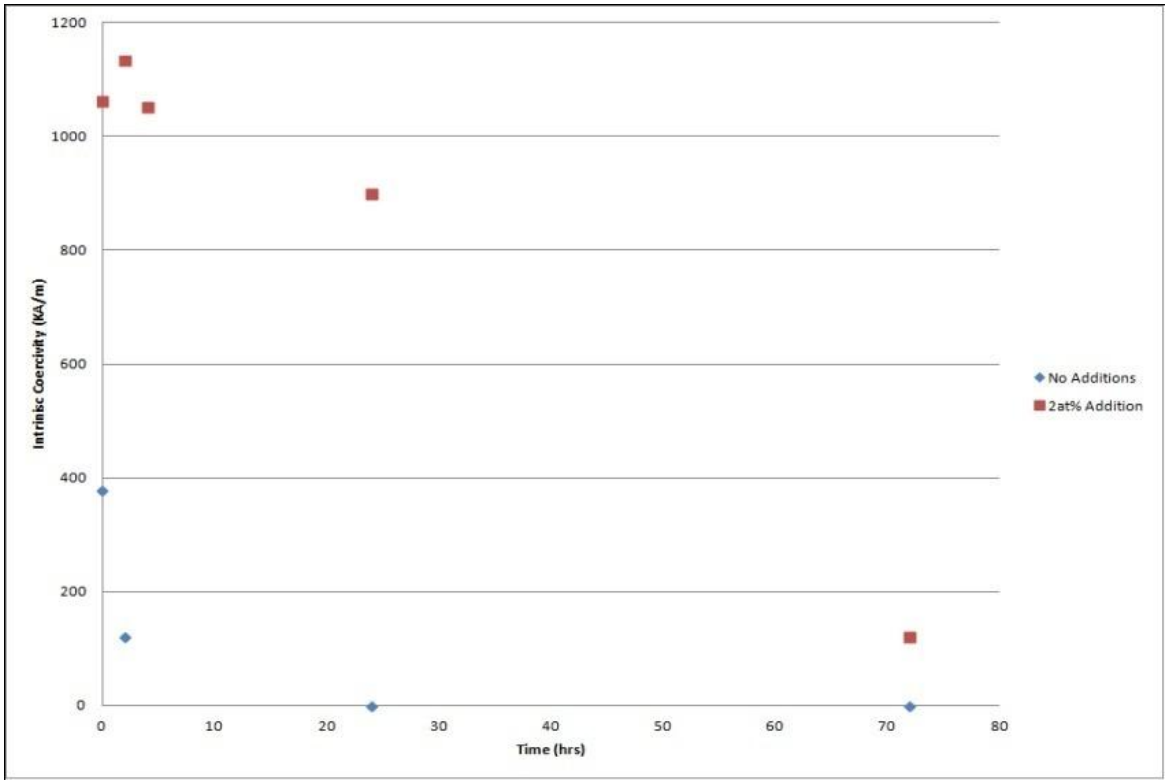

Fig.140. Graph showing drop in coercivity over time.

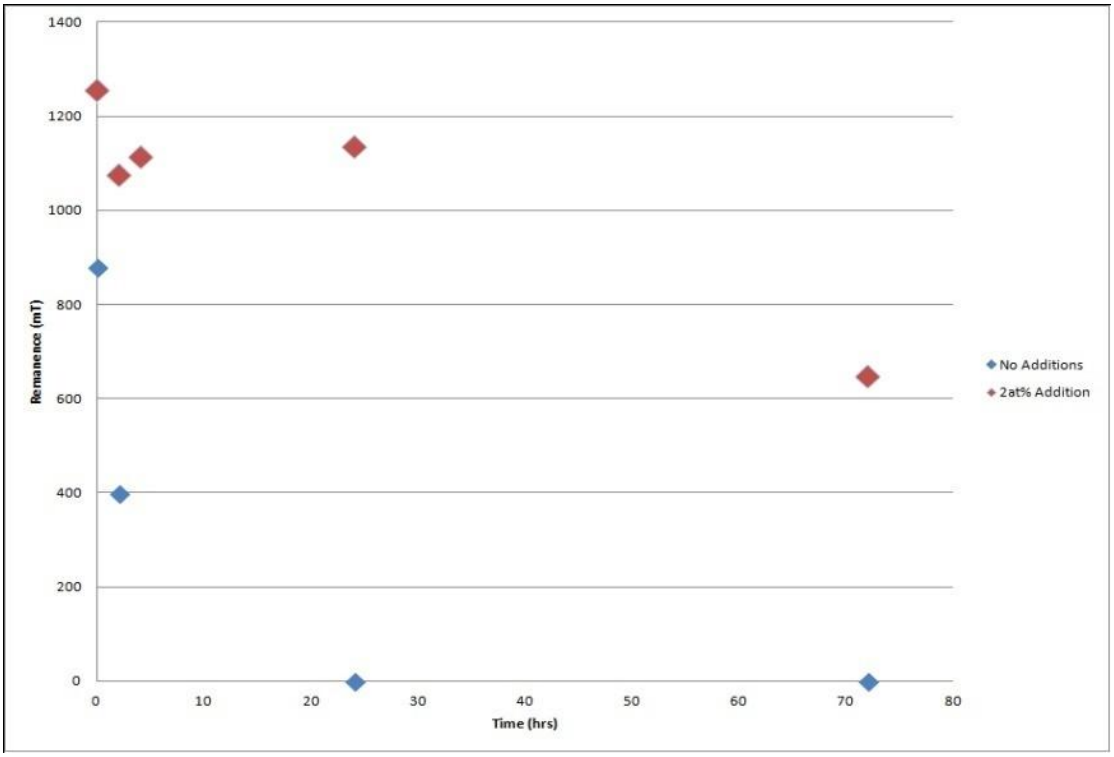

Fig.141. Graph showing a reduction in remanence vs. exposure time with and without additions.

14.3. Comparison of Grain Size of Recycled Sintered Magnets

The grain size of the sintered material used as the feed stock and the particle size of the burr milled powder used showed a similar mean grain size and particle size (8.3µm and 8.93µm). They had a mode of 7µm for the grain size and a mode of 9µm for the particle size. Particles that did not interact with an applied magnetic field of ~200mT were also observed. These were assumed to be a combination of attrition particles (table 38) and Nd-rich phase, (already discussed).

Investigating the grain size of the recycled sintered magnets should provide information on the degree of grain growth during sintering. The mean particle size of the powder

used will have an impact on the final grain size. Lowering the mean grain size gives an improvement to coercivity.

The recycled sintered magnets were etched with a 5% citric acid solution to reveal the grain boundaries and image analysis was performed.

	Average (µm)	**Max (µm)**	**Min (µm)**	**Median (µm)**	**Mode (µm)**	**SD**
Powder Aligned (198)	8.93	19	4	9	9	2.77
Powder Attrition (1543)	3.38	9.9	0.5	2.9	0.7	2.17
Etched Starting Material (541)	8.3	26	2	8	7	3.37
Etched 0hrs 2at% (712)	11.29	32	2	11	10	4.88
Etched 2hrs 2at% (618)	10.50	32	1	10	8	4.35
Etched 4hrs 2at% (740)	9.87	35	1	9	7	4.86

Table 39. Data on the particle size of sub 45µm powder and etched sintered magnets. Errors ±0.5µm.

The particle size distribution of the powder used consisted of ~20% of polycrystalline powder between 45 and 75µm, as well as ~80% of powder closer to that of the grain size of the starting material. The grains inside the polycrystalline powder are likely to grow quicker than the single grain particles during sintering.

Comparing the recycled material with limited exposure to air (0 hours) and with intergranular additions of 2at% $NdH_{\sim 3,}$ the grain size of the starting material showed an increase in the mean grain size from 8µm to 11.29µm. The mode value also rose from 7µm to 10µm. The minimum grain size recorded was 2µm and this shows that the smaller particles observed during characterization of the milled powder,(that did not interact with the applied field), are likely to be attrition particles. From fig. 142 it can be seen that there are a significant number

of grains less than 5µm which is less than the mean grain size of the starting material (8µm). The recycled magnets also showed a larger variance in grain size than the starting material. The maximum size of grains recorded increased from 26µm to 32µm.

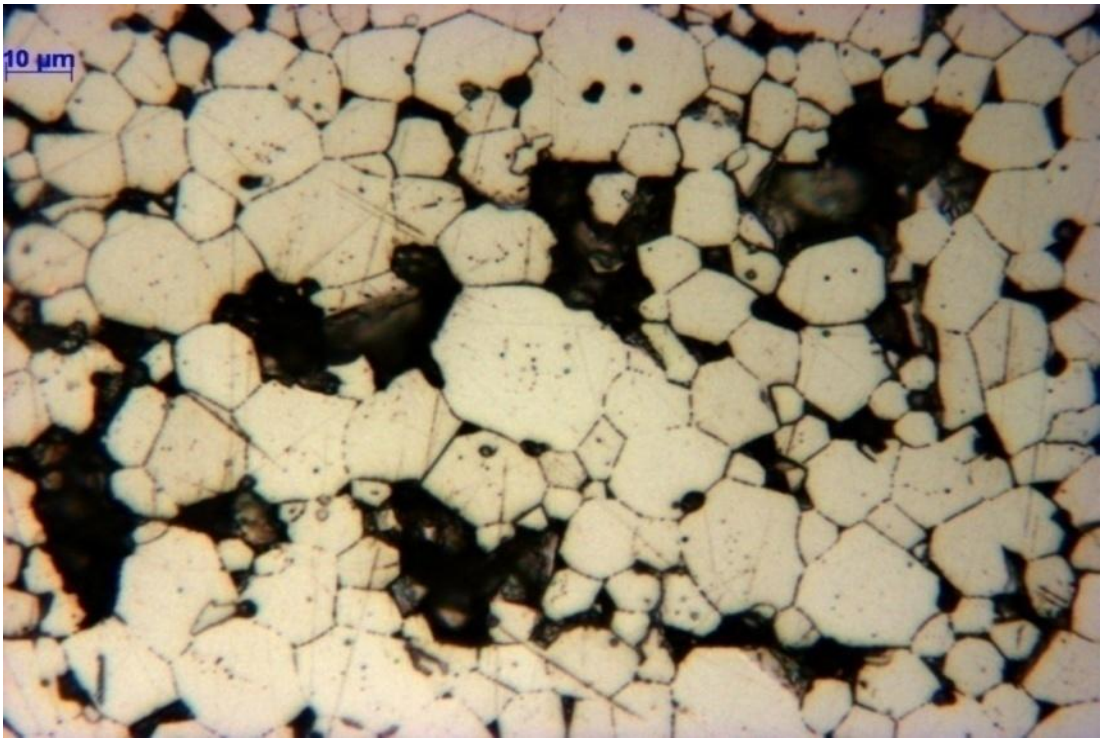

Fig.142. Sample exposed for 0 hours 2at% $NdH_{\sim 3}$ etched (micron marker 10µm).

14.3.1 Comparing grain size of Magnets Made from Powder Exposed to air - 2 hours 2at%

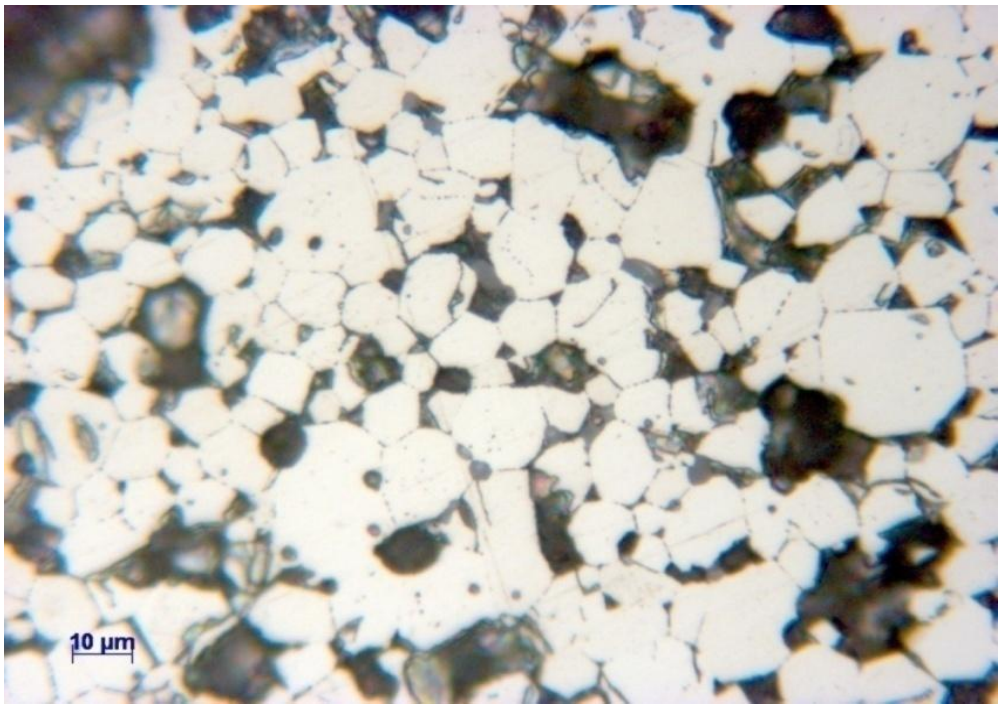

Fig.143. Etched microstructure of sintered magnet produced from powder exposed to air for 2 hours with additions (micron marker 10µm).

The powder with intergranular additions of 2at% $NdH_{\sim 3}$ exposed to air for 2 hours showed a reduction in average grain size compared to that of the non-exposed sample (with 2at% $NdH_{\sim 3}$ added). The mean grain size dropped from 11.3µm to 10.5µm. The mode value also dropped from 10µm to 8µm. This shows that exposure to air appears to be limiting the subsequent grain growth.

14.3.2. Exposure to air for 4 hours 2at%

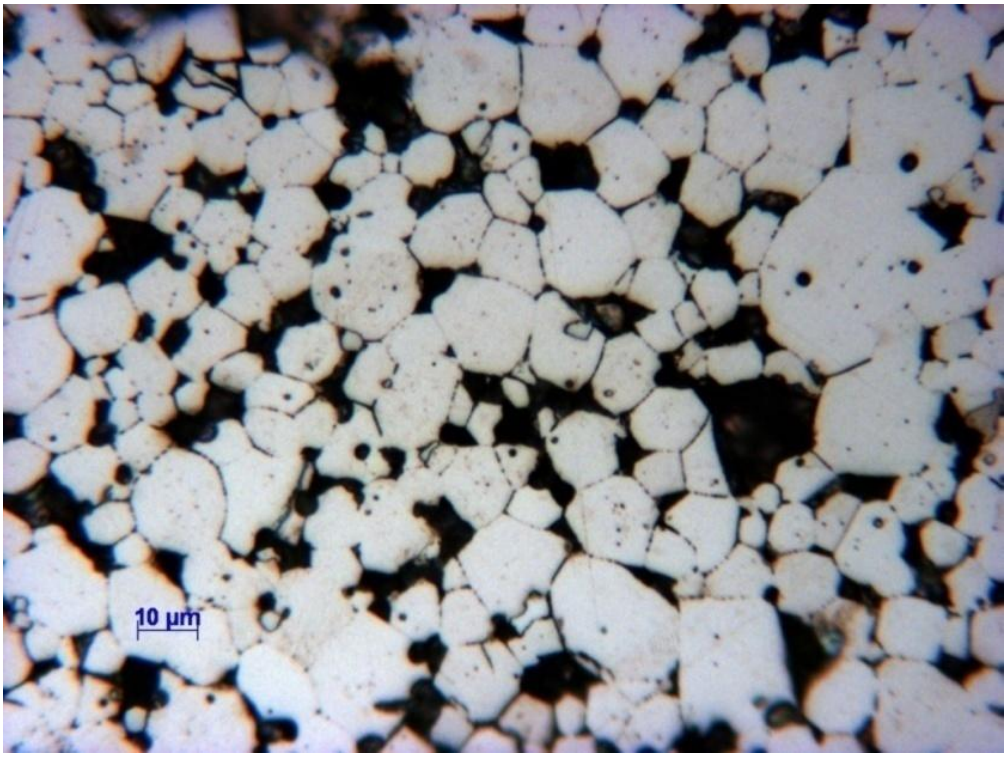

Fig.144. Powder exposed to air for 4hrs with 2at% added prior to sintering (micron marker 10µm).

The powder exposed to air for four hours with intergranular additions of 2at% $NdH_{\sim 3}$ prior to sintering also displayed a lower average grain size than the powder that was not exposed to air and also displayed a lower grain size than the powder exposed for 2 hours with additions added prior to sintering. The mean grain size reduced from 11.29µm (±0.5µm) for the unexposed sample to 10.5µm for the powder exposed for 2 hours and 9.87µm for the powder exposed for 4 hours. The mode value also reduced as the exposure time increased, 0 hours / 10µm, 2 hours / 8µm and 4 hours / 7µm. The minimum particle size observed was also lower

at 1µm. The maximum grain size was 35µm and the mode was lower at 7µm compared to 10µm for the non-exposed samples.

14.4. Discussion on Alloying Additions

The intergranular addition of 2 at% neodymium hydride improved the density of the powder for all exposure times compared to the behaviour of the sintered magnets with no additions. The increase in density is evident in the micrographs in figs. 137 and 138.

Fig. 139 indicates a significant increase in the final peak associated with the Nd rich phase thus indicating the presence of neodymium.

The powder exposed for 2 hours shows a significant degree of porosity. Porosity is still present in the sample even with the 2at% additions but it is much reduced.

The same can be seen for the powder exposed for 24 hours with and without additions. The improvement in density also results in a significant improvement in the magnetic properties. The coercivities of the powder atmosphere exposed for 2 and 4 hours, showed similar values to the freshly milled powder plus additions. There was an associated reduction in the remanence from 1256mT for the starting material to 1077mT for the 2 hour sample and 1116mT for the powder with additions exposed to air for 4 hours. After 72 hours the exposed powder with additions shows an average density of 6.8g / cc and an intrinsic coercivity of 122KA/m as well as a remanence of only 650mT. The same quantity of alloying additions was added to all the exposed powder and increasing potentially the amount of neodymium hydride additions could have improved further the properties of the powder exposed for 72 hours.

A reduction in the average grain size with exposure time was observed in the magnets made from exposed powder with alloying additions of 2at% $NdH_{\sim 3}$, added prior to sintering. There was also a reduction in the mode value as the exposure time increased. The reduction in average grain size and the reduction in the mode for the powder exposed to air for 2 hours and 4 hours shows that the exposure to air is likely to be influencing grain growth during subsequent sintering. This agrees with the work of Zakotnik et al, (2009) who showed that, for recycled magnets with additions of neodymium hydride; grain growth was limited compared to those with no additions. They suggested that the presence of Nd_2O_3 at the grain boundaries, due to an increase in the oxygen content, inhibited the grain growth.

The decrease in the mean grain size would explain the increase in coercivity observed for the powder with an exposure time of 2 hours compared to that of the non exposed samples. The subsequent reduction of the coercivity of the 4 hour exposed sample compared to that of the 2 hour exposed sample, is likely to be due to the reduction in density of the 4 hour sample.

The observation of grains less than 3µm diameter shows that the particles that were observed not to be interacting with an applied magnetic field are likely to consist of at least a percentage of $Nd_2Fe_{14}B$ attrition particles. Grain growth will have occurred during sintering so that the initial particle size is likely to have been less than 3µm. The minimum grain size observed was 1µm. The presence of closed porosity within some of the grains indicates the possibility of multiple powder particles coalescing to form a larger grain and thus trapping porosity.

The large grains observed in the magnets recycled with added alloying additions, are likely to be due partly to the grains inside the polycrystalline powder of the 75 – 45µm fraction. The grains within the 75 – 45µm powder will remain the same size as the starting grain size

whereas the single grain powder has the potential to be slightly lower than that of the starting material due to attrition of particles. The grains are likely to grow quicker than the single grain particles during sintering.

The reduction in the remanence observed for the 2 hours and 4 hours samples will be related partly to the reduction in the density and partly to the increase of the Nd-rich phase (due to the additions). There is also the possibility of misalignment reducing the remanence. Evidence of misalignment can be seen in samples recycled with the alloying additions and observed using the Kerr effect.

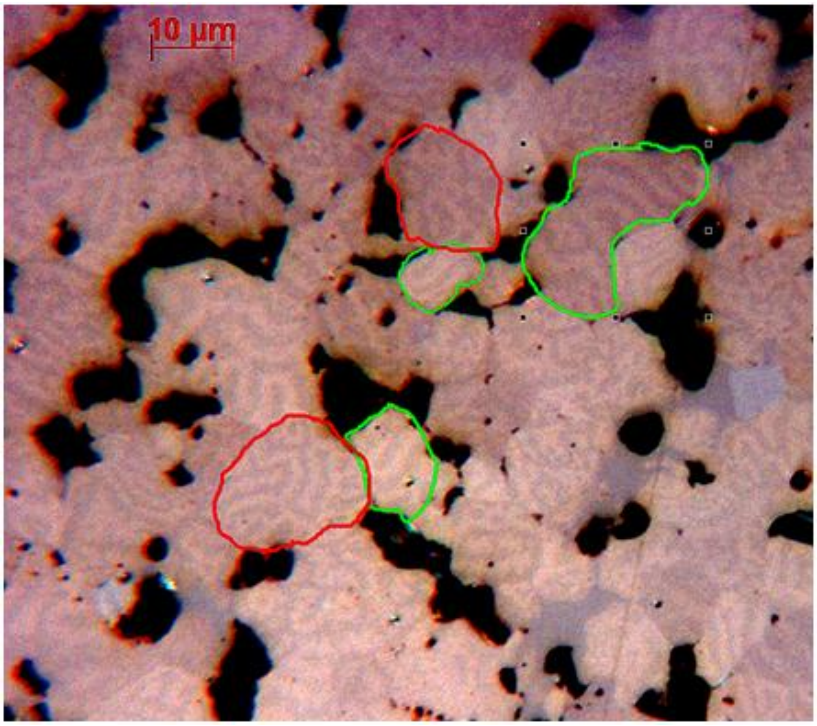

Fig.145 Kerr effect microscopy, (perpendicular to the c-axis). Magnet made with powder exposed to the air for 2 hours with 2at% addition of neodymium hydride.

Fig. 145 shows misalignment in some of the grains from a magnet made with powder with additions of 2at% $NdH_{\sim 3}$ added prior to sintering exposed to air for 2 hours. The sample in fig. 145 was imaged perpendicular to the direction of alignment and should show all grains with a cog wheel pattern as the viewer is looking down the c axis. The presence of grains with stripes indicates grains not fully aligned.

14.5. Stability of the $Nd_2Fe_{14}B$ Hydride Phase

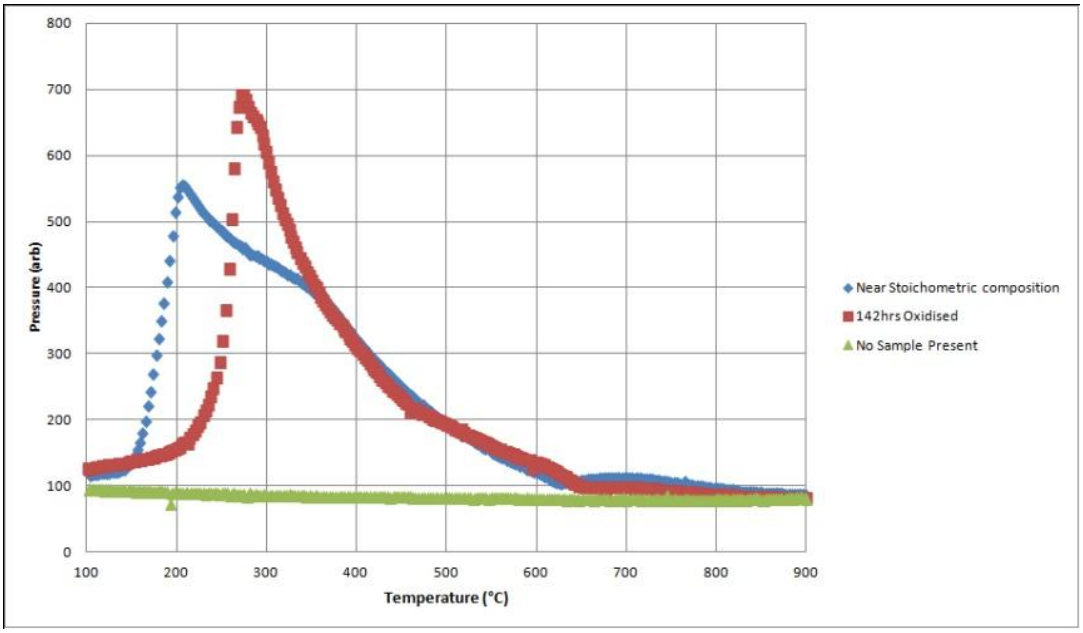

Fig.146. Desorption of the #R powder exposed to air for 142 hours compared with desorption from a single phase $Nd_2Fe_{14}B$ alloy.

The final peak associated with the NdH_2 to Nd + H_2 desorption is not present. The HD powder exposed to air and the hydrided stoichometric alloy had different processing routes namely, burr milling for the exposed powder and 20 hours ball milling for the stoichiometric

alloy. So the mean particle size of the stoichiometric alloy should be much smaller than that of the burr milled powder.

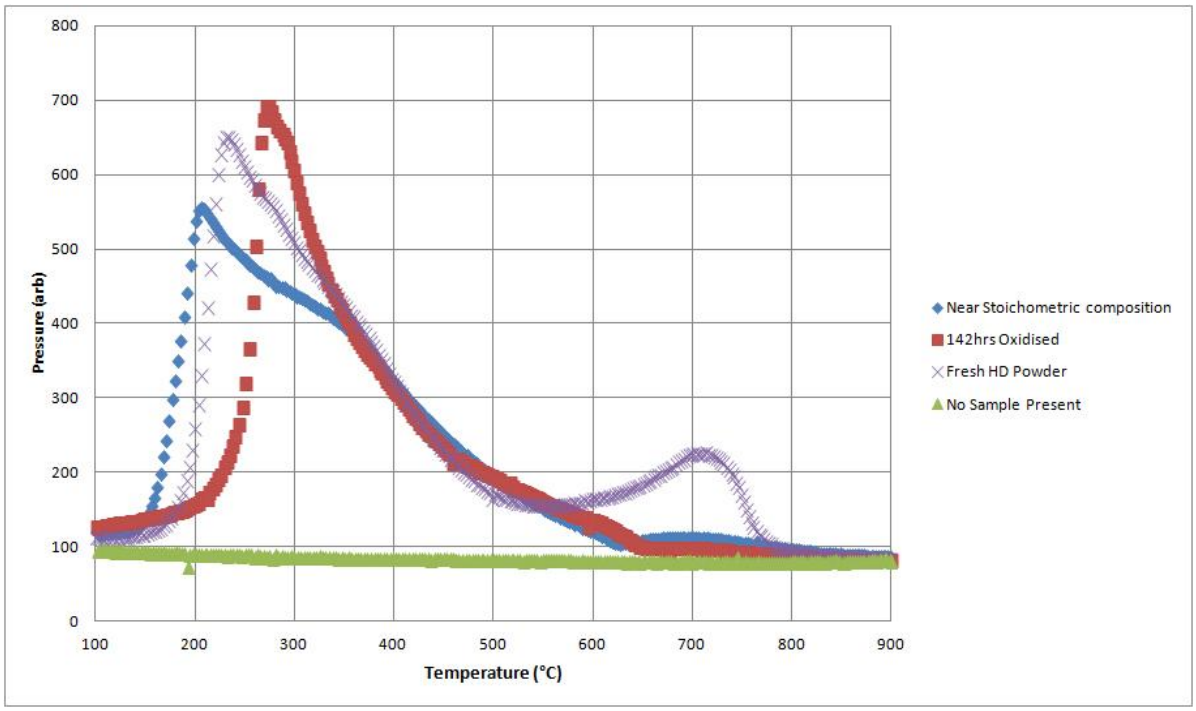

Fig.147. Desorption of $Nd_2Fe_{14}B$ powder exposed to air and fresh HD powder.

The exposed and fresh HD powder should have a very similar mean particle size and similar particle size distributions. The desorption of the powder exposed for 142hr starts later than the fresh powder, leading to the conclusion that the oxidation of the powder means higher temperatures are required before desorption begins.

Chapter 15. Influence of Alloying Additions on HD Powder Exposed to Air

The experiments with exposure to air were repeated. This time the aim was to investigate the behaviour of HD powder with differing compositions.

ICP	B	Fe	Nd	Dy	Pr	Al	Co	C	N	O	Nb
	%	%	%	%	%	%	%	Ppm	Ppm	%	%
#R	1.02	66.01	29.17	1.98	0.1	0.29	0.36	572.5	95	0.42	0.4
#S	1	58.16	25.95	4.21	0.34	0.34	4.22	671	222	0.41	0.83

Table 40. ICP compositional data of the two starting materials (referred to as #S and #R from now on).

From table 40 it can be seen that there is a difference in the composition between the two magnets. The #S composition has a greater Co content compared to the #R composition. There is also a difference in Dy content between the two magnets. A difference in N in the #S composition was also observed.

Following on from the previous work, the starting material was hydrogenated at room temperature at 4 bar. The HD powder was then milled in a glove box using a burr mill. The grinding of the powder was carried out in the glove box to limit corrosion of the material. Powder with a particle size less than 75μm was used to make the green compacts with a mass of 15g ± 0.01g. Samples of powder with the two compositions were left in air for varying amounts of time and then aligned, pressed and vacuum degassed, with desorption behaviour monitored using the pressure logging system described earlier.

	#R %	#S %
Dy	1.98	4.21
Nd	29.17	25.95
Pr	0.1	0.34
Total	**31.25**	**30.5**

Table 41. Rare earth content of #R and #S compositions in wt%.

Powder with compositions denoted by #R and #S were exposed to air for varying times and then transferred to a glove box prior to sintering. Both compositions were exposed at the same time so that the humidity and temperature profiles observed by both samples would be identical.

There was an error experienced with the thermocouple during the experiment. Sporadically the thermocouple stopped working leaving gaps in the heating profile data. This meant that plotting the change in pressure versus temperature for certain desorption traces was impossible. So instead the change in pressure was plotted with time. The heating rate for all desorption events was set at a constant 7°C per minute. The temperature data could have provided information on whether oxidation causes the peaks to shift to higher temperatures.

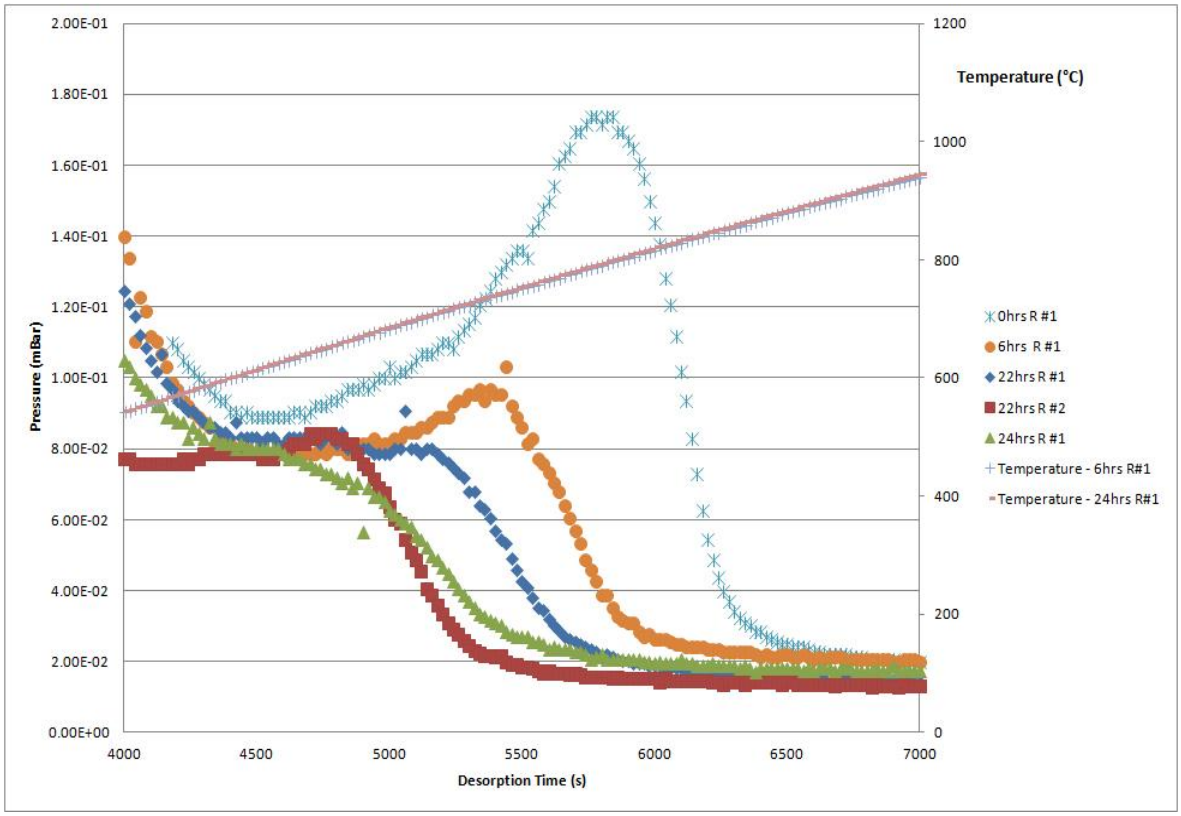

Fig.148. Reduction in peak height with exposure time for #R composition.

Desorption of the #R composition shows a similar decrease in peak height to that seen previously (see fig) with the final neodymium rich peak almost completely gone after the 24hrs exposure.

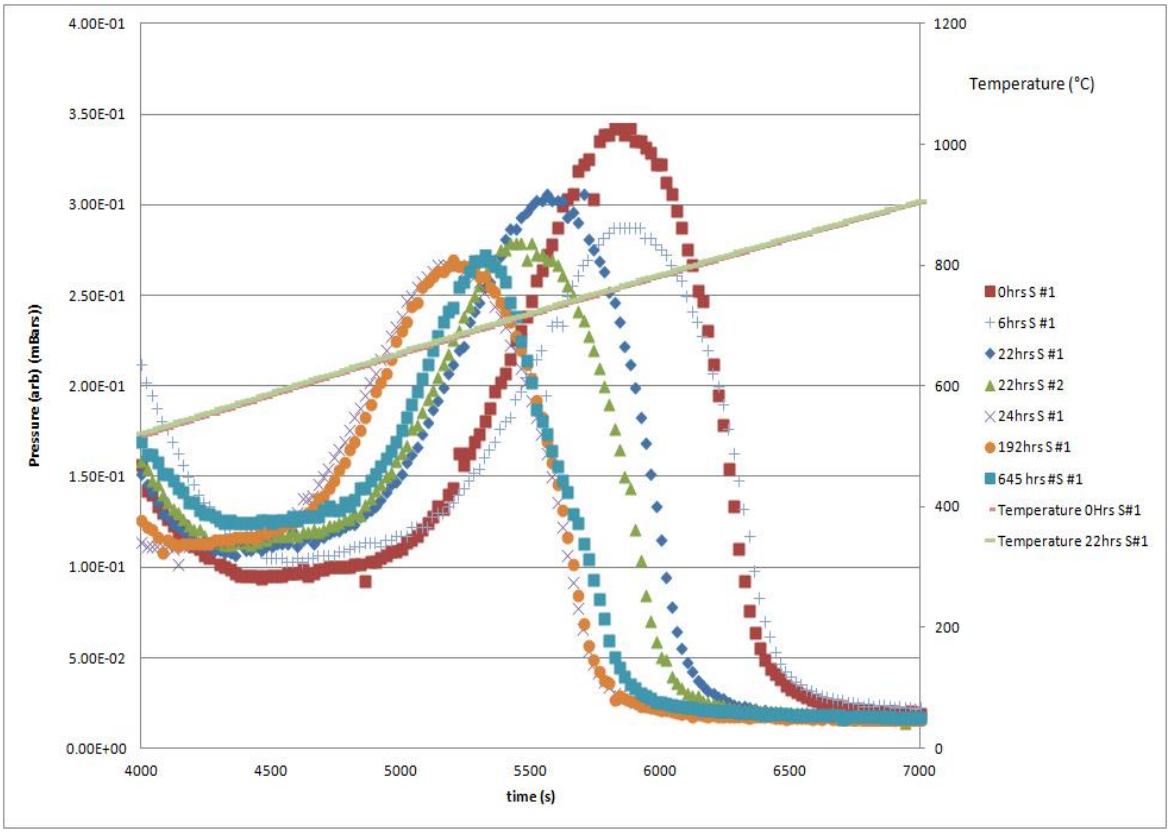

Fig.149. Reduction in peak height over time for #S composition.

	#S	#R
Time (hrs)	**Max peak height (arb)**	**Max peak height (arb)**
0	3.42E-01	1.74E-01
6	2.88E-01	1.38E-01
22	3.06E-01	8.02E-02
22	2.79E-01	8.46E-02
24	2.67E-01	8.02E-02
192	2.70E-01	-

Table 42. Maximum peak heights for the $NdH_{\sim 2}$ to Nd and H_2 desorption event.

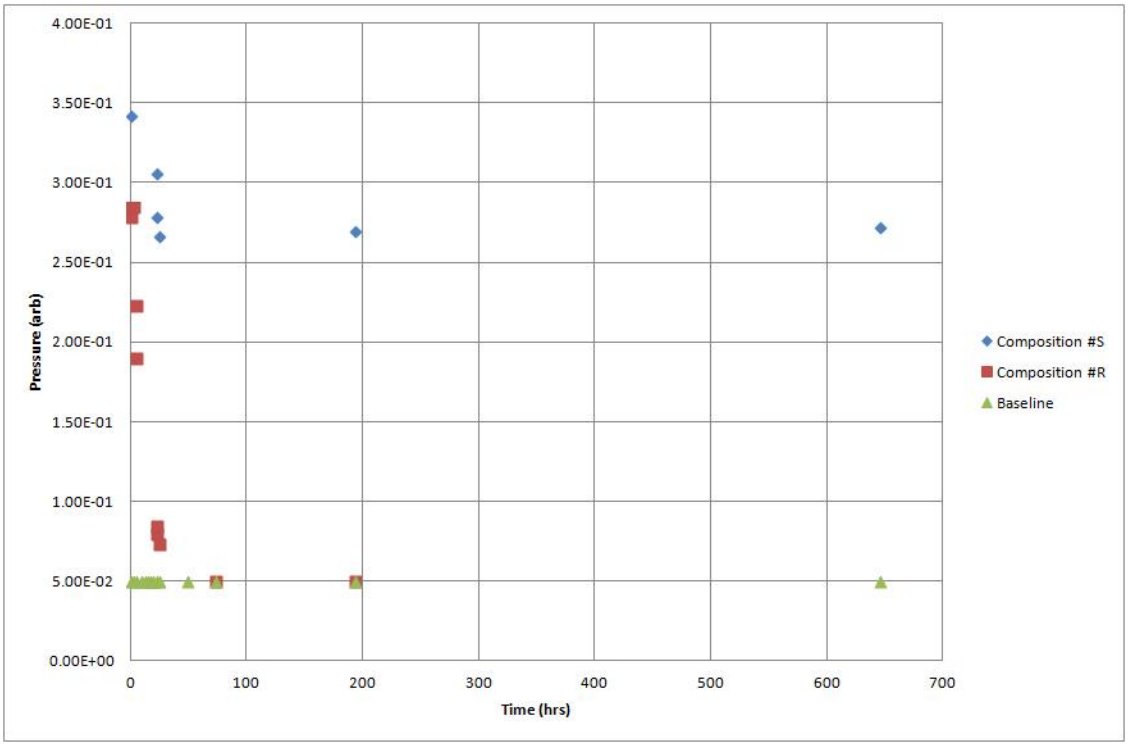

Fig.150. Maximum peak heights for #R and #S materials in air for differing exposure times.

From table 42 and fig. 149 it can be seen that the desorption peak corresponding to #S composition reduces in height until the 22 – 24 hour exposure mark and after this point, there is no further reduction in the maximum peak height. Powder exposed to air for 645 hours still exhibited a similar peak height to the 22 hour and 24 hour samples.

This is in clear contrast to the behaviour of #R composition, where the peak reduces to almost zero at 22 hours and by 72 hours there is no peak present. The presence of the peak in #S compositon after exposure to air for 645 hours is clear evidence of a marked difference in stability of the rare earth rich phase between #S and #R compositions.

The only difference between the powders is likely to have been compositional. The starting materials were both hydrided at room temperature, at 4 bar gauge pressure and transferred inertly to a glove box . The powders were burr milled in the glove box to a particle size of less than 75µm. The resulting powder was re-seived to determine the percentage mass between 75 and 45µm and sub 45µm. The mass fractions were similar with approximately 20% between 75 and 45µm and 80% less than 45µm. At the same time the powders were exposed to air and so would have been exposed to the same humidity and temperature profiles. The ramp rate for the desorption runs was identical throughout, at 7°C per minute.

ICP	**Nd**	**Dy**	**Co**	**N**	**Nb**
	wt%	**wt%**	**wt%**	**ppm**	**wt%**
#R	29.17	1.98	0.36	95	0.4
#S	25.95	4.21	4.22	222	0.83

Table 43. Differences in composition between #R and #S.

Table 43 shows the significant differences in the compositon between the two magnets. The main difference is the Dy and the Co content. There is an increase in nitrogen in #S material. Cygan and McNallan, (1994) suggested that the presence of nitrogen improves the corrosion resistance. The clear improvement in stability observed here is unlikely to be related to the nitrogen content as the difference between the two compositions is in the ppm range. The likely reason for the improved stability therefore, is the differing amounts of Dy and Co.

At up to 22 hours the reduction in peak height for both compositions reduces at a similar rate, however, after 22 hours, #R material reduces to zero whereas that for #S composition remains stable.

It is possible that, some of the initial reduction in #S material is due to the creation of a passivating layer, which prevents further reactivity of the hydride phase. Desorption traces for 24 hours, 72 hours and 645 hours were very similar indicating a stabilised condition.

Yu et al, (2004) investigated the effect of alloying additions of Nb and Dy on the corrosion resistance of sintered magnets. They suggested that as the Dy and Nb content increased, "more stable intermetallic phases develop within the intergranular regions. This can promote the electrochemical potentials of intergranular phases, resulting in the improvement of corrosion resistance".

Verdier et al, (1994) exposed various hydrogenated alloys to air for varying times whilst recording the weight gain with time. The compositions $Nd_{l5}Fe_{75.l}Ga_{l.9}B_8$ and $Nd_{15}Fe_{77}Co_5V_4B_8$ exhibited a reduction in the percentage mass increase compared to that of the $Nd_{l5}Fe_{77}B_8$ composition. They concluded that "Ga forms some $Nd_6Ga_3Fe_{ll}$ around the matrix grains" and that this phase was more resistant to corrosion, as is the intergranular Nd_3Co phase in the case of the Co additions." Verdier et al, (1994).

Szymura et al, (1991) also investigated the effect of additions of cobalt on improving the corrosion resistance of alloys of the composition, $Nd_{16}Fe_{76-x}Co_xB_8$. Their corrosion tests showed that the Co additions inhibited the atmospheric corrosion of the Nd-Fe-B permanent magnets, especially in a salt spray environment. They attributed the changes in corrosion resistance to the cobalt segregation in the $Nd_2F_{14}B$ and $Nd_{1+E}Fe_4B_4$ phases and the formation of the intergranular $Nd(Fe,Co)_2$ Laves phase.

Motram et al, (2001) investigated the effect of intergranular additions on the NdFeB hydrogenated alloys. They showed that magnets containing small additions of Co and Al were

found to exhibit excellent corrosion resistance in an autoclave at 115°C and saturated steam. The improvements were attributed to the presence of Nd_3Co at the grain boundaries.

It is likely that either Co and / or Dy are stabilising the rare earth rich phase possibly with the formation of $NdCo_2$ phase, (as suggested by Szymura et al1991), or by the Nd_3Co phase suggested by Verdier et al (1994) and Mottram et al (2001). Further work needs to be done to determine the presence of Co in the rare earth rich phase and if present, the form in which it is present.

To prove whether Co or Dy, or both are modifying the rare earth rich phase, alloys of neodymium with cobalt and dysprosium at varying ratios could be prepared. The subequent hydrogenated material could be exposed to air for varying times and desorption traces monitored.

Chapter 16. Overall Discussion

The ball and burr milling techniques showed very similar particle size distributions and these distributions were also very similar to the grain size of the starting material. The similarity is due largely to the nature of fracture of the HD powder which tends to be intergranular in nature. The expansion mis-match between the Nd-rich hydride phase and the $Nd_2Fe_{14}B$ solution phase during the HD process is likely to encourage this intergranular fracture. Therefore, minimal energy should be required to break up the HD powder to a particle size similar to the grain size of the starting material, (described earlier). During this process fine attrition particles can be formed and evidence of these was seen in micrographs of the milled powder. Additional milling is likely to reduce the mean particle size even further.

Observation of the HD powder particles under the influence of magnetic fields, using optical microscopy (developed in this present work), enabled clearer observation of the $Nd_2Fe_{14}B$ particles. This technique has been proven to be an effective way of gaining more information on the size distribution of the particles, which align with the applied field. This technique combined with image analysis showed that the mean particle size obtained from both the 1 hour ball milled and the sub-45µm burr milled powder both exhibited a similar mean particle size, (8.9µm) which was very similar to the mean grain size of the starting material. This shows that burr milling could be an alternative to jet milling recycled HD powder.

In the present work, it has been shown that the actual mean particle size of the ball and burr-milled powder is likely to be lower than 9µm due to the attrition particles observed. The presence of attrition particles reduces the mean particle size and further milling is likely to reduce the mean particle size even further. From the literature it has been reported that the

optimum particle size is in the region of 5μm (Nothnagel et al 1991, Namkung et al 2011 and Li et al 2009).

16.1. Thermomanometric Analysis

Desorption behaviour of neodymium hydride, the HD powder and the green compacts from the recycled magnets, was observed using a vacuum sintering furnace, a Pirani gauge and a data logging system.

This work has shown that a logging system based on the output from a Pirani gauge, can be effective in the analysis of desorption of hydrogenated NdFeB material. The system outlined in this work was successful in monitoring desorption of hydrogen from powder amounts ranging from 330mg to 15g, with the potential to monitor desorption of hydrogen from even larger amounts of powder.

The desorption of neodymium, hydrided at room temperature, was studied with significant differences observed between hydride powder milled in cyclohexane, loaded in air and inertly loaded, non-milled samples. The neodymium hydride milled in cyclohexane began desorbing at between 70 to 80°C and this was far earlier than that of the inertly loaded, non-milled samples (~180°C).

The non-milled samples consisted of a lump weighing 330mg and coarse powder also weighing around 330mg. This material was desorbed in the thermomanometric system and displayed a desorption start temperature of 181°C. This was lower than in the literature where Yartys et al, (1997) showed that the start point for desorption of $NdH_{\sim 3}$ was in the region of 220°C. N. Yoshihiro et al, (2006) also showed that desorption of $NdH_{\sim 3}$ started at above 200°C.

The Nd-hydride milled in cyclohexane for 20 hours, (dried under vacuum and loaded in the presence of air), displayed a desorption start temperature of 70 to 80°C. This low temperature desorption could possibly be due to the formation of $Nd(OH)_3$. Verdier et al, (1994) discussed the exposure of neodymium hydride formed at room temperature and they confirmed by XRD, that after exposure to air, neodymium hydride formed $Nd(OH)_3$. It is therefore likely that either during the milling in cyclohexane or during the non-inert loading of powder, formation of the hydroxide occurred.

During desorption of the neodymium hydride powder there was also evidence of two low temperature peaks below 500°C. These peaks were present in the powder milled in cyclohexane, loaded in air and in the inertly loaded samples. However, these peaks were better defined in the desorption trace for the inertly loaded single 330mg lump of hydride. The inertly loaded batch of 330mg powder with a coarse mean particle size of between 100µm – 200µm, also exhibited two defined peaks, albeit slightly broader than those characteristic of the single lump and with a lower magnitude. The milled powder showed the poorest definition of these peaks.

For the inertly loaded samples, both desorption curves indicated the start of desorption at approximately 180°C, with a main peak at 240°C and a secondary peak between 320°C and 330°C, finishing at approximately 420°C. The evidence of two overlapping, low temperature peaks was discussed by Yartys et al, (1997) who stated that "for the group 1 elements the low temperature NdH_{2+x} to NdH_2 consists of two overlapping desorption events."

They also observed that the most pronounced effects were exhibited by Pr. They reported that the main desorption occurred at 340°C with a smaller but clearly defined peak at 255°C.

The two low temperature peaks observed in the present work, match closely those discussed by Yartys et al, (1997). However, the relative magnitudes of the peaks were different and in the present work, the lower temperature peak was greater in magnitude than the higher one. This is opposite to the relative magnitudes observed by Yartys et al, (1997). The sharpness and magnitude of the low temperature peaks appear to diminish as the particle size reduces. This indicates the possibility that the differences in the magnitude of the peaks are related to the microstructure of the different samples. They may relate to the nature and extent of the grain boundaries.

16.2. Desorption of Hydrogenated $Nd_2Fe_{14}B$

The desorption trace observed for a homogenised $Nd_2Fe_{14}B$ alloy showed similar features to those described in the literature. Williams et al, (1991) showed that for the $Nd_2Fe_{14}B$ alloy the trace consisted of a sharp peak which centred on 150°C, followed by a broad shoulder which indicates a peak centred on approximately 250°C. Williams et al, (1991) suggested that this apparent dual stage "could be due to desorption of hydrogen from different sites within the $Nd_2Fe_{14}B$ phase and / or to micro-structural effects such as separate desorption of hydrogen from the grain boundaries and the matrix".

Harris et al, (1987) used mass spectrometry to observe desorption of hydrogen from $Nd_2Fe_{14}B$ and also confirmed that the first peak centered on approximately 150°C. Their trace started at a lower temperature than either of the traces observed here or in the work by Williams et al, (1991). The shift in the temperatures could be related to the degree of corrosion of the powder during processing.

16.3. Desorption of Hydrogenated NdFeB

Desorption behaviour of the green compacts in this work was directly related to the microstructure and magnetic properties. The typical mass of the green compacts was ~15g. Whilst desorption data in the literature is in the mg range and is not directly related to the microstructure and magnetic properties.

Desorption traces for powder made from sintered blocks with a composition of $Nd_{29}Fe_{66}Dy_{1.98}B$ wt% , hydrogenated at room temperature at 4 bar H_2- pressure, displayed multiple peaks during desorption. This agrees with the work reported by Harris et al, (1987) who showed that desorption of a $Nd_{16}Fe_{76}B_8$ alloy is a multi-stage process and that the hydrogenation of the $Nd_2Fe_{14}B$ matrix phase can only be achieved in the presence of the Nd-rich grain boundary phase.

16.4. Change in Desorption of HD Powder with Particle Size

HD powder with varying mean particle sizes was loaded in the presence of air into the desorption system and then degassed. As the mean particle size was reduced, the final peak height also reduced. The powder with a lower mean particle size also showed a lower initiation temperature for the desorption process. The powder was loaded in air so that the powder was partially oxidised. Williams et al, (1991) showed that HD powder exposed to air exhibited a reduction in the height of the final $NdH_{\sim 2}$ to Nd peak, when desorbed and analyzed using a mass spectrometer.

Nothnagel et al, (1991) found that with decreasing mean grain size, (varied by milling time), the coercivity, jHc of the sintered material passed through a maximum at a critical value of mean grain size and oxygen content, respectively. After this, the coercivity decreased drastically. They showed that the abrupt deterioration of the coercivity was accompanied by a

substantial change in the micro-structure. From their results, the critical mean particle sizes were shown to be between approximately 1.5µm and 2.5µm, depending on the size of the milling ball used, (Nothnagel et al 1991). They concluded that the increase in oxygen content associated with the decrease in mean particle size caused the annihilation of the Nd-rich phase and, as a consequence of this process, there was negative impact on the liquid phase sintering.

Namkung et al, (2011) investigated the effect of particle size distribution on the micro-structure and magnetic properties of sintered NdFeB magnets. They showed that reducing the mean particle size to 3.35µm gave an increase in oxygen content of 4000 ppm, whereas the value in the starting powder was 2082 ppm.

A difference in the maximum peak height was observed between the sub 45µm powder and the powder with a mean particle size greater than 500µm, despite loading the powder inertly.

ICP was performed on samples aligned and sintered with the sub 45µm powder and greater than 500µm powders inertly loaded. The analysis of these samples showed an increase in oxygen content as the mean particle size dropped to less than 45µm. The values were 0.50 at% oxygen for the sample with a mean particle size greater than 500µm and a value of 0.66 at% for the powder with a mean particle size less than 45µm. These results indicate that corrosion of the powder had occurred.

The analysis also showed an increase in nitrogen as observed by Li et al, (2009). The evidence of an increase in oxygen content with the reduction in mean particle size agrees with observations in the literature, namely, Nothnagel et al (1991), Namkung et al (2011) and Li et al (2009).

The reduction in peak height could also be related to a physical loss of the Nd -rich phase during processing. The powder particles observed not interacting whilst under the influence of an ~200mT magnetic field, are likely to consist of attrition particles and the Nd-rich phase. The neodymium rich phase is at the grain boundaries of the $Nd_2Fe_{14}B$ phase and the HD powder has been shown to break up along the grain boundaries. The Nd rich phase is likely to stay attached to the surface of the $Nd_2Fe_{14}B$ grains but there is a possibility that the Nd-rich phase can transfer to the milling media during the processing.

To verify the possible loss of neodymium during processing an ICP analysis was carried out. This indicated a reduction in the Nd- content, however there was insufficient data to prove definitively that the reduction in peak height was partly due to physical loss of the Nd- rich phase during the processing. Further work needs to be done to determine whether there is such a physical loss and if so, the degree of loss.

16.5. Alloying Additions of $NdH_{\sim 3}$ to HD Powder

The recycled magnets made from the sintered starting material with a composition based on $Nd_{29}Fe_{66}Dy_{1.98}B$ wt%, sintered at 1060 °C (± 5°C) for 1 hour and furnace cooled, did not achieve full density. As a consequence, the magnetic properties were much less than the properties of the sintered starting material.

As expected, optical microscopy of the micro-structure showed large degrees of porosity. As discussed previously, a reduction in the mean particle size led to a reduction in the peak height of the final $NdH_{\sim 2}$ to Nd desorption event. Additions of $NdH_{\sim 3}$ were added in an attempt to improve the density and hence magnetic properties.

An increase in the at% of additions to the HD powder resulted in an increase in the $NdH_{\sim 2}$ to Nd desorption peak.

The early onset of desorption was again observed with an increase in intensity, with increasing additions of milled neodymium hydride. It is possible that during the milling process, the neodymium hydride is also partially forming a hydroxide, (the presence of low temperature desorption indicating the release of H_2O).

The density and magnetic properties improved with these alloying additions. The sintered magnets with 2at% Nd-hydride additions met the minimum coercivity, remanence and $BH_{(max)}$ values for the N30 commercial specification for sintered magnets. A post sintering annealing treatment was shown to improve the intrinsic coercivity by approximately 100KA/m. This shows that there is still room for further improvement in improving the magnetic properties of recycled magnets.

The remanence of the recycled magnets was lower than that of the starting material and this could be due to an increase in the extent of the Nd-rich phase. However, Kerr effect imaging also showed the presence of misaligned grains. The presence of such misaligned grains indicates that there is a possibility for further improving the remanence by:

- improving the particle size distribution
- increasing the applied field
- partially degassing the powder prior to sintering

Improving particle size distribution could have the effect of easing the rotation of particles under the influence of an applied field, while increasing the applied field would increase the

torque observed by the particles. It should also be borne in mind that misalignment could have been present in the original magnet.

16.6. HD Powder Exposed to Air

Exposure of the hydrogenated powder to air (containing a degree of humidity) results in the corrosion of the rare earth rich phase. The impact of the corrosion of this phase can be observed as a reduction in the final desorption peak, which represents the transformation of $NdH_{\sim 2}$ to Nd. The present results show that, for #R composition ($Nd_{29}Fe_{66}Dy_{1.98}B$ wt% ($Nd_{13}Fe_{76}$ $Dy_{0.78}B_6$ at%), when exposed to air for between 24 and 72 hours, the final desorption peak disappeared altogether. This shows that the rare earth rich phase had corroded extensively. This broadly agrees with the work done by Verdier et al, (1994) who investigated the mass gain of HD powder on exposure to air. They showed that the weight of a hydrogenated $Nd_{15}Fe_{77}B_8$ alloy stopped increasing between 50 and 100 hours of exposure.

The density of the magnets produced from this powder dropped on exposure time and the microstructure exhibited an increased porosity with the magnetic properties decreasing rapidly with exposure time.

16.7. Alloying Additions to Powder Exposed to Air

To see if the magnetic properties could be recovered, 2at% Nd-hydride was added to the powder exposed to air. The density and magnetic properties were compared with those of the starting material. An improvement in the density was observed for all the samples tested, with an associated improvement in the magnetic properties. The magnetic properties for the powder exposed in air for 2 hours and 4 hours with additions, were close to those of the magnets made from the non-exposed powder and 2at% additions.

There was a slight reduction in the density of the powder exposed to air and the coercivity values for the 0 hours, 2 hours and 4 hours samples were similar. The remanence value was slightly lower for the powder exposed for 2 hours with additions, and for the powder exposed for 4 hours with additions. The reduction in remanence could be due partly to the increase in the Nd- rich phase, but could also be related to the observed misalignment observed.

Even after the powder was exposed for 72 hours, a recovery of magnetic properties was observed when additions of 2 at% $NdH_{\sim 3}$ were added. This has implications for the manufacture of recycled magnets as substantial exposure of the HD powder to air can be overcome by the addition of virgin $NdH_{\sim 3}$.

16.8. Exposure of HD Powder to air with Differing Compositions

As seen previously with #R ($Nd_{29}Fe_{66}Dy_{1.98}B$ wt%) composition, the Nd- rich phase corrodes rapidly and the consequence of this is a marked reduction in the final desorption peak. To investigate this effect further, HD powder from magnets with different compositions #S, ($Nd_{25.9}$ $Fe_{58}Dy_{4.2}B$ wt%) and #R, ($Nd_{29}Fe_{66}Dy_{1.98}B$ wt%) were exposed to laboratory air for varying times. The results showed that #S composition initially displayed a reduction in the maximum peak height up to the 22 hours mark.

After 22 hours however, there was a minimal reduction in peak height, even after exposure to air for as long as 645 hours. The final desorption peak still remained similar in magnitude to that observed after 22 hours. The main differences between the two compositions were the Dy and Co contents, with the #S composition having a higher dysprosium and cobalt content.

#S composition still liberated hydrogen after the 645 hours exposure, so it is possible that passivation of the $Nd_{1-x}Dy_x$ rich phase occurs. This would explain the initial drop observed in the final desorption peak and once passivated, further corrosion would be limited. This was seen in the 645 hour sample, which still showed a desorption peak of the same magnitude as that of the after 20 hours sample. Cygan and McNallan, (1994) suggest that the presence of nitrogen improved the corrosion resistance. The improvement in stability observed in the present work is unlikely to be related to the nitrogen content as the difference between the compositions (#R and #S) was in the ppm range and the observed improvement in corrosion resistance was substantive. Thus, the likely cause for the improved stability is due to the differing amounts of Dy and Co in the sintered magnets. Yu et al, (2004) investigated the effects of alloying additions of Nb and Dy on the corrosion resistance of sintered magnets. They suggest that, as the Dy and Nb content increase, more stable intermetallic phases develop within the intergranular regions.

This could promote the electrochemical potentials of intergranular phases, thus resulting in the observed improvement in the corrosion resistance.

It is likely that the Co and Dy additions are stabilising the rare earth rich phase, possibly with the formation of the $NdCo_2$ phase suggested by Szymura et al, (1991) or by the Nd_3Co phase suggested by Verdier et al, (1994) and Mottram et al, (2000) or both. Further work needs to be carried out to determine the presence of Co in the rare earth rich phase and, if present, the form it is present in.

Chapter 17. Conclusion

Sintered magnets of a typical composition $Nd_{29}Fe_{66}Dy_{1.98}B$ (wt%) exposed to hydrogen at room temperature become fully hydrogenated. Burr milling HD powder produces a similar particle size distribution to that of the powder produced by ball milling for 1 hour. It has been shown that HD powder has a tendency to break up along the grain boundaries forming single grain particles, with some smaller attrition particles. Therefore, to reduce HD powder to a particle size similar to that of the starting grain size should only require minimal milling. The burr milling technique applied in this work has the advantage of simplicity and the ease of up-scaling. No solvents are required and hence there is no requirement to dry the powder. The work on the breakup of sintered NdFeB type magnets during the HD process and the use of burr milling to further break up the HD powder was presented at the Joint European Magnetic Symposia 2013.

With the application of a weak magnetic field to the hydrogenated powder during optical microscopy, agglomeration of the powder can be overcome. The HD-$Nd_2Fe_{14}B$ particles are ferromagnetic (relatively soft) so they can be aligned with a magnetic field. This alignment allows more information to be obtained on the particle size of the powder and, greatly enhances the ability to determine the individual particle sizes.

It has been shown that hydrogen desorption of rare earth HD powders can be monitored using a modified sintering furnace logging system. The Pirani gauge is employed to monitor the pressure and is very sensitive to changes in the hydrogen pressure, due to the excellent thermal conductivity of the gas. The process has potential for further development to improve quality control.

The reduction in the particle size of the HD powder from the sintered magnets with a composition of $Nd_{29}Fe_{66}Dy_{1.98}B$ wt%, exhibited a corresponding reduction in the rare earth $NdH_{\sim 2}$ to Nd peak. Loading the sample under inert conditions still showed a reduction in the final peak height. Recycling the HD powder sintered magnets based on the composition $Nd_{29}Fe_{66}Dy_{1.98}B$ wt%, required the additions of Nd- hydride to improve the density and magnetic properties.

The reduction in the final desorption peak ($NdH_{\sim 2}$ to Nd) was investigated on HD-$Nd_{29}Fe_{66}Dy_{1.98}B$ wt% powder exposed to air. After 24 hours of exposure, the peak was no longer visible, whilst the peak corresponding to desorption of hydrogenated $Nd_2Fe_{14}B$ was still clearly visible. The magnetic properties of the magnets made from the powder exposed to air deteriorated rapidly as the exposure time increased.

It was also shown that additions of neodymium hydride to the powder, post exposure to air, increased density and magnetic properties significantly. This indicates the importance of the rare earth rich phase during sintering and highlights the possibility of improving the properties of powders which have been exposed to air. Thermomanometric analysis during sintering could be used to determine the amount of the clean rare earth rich phase present and from this, it may be possible to determine the required amount of additional Nd- hydride to achieve the density and magnetic properties required.

There is potential for the particle size of the HD powder to be reduced even further, closer to that of the domain size (~300nm). In the literature (Nothnagel et al 1991, Namkung et al, 2011 and Li et al, 2009), it has been suggested that the decrease in properties with particle size is related to the oxidation of the rare earth rich phase. If the rare earth rich phase could be added after the $Nd_2Fe_{14}B$ particle size reduction, then oxidation of the rare earth rich phase

whilst milling would no longer be an issue. As seen in this work, the addition of neodymium hydride to the HD powder with minimal Nd-rich phase, due to corrosion, resulted in an improvement in the magnetic properties and the density. The external addition of Nd-hydride could be an effective way of targeting the intergranular region.

Chapter 18. Future Work

There is considerable scope for further investigations into various aspects of this research, with the potential for further improvements of the magnetic properties of recycled magnets and the possibility of the reduction in processing costs.

18.1. Particle Size

There is potential for improving the observation of aligned HD (milled) $Nd_2Fe_{14}B$ particles in a weak magnetic field. The current method consists of a static field generated by a sintered NdFeB magnet. The technique could be improved by employing an electromagnet so that a variable field could be applied below the mirrored surface. There could be several advantages to using a variable field. An increase in the magnitude of the field over the 200mT, employed currently, should enable the alignment of the powders with a smaller particle size to be observed. The torque observed by the magnetic particles depends on the magnetic moment and the magnitude of the applied field. This means that, potentially, the size of the particles could be determined by knowing the magnitude of the field required to cause them to align. This could provide an alternative method of determining the particle size distribution of the $Nd_2Fe_{14}B$ particles. It might also provide a means of distinguishing the Nd-rich hydride phase from the matrix particles.

18.2. Thermomanometric Analysis Technique

There are extensive potential improvements to be made to the thermomanometric analysis technique. The sensitivity of the system could be improved further by changing the volume of the system. Reducing the volume should result in a much increased sensitivity. Also, the placement of the Pirani gauge could be optimized further to increase sensitivity. There is

scope for modeling the amount of hydrogen desorbed. The voltage to pressure conversion is not linear and the conversion for output voltage to pressure was not available for hydrogen.

Comparing desorption traces of known masses of neodymium hydride or a well characterized binary hydride could give the amount of hydrogen desorbed and the corresponding voltage values recorded. From this a more accurate conversion and a model could be established.

18.3. Intergranular Additions of $NdH_{\sim 3}$ to HD Powder

The further addition of $NdH_{\sim 3}$ to the sintered magnets to see if additional $NdH_{\sim 3}$ further increases the coercivity of burr milled powder. This work is currently being carried out within the group.

18.4. Hydrogenated NdFeB Powder Exposed to Air

The corrosion of the HD powders in air showed that, for a composition of #R, the Nd rich phase corroded rapidly, whereas the composition #S showed a minimal reduction in the final $NdH_{\sim 2}$ to Nd peak, after which it appeared to be stable even up to 645 hours in air. Reports in the literature discuss the role of H_2O in the corrosion behaviour of sintered NdFeB. Unfortunately, in this study the humidity of the air was not monitored and could not be controlled during the exposure to air. Building on the current exposure to air experiments, the humidity could be recorded every 20 seconds as the sample is exposed to air.

The availability of calibrated humidity sensors presents the potential opportunity for logging the humidity of samples on exposure to air. The experiment could also be repeated in an environmental chamber where the humidity can be carefully controlled and super dry air is employed. This would have particular relevance in industrial conditions.

Exposure to air and desorption experiments could be repeated with partially degassed powder. According to the literature of Verdier et al (1994), this should show an improvement in resistance to corrosion.

More work also needs to be carried out on investigation of the intergranular Nd-rich phase in the powder exposed to air with additions such as Dy and Co. It is likely that neodymium oxides are present, potentially pinning grain boundaries and could be added deliberately as a blending agent.

The rare earth rich phase for the #S composition needs to be investigated further. It needs to be established whether the corrosion resistance is due to Co or Dy or a combination of both. The composition and structure of the rare earth rich phase should be investigated further using TEM and high resolution SEM techniques. This could be achieved by the production of a Nd Co alloy and a Nd Dy alloy. The alloys could be hydrided and added as intergranular additions to a stoichometric $Nd_2Fe_{14}B$ powder. This should provide samples with a known Nd- rich composition and guaranteeing that the Co and Dy would be contained in the Nd-rich phase. Further corrosion and exposure to air experiments can be done to determine any improvements in corrosion resistance. Co and Nd-hydride can be added to the HD-$Nd_2Fe_{14}B$ with varying ratios and the corrosion behaviour observed.

18.5. Coercivity Improvements

There is significant scope for improving the coercivity of recycled magnets by optimising the particle size distribution and reducing the particle size even further. The furnace cooling of the sintered magnets has not been optimised and various annealing treatments could be investigated in an attempt to improve the coercivity.

Appendix 1 - Table containing complete list of elements present in the ICP Sintered and starting materials.

	Al	B	Cu	Dy	Fe	Nd	Pr	Mn	Si	O	N
	%	%	%	%	%	%	%	ppm	ppm	ppm	ppm
ICP Starting Material #1	0.29	1.02	0.05	1.98	66.01	29.17	0.1	453.72	355.03	4265	95
ICP Starting Material #2	0.28	0.97	0.04	1.57	63.64	27.92	0.09	512	427	2665	90
ICP Sintered Greater Than 500 µm	0.28	0.98	0.05	1.56	64.24	28.49	0.09	476	480	5080	125
ICP Sintered Less Than 45 µm	0.28	0.99	0.06	1.58	63.45	27.71	0.1	495	427	6620	361

List of References

Arai, S. and Shibata, T. (1985) **IEEE Transactions on Magnetics**, 21 (5) p. 1952.

Bayanov, A.P. and Serebrennikov, V.V. (1964) **Distribution of Some Rare Earth Elements Between Two Molten Metals**, Zh. Neorg. Khim. Vol. 9, pp.1658 – 1661.

Bayanov, A.P. Gurskaya, S.F. and Serebrennikov, V.V. (1966) **Distribution of theRare Earth Metals and of Yttrium During the Crystallization of Zinc From a Lead Melt**, Zh. Prikl Khim, St Petersburg Russian Federation, Vol. 39, pp. 447 – 448.

Bera, P. Rajamathi, M. Hegde, M. S. and Vishnu Kamath, P. (2000) **Thermal Behaviour of Hydroxides, Hydroxysalts and Hydrotalcites Bulletin of Materials Science April 2000**, Vol. 23, Issue 2, pp. 141-145.

Boltich,E.B. Oswald,E. Huang , M.Q. Hirosawa, S. Wallace, W.E. Burzo, E. (1985) **Journal of Applied Physics** 57 (8), pp. 4106–4108.

Burns, V.S.J., Williams, A. J., Harris, I. R. (2000) **Proceedings of the 16th International Workshop on Rare-Earth Magnets and Their Applications** Japan, p. 355.

Buschow, K.H.J. (March 13, 2006) **Consice Encyclopedia of Magnetic & Superconducting Materials** Second Edition, Elsevier Science. www.elsevier.com

Cadogan, J. M. Coey, M. D, (1985) **Hydrogen absorption and desorption in Nd2Fe14B** Applied Physics Letters, Vol. 48, Issue 6.

Cadogan, J. M. Gavigan, J.P. Givord, D. Li, H.S. (1988) **A New Approach to the Analysis of Magnetisation Measurements in Rare-Earth / Transition-Metal Compounds: Application to Nd2Fe14B**, Journal of Physics F, Metal Physics, Vol.18, Number 4.

Cygan, D. F. McNallan, M. J. (1993) **Corrosion of NdFeB permanent magnets in humid environments at temperatures up to 150°C** Journal of Magnetism and Magnetic Materials, Vol. 139, Issue 1- 2, pp. 131-138.

Du, X.Y. and Graedel, T.E. (2011) **Uncovering the Global Life Cycles of Rare Earth Elements**, Scientific Reports, Vol. 3, pp. 24 – 26.

Edgley, D.S. Le Breton, J.M. Steyaert, S. Ahmed, F.M. Harris, I.R. and Teillet, J. (1997) **Characterisation of High Temperature Oxidation of Nd-Fe-B Magnets**, Journal of Magnetism and Magnetic Materials, Vol. 173, pp. 29 – 42.

Ellis, T. Schmidt, F.A. and Jones, L.L. (1994) **Methods and Opportunities in the Recycling of Rare Earth Based Materials**, in: Lidell, K.C. Bautista, R.G., Orth, R.J. (Eds.) Symposium on Metals and Materials Waste Reduction, Recovery and Remediation, at the 1994 Materials Week Meeting, Oct 1994, The Minerals, Metals & Materials Society, Pennsylvania. pp. 199 – 2006.

Feynman, Richard P. (April 1, 1999) **The Feynman Lectures on Physics**, Vol. 4. Electrical and Magnetic Behavior , Audiobook.

Fidler, J. (1985) **IEEE Transactions on Magnetics 21**, p.1955.

Fidler, J. (1987a) **Proceedings of the 5th International Symposium on Magnetic Anisotropy and Coercivity in Rare-Earth Transition Metal Alloys,** Bad-Soden, p. 363.

Fidler, J. and Skalicky, P. Mikrochim, Acta. 1 (1987b) p.115

Fidler, J. (1987c) **IEEE Transactions on Magnetics 23**, (5) p. 2106.

Harris, I. R. McGuiness, P. J. Jones, D. G. R. and Abell, J. S. (1987) **Nd-Fe-B Permanent Magnets: Hydrogen Absorption/Desorption Studies (HADS) on Nd16Fe76B8 and Nd2Fe14B**, Physica Scripta, 1987 435.

Harris, I.R. and McGuiness, P.J. (1991) **Journal of Less Common Metals**, (174) p. 1273.

Harris, I.R. Williams,A. Walton, A. Speight, J. (2012) **Magnet Recycling**, US Patent :2012/0137829.

Holc, J. Besebicar, S. and Kolar, D. (1990) **Journal of Materials Science**, 25, p. 215.

Hua, J. Yiying, H. And Jinkui, L. (1987) Sci. Sinica – A 30, p. 607.

Jiang, J. Zeng, Z. Yu, J. Wu, J. Tokunaga, M. (2001) **The Effect of Co Addition on the Fracture Strength of NdFeB Sintered Magnets**, Elsevier Science Vol. 9, Issue 4, pp. 269 – 272. www.elsevier.com.

Katter, M. Zapf , L . Blank , R. Fernengel, W. Rodewald, W. (2001) **Corrosion Mechanism of RE-Fe-Co-Cu-Ga-Al-B Magnets** 8th Joint MMM-Intermag Conference, San Antonio, Texas.

Kianvash, A. and Harris, I.R. (1991) **Journal of Applied Physics** 70 (10) p. 6453.

Kianvash, A. Knoch, K..G. and Harris, I.R. (1992a) **Journal of Alloys and Compounds** 182 p. 223.

Kianvash, A. and Harris, I.R. (1992b) **Journal of Alloys and Compounds** 178, p. 325.

Kim, J.W., Song, S.Y. & Kim, Y.D. (2012) Effect of cyclic sintering process for NdFeB magnet on microstructure and magnetic properties. Journal of Alloys and Compounds 540 p141-144

Li, W. F. Ohkubo, T. Hono, K. Sagawa, M. (2009) **The origin of coercivity decrease in fine grained Nd–Fe–B sintered magnets**, Journal of Magnetism and Magnetic Materials Vol. 321, pp. 1100 – 1105.

Liszowski, P. Turek, K. Figiel, H. and Gajerski, R. (2001) **The Intermediate Stages of the Corrosion of N-d-Fe-B Powders in Ambient Air**, Journal of Alloys and Compounds, Vol. 315, 1 – 2, pp. 270 – 275.

Lyman, J.W. & Palmer, G.R. Scrap treatment method for rare earth transition metal alloys. US Patent 5,129,945.

Matsuura, M. Fukada, T. Goto, R. Tezuka, N. and Sugimoto, S. (2010) **Influences of Oxidation State of Nd-Rich Phase on the Coercivity of Nd-Fe-B/Nd Thin Films** Materials Transactions, Vol. 51, No.10, pp. 1901 – 1904.

Meyer, L. and Bras, B. (2011) **Rare Earth Metal Recycling, Sustainable Systems and Technology**, IEEE International Symposium 16-18 May 20011, Chicago.

McGuiness, P. J. Harris, I.R. Rozendaal , E. Ormerod,. J. Ward, M. and Mate, J. (1986) Sci. 21 4107.

McGuiness, P. J. and Harris, I. R. (1988) **The Use of Hydrogen in the Production and Characterization of NdFeB magnets**, Journal of Applied Physics, Vol. 64, Issue 10.

McGuiness, P. J. Devlin, E. Harris, I.R. Rozendaal, E. and Ormerod, J. (1989) **A Study of Nd-Fe-B Magnets Produced Using a Combination of Hydrogen Decrepitation and Jet Milling**, Journal of Materials Science, Vol. 24, pp.2541 – 2548.

McGuiness, P.J. Xhang, X.J. Forsyth, H. and Harris, I.R. (1990) **Disproportionation in $Nd_{16}Fe_{76}B_8$-Type Hydrides**, Journal of The Less Common Metals, Vol. 162, pp379 – 387.

McGuiness, P.J. Fitzpatrick, L. Yartys, V.A. and Harris, I.R. (1994) **Anisotrophic Hydrogen Decrepitation and Corrosion Behaviour in NdFeB Magnets**, Journal of Alloys and Compounds, Vol. 206, pp.7 – 10.

McGuiness, P.J. Škulj, I. Porenta, A. and Kobe, S. (1998) **Magnetic Properties and Microstructure in NdDyFeBZr-HDDR**, Journal of Magnetism and Magnetic Materials, Vol 188, pp.119 – 124.

McGuiness, P.J. Kobe, S. Škulj, I. Bollero, A. Gutfleisch, O. Devlin, E.J. and Niarchos, D. (2001) **Coercivity Variations With Pr- and Zr- Substituted NdDyFeB-Based Powders**, Journal of Magnetism and Magnetic Materials, Vol237, pp. 267 - 275.

McLellan, B.C. Corderb, G.D. Golev, A. and Ali, S.H. (2013) **Sustainability of The Rare Earths Industry**, 4th International Conference on a Sustainable Future For Human Security.

Mottram, R.S. Williams, A.J. and Harris, I.R. (2000) **The Effects of Blending Additions of Copper and Cobalt to Nd16Fe76B8 Milled Powder to Produce Sintered Magnets**, Journal of Magnetism and Magnetic Materials Vol. 234, Issue 1, pp. 80 – 89.

Mottram, R.S. Davis, B. Yartys, V.A. and Harris, I.R. (2001) **The Use of Metal Hydride Powder Blending in the Production of NdFeB-type Magnets**, International Journal of Hydrogen Energy, 26 (5) pp. 441- 448, ISSN 0360-3199.

Namkung, S. Kim, D.H. and Jang, T.S. (2011) **The Effect of Particle Size Distribution on the Microstructure and Magnetic Properties of Sintered NdFeB Magnets**, Journal of Materials Science 28, pp. 185-189.

Nothnagel, P. Miiller, K. H. Eckert, D. and Handstein, A. (1991) **The Influence of Particle Size on The Coercivity of Sintered NdFeB Magnets**, Journal of Magnetism and Magnetic Materials, Vol. 101, Issues 1–3, pp. 379 – 381.

Neumann, A. and Walter, D. (2006) **The thermal transformation From Lanthanum Hydroxide to Lanthanum Hydroxide Oxide**, Thermochimica Acta 445, pp. 200 – 204.

Ohkubo, T. Hono. K, and Sagawa, M. (2009) **The origin of Coercivity Decrease in Fine Grained Nd–Fe–B Sintered Magnets**, Journal of Magnetism and Magnetic Materials Vol. 321, Issue 8, pp. 1100 –1105.

Rivoirard, S. Noudem, J.G de Rango, P. Fruchart, D. Liesert, S, and Soubeyroux, J.L. (2000) **Proceedings of the 16th International Workshop on Rare-Earth Magnets and Their Applications**, Sendai, Japan, p. 347.

Ryan, D.H. Coey, J.M.D. (1985) **An Automatic Thermanomometer for Hydrogen Absorption and Desorption Studies on Milligram Samples**, Surface and Coatings Technology, Vol. 28, Issues 3–4, July–August 1986, pp. 383 – 386.

Sagawa, M. and Nagata, H. (1993) **IEEE Transactions on Magnetics 29**, (6) (1993) p. 2747.

Sheridan, R.S. Sillitoe, R. Zakotnik, M. Harris, I.R. Williams, A.J. (2012) **Anisotropic Powder From Sintered NdFeB Magnets by the HDDR Processing Route**, Journal of Magnetism and Magnetic Materials, Vol. 324, pp. 63 – 67.

Sprecher B, Xiao Y, Walton A, Speight J, Harris R, Kleijn R, Visser G, Kramer GJ (2014) Life cycle inventory of the production of rare earths and the subsequent production of NdFeB rare earth permanent magnets. Environmental Science & Technology *48* (7), pp 3951–3958

Szymura, S. Bala, H. Pawlowska, G. Rabinovich, Y. M. Sergeev, V. V. and Pokrovskii, D.V. (1991) **Modification of the Magnetic Properties and Corrosion Resistance of Nd-Fe-B Permanent Magnets With Addition of Cobalt**, Journal of the Less Common Metals, Vol. 175, Issue 2, 1 October 1991, pp. 185 – 198.

Tang , W. Zhou, S. R. Wang, C.D.Graham, (1988) **An investigation of The Nd-rich phases in The Nd-Fe-B System**, Journal of Applied Physics, Vol. 64 Issue 10.

Tenaud, P. Vial, F. Barzasi , A. Duchene, A. and Sagawa, M. (1990b) **Proceedings of the 6th International Symposium on Magnetic Anisotropy and Coercivity in Rare-Earth Transition Metal Alloys**, Pittsburgh, p. 123.

Verdier, M. Morros, J. and Pere, D. (1994) **Stability of Nd-Fe-B Powders Obtained by Hydrogen Decrepitation, Magnetics**, IEEE Transactions on Magnetics, Vol. 30, Issue 2.

Viala, F. Jolya, F. Nevalainen, B. Sagawa, M. Hiragad, K. and Park, K.T. (2002) **Improvement in Coercivity of Sintered NdFeB Permanent Magnets By Heat Treatment**, Journal of Magnetism and Magnetic Materials 242–245, pp. 1329 – 1334.

Walton, A. and Williams, A. (2011) **Rare Earth Recovery**, Materials World Journal, Vol. 19, pp. 24 – 26.

Walton, A. Yi, H. Mann, V.S.J. Bevan, A.I. Speight, J.D. Harris, I.R. and Williams, A.J. (2012) **The Use of Hydrogen to Separate and Re-cycle NdFeB Magnets From Electronic Waste**, Proceedings of the 22nd International Workshop on Rare Earth Permanent Magnetics and Their Applications, Nagasaki, Japan, Sept 2012. pp. 10 – 13.

Wang, S.C. Li, Y. (2005) **In Situ TEM Study of Nd-rich Phase in NdFeB Magnets**, Journal of Magnetism and Magnetic Materials, Vol. 285, pp.177 – 182.

Wellens, S. Thijs, B. and Binnemans, K. (2012) **An Environmentally Friendlier Approach to Hydromettallurgy: Highly Selective Separation of Cobalt From Nickel By Solvent Extraction With Undiluted Phosphoniumionic Liquids**, Green Chemistry, Vol. 14, pp.1657 – 1665.

Williams A. J. McGuiness P. J. Harris, I. R. (1991) **Mass Spectrometer Hydrogen Desorption Studies on Some Hydrided NdFeB-type Alloy**s, Journal of the Less Common Metals, Vol. 171, Issue 1, 10 August 1991, pp. 149 – 155.

Xinhuanet, (2012) **Situation and Policies of China's Rare Earth Industry** [Online] Available from: http://news.xinhuanet.com/english/business/2012-06/20/c_131665123.htm

Xu, Y. (1999) **Liquid Metal Extraction of Nd from NdFeB Magnet Scrap**, M.S. Thesis submitted to Iowa State University, Available from: http://www.osti.gov/bridge/servlets/purl/754780-ENgwOe/ (webviewable)

Yan, G. McGuiness, P.J. Farr, J.P.G and Harris, I.R. (2010) **Optimisation of the Processing of Nd–Fe–B With Dysprosium Addition**, Journal of Alloys and Compounds, Vol. 491, Issues 1–2, 18 February 2010, pp. L20 – L24.

Yan , G. Williams, A.J. Farr, J.P.G. and Harris, I.R. (1999) **The effect of Density on the Corrosion of NdFeB magnets**, Journal of Alloys and Compounds, Vol. 292, Issues 1–2, 15 November 1999, pp. 266 – 274.

Yartys, V.A. Gutfleisch, O. Panasyuk, V.V. and Harris, I.R. (1997) **Desorption Characteristics of Rare Earth (R) hydrides (R=Y, Ce, Pr, Nd, Sm, Gd and Tb) in Relation to The HDDR Behaviour of R–Fe-Based-Compounds**, Journal of Alloys and Compounds, 253–254, pp. 128 – 133.

Yoshihiro, N. Kadono, J. Nishiuchi, S. Yamamoto, S. Tanabe, T . and Miyake, H. (2006) **Hydrogen-Desorbing Behavior of The Hydrides in 15 Rare Earth Elements Measured By Temperature Swing Column Chromatography**, Journal of Alloys and Compounds Vols. 408 – 412, 9 February 2006, pp. 355–358 Proceedings of Rare Earths '04 in Nara, Japan.

Yu, L.Q. Wen, Y.H. and Yan, M. (2004) **Effects of Dy and Nb on The Magnetic Properties and Corrosion Resistance of Sintered NdFeB**, Journal of Magnetism and Magnetic Materials, Vol. 283, Issues 2–3, December 2004, pp. 353 – 356.

Zakotnik, M. Harris, I.R. and Williams, A.J. (2008) **Possible Methods of Recycling NdFeB-type Sintered Magnets Using The HD / Degassing Process**, Journal of Alloys and Compounds, Vol. 450, (2008) pp. 525 – 531.

Zakotnik, M. Harris, I.R. and Williams, A.J. (2009) **Multiple recycling of NdFeB-type Sintered Magnets**, Journal of Alloys and Compounds, 469 (1-2). pp. 314 – 321. ISSN 0925-8388.

Additional References:

http://www.birmingham.ac.uk/documents/college-eps/metallurgy/research/magnetic-materials-background-8-domain-observation.pdf **The Kerr effect**.

www.elsevier.com/locate/jallcom (2001) **Oxidation**, Journal of Alloys and Compounds Vol. 315, pp. 270 – 275.

The Authors, Procedia Environmental Sciences 20, (2014) Published by Elsevier B.V. This is an open access article under the CC BY-NC-ND licence. http://creativecommons.org/licence/by-nc-nd/3.0/ Selection and peer-review under responsibility of the Sustain Conference Committee and supported by Kyoto University; RISH, OPIR, GCOE-ARS, and GSS as co-hosts. Also available online at: www.sciencedirect.com

Guardian. (2012) **Rare-earth mining in China comes at a heavy cost for local villages** [Online] Available from: http://www.guardian.co.uk/environment/2012/aug/07/china-rare-earth-village-pollution .

Reuters. (2009) **As Hybrid Cars Gobble Rare Metals, Shortage Looms** [Online] Available from: http://www.reuters.com/article/2009/08/31/us-mining-toyota - idUSTRE57U02B20090831